Mode-division-multiplexing as a possibility to cope with the increasing capacity demand in optical transmission systems

Clemens Koebele

Thèse de doctorat de Télécom SudParis dans le cadre de l'école doctorale S&I en co-accréditation avec l' Université d'Evry-Val d'Essonne

Spécialité :
<Télécommunications>

Par
M. Clemens KOEBELE

Thèse présentée pour l'obtention du diplôme de Docteur
de Télécom SudParis

Mode-Division-Multiplexing as a Possibility to Cope with the Increasing Capacity Demand in Optical Transmission Systems

Soutenue le 28 juin 2012 devant le jury composé de :

M.	Peter KRUMMRICH	Rapporteur
M.	Gilles PAULIAT	Rapporteur
M.	Nicolas TREPS	Président du Jury
M.	Yann FRIGNAC	Examinateur
M.	Gabriel CHARLET	Examinateur
M.	Badr-Eddine BENKELFAT	Directeur de Thèse

Thèse n° 2012TELE0014

Acknowledgements

First of all I would like to thank Sébastien and Jean-Pierre for having given me the opportunity to this work by accommodating me in their department respectively domain. I still remember very well how Sébastien analyzed my personality during the interview for my internship leading subsequently to this PhD thesis. I have actually no idea about his success rate in correctly identifying the candidates' profiles, but the quality of his team - both in personal and in professional regard - totally justifies this method, which I admittedly found a little strange in the beginning.

Secondly I would like to thank the two people who contributed the most to my professional evolution over the last almost five years: Gabriel and Max. It was a privilege and a priceless advantage to work in the same office, day by day with two of the most distinguished experts in our field. Besides, your personalities made most of the time working with you a pleasure, even though I don't share all your opinions on world politics and on conspiracy theories. Altogether I think that better conditions for a PhD thesis are hardly possible.

I would also say a big thank you to the rest of our team. Haik, Patrice, I deeply appreciate your work and the time that I could spend with you. The results of my thesis wouldn't have been possible if you hadn't been constantly "au dessus du seuil". Jérémie, Oriol, thank you for always having an open ear for questions, especially in the beginning of my work, and for enriching my time at Bell Labs. I will especially miss the Friday football sessions. Adrian, Eric, Patrick and especially Jean-Marc: be relieved, it is now official that I will never try to take over your laboratory again. Thanks nevertheless for having shared it with me over several months and also for your sense of humor and your team spirit. Amir, as the newest member of the crew you brought along another element of cultural diversity (making you perfect for the role of the scapegoat in Gabriel's sophisticated world political analyses). I hope you don't suffer too hard from it. But more important, you brought along your personality and your expertise, which both added a very positive dimension to our open space. Thanks a lot, and now enjoy your new desk!

I also express my thanks to all the other colleagues who accompanied me during these years: Jean-Christophe and his team, the members of the Bell Labs optical research domain in Stuttgart and in New Jersey, the numerous interns that contributed to our success and of course all the members of the football, ultimate Frisbee and basketball sections in Villarceaux.

Outside Bell Labs I would like to thank the project partners from the French ANR project STRADE coming from Prysmian (formerly Draka), Kylia, the IRCICA laboratory of the Université de Lille 1, Télécom SudParis and the IRISA laboratory. For my work, this project was essential, and most of the results have been enabled by the collaboration with you and I think you all did a great job.

Furthermore I express my gratitude to my Doctoral advisor, Badr-Eddine Benkelfat, and to Yann, my tutor at Télécom SudParis, as well as to the other members of the Jury.

Finally I deeply thank my family and my friends, who made this thesis possible by their constant support in all kinds of situations and by always believing in me.

Contents

List of Acronyms

ADC	Analog to digital converter
ASE	Amplified spontaneous emission
AWGN	Additive white Gaussian noise
B2B	Back to back
BPSK	Binary phase shift keying
BtB	Back to back
c.c.	Complex conjugate
CAGR	Compound average growth rate
CD	Chromatic dispersion
CDM	Code division multiplexing
CFE	Carrier frequency estimation
CMA	Constant modulus algorithm
CNLSE	Coupled nonlinear Schrödinger equation
CPE	Carrier phase estimation
DCF	Dispersion compensating fiber
DCM	Dispersion compensating module
DEMUX	Demultiplexer
DGD	Differential group delay
DGE	Dynamic gain equalizer
DSF	Dispersion shifted fiber
DSP	Digital signal processing
ECOC	European Conference and Exhibition on Optical Communication
EDFA	Erbium doped fiber amplifier
FDM	Frequency division multiplexing
FEC	Forward error correction
FIR	Finite impulse response
FMF	Few-mode fiber
FT	Fourier transform
FWM	Four wave mixing
GFF	Gain flattening filter
GVD	Group velocity dispersion
iFT	Inverse Fourier transform
ITU	International Telecommunication Union

LO	*Local Oscillator*
MDM	*Mode division multiplexing*
MIMO	*Multiple input multiple output*
MMF	*Multimode fiber*
MUX	*Multiplexer*
MZDI	*Mach-Zehnder delay interferometer*
MZM	*Mach-Zehnder modulator*
NCG	*Net coding gain*
NF	*Noise figure*
NLSE	*Nonlinear Schrödinger equation*
NLT	*Nonlinear threshold*
MM-GNLSE	*Multimode generalized nonlinear Schrödinger equation*
OFC	*Optical Fiber Communication Conference and Exhibition*
OOK	*On-off keying*
OSA	*Optical spectrum analyzer*
OSNR	*Optical signal to noise ratio*
PDF	*Probability density function*
PDL	*Polarization dependent loss*
PDM	*Polarization division multiplexing*
PMD	*Polarization mode dispersion*
PMF	*Polarization maintaining fiber*
PSK	*Phase shift keying*
PSP	*Principal state of polarization*
QAM	*Quadrature amplitude modulation*
QPSK	*Quaternary phase shift keying*
RMS	*Root mean square*
ROADM	*Reconfigurable optical add and drop multiplexer*
Rx	*Receiver*
SBS	*Stimulated Brillouin scattering*
SDM	*Space division multiplexing*
SE	*Spectral efficiency*
SMF	*Single mode fiber*
SNR	*Signal to noise ratio*
SOA	*Semiconductor optical amplifier*
SOP	*State of polarization*
SPM	*Self phase modulation*
SRS	*Stimulated Raman scattering*
SSFM	*Split step Fourier method*
SSMF	*Standard single mode fiber*
TDM	*Time division multiplexing*
Tx	*Transmitter*

WDM	*Wavelength division multiplexing*
XPM	*Cross phase modulation*

List of Symbols

∇	*Nabla operator*
$\partial/\partial x$	*Partial derivative with respect to x*
$\tilde{\alpha}(\omega)$	*Complex, frequency dependent absorption coefficient*
$\alpha(\omega)$	*Frequency dependent linear absorption coefficient*
α_2	*Two-photon absorption coefficient*
β	*Linear propagation constant*
β_n	*n-th order Taylor coefficient of the linear propagation constant*
$\beta_n^{(p)}$	*n-th order Taylor coefficient of the linear propagation constant for the mode with index p*
$\tilde{\beta}(\omega)$	*Sum of linear and nonlinear propagation constant*
γ	*Nonlinear coefficient*
γ_{pq}	*Intermodal nonlinear coefficient between the modes 'p' and 'q'*
$\Delta\beta$	*Nonlinear propagation constant*
ΔD	*Differential chromatic dispersion between two modes*
δ_{mn}	*Kronecker delta*
$\varepsilon(\omega)$	*Dielectric constant*
ε_0	*Vacuum permittivity*
ε_{NL}	*Nonlinear dielectric constant*
λ	*Wavelength*
λ_0	*Carrier wavelength*
λ_c	*Cuttoff wavelength*
μ_0	*Vacuum permeability*
ρ	*Cylindrical spatial coordinate (radial distance)*
ρ_f	*Free charge density*
σ	*Standard deviation*
σ_3	*Third Pauli matrix*
ϕ	*Cylindrical spatial coordinate (azimuth)*

$\chi^{(j)}$	*j-th order susceptibility (tensor of rank j+1)*
$\chi^{(1)}_{mn}$	*Element with index 'mn' of the 1st order susceptibility*
$\chi^{(3)}_{plmn}$	*Element with index 'plmn' of the 3rd order susceptibility*
ω	*Angular frequency*
ω_0	*Angular frequency of the carrier wave*
A	*Slowly varying complex envelope of the electrical field*
A_p	*Slowly varying complex envelope of the electrical field of mode 'p'*
$Aeff$	*Effective Area*
$Aeff,pq$	*Intermodal effective area between the modes 'p' and 'q'*
$\underline{\boldsymbol{B}}$	*Magnetic field (vectorial)*
B	*Bandwidth*
C	*Capacity*
c	*Number of bits per symbol ("subsequence length")*
c	*Speed of light*
c_{lm}	*Proportionality constant between radial mode function in core and cladding for the modes with indices l and m*
$\underline{\boldsymbol{D}}$	*Electric displacement field*
D	*Chromatic dispersion coefficient*
D_p	*PMD coefficient (or PMD link design value)*
$\underline{\boldsymbol{E}}$	*Electrical field (vectorial)*
$\boldsymbol{E}$	*Electrical field (scalar)*
E	*Slowly varying complex part of the electrical field (scalar)*
E_p	*Slowly varying complex part of the electrical field of the mode 'p'*
F	*Mode function*
F^{ρ}	*Radial mode function*
F^{ϕ}	*Angular mode function*
f	*Frequency*
f_0	*Carrier frequency*
f_{pq}	*Overlap integral between the modes 'p' and 'q'*
$\underline{\boldsymbol{H}}$	*Magnetizing field*
I	*Electrical current*
i	*Imaginary unit*
j	*Imaginary unit*
J_f	*Free current density*
$Jl(x)$	*Bessel function of first kind and of order l*
k_0	*Wavenumber*
$K_l(x)$	*Modified Bessel function of order l*
$L^{(p)}$	*Linear part of the propagation equation for the mode 'p'*
$\underline{\boldsymbol{M}}$	*Magnetic polarization*
$N^{(p)}$	*Nonlinear part of the propagation equation for the mode 'p'*

$\tilde{n}(\omega)$	Frequency dependent refractive index
$n(\omega)$	Frequency dependent linear refractive index
n_2	Nonlinear refractive index
n_{cl}	Refractive index in the fiber cladding
n_{co}	Refractive index in the fiber core
$\underline{\boldsymbol{P}}$	Electric polarization (vectorial)
$\boldsymbol{P}$	Electric polarization (scalar)
P	Power
$P_{j->i}$	Power transferred from the mode 'j' to the mode 'i'
$\underline{\boldsymbol{P}}_L$	Linear electric polarization (vectorial)
$\boldsymbol{P}_L$	Linear electric polarization (scalar)
$\underline{\boldsymbol{P}}_{NL}$	Nonlinear electric polarization (vectorial)
$\boldsymbol{P}_{NL}$	Noninear electric polarization (scalar)
P	Slowly varying complex part of the electrical polarization (scalar)
P_L	Slowly varying complex part of the linear electrical polarization (scalar)
P_L	Slowly varying complex part of the nonlinear electrical polarization (scalar)
P_{signal_i}	Average signal power of the mode 'I'
Q_{plmn}	Measure for the nonlinear interactions between the modes 'p', 'l', 'm' and 'n'
$\underline{r}$	Spatial coordinate (vectorial form)
s_n	Sequence that is to be transmitted
t	Time
T_S	Symbol duration
v_g	Group velocity
v_p	Phase velocity
x	Cartesian spatial coordinate orthogonal to the propagation direction
y	Cartesian spatial coordinate orthogonal to the propagation direction
z	Spatial coordinate in propagation direction

Introduction

In 1858, the first transatlantic cable was completed between Europe and North America. The cable not only connected the two continents, but it also opened the door for worldwide telecommunication. Since then, more and more people all over the world have been connected to a telecommunication network that has never stopped growing. Improved technologies have allowed continuously higher transmission rates and thereby have enabled various new applications, which at the same time, have boosted the demand for higher capacity.

The advent of optical data transmission in the 1980s revolutionized transmission over long distances by providing an unmatched combination of transmission capacity and reach. Since then optical transmission systems have seen a tremendous evolution, boosted by technological breakthroughs such as the erbium doped fiber amplifier (EDFA), wavelength division multiplexing (WDM) or recently the coherent detection in combination with digital signal processing (DSP). However, exponential worldwide data traffic growth by 30%-50% per year requires a steady further progress in telecommunication infrastructure including optical transmission systems. In this thesis I deal with the question of how to continue this capacity growth and one particular option called mode division multiplexing (MDM). The manuscript is structured in the following way:

In chapter 1, I will recap the required background information for the understanding of my work. First, I will discuss some basic concepts of digital communication systems, before focusing on the special case of optical fiber communication systems. Here, the physical properties of the optical fiber as a transmission channel are explained, pointing out the most important effects that limit transmission capacity and system reach. Finally, the practical realization of optical telecommunication systems is presented, arranged according to the system's three major elements: transmitter, transmission line and receiver.

Chapter 2 is devoted to the historical evolution of optical transmission systems and to the need for new technologies in order to continue the capacity growth. I start with a comparison between the growth of capacity demand and provided capacity per optical fiber over the last years. Then I discuss the technologies that enabled this capacity growth as well as the state of the art in current 100Gbit/s coherent transmission systems, to which I also contributed during this work. Looking into the future, I consider the potential that is left without a next, significant technological breakthrough, which leads to the introduction of the concept of space division multiplexing (SDM) and of the different ways to realize it. After having shortly discussed the potentials and challenges of each of these realizations, I focus on MDM as the solution, which this particular work is mainly about.

Chapter 3 is about the practical design of an MDM system: after a global system overview, each of the four new key elements is investigated in detail. These key elements are the few-mode fiber (FMF), the mode-multiplexer and mode–demultiplexer, the few-mode amplifier and the few-mode receiver including a digital signal processor.

The idea of this work was to perform experimental and/or numerical studies concerning all of these elements, in order to draw a global picture of an MDM system. Of course, this comes along with a less detailed view of the single components, where there are still numerous challenges to solve.

Finally in chapter 4 some pioneer MDM transmission experiments are presented. Our team was among the first research teams worldwide to demonstrate a mode division multiplexed transmission by transmitting independent signals over 40km using two spatial modes. Later we increased the number of exploited spatial modes to five and added optical few-mode amplification.

Chapter 1: Generalities about Optical Transmission Systems

Today's telecommunication infrastructure is not imaginable without optical transmission systems. No other technology can provide similar transmission capacity over long distances in an economically comparable way, and so optical transmission systems are the virtually exclusive solution used by telecommunication providers for their metropolitan, regional and backbone networks. The transmission distances can vary significantly: in terrestrial networks we can distinguish between metropolitan transmission links that are in the order of 100 km and backbone links connecting main cities and reaching up to more than 1000 km. With submarine cables, distances higher than 10.000 km can be bridged. Using another terminology, we also speak of long-haul transmission systems at distances between ~300 km and ~1500 km and of ultra-long-haul transmission systems at distances greater than ~1500 km.

In this chapter I will give an overview over the generalities of optical transmission systems that are important for the further understanding of my work. To do so, I will start with an introduction into some general concepts of digital transmission systems, which are also applicable to optical transmission systems. Then I will introduce the optical fiber as a physical transmission medium, since its properties are the basis of the system design around it. Finally I will describe the concrete realization of optical long-haul and ultra-long-haul transmission systems together with the key issues for performance optimization.

1.1 Transmission of Digital Signals

The objective of a digital transmission system is to transmit information from a given source to a given destination and to preserve the information despite the presence of noise and other signal perturbations. To do so, several steps are necessary, which can be broken down as depicted in Fig. 1.1.1 [1], [2]. First, the original information, such as spoken words for example, is generated by a source and is then passed into a source encoding device in order to convert the analog information into a digital signal. Afterwards, the signal is channel encoded in order to increase its robustness to signal degradations. This technique is also known as forward error correction (FEC). The resulting sequence is then modulated onto a carrier wave, transmitted over a transmission channel, detected and recovered.

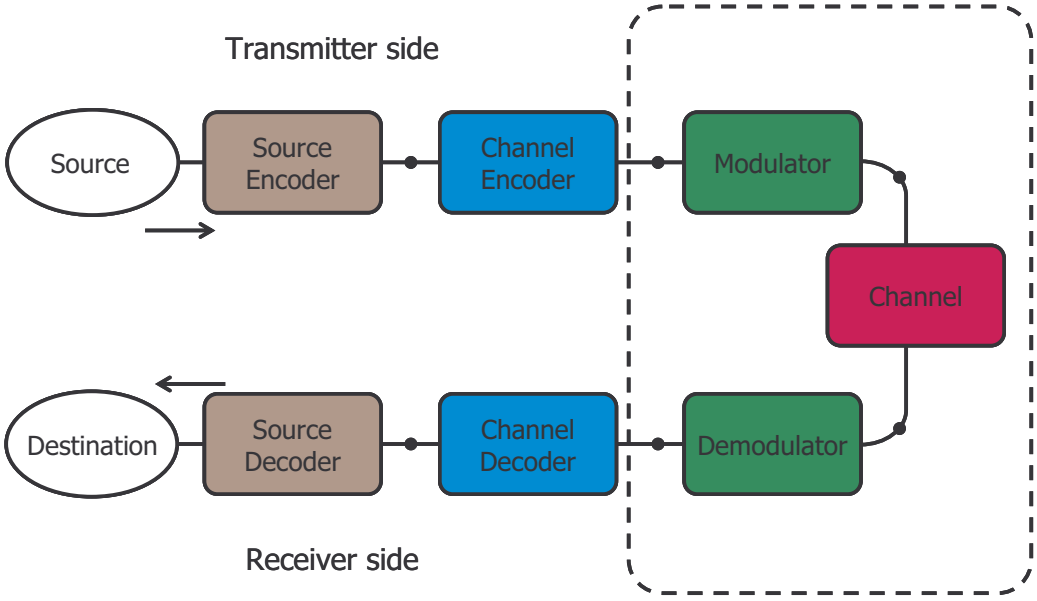

Fig. 1.1.1: Abstract representation of a digital transmission system.

In the rest of section 1.1, I will now describe the blocks of Fig. 1.1.1 that are important for the understanding of my work from an abstract point of view, while not yet taking into account the particularities of optical transmission systems. These blocks are mainly the three central ones, modulator, transmission channel, and demodulator, since the optical transmission systems considered later on can be seen as concrete realizations of them. Besides, although I will not deal with the realization of FEC, channel encoder and channel decoder are briefly described as well since they form the interface at the input and at the output of the studied systems.

1.1.1 Communication Channel

When talking about a "channel", a "transmission channel" or a "communication channel", the same expressions are used to describe two different subjects. On the one hand, they describe the physical medium that is used for signal propagation, such as an optical fiber or a copper wire. On the other hand, they describe a theoretical concept of a connection between a transmitter and receiver, as we will see more precisely in section 1.1.5 when dealing with multiplexing techniques.

In this section we will have a look at the physical transmission channel, which Proakis simply defines as "the medium that is used to send the signal from the transmitter to the receiver" [1, p. 3]. In most of the cases, signals in digital communication systems are transmitted in the form of electromagnetic waves, and so the transmission channel can be any kind of medium that allows their propagation. However, in particular, different transmission channels can vary significantly from each other and based on the more precise characteristics of the given transmission channel, the whole digital communication system is designed around it [1]. One key property is for example the classification as a guided (or bounded) medium, such as a copper wire, or as an unguided (or wireless) medium such as the atmosphere in mobile telephony. Another key property is the exploitable frequency range. Claude Elwood Shannon showed that the theoretical limit for the capacity C of a transmission channel is given by [3]

$$C = B \cdot \log_2(1 + SNR) \tag{1.1.1}$$

Nowadays, we talk about this bound as the "Shannon limit". *C* is given in *b/s* and it depends on two variables. It is proportional to the exploited bandwidth *B* given in *Hz* and proportional to the logarithm of the so-called signal to noise ratio (SNR). Noise occurs in any digital communication system, for example during detection or during amplification. It is a random signal distortion that is usually modeled as so-called additive white Gaussian noise (AWGN). AWGN is linearly superposed to the signal (additive), its value at every moment is independent of its value at any other moment (this is equivalent to an infinitely large, constant spectrum, hence it is called white) and its probability density function (PDF) follows a Gaussian distribution. In this case, the average noise power is given by its variance σ^2, where σ is the standard deviation. The importance of noise on the transmission quality is linked to the ratio between the average signal power and the average noise power, the aforementioned SNR. Assuming that the received signal has the form of a current *I*, it can be written as

$$SNR = \frac{\langle I^2 \rangle}{\sigma^2}, \tag{1.1.2}$$

where $\langle I^2 \rangle$ stands for the time average of I^2.

During propagation over the communication channel, additional signal distortions can occur. They are more difficult to generalize than noise, since they originate from the physical properties of the respective transmission medium. However, in order to exploit the capacity of a transmission channel to a maximum, it is important to know these physical properties and to develop strategies to make signal transmission as robust as possible towards the occurring effects. Thus, in section 1.2, the standard model of the optical single mode fiber transmission channel is described, and in section 3.2.1.1 it is extended to the case where signals propagate over two spatial modes at the same time.

1.1.2 Modulator and Demodulator

In order to transmit an information sequence s_n over a desired distance, it is "modulated" onto a carrier wave, which is able to propagate over the physical transmission channel.

We assume that s_n is a binary sequence of so-called bits that can take the values "0" or "1". The easiest way to modulate such a sequence onto a given carrier wave is to "shape" the wave differently for each of the two possible values. For example, this can be done by attributing high amplitude to the value "1" and low amplitude to the value "0". This modulation format is called "on-off keying" (OOK).

In order to transmit more information in the same time interval, a short subsequence $[s_k;s_{k+c}]$ of s_n can be transmitted at once, by using a modulation format that provides more than two possible states. In this case, every possible subsequence of length *c* corresponds to a so called "symbol" which is mapped onto a particular state of the electromagnetic field. An example for this method is modulation by "quadrature phase shift keying" (QPSK). Here, subsequences of length $c=2$ are formed, and the four possible combinations of "0" and "1" having the length *2* ("00", "01", "10", "11") are attributed to four different phase levels of the carrier wave. As a result, the transmitted information per time interval is doubled, since each received symbol contains two bits instead of one, as it was the case when using OOK. In this way, the number of bits per symbol can even be further increased. However, a given number of bits per symbol *c* require a number of 2^c different modulation states. This exponential growth of

modulation states with the number of bits per symbol explains the logarithmic scaling of the Shannon limit with the SNR. It makes it obvious that, in practice, the number of bits per symbol cannot be arbitrarily high.

To mathematically describe modulation, the transmitted signal can be written as the product of the carrier wave $exp(j2\pi f_0 t)$ at the carrier frequency f_0 and a term $A(t)$ accounting for modulation.

$$x(t) = A(t) \cdot \exp(j 2\pi f_0 t) \tag{1.1.3}$$

Here, $A(t)$ is given through a relationship between s_n and the modulation format. Using OOK, for example, this relationship can be written as

$$A(t) = A_0 \cdot s_n \quad ; \quad with \quad n = \left\lceil \frac{t}{T_{symb}} \right\rceil \quad . \tag{1.1.4}$$

T_{symb} is the duration of one symbol and $\lceil \ \rceil$ stands for "round upwards". For more complex modulation formats, it is more convenient to visualize them graphically. A widely used representation is the constellation diagram, which depicts the possible values for the modulation term $A(t)$ in the complex plane. Fig. 1.1.2 shows examples of constellation diagrams for some important modulation formats. I stands for the in-phase component (or the real part) and Q for the quadrature component (or the imaginary part) of a complex signal.

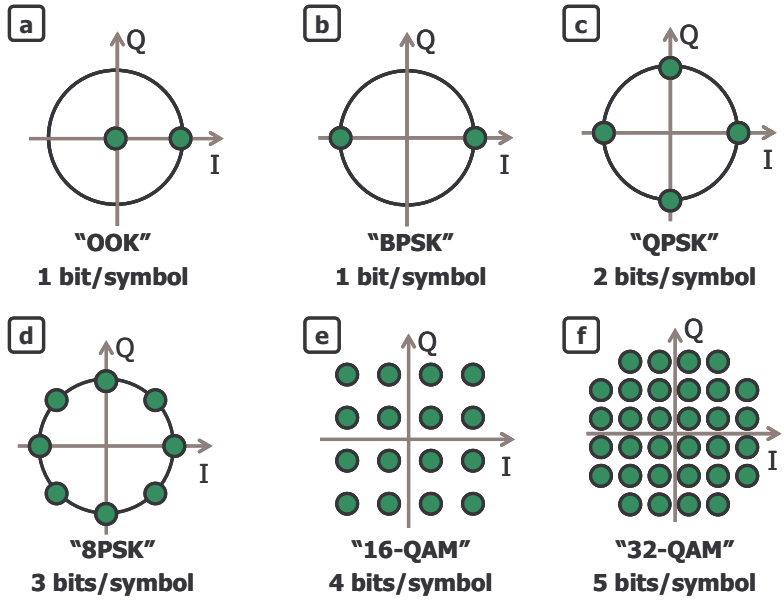

Fig. 1.1.2: Common modulation formats. (a) On-off keying (OOK). (b) Binary phase shift keying (BPSK). (c) Quaternary phase shift keying (QPSK) (d) 8-level phase shift keying (8PSK). (e) 16-state quadrature amplitude modulation (16-QAM). (f) 32-state quadrature amplitude modulation (32-QAM).

In order to recover the transmitted data sequence at the receiver side, the signal has to be demodulated. For this purpose, the information of the modulation term $A(t)$ is separated from the carrier wave before the state of each received symbol is identified.

To extract the modulation term, different demodulation schemes can be applied. Their required complexity depends on the employed modulation format. For example, with

OOK modulation, it is sufficient to measure only the intensity information during demodulation, whereas with QPSK modulation, the phase information has to be detected. QAM modulation formats require detection of both amplitude and phase. Examples for the concrete realization of different demodulation schemes in optical transmission systems will be given in section 1.3.2.

Due to noise and transmission impairments as mentioned in section 1.1.1 and due to implementation penalties in the transmitter and in the receiver, each received symbol state does usually not correspond exactly to the one initially generated at modulation. Using the representation in the complex plane this results in a spreading of the received symbol states around the initial state. Fig. 1.1.3 depicts two BPSK-constellations that suffer from different degradations. The constellation in Fig. 1.1.3a is only degraded by AWGN, whereas the constellation in Fig. 1.1.3b additionally experiences a phase shift caused by physical transmission effects in the channel.

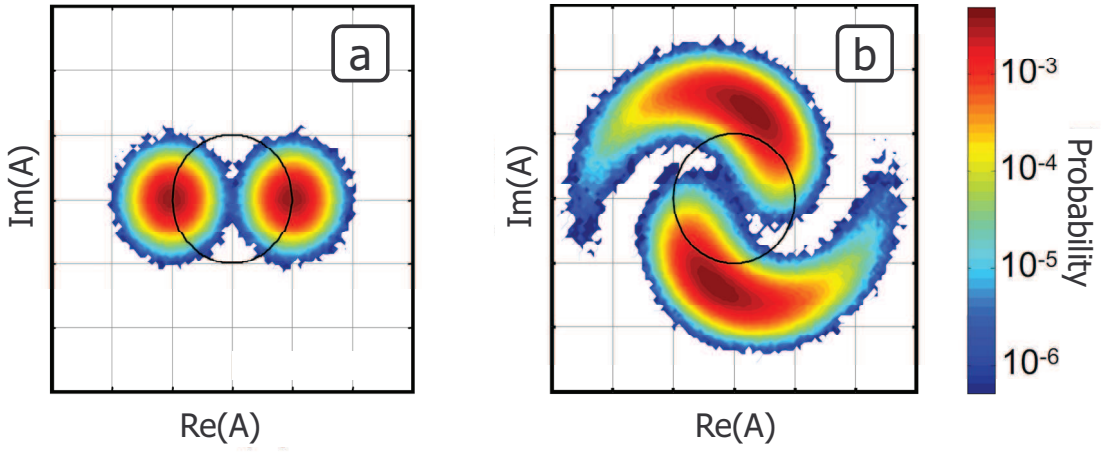

Fig. 1.1.3: BPSK-constellations after suffering from different transmission impairments.

Symbol identification is done by establishing regions in the complex plane, inside which every received symbol is attributed to the same initial symbol state. However, if signal distortions are high and the received symbols are spread too widely, they can fall into decision regions belonging to the wrong initial symbol. Then, they are identified incorrectly and so-called symbol errors occur. Depending on the mapping of bit sequences onto symbol states, each symbol error results in one or more bit errors. It is intuitive that the number of symbol errors and bit errors not only increases when the distortions get stronger but also when the distances between the possible symbol states get smaller. This is the reason why higher order modulation formats are in general more susceptible to symbol errors and bit errors. Consequently, the choice of a modulation format is usually a tradeoff between transmitted capacity and robustness to signal distortions.

1.1.3 Performance Criteria

As mentioned in the introduction to section 1.1, the objective of a digital transmission is an error free transmission. However, in reality, small perturbations are always there, and so bit errors can never be completely excluded. Hence, instead of demanding a totally error free transmission, a realistic objective is to achieve the lowest possible probability for bit errors. To measure it, we define the bit error rate (BER, sometimes

also referred to as "bit error ratio") as the number of incorrectly detected bits divided by the total number of transmitted bits.

$$BER = \frac{N_{Errors}}{N_{bits}} \tag{1.1.5}$$

Using this definition, the system performance can be estimated straight forward by transmitting a sufficiently high number of bits and by counting the received bit errors. This method is called "Monte Carlo" method. Its main drawback is its accuracy for low BERs: in order to obtain a reliable measurement, a sufficiently high number of bit errors have to be counted. It is typically in the range of ~100 to ~500 depending on the desired precision [4]. So if the required number of bit errors remains constant while the BER decreases, the number of required transmitted bits grows with *1/BER*. In the past, when systems worked at BERs between 10^{-12} and 10^{-15} [5 p.159], this made Monte Carlo method practically impossible and therefore other techniques, such as analytical BER determination have been developed. Today, thanks to progress in channel encoding and decoding (see section 1.1.4), much higher BERs are aimed at and so the problem of computational effort when using the Monte Carlo method has become less important.

Quality Factor (Q²-factor)

Originally, the Q²-factor was introduced in order to allow analytical BER determination in OOK-modulated transmission systems. [5 pp.160-163] For this purpose we suppose the scenario depicted in Fig. 1.1.4. The received signal is considered to take two different levels, one for the bit "0" and one for the bit "1". Both bits are supposed to occur with equal probability. The two states are represented by two currents I_1 and I_0. All signal distortions are modeled by additive white Gaussian noise (AWGN) with standard deviation σ_0 and σ_1. The decision threshold I_D is at the optimum level between I_1 and I_0, which can be determined as

$$I_D = \frac{\sigma_0 I_1 + \sigma_1 I_0}{\sigma_0 + \sigma_1}. \tag{1.1.6}$$

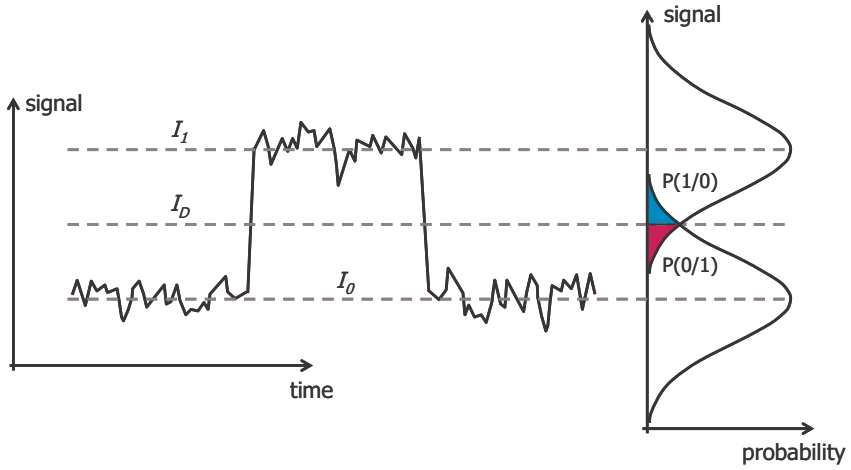

Fig. 1.1.4: Assumptions for analytical BER calculation with an OOK modulated signal, which leads to the definition of the Q²-factor [5].

In this scenario, the BER can be calculated as

$$BER = \frac{1}{2} erfc\left(\frac{Q}{\sqrt{2}}\right) \tag{1.1.7}$$

Where *erfc(x)* stands for the complementary error function defined as

$$erfc(x) = \frac{2}{\sqrt{\pi}} \int_x^\infty \exp(-y^2) dy \tag{1.1.8}$$

according to [6], and where Q is defined as

$$Q = \frac{I_1 - I_0}{\sigma_1 + \sigma_0}. \tag{1.1.9}$$

Q can be directly related to the SNR as it was defined in section 1.1.1. The relation between Q and *SNR* becomes very simple, when making two more realistic assumptions: firstly we assume that the noise is dominated by thermal noise leading to $\sigma_1 \approx \sigma_0 = \sigma_T$ and secondly we assume that $I_0 = 0$. Then we obtain [5 p.163]:

$$SNR = 4Q^2 \tag{1.1.10}$$

Since the SNR isn't proportional to Q but to Q^2 and the SNR is usually given in decibel (dB), it has been established to use Q^2 in a dB scale according to the following definition:

$$Q_{dB}^2 = 20 \cdot \log_{10} Q \tag{1.1.11}$$

Because of the linear relation between the SNR and Q^2, it is convenient to work with Q^2 instead of the BER. During this thesis, BER measurements have generally done using the Monte-Carlo method and afterwards, the corresponding Q^2-factors have been calculated from the BER by inverting equation (1.1.7) and using the result in equation (1.1.11). It leads to

$$Q_{dB}^2 = 20 \cdot \log_{10}\left(\sqrt{2} \cdot erfc^{-1}(2 \cdot BER)\right) \tag{1.1.12}$$

with *erfc^{-1}(x)* standing for the inverse complementary error function that has to be calculated numerically, as it is described in [6] for example.

1.1.4 Channel Encoder and Decoder (Forward Error Correction)

Channel encoding and decoding (or forward error correction, FEC) is not imperatively required in digital transmission systems, but it is an essential reason for the high performances obtained today. In the channel encoder, redundancy is added to the signal and thereby it is encoded in a way that a certain number of bit errors can be detected and corrected at the receiver side, as long as the bit errors remain within certain statistical properties (for example, too many subsequent bit errors can lead to a failure of the FEC). Consequently, to transmit the same amount of effective information per

time, the data rate has to be increased as a result of the transmitted redundancy. But at the same time the transmission system gets more robust to signal degradations.

In the following, we account for channel encoding and decoding by adding a so-called FEC overhead to the transmitted signal, which, in exchange, allows us to assume a threshold for a maximum BER (respectively a minimum Q^2-factor) that is sufficient for error-free transmission. We call this threshold the FEC-limit. To justify this assumption, it has been verified regularly that the occurring bit errors fulfilled the necessary statistical requirements for the application of the assumed FEC codes. Two different types of FEC codes are assumed in this work: The first one requires an FEC-overhead of 7% and provides an FEC limit at a BER of $4 \cdot 10^{-3}$ [7]. The second one requires an overhead of 25% and provides an FEC limit at a BER of $2 \cdot 10^{-2}$ [8], [9].

Finally it should be underlined that when using FEC, the design objective of the system from modulation to demodulation is no longer an error free transmission, but a transmission with a BER just below the FEC limit and the errors being distributed according to the statistical requirements of the applied code.

1.1.5 Multiplexing Techniques

Usually, the physical medium that provides the transmission channel is a limited resource which has to be used as efficiently as possible. At the same time, a single transmission channel is often not able to make use of this resource entirely, since its bandwidth might be limited. In this case, several transmission channels can be combined and sent over a shared physical medium. This technique is called "multiplexing". Motivations for multiplexing can be, for example, technological constraints such as limited transmitter- or receiver bandwidth, which then limit the channel bandwidth as well, or particular preferences on a higher system level, where in some cases a larger number of channels with lower capacity per channel might be more convenient (for example to increase the number of clients in a mobile phone cell).

Multiplexing can be done in different ways, where the channels are combined along different dimensions. Accordingly, diverse multiplexing techniques exist, such as space division multiplexing (SDM), time division multiplexing (TDM), frequency division multiplexing (FDM), or code division multiplexing (CDM).

In optical transmission systems, wavelength division multiplexing (WDM), which uses actually the same principle as FDM, is already a key technology, and SDM is considered to be a potential solution to further increase the capacity in the future [10], [11]. This work will deal with a special variant of SDM called mode-division multiplexing (MDM).

A basic element of all multiplexing techniques is that the channels must remain orthogonal with respect to each other during the whole transmission chain so that they can be separated ("demultiplexed") correctly at the receiver side without any negative impact on signal quality.

1.1.5.1 Crosstalk

In real systems, orthogonality between different multiplexed channels can be compromised. Hereby, energy from one or more channels is transferred to other channels due to various possible reasons. This phenomenon is known as "crosstalk", and obviously, the performance of a channel that suffers from crosstalk is degraded. As with any other transmission impairment, we are interested in a characterization of crosstalk and in an evaluation of its impact on system performance. Crosstalk can be very well characterized by the amount of transferred power and by the spectral overlap of the interacting signals [12–17].

Here, to account for the spectral properties, we use a simplified model, where we distinguish between two types of crosstalk to describe the majority of practically relevant cases in optical transmission systems. We call them WDM crosstalk and in-band crosstalk. Fig. 1.1.5 depicts these two crosstalk forms schematically. WDM crosstalk typically occurs in WDM systems, when channels are densely spaced and not sufficiently tightly filtered. In-band crosstalk occurs for example at optical reconfigurable add and drop multiplexers (ROADMs) or in space division multiplexed transmission systems.

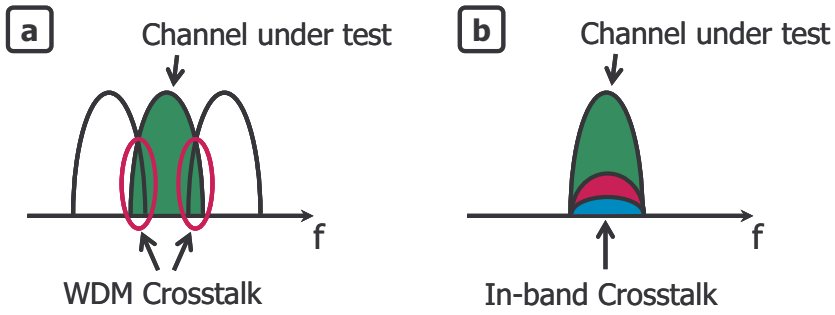

Fig. 1.1.5: Two different forms of crosstalk. (a) Side-band crosstalk. (b) In-band crosstalk.

To account for the transferred power we quantify the amount of crosstalk from channel *k* to channel *i* by the following definition.

$$Crosstalk_i = \frac{P_{k \to i}}{P_{signal\_i}} \tag{1.1.13}$$

It is thus the ratio between the disturbing signal power coming from the co-propagating channel *k* and the "useful" signal power originally present in channel *i*.

With this model the impact of crosstalk on the transmission performance can be estimated as a function of the modulation format used in the detected channel [18]. However it is virtually independent of the modulation format in the interfering channel(s) and of the modulation rate.

1.2 The Optical Fiber as a Physical Transmission Medium

In order to optimize the transmission over a given communication channel, we need to know as precisely as possible, which distortion the signal suffers from during propagation. For this purpose we will now, in section 1.2, take a look at the physical properties of the transmission medium, which in our case is the optical fiber.

1.2.1 Light Guiding in Optical Fibers

We consider the optical fiber as an ideal cylindrical structure inside a coordinate system, as depicted in Fig. 1.2.1. Light propagates in *z*- or –*z*-direction and the orthogonal plane, also called transverse plane, can be described with Cartesian coordinates *x* and *y* or with polar coordinates ϕ and ρ.

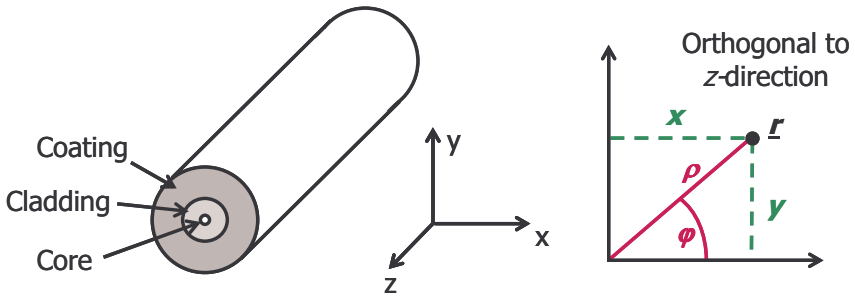

Fig. 1.2.1: Model of an optical fiber and coordinate systems

Here, "Light" will be described as an electromagnetic wave, consisting of an electrical field $\underline{\boldsymbol{E}}$ and a magnetic field $\underline{\boldsymbol{B}}$. The symbols are underlined, since we are talking about vectorial quantities and they are in bold to distinguish them from the complex, slowly varying functions introduced later. In order to precisely describe light propagation, the final objective is to know the complex values of $\underline{\boldsymbol{E}}$ and $\underline{\boldsymbol{B}}$ at any time t for any spatial coordinate $\underline{r}$. $\underline{r}$ can be decomposed into the three spatial coordinates x, y (respectively ρ, ϕ) and z according to Fig. 1.2.1. $\underline{\boldsymbol{E}}$ and $\underline{\boldsymbol{B}}$ are linked by Maxwell's equations, as we will see later, and so it is sufficient to focus on the description of one of them. Here we choose the electrical field $\underline{\boldsymbol{E}}$.

Properties of the Electrical Field

The cylindrical structure of the optical fiber has for consequence that the field distribution in the x-y-plane is independent of what happens in the propagation direction z. Hence, we can choose an approach for the electrical field as a product of two separate functions: one, depending only on x and y, which accounts for the spatial distribution of the field orthogonal to the propagation direction, and another, depending on z and t, which accounts for wave propagation. Then, the solutions for these terms can be found independently, as it will be seen at the end of this section by the equations (1.2.51) and (1.2.52), but being related to each other by the so-called propagation constant β.

As already mentioned, the electrical field should be represented by a vector in order to account for its spatial orientation – ideally by a 3-dimensional vector so that the field can point into any possible direction. However, for many applications it is sufficient to work with simpler approaches leading to reduced complexity.

The least complex, but also least general approach is to model the electric field as a scalar. It should only be used if the signal's state of polarization is not supposed to play an important role in the considered system. But in exchange, the mathematical treatment is easier. In this case, the electrical field can be written as

$$\boldsymbol{E}_{SM\_scalar}(\underline{r},t) = \frac{1}{2}\left[F(x,y)A(z,t)\exp\left(i\left(\beta_0 z-\omega_0 t\right)\right)+c.c.\right]. \qquad (1.2.1)$$

According to the considerations above, $F(x,y)$ represents the field distribution in the transverse plane, and the two other terms account for wave propagation in z-direction. Hereby, $A(z,t)$ stands for a slowly varying term, which accounts for example for signal modulation, and $\exp(i(\beta_0 z-\omega_0 t))$ represents the carrier wave at the angular frequency ω_0, propagating with the propagation constant β_0. The angular frequency ω_0 is defined as

$$\omega_0 = 2\pi f_0 \qquad (1.2.2)$$

with f_0 being the carrier frequency. c.c. stands for "complex conjugate" and its existence makes $\boldsymbol{E}_{SM\_scalar}$ always real valued. For the following mathematical considerations, it is convenient to define a complex, slowly varying expression for the electrical field, which we denote with E and which we define as:

$$E(\underline{r},t) = F(x,y)A(z,t)\exp(i\beta_0 z) \tag{1.2.3}$$

The relation between E and $\boldsymbol{E}_{SM\_scalar}$ is

$$\boldsymbol{E}_{SM\_scalar}(\underline{r},t) = \frac{1}{2}\left[E\exp(-i\omega_0 t) + \mathrm{E}^{*}\exp(i\omega_0 t)\right] \tag{1.2.4}$$

In modern optical transmission systems, signals are encoded along both polarization axes orthogonal to the propagation direction and so when modeling the optical field, polarization direction should be taken into account. To do so, the electrical field is represented as a vector with an x- and a y-component. Assuming that the z-component of the electrical field is negligible this can represent any possible state of polarization and thus allows the investigation of polarization dependent propagation effects. In this case, we can write the electrical field as:

$$\underline{\boldsymbol{E}}_{SM\_vector}(\underline{r},t) = \frac{1}{2}\begin{bmatrix} F_x(x,y)A_x(z,t)\exp(i(\beta_{0x}z-\omega_{0x}t)) + c.c \\ F_y(x,y)A_y(z,t)\exp(i(\beta_{0y}z-\omega_{0y}t)) + c.c \end{bmatrix} \tag{1.2.5}$$

or

$$\underline{\boldsymbol{E}}_{SM\_vector}(\underline{r},t) = \frac{1}{2}\begin{bmatrix} E_x\exp(-i\omega_{0x}t) + E_x^{*}\exp(i\omega_0 t) \\ E_y\exp(-i\omega_{0y}t) + E_y^{*}\exp(i\omega_0 t) \end{bmatrix} \tag{1.2.6}$$

In principal, all terms have the same signification as in the scalar case, except that now, the x- and the y-component of the electrical field are treated separately.

Both approaches require the optical field to be quasi-monochromatic, which means that the spectral width Δf of the considered pulse has to be much smaller than its carrier frequency $f_0 = \omega_0/(2\pi)$. This is the case here, since the carrier wavelength is around 1550 nm corresponding to a carrier frequency around 200 THz, and channel bandwidths are ~50 GHz. Even if we consider the whole transmission band, we obtain a bandwidth of ~4.5 THz and so the assumption is still acceptable.

In the following, we will now derive a theoretical model to find the solutions for the field distribution in the x-y-plane $F(x,y)$ (respectively F_x and F_y) and for the slowly varying envelope $A(z,t)$ (respectively A_x and A_y) after propagation in z-direction.

Derivation of the Wave Equation

In order to determine F and A for particular scenarios, we need to take a closer look at the physical conditions in an optical fiber. For that, we start with Maxwell's equations:

$$\nabla \cdot \underline{\boldsymbol{D}} = \rho_f \tag{1.2.7}$$

$$\nabla \cdot \underline{\boldsymbol{B}} = 0 \tag{1.2.8}$$

$$\nabla \times \underline{\boldsymbol{E}} = -\frac{\partial \underline{\boldsymbol{B}}}{\partial t} \tag{1.2.9}$$

$$\nabla \times \underline{\boldsymbol{H}} = \underline{\boldsymbol{J}}_f + \frac{\partial \underline{\boldsymbol{D}}}{\partial t} \tag{1.2.10}$$

E is the electric field, ***B*** is the magnetic field, ***D*** is the electric displacement field and ***H*** is the magnetizing field. $\underline{\boldsymbol{J}}_f$ is the free current density, ρ_f is the free charge density and ∇ is the Nabla-operator. Underlined symbols always represent vector quantities.

In our particular case, that is in an optical fiber, $\underline{\boldsymbol{J}}_f$ and ρ_f are zero. ***E*** and ***D*** as well as ***B*** and ***H*** are related by the so called constitutive equations:

$$\underline{\boldsymbol{D}}(\underline{r},t) = \varepsilon_0 \underline{\boldsymbol{E}}(\underline{r},t) + \underline{\boldsymbol{P}}(\underline{r},t), \tag{1.2.11}$$

$$\underline{\boldsymbol{H}}(\underline{r},t) = \frac{1}{\mu_0}\underline{\boldsymbol{B}}(\underline{r},t) + \underline{\boldsymbol{M}}(\underline{r},t), \tag{1.2.12}$$

where ***P*** is the electric polarization, ***M*** is the magnetic polarization, ε_0 is the vacuum permittivity and μ_0 is the vacuum permeability. ***M*** is *0* in a non-magnetic medium such as an optical fiber. Out of the remaining five quantities ***E***, ***B***, ***D***, ***H*** and ***P*** we can eliminate ***B***, ***D*** and ***H*** using the equations (1.2.9), (1.2.10), (1.2.11) and (1.2.12). Together with the relation $\mu_0\varepsilon_0 = 1/c^2$, we obtain

$$\nabla \times \nabla \times \underline{\boldsymbol{E}} = -\frac{1}{c^2}\frac{\partial^2 \underline{\boldsymbol{E}}}{\partial t^2} - \mu_0 \frac{\partial^2 \underline{\boldsymbol{P}}}{\partial t^2}. \tag{1.2.13}$$

We can then use the general relation

$$\nabla \times \nabla \times \underline{\boldsymbol{E}} \equiv \nabla(\nabla \cdot \underline{\boldsymbol{E}}) - \nabla^2 \underline{\boldsymbol{E}}. \tag{1.2.14}$$

Together with the fact that ρ_f is zero, expressed by

$$\nabla \underline{D} = \nabla(\varepsilon_0 \underline{\boldsymbol{E}} + \underline{\boldsymbol{P}}) = 0 \tag{1.2.15}$$

and the fact that both fiber core and fiber cladding are homogeneous media, thus leading to

$$\nabla \underline{\boldsymbol{E}} = 0, \tag{1.2.16}$$

we can simplify equation (1.2.13) to

$$\nabla^2 \underline{\boldsymbol{E}} = \frac{1}{c^2}\frac{\partial^2 \underline{\boldsymbol{E}}}{\partial t^2} + \mu_0 \frac{\partial^2 \underline{\boldsymbol{P}}}{\partial t^2}. \quad (1.2.17)$$

To solve this equation, it is convenient to work in the frequency domain. Applying a Fourier transform according to the definition

$$\underline{\hat{f}}(\underline{r},\omega) = FT\left(\underline{f}(\underline{r},t)\right) = \int_{-\infty}^{\infty} \underline{f}(\underline{r},t)\exp(i\omega t)dt \quad (1.2.18)$$

gives

$$\boxed{\nabla^2 \underline{\hat{\boldsymbol{E}}} = -\frac{\omega^2}{c^2}\underline{\hat{\boldsymbol{E}}} - \omega^2 \mu_0 \underline{\hat{\boldsymbol{P}}}}. \quad (1.2.19)$$

Relation between Electrical Field and Electrical Polarization

In order to further simplify equation (1.2.17) or equation (1.2.19) for the case of the optical fiber, we need to take into account the relation between the electrical field ***E*** and the electric polarization ***P***. In fact, it is this relation between ***E*** and ***P*** that accounts for the interactions between propagating light and our propagation medium optical fiber. Hence, it is at the origin of the physical transmission impairments that I will discuss in detail in section 1.2.4. In a general way, ***P*** can be written as [19]:

$$\begin{aligned}\underline{\boldsymbol{P}}(\underline{r},t) = {} & \varepsilon_0 \int_{-\infty}^{\infty} \chi^{(1)}(t-t')\cdot \underline{\boldsymbol{E}}(\underline{r},t')dt' \\ & + \varepsilon_0 \int\int_{-\infty}^{\infty} \chi^{(2)}\left(t-t_1^{(2)}, t-t_2^{(2)}\right) : \underline{\boldsymbol{E}}\left(\underline{r},t_1^{(2)}\right)\underline{\boldsymbol{E}}\left(\underline{r},t_2^{(2)}\right)dt_1^{(2)}dt_2^{(2)} \\ & + \varepsilon_0 \int\int\int_{-\infty}^{\infty} \chi^{(3)}\left(t-t_1, t-t_2, t-t_3\right) : \underline{\boldsymbol{E}}\left(\underline{r},t_1\right)\underline{\boldsymbol{E}}\left(\underline{r},t_2\right)\underline{\boldsymbol{E}}\left(\underline{r},t_3\right)dt_1\,dt_2\,dt_3 \\ & + \ldots\end{aligned} \quad (1.2.20)$$

Where $\chi^{(j)}$ is the so-called *j*-th order susceptibility, represented by a tensor of rank *j+1*. Clearly, this general approach would lead to an enormous complexity in the resulting equations, and so it is crucial to simplify it as much as possible without neglecting any important physical effect. Since the importance of different physical effects depends on the operating regime, this task has to be adapted to the working context.

Let us now have a look at the simplifications that are traditionally applied when dealing with optical telecommunication systems. First of all, all susceptibility terms of order higher than 3 are neglected [19 p.32]. Furthermore, thanks to symmetry of the SiO_2 molecule, $\chi^{(2)}$ vanishes for silica glass, which optical fibers consist of [19 p.17]. This leaves us with first-order susceptibility, accounting for linear propagation effects, and with third-order susceptibility, accounting for nonlinear propagation effects. Thus ***P*** can be separated into a linear and into a nonlinear polarization leading to

$$\underline{\boldsymbol{P}}(\underline{r},t) = \underline{\boldsymbol{P}}_L(\underline{r},t) + \underline{\boldsymbol{P}}_{NL}(\underline{r},t) \quad (1.2.21)$$

in the time domain, or to

$$\underline{\hat{\boldsymbol{P}}}(\underline{r},\omega) = \underline{\hat{\boldsymbol{P}}}_L(\underline{r},\omega) + \underline{\hat{\boldsymbol{P}}}_{NL}(\underline{r},\omega) \quad (1.2.22)$$

in the frequency domain, where we now continue our calculations based on equation (1.2.19).

The linear polarization is

$$\underline{\boldsymbol{P}}_L(\underline{r},t) = \varepsilon_0 \int_{-\infty}^{\infty} \chi^{(1)}(t-t') \cdot \underline{\boldsymbol{E}}(\underline{r},t')dt'. \quad (1.2.23)$$

Thanks to its linearity it can be directly transformed into the frequency domain, where the convolution of equation (1.2.23) becomes a simple product:

$$\hat{\underline{\boldsymbol{P}}}_L(\underline{r},\omega) = \varepsilon_0 \hat{\chi}^{(1)}(\omega)\hat{\underline{\boldsymbol{E}}}(\underline{r},\omega) \quad (1.2.24)$$

The expression for the nonlinear part is much more complicated:

$$\underline{\boldsymbol{P}}_{NL}(\underline{r},t) = \varepsilon_0 \iiint_{-\infty}^{\infty} \chi^{(3)}(t-t_1,t-t_2,t-t_3) \vdots \underline{\boldsymbol{E}}(\underline{r},t_1)\underline{\boldsymbol{E}}(\underline{r},t_2)\underline{\boldsymbol{E}}(\underline{r},t_3)dt_1dt_2dt_3 \quad (1.2.25)$$

In order to be able to apply equation (1.2.19), we also have to transform $\underline{\boldsymbol{P}}_{NL}$ into the frequency domain. However, in its original form this is not directly possible due to the nonlinearity. As a consequence, we have to apply some simplifications that are justifiable in our special case of optical fiber transmission systems. We start by assuming an instantaneous impulse response of the nonlinear polarization to the electrical field, which means that in equation (1.2.25) the integrals disappear and we obtain:

$$\underline{\boldsymbol{P}}_{NL}(\underline{r},t) = \varepsilon_0 \chi^{(3)} \vdots \underline{\boldsymbol{E}}(\underline{r},t)\underline{\boldsymbol{E}}(\underline{r},t)\underline{\boldsymbol{E}}(\underline{r},t), \quad (1.2.26)$$

which is equivalent to

$$\boldsymbol{P}_{NL\_p}(\underline{r},t) = \varepsilon_0 \sum_{l,m,n} \chi^{(3)}_{plmn} \cdot \boldsymbol{E}_l(\underline{r},t) \cdot \boldsymbol{E}_m(\underline{r},t) \cdot \boldsymbol{E}_n(\underline{r},t). \quad (1.2.27)$$

With *p,l,m,n = x,y or z* indicating the polarization directions of the electrical field $\underline{\boldsymbol{E}}$ components and the nonlinear polarization $\underline{\boldsymbol{P}}_{NL}$. In reality, the impulse response occurs over a timescale of 60 – 70 fs [19]. So for pulse widths of > 1 ps, which would allow modulation rates of 1 Tbaud in a single channel, the assumption is justified. However, if the whole spectrum of a wavelength division multiplexed (WDM) system (see section 1.3 for the more details on WDM) is considered, it can become necessary to include the delayed impulse response of the nonlinear polarization $\underline{\boldsymbol{P}}_{NL}$. In this case, the most important consequence is typically that energy is transferred from high-frequency components to low-frequency components due to the so-called Raman effect. The Raman effect is further described in section 1.2.4.2, but it is not included in the theoretical model presented here, since it is negligible for all theoretical considerations in this work and since its mathematical description would be quite involved.

For the next step, we need to choose between the scalar and the vectorial representation of the electrical field, as presented above in the subsection "Properties of the Electric Field". We will first have a look at the simpler case, the scalar one:

Solving the Wave Equation for a Scalar Electrical Field

For a scalar electrical field $\boldsymbol{E}$, the polarization, and consequently the first order susceptibility become scalars as well ($\underline{\boldsymbol{P}}_L$ becomes $\boldsymbol{P}_L$ and $\underline{\boldsymbol{P}}_{NL}$ becomes $\boldsymbol{P}_{NL}$). Furthermore, we can also introduce a complex, slowly varying linear polarization P_L and

a complex, slowly varying nonlinear polarization P_{NL}. They can be expressed in the following way, similar to the expression of the complex slowly varying electrical field E in equation (1.2.3):

$$\boldsymbol{P}_L(\underline{r},t) = \frac{1}{2}\left[P_L \exp(-i\omega_0 t) + \mathrm{P}_\mathrm{L}^* \exp(i\omega_0 t)\right] \quad (1.2.28)$$

$$\boldsymbol{P}_{NL}(\underline{r},t) = \frac{1}{2}\left[P_{NL} \exp(-i\omega_0 t) + \mathrm{P}_\mathrm{NL}^* \exp(i\omega_0 t)\right] \quad (1.2.29)$$

Hence, the linear polarization from equation (1.2.24) simply becomes

$$\hat{\boldsymbol{P}}_L(\underline{r},\omega) = \varepsilon_0 \hat{\chi}_{xx}^{(1)}(\omega)\hat{\boldsymbol{E}}(\underline{r},\omega). \quad (1.2.30)$$

And with the equations (1.2.3) and (1.2.28) we can write for the complex, slowly varying parts

$$\hat{P}_L(\underline{r},\omega) = \varepsilon_0 \hat{\chi}_{xx}^{(1)}(\omega)\hat{E}(\underline{r},\omega). \quad (1.2.31)$$

At the same time, the nonlinear polarization becomes

$$\boldsymbol{P}_{NL}(\underline{r},t) = \varepsilon_0 \chi_{xxxx}^{(3)} \boldsymbol{E}(\underline{r},t)\boldsymbol{E}(\underline{r},t)\boldsymbol{E}(\underline{r},t). \quad (1.2.32)$$

Together with the scalar field approach of equation (1.2.1) - (1.2.4) this can be further resolved into

$$\boldsymbol{P}_{NL}(\underline{r},t) = \frac{\varepsilon_0 \chi_{xxxx}^{(3)}}{8}\left[E^3 \exp(-i3\omega_0 t) + 3\cdot|E|^2 E \exp(-i\omega_0 t) + c.c.\right]. \quad (1.2.33)$$

The first term containing the angular frequency $3\omega_0$ can be neglected because it requires phase matching and this is not the case in the optical fibers that we are dealing with [19 p. 41]. The resulting expression can be simplified to

$$\boldsymbol{P}_{NL}(\underline{r},t) \approx \varepsilon_0 \varepsilon_{NL} \boldsymbol{E}(\underline{r},t) \quad (1.2.34)$$

also giving

$$P_{NL}(\underline{r},t) \approx \varepsilon_0 \varepsilon_{NL} E(\underline{r},t) \quad (1.2.35)$$

with

$$\varepsilon_{NL} = \frac{3}{4}\chi_{xxxx}^{(3)}|E|^2 . \quad (1.2.36)$$

For the further derivation of the propagation equation, we now assume that ε_{NL} is quasi constant in t. This is justified since the only time-dependence of E, the envelope $A(z,t)$, is varying very slowly compared to the carrier wave and by the fact that the

optical fiber is only a slightly nonlinear medium and so $\underline{\boldsymbol{P}}_{NL}$ is very small compared to $\underline{\boldsymbol{P}}_{L}$ [19]. Then we are able to perform the Fourier transform of P_{NL} and as a result, equation (1.2.35) becomes

$$\hat{P}_{NL}(\underline{r},\omega) \approx \varepsilon_0 \varepsilon_{NL} \hat{E}(\underline{r},\omega). \tag{1.2.37}$$

Afterwards, we take equation (1.2.19), replace the vectors $\underline{\boldsymbol{E}}$ and $\underline{\boldsymbol{P}}$ by the complex scalars E and P, and substitute P by making use of the equations (1.2.21), (1.2.28) to (1.2.30) and (1.2.37). Thereby we obtain

$$\nabla^2 \hat{E} = -\frac{\omega^2}{c^2}\hat{E} - \omega^2 \mu_0 \left(\varepsilon_0 \hat{\chi}_{xx}^{(1)}(\omega)\hat{E} + \varepsilon_0 \varepsilon_{NL} \hat{E}\right). \tag{1.2.38}$$

Further simplifying this equation, while applying once more the relation $\mu_0\varepsilon_0 = 1/c^2$, leads to a form of the so-called Helmholtz equation:

$$\nabla^2 \hat{E} + \varepsilon(\omega) k_0^2 \hat{E} = 0 \tag{1.2.39}$$

With the so-called "wavenumber" k_0 being

$$k_0 = \frac{\omega}{c} = \frac{2\pi}{\lambda} \tag{1.2.40}$$

and

$$\varepsilon(\omega) = 1 + \chi_{xx}^{(1)}(\omega) + \varepsilon_{NL} = 1 + \chi_{xx}^{(1)}(\omega) + \frac{3}{4}\chi_{xxxx}^{(3)}|E|^2 . \tag{1.2.41}$$

Since $\hat{\chi}_{xx}^{(1)}(\omega)$ and $\chi_{xxxx}^{(3)}$ can be complex in general, $\varepsilon(\omega)$ can be complex as well, and we define the following relationship:

$$\varepsilon(\omega) = \left(\tilde{n}(\omega) + i\frac{\tilde{\alpha}(\omega)}{2k_0}\right)^2 \tag{1.2.42}$$

Here, $\tilde{n}(\omega)$ is the refractive index and $\tilde{\alpha}(\omega)$ is the absorption coefficient. $\tilde{n}(\omega)$, respectively $\tilde{\alpha}(\omega)$, can be decomposed into a frequency dependent linear part $n(\omega)$, respectively $\alpha(\omega)$, and into a nonlinear part n_2, respectively α_2, which depends only on the intensity. They are defined by the relations

$$\tilde{n}(\omega) = n(\omega) + n_2|E|^2 \tag{1.2.43}$$

and

$$\tilde{\alpha}(\omega) = \alpha(\omega) + \alpha_2|E|^2 . \tag{1.2.44}$$

Using the equations (1.2.41), (1.2.42), and (1.2.43), $n(\omega)$ and n_2 can be calculated as

$$n(\omega) = 1+\frac{1}{2}\mathrm{Re}\left[\hat{\chi}_{xx}^{(1)}(\omega)\right] \tag{1.2.45}$$

and

$$n_2 = \frac{3}{8n}\mathrm{Re}\left(\chi_{xxxx}^{(3)}\right). \tag{1.2.46}$$

Similarly, with the equations (1.2.41), (1.2.42), and (1.2.44), $\alpha(\omega)$ and α_2 can be calculated as

$$\alpha(\omega) = \frac{\omega}{n(\omega)c}\mathrm{Im}\left[\hat{\chi}_{xx}^{(1)}(\omega)\right] \tag{1.2.47}$$

and

$$\alpha_2 = \frac{3\omega_0}{4nc}\mathrm{Im}\left(\chi_{xxxx}^{(3)}\right). \tag{1.2.48}$$

α_2 is very small in common optical fibers, and therefore it will be ignored in the following.

In order to solve the differential equation (1.2.39) we now use the definition of the electrical field according to equation (1.2.1) and equation (1.2.3), however transformed into the frequency domain:

$$\hat{E} = FT(E) = F(x,y)\hat{A}(z,\omega-\omega_0)\exp(i\beta_0 z) \tag{1.2.49}$$

Then we can substitute $\hat{E}$ in equation (1.2.39) and continue the solution by separating *F*, which depends only on *x* and *y*, from $\hat{A}$, which depends only on *z and* ω. Hereby, we can neglect the second derivative of $\hat{A}$ in *z,* because $\hat{A}$ is a slowly varying function of *z*. As a result, we obtain the following equation, which defines the eigenvalue $\tilde{\beta}$:

$$\left(\frac{\partial^2 F}{\partial x^2}+\frac{\partial^2 F}{\partial y^2}\right)\frac{1}{F}+\varepsilon(\omega)k_0^2 = \left(\beta_0^2\hat{A}-2i\beta_0\frac{\partial\hat{A}}{\partial z}\right)\frac{1}{\hat{A}} := \tilde{\beta}^2 \tag{1.2.50}$$

It leads directly to two equations for *F(x,y)* and $\hat{A}(z,\omega-\omega_0)$:

$$\boxed{\frac{\partial^2 F}{\partial x^2}+\frac{\partial^2 F}{\partial y^2}+\left(\varepsilon(\omega)k_0^2-\tilde{\beta}^2\right)F = 0} \tag{1.2.51}$$

$$\boxed{2i\beta_0\frac{\partial\hat{A}}{\partial z}+\left(\tilde{\beta}^2-\beta_0^2\right)\hat{A} = 0} \tag{1.2.52}$$

The solutions to equation (1.2.51), which are called "propagation modes" or simply "modes", give the electrical field's spatial distribution in the *x*-*y*-plane. At the same time, for each solution its eigenvalue $\tilde{\beta}$ can be determined, which turns out to be the propagation constant of the respective mode. It can also be decomposed into a linear, frequency dependent part $\beta(\omega)$, and into a nonlinear part $\Delta\beta$ according to

$$\tilde{\beta}(\omega) = \beta(\omega) + \Delta\beta . \tag{1.2.53}$$

With these pieces of information, we can then analyze wave propagation in *z*-direction by solving equation (1.2.52).

1.2.2 The Propagation Modes

In order to determine *F(x,y)*, we start solving equation (1.2.51) by making two assumptions: firstly, thanks to low optical loss in the wavelength region of interest, $\varepsilon(\omega)$ can be reduced to $\tilde{n}^2(\omega)$. Secondly, we assume that $\boldsymbol{P}_{NL}$ is a small perturbation compared to $\boldsymbol{P}$ resulting in $\boldsymbol{P} = \boldsymbol{P}_L$. The assumption is justified by the fact that the optical fiber is a very weakly nonlinear medium and it allows us to further replace $\tilde{n}(\omega)$ by $n(\omega)$. As a consequence, the nonlinear part of $\tilde{\beta}$ doesn't need to be considered either, and so we can replace it by β.

We then transform equation (1.2.51) into polar coordinates. Given the rotational symmetry of the optical fiber, this simplifies the calculations significantly. We use the identity for the two-dimensional Laplace-operator to do the coordinate transformation and obtain:

$$\frac{\partial^2 F}{\partial r^2} + \frac{1}{r}\frac{\partial F}{\partial r} + \frac{1}{r^2}\frac{\partial^2 F}{\partial \phi^2} + \left(n^2(\omega)k_0^2 - \beta^2\right)F = 0 \tag{1.2.54}$$

1.2.2.1 General Considerations for all Cylindrical Fiber Types

Given the rotational symmetry in the *x*-*z*-plane, it is more convenient to use polar coordinates, which allows splitting F into a part depending on ρ and another part depending on ϕ:

$$F(x,y) = F(\rho,\phi) = F^{\rho}(\rho)F^{\phi}(\phi) \tag{1.2.55}$$

The ϕ-dependence must be periodic with a period of integer multiples of 2π. We assume the harmonic solution

$$F^{\phi}(\phi) = \exp(-il\phi) \qquad l = 0, \pm 1, \pm 2, \ldots . \tag{1.2.56}$$

For the ρ-dependence, the case is more complicated. Fundamentally, it is determined by the so-called "index-profile" of the fiber, which specifies the refractive index *n* as a function of ρ. The index profile can be chosen by the fiber designer in order to obtain a fiber that provides the required properties such as number of modes, chromatic dispersion, effective area, etc. The most basic index-profile is the so-called step-index, where there is a constant refractive index in the fiber-core, a constant index in the fiber-

cladding and an abrupt transition between the two zones. Other common possibilities are so-called graded-index fibers, where there is a smooth transition between the refractive indices of core and cladding, or fibers with a profile consisting of a higher number of zones with different refractive indices. In Fig. 1.2.2 some examples for different index-profiles are shown.

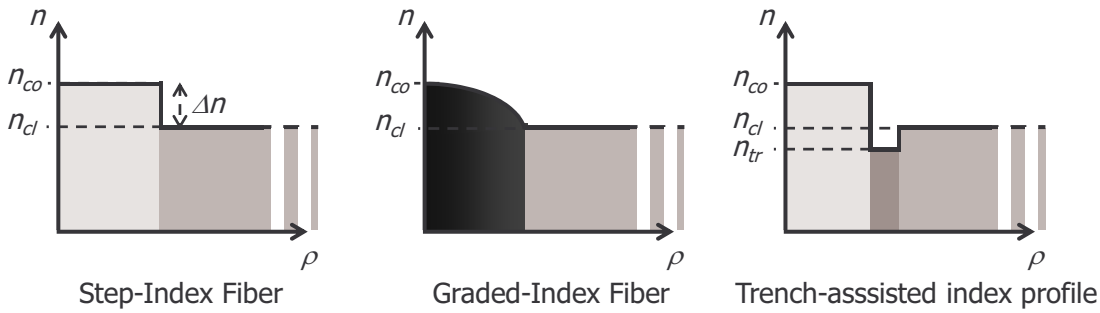

Fig. 1.2.2: Typical examples for fiber index-profiles.

So depending on the index-profile, the solution for $F_\rho(\rho)$ has to be found for the respective boundary conditions. The first step is substituting equation (1.2.56) in equation (1.2.54) to obtain the following ordinary differential equation for $F^\rho(\rho)$:

$$\frac{d^2F^\rho}{d\rho^2}+\frac{1}{\rho}\frac{dF^\rho}{d\rho}+\left(n^2k_0^2-\beta^2-\frac{l^2}{\rho^2}\right)F^\rho \quad = \quad 0 \tag{1.2.57}$$

Solving this differential equation for the boundary conditions given by the index profile $n(\rho)$leads to one solution for every guided mode. It then provides its spatial distribution by the so-called mode function *F(x,y)* as well as its propagation constant β. In the following, I will demonstrate the solution of this equation using the example of a step-index fiber.

1.2.2.2 Mode Functions for a Step-Index Fiber in the Weakly Guiding Limit

A step index fiber consists of a core with radius *a* and refractive index n_{co}, surrounded by a cladding with the refractive index n_{cl} and a radius that can be considered as being infinite. Fig. 1.2.3 depicts this schematically in form of a cut through the fiber along the *x*-*y*-plane.

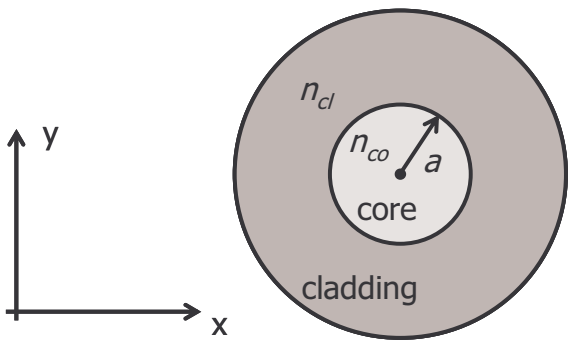

Fig. 1.2.3: Cut of a step-index fiber

The condition for light guiding requires that the propagation constant in the core is smaller than the product of wavenumber and refractive index ($\beta < n_{co}k_0$) and that the propagation constant in the cladding is higher than the product of wavenumber and refractive index ($\beta > n_{cl}k_0$) [20 p.278]. So necessarily it follows the relation $n_{co} > n_{cl}$. Based on these conditions we define two variables:

$$k_T^2 = n_{co}^2 k_0^2 - \beta^2 \tag{1.2.58}$$

is used for the solution inside the fiber core, and

$$\gamma^2 = \beta^2 - n_{cl}^2 k_0^2 \tag{1.2.59}$$

is used for the solution in the fiber cladding. For guided waves, k_T^2 and γ^2 are positive, which means that k_T and γ are real valued. The differential equation (1.2.57) can then be written in two different ways for core and cladding:

$$\frac{d^2F^\rho}{d\rho^2} + \frac{1}{\rho}\frac{dF^\rho}{d\rho} + \left(k_T^2 - \frac{l^2}{\rho^2}\right)F^\rho = 0, \text{ for } \rho < a \text{ (core)} \tag{1.2.60}$$

$$\frac{d^2F^\rho}{d\rho^2} + \frac{1}{\rho}\frac{dF^\rho}{d\rho} - \left(\gamma^2 + \frac{l^2}{\rho^2}\right)F^\rho = 0, \text{ for } \rho > a \text{ (cladding)} \tag{1.2.61}$$

Both differential equations are well known and their solutions belong to the family of Bessel functions [20 p. 278]. Since the solutions have to be physically meaningful, we exclude solutions that approach ∞ for $\rho = 0$ in the core and for r $\rightarrow \infty$ in the cladding. We then obtain:

$$F_{\rho\_core}(\rho) \propto J_l(k_T\rho), \quad \text{for } \rho < a \text{ (core)} \tag{1.2.62}$$

$$F_{\rho\_cladding}(\rho) \propto K_l(\gamma\rho), \quad \text{for } \rho > a \text{ (cladding)} \tag{1.2.63}$$

$J_l(x)$ is the Bessel function of the first kind and of order l, $K_l(x)$ is the modified Bessel function of the second kind and of order l.

Now k_T, γ and a proportionality constant have to be determined by making use of the boundary conditions. Originally, the boundary conditions require that the tangential field components of the electrical and of the magnetic field (B_z, E_z, B_φ and E_φ) are continuous at the transition of core and cladding. However, most optical fibers can be considered to be "weakly guiding" ($n_{co} \approx n_{cl}$) having for consequence that the fields in z-direction are negligible. Using this assumption, the electrical field can be described by a superposition of a polarization component in x- and in y-direction. In this case, both remaining polarization components E_x and E_y can be considered as two different propagation modes having the same propagation constant and the same spatial mode function F. Therefore we also call them "polarization modes" of the same "spatial mode". The propagation constant β and the mode function F of the two polarization modes of one spatial mode can be determined by the scalar approach for the electrical field applied here. The boundary conditions in the weakly guiding limit can be approximated by the

requirements that *F* has to be continuous at the transition between core and cladding and that it has to have a continuous derivative [20 p. 280]. Mathematically it can be expressed by:

$$F^{\rho\_core}(a) = F^{\rho\_cladding}(a) \tag{1.2.64}$$

$$\left.\frac{\partial F^{\rho\_core}}{\partial \rho}\right|_{\rho=a} = \left.\frac{\partial F^{\rho\_cladding}}{\partial \rho}\right|_{\rho=a} \tag{1.2.65}$$

In order to satisfy these conditions, it is necessary that [20 p. 280]

$$\frac{(k_T a)J_l'(k_T a)}{J_l(k_T a)} = \frac{(\gamma a)K_l'(\gamma a)}{K_l(\gamma a)}, \tag{1.2.66}$$

which allows determining k_T and γ. Equation (1.2.66) can have several solutions for each value of *l*, to which we give the index *lm*. With the results for k_{T_lm} and γ_{lm} the proportionality constant between the mode functions in core and cladding, let's call it c_{lm} for the solution *lm*, can be determined by

$$J_l(k_{T\_lm}a) = c_{lm} \cdot K_l(\gamma_{lm}a). \tag{1.2.67}$$

In order to solve equation (1.2.66), the derivatives of the Bessel functions, J_l' and K_l', can be expressed by

$$J_l'(x) = \pm J_{l\mp1}(x) \mp l\frac{J_l(x)}{x} \tag{1.2.68}$$

and by

$$K_l' = -K_{l\mp1}(x) \mp l\frac{K_l(x)}{x}. \tag{1.2.69}$$

We substitute these identities in (1.2.66), and we replace the arguments $k_T a$ and γa by defining:

$$X = k_T a \tag{1.2.70}$$

and

$$Y = \gamma a. \tag{1.2.71}$$

This leads to the characteristic equation:

$$(X)\frac{J_{l\pm1}(X)}{J_l(X)} = \pm(Y)\frac{K_{l\pm1}(Y)}{K_l(Y)} \tag{1.2.72}$$

If we have a look at the relation between X and Y given through the equations (1.2.58) and (1.2.59), it can be observed that the characteristic equation has only one independent variable. By summing up k_T^2 and γ^2, the unknown part β disappears and the result is a constant, determined directly by design parameters:

$$k_T^2 + \gamma^2 = n_{co}^2 k_0^2 - \beta^2 + \left(\beta^2 - n_{cl}^2 k_0^2\right) = \left(n_{co}^2 - n_{cl}^2\right)k_0^2 = NA^2 \cdot k_0^2 \quad (1.2.73)$$

Consequently, the sum of X^2 and Y^2 is constant as well only differing by a factor a^2. Based on this sum we define the so-called V-parameter with

$$V^2 = X^2 + Y^2 = a^2 \cdot \left(k_T^2 + \gamma^2\right) = a^2 \cdot NA^2 \cdot k_0^2 \quad (1.2.74)$$

and thus

$$V = a \cdot NA \cdot k_0 . \quad (1.2.75)$$

With this relation we can rewrite the characteristic equation as a function of one single independent variable X:

$$(X)\frac{J_{l\pm1}(X)}{J_l(X)} = \pm\left(\sqrt{V^2 - X^2}\right)\frac{K_{l\pm1}\left(\sqrt{V^2 - X^2}\right)}{K_l\left(\sqrt{V^2 - X^2}\right)} \quad (1.2.76)$$

This makes it clear that the solutions to the characteristic equation, which define the number of guided modes, are governed by the V-parameter. In other words: for a given V parameter, there are always the same solutions to the characteristic equation and so there is always the same number of guided modes. However, the concrete properties of the guided modes, notably mode function F and propagation constant β, depend also on the interplay of the other parameters n_{co}, n_{cl}, a and ω (respectively λ).

Today, the easiest way to solve the characteristic equation is to do it numerically, but for a better understanding, the solutions can also be determined graphically. Fig. 1.2.4 shows an example for the graphical solutions to some characteristic equations of the same fiber. Please note that for every fiber, there are different characteristic equations for different values of l. However, it is possible that a characteristic equation for a given value of l has no solution for $X > 0$ and $Y > 0$. And if this is the case for $l = l_{stop}$, it is also the case for $l > l_{stop}$. Hence, the characteristic equations for these higher values of l are of no practical interest. The only characteristic equation that has always at least one solution is the one for $l = 0$.

In traditional optical transmission systems the fibers are designed in a way that only this single solution exists for the wavelengths of interest. Therefore fibers are called single mode fibers (SMF) and they have the advantage that light propagation is much easier to deal with since potential interactions between different spatial modes with different propagation constants cannot occur. For shorter wavelengths the number of guided modes increases and so an important property of SMFs is their cutoff wavelength λ_c. When working below λ_c the fiber is no longer single-mode.

The concept of MDM presented in this work is based on a completely different approach: here we use fibers with a few guided spatial modes and try to transmit independent signals over each mode.

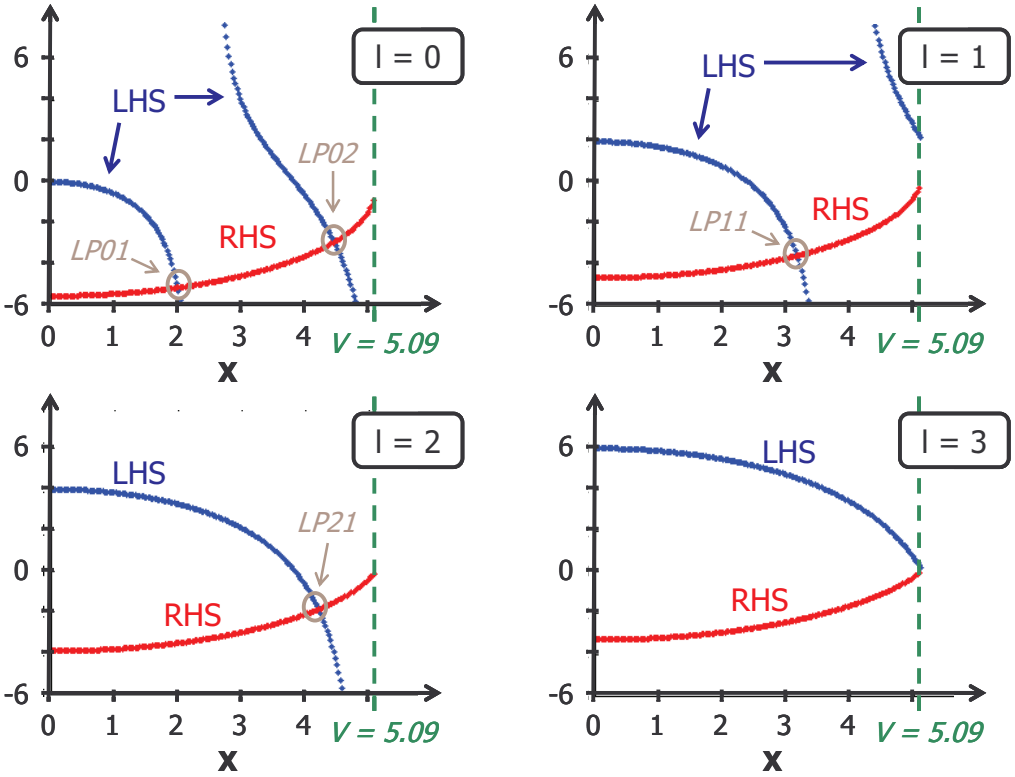

Fig. 1.2.4: Graphical solutions of characteristic equation in a step-index fiber with V = 5.09, for $l \geq 0$. RHS stands for the right hand side of equation (1.2.76) and LHS stands for the left hand side of equation (1.2.76).

The propagation modes obtained by the solutions of the set of characteristic equations are denoted as "*LPlm*" with *l* having been introduced in equation (1.2.56) and with *m* being a running index for the solutions to each characteristic equation as it already appears in equation (1.2.67). In the example of Fig. 1.2.4 this results in the modes LP01, LP02, LP11 and LP21. LP stands for "linearly polarized" originating in the simplifying assumptions that we have made during the definition of the boundary conditions.

With the solutions of the characteristic equations, $k_{T\_lm}^2$ and γ_{lm}^2 can be determined straight forward for each mode *LPlm* by making use of equations (1.2.70) and (1.2.71). Then β can be calculated with equation (1.2.58) or equation (1.2.59). Another widely used parameter to characterize a propagation mode is its effective mode index n_{eff}. It is defined according to

$$n_{eff} = \frac{\beta}{k_0}. \tag{1.2.77}$$

In order to obtain the radial dependence F_{lm}^{ρ} of the spatial mode function F_{lm}, the results of $k_{T\_lm}^2$ and $\gamma_{\_lm}^2$ can be used in equation (1.2.67) to determine the proportionality constants c_{lm} between the radial mode functions in the core, $J_l\left(k_{T\_lm}\rho\right)$, and in the cladding, $K_l\left(\gamma_{lm}\rho\right)$, belonging to the mode *LPlm*.

It turns out that the modes *LPlm* and *LP-lm* have the same propagation constant and so they form a basis for any linear combination of them, which has the same propagation constant as well. All the modes resulting herefrom are called "degenerate".

Now we combine radial and azimuthal mode functions and use two orthogonal linear combinations of *LP-lm* and *LPlm* in order to form a new basis, whose azimuthal dependence is purely real or purely imaginary. We make use of the property

$$F_{lm}^{\rho} = -F_{-lm}^{\rho} \tag{1.2.78}$$

and then we choose the new basis according to:

$$F_{lma} = -\frac{i}{2}\left(F_{lm}^{\rho}\exp(-il\phi)+F_{-lm}^{\rho}\exp(il\phi)\right) = F_{\rho\_lm}\sin(l\phi) \tag{1.2.79}$$

$$F_{lmb} = \frac{1}{2}\left(F_{lm}^{\rho}\exp(-il\phi)-F_{-lm}^{\rho}\exp(il\phi)\right) = F_{\rho\_lm}\cos(l\phi) \tag{1.2.80}$$

We denote the two resulting real valued mode functions as *LPlma* and *LPlmb*. To get an idea of typical mode functions in step index fibers, Fig. 1.2.5 shows the mode functions for a slightly multimodal step index fiber with a *V*-parameter of 7.48.

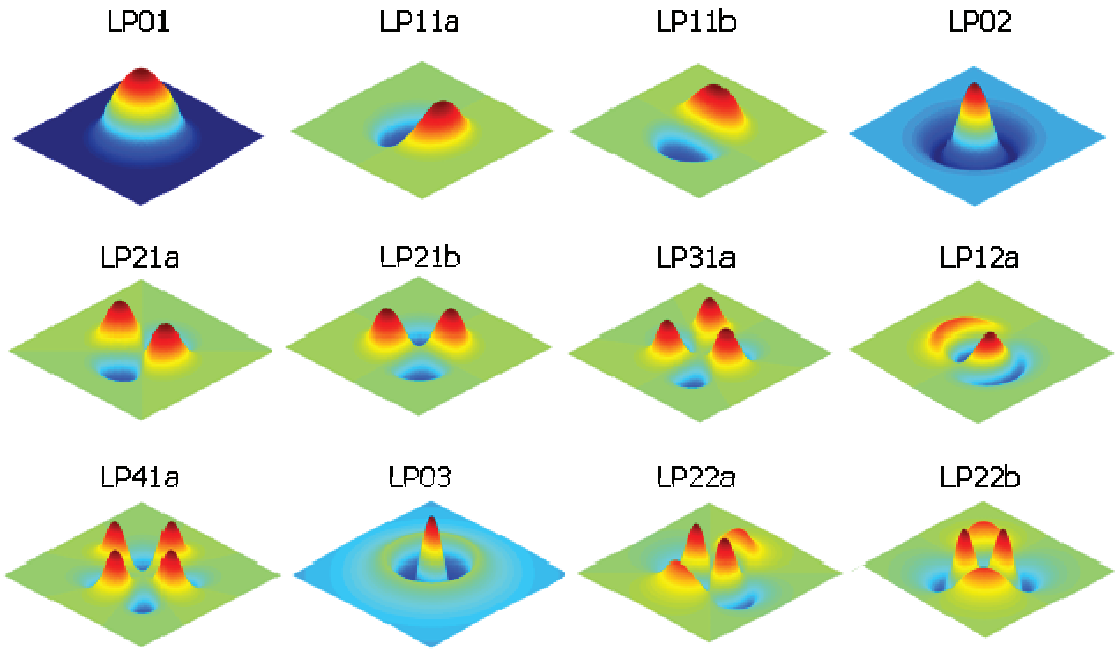

Fig. 1.2.5: Mode functions in order of appearance in a step-index fiber with V = 7.48 (not all degenerate modes are depicted).

Ending this section I would like to underline once more that the *LP*-modes presented here are a good approximation but not the exact solution to the physical problem. In the rest of this work I will work with this approximation by referring to the *LP*-modes and by basing myself on their properties. A detailed description of a more realistic model and of its derivation can be found in [20 chapters 7 & 8] for example.

Limitations of the *LP*-model concern especially two modes that are degenerate in that approach. The fact that they are degenerate leads to a DMGD of 0, whereas using a more realistic model, DMGD is usually in the order of magnitude of 10 ps/km depending

on the modes and on the fiber design. This aspect is crucial for DSP and so it will be considered again in section 3.5.2.

1.2.3 Signal Propagation

A typical scenario for numerical studies is, that a signal *A(t,0)* is given at the fiber input defined as *z = 0*, and the signal *A(t,d)* at the fiber output *z = d* shall be calculated. To do so, we have to describe how the electrical field evolves during propagation in *z*- (or –*z*-) direction.

1.2.3.1 Propagation Equation for a Scalar Field

To get a good approximation of propagation effects, we have to reintroduce attenuation and nonlinear index-coefficient, which have been omitted during the calculation of the propagation mode, both together manifested by a term Δn. The equations (1.2.42) - (1.2.47) can be written differently in order to obtain a convenient definition for Δn (Remember that the nonlinear attenuation term α_2 is neglected). It results in

$$\varepsilon(\omega) = \left(n(\omega) + n_2 |E|^2 + i \frac{\tilde{\alpha}(\omega)}{2k_0} \right)^2 := \left(n(\omega) + \Delta n(\omega) \right)^2 , \tag{1.2.81}$$

and so it follows

$$\Delta n(\omega) = n_2 |E|^2 + i \frac{\alpha(\omega)}{2k_0} . \tag{1.2.82}$$

Δn has only a negligible impact on the mode functions $F_p(x,y)$, but now for the modeling of the propagation of the field in *z*-direction the eigenvalue $\tilde{\beta}$ has to be considered including its nonlinear term $\Delta\beta$ as it has been introduced in equation (1.2.53). $\tilde{\beta}(\omega)$ can be recalculated in consideration of Δn, resulting in the following expression for the nonlinear propagation constant $\Delta\beta$ [19 p.43]:

$$\Delta\beta = \frac{k_0 \iint \Delta n |F(x,y)|^2 \, dxdy}{\iint |F(x,y)|^2 \, dxdy} \tag{1.2.83}$$

We now start solving equation (1.2.52) by substituting $\tilde{\beta}(\omega)$ with equation (1.2.53) and by using the approximation

$$\tilde{\beta}^2 - \beta_0^2 \approx 2\beta_0 \left(\tilde{\beta} - \beta_0 \right). \tag{1.2.84}$$

It leads to

$$\frac{\partial \hat{A}}{\partial z} = i \left(\beta(\omega) + \Delta\beta - \beta_0 \right) \hat{A} . \tag{1.2.85}$$

This equation expresses that the propagating signal experiences a phase-shift that depends on its frequency, manifested by ($\beta(\omega)$), and a phase-shift that depends on its intensity, manifested by ($\Delta\beta$). To continue the solution, the frequency dependent propagation constant $\beta(\omega)$ can be decomposed into a Taylor-series:

$$\beta(\omega) = \beta_0 + (\omega-\omega_0)\beta_1 + \frac{1}{2}(\omega-\omega_0)^2\beta_2 + \frac{1}{6}(\omega-\omega_0)^3\beta_3 + \ldots \quad (1.2.86)$$

with

$$\beta_m = \left(\frac{d^m\beta}{d\omega^m}\right)_{\omega=\omega_0}, \text{ with } m = 1,2,\ldots \quad (1.2.87)$$

The different β_m-terms account for different propagation effects: β_0 (which falls away because of the opposite signs in equations (1.2.85) and (1.2.86)) is related to the phase velocity v_p of the radial frequency ω_0 by the relation

$$v_p = \frac{\omega_0}{\beta_0}, \quad (1.2.88)$$

β_1 is the inverse of the group velocity v_g; β_2 is related to the chromatic dispersion and β_3 to the dispersion slope. A more detailed interpretation of the physical propagation effects related to β will be given in section 1.2.4. For our application, it is usually sufficient to consider no β_m with $m > 3$. Even β_3 can often be neglected, except when the chromatic dispersion around the wavelength of interest is close to zero or when the considered band is very large.

For the next step, we replace ($\beta(\omega)$) in equation (1.2.85) by its Taylor-series until the term containing β_3, and we apply the inverse Fourier transform to the resulting equation, according to the following definition:

$$\underline{f}(\underline{r},t) = FT^{-1}\left(\hat{\underline{f}}(\underline{r},\omega-\omega_0)\right) = \frac{1}{2\pi}\int_{-\infty}^{\infty}\hat{\underline{f}}(\underline{r},\omega-\omega_0)\exp(-i(\omega-\omega_0)t)dt \quad (1.2.89)$$

Through the Fourier transform, $(\omega-\omega_0)$ is replaced by $i(\partial/\partial t)$ and so equation (1.2.85) becomes:

$$\frac{\partial A}{\partial z} = -\beta_1\frac{\partial A}{\partial t} - \frac{i\beta_2}{2}\frac{\partial^2 A}{\partial t^2} + \frac{1}{6}\beta_3\frac{\partial^3 A}{\partial t^3} + i\Delta\beta A \quad (1.2.90)$$

Finally we replace $\Delta\beta$ by an expression accounting for the nonlinear phase shift. Therefore we use equation (1.2.83), substitute Δn with equation (1.2.82), and after simplifying the expression we obtain

$$\Delta\beta = \gamma|A|^2 + i\frac{\alpha}{2} \quad (1.2.91)$$

with the nonlinear coefficient γ being

$$\gamma = \frac{n_2 \omega_0}{c A_{eff}} \tag{1.2.92}$$

and the effective area being

$$A_{eff} = \frac{\left(\iint |F(x,y)|^2 dxdy\right)^2}{\iint |F(x,y)|^4 dxdy}. \tag{1.2.93}$$

Substituting equation (1.2.91) in equation (1.2.90) yields the so called nonlinear Schrödinger equation (NLSE):

$$\frac{\partial A}{\partial z} + \frac{\alpha}{2} A + \beta_1 \frac{\partial A}{\partial t} + \frac{i}{2} \beta_2 \frac{\partial^2 A}{\partial t^2} - \frac{1}{6} \beta_3 \frac{\partial^3 A}{\partial t^3} = i\gamma |A|^2 A \tag{1.2.94}$$

1.2.3.2 Propagation Equation for a Vectorial Field in x- and y-Direction

For the propagation of a scalar field, we only used one element of the third order susceptibility. But in fact, since it is actually a fourth-rank tensor in three dimensions, it consists of $3^4 = 81$ elements. Fortunately in our case, we can limit its complexity considerably. First of all, we consider the z-component of the electric field as negligible, which reduces the number of elements to $2^4 = 16$. And then, the silica glass which the optical fiber consists of can be treated as an isotropic medium. This has the consequence, that only three independent elements remain, and all the other elements can be expressed in terms of them according to the following relation [21]:

$$\chi^{(3)}_{plmn} = \chi^{(3)}_{xxyy} \delta_{pl} \delta_{mn} + \chi^{(3)}_{xyxy} \delta_{pm} \delta_{\ln} + \chi^{(3)}_{xyyx} \delta_{pn} \delta_{lm} \tag{1.2.95}$$

The indices are $p,l,m,n = x$ or y, and δ_{mn} is the Kronecker delta, which is defined such that $\delta_{mn} = 1$ when $m = n$, and $\delta_{mn} = 0$ when $m \neq n$. Substituting equation (1.2.95) in equation (1.2.26), followed by a procedure similar to the one described in the scalar case (section "Solving the Wave Equation for a Scalar Electrical Field") gives

$$P_{NL\_p} = \frac{3\varepsilon_0}{4} \sum_l \left(\chi^{(3)}_{xxyy} E_p E_l E_l^* + \chi^{(3)}_{xyxy} E_l E_p E_l^* + \chi^{(3)}_{xyyx} E_l E_l E_p^* \right) \tag{1.2.96}$$

with $p,l = x$ or y. From equation (1.2.95) we can also see that it is

$$\chi^{(3)}_{xxxx} = \chi^{(3)}_{xxyy} + \chi^{(3)}_{xyxy} + \chi^{(3)}_{xyyx}. \tag{1.2.97}$$

Hereby $\chi^{(3)}_{xxxx}$ is the term that has been used in the scalar case, notably in the definition of n_2. The relative importance of $\chi^{(3)}_{xxyy}$, $\chi^{(3)}_{xyxy}$ and $\chi^{(3)}_{xyyx}$ depends on the physical properties of the considered medium. In our case, we can suppose that all three values are identical [22]. With this information we can simplify equation (1.2.96) and write it down for $p = x$ and q = y, respectively for $p = y$ and $q = x$.

$$P_{NL\_x} = \frac{3\varepsilon_0}{4}\chi^{(3)}_{xxxx}\left[\left(\left|E_x\right|^2+\frac{2}{3}\left|E_y\right|^2\right)E_x+\frac{1}{3}\left(E_x^*E_y\right)E_y\right] \quad (1.2.98)$$

$$P_{NL\_y} = \frac{3\varepsilon_0}{4}\chi^{(3)}_{xxxx}\left[\left(\left|E_y\right|^2+\frac{2}{3}\left|E_x\right|^2\right)E_y+\frac{1}{3}\left(E_y^*E_x\right)E_x\right] \quad (1.2.99)$$

Together with the linear polarization terms being

$$\hat{P}_{L\_x}(\underline{r},\omega) = \varepsilon_0\hat{\chi}^{(1)}_{xx}(\omega)\hat{E}(\underline{r},\omega) = \varepsilon_0\hat{\chi}^{(1)}_{xx}(\omega)F(x,y)\hat{A}(\underline{r},\omega) \quad (1.2.100)$$

and

$$\hat{P}_{L\_y}(\underline{r},\omega) = \varepsilon_0\hat{\chi}^{(1)}_{yy}(\omega)\hat{E}(\underline{r},\omega) = \varepsilon_0\hat{\chi}^{(1)}_{yy}(\omega)F(x,y)\hat{A}(\underline{r},\omega) \quad (1.2.101)$$

as well as the slowly varying, complex valued part of the electrical field in the frequency domain given by

$$\underline{\hat{E}}_{SM\_vector}(\underline{r},\omega) = \begin{bmatrix}F_x(x,y)\hat{A}_x(z,\omega-\omega_0)\\F_y(x,y)\hat{A}_y(z,\omega-\omega_0)\end{bmatrix}\exp(i\beta_0 z), \quad (1.2.102)$$

we can transform the wave equation (1.2.19) in its general vectorial form into a set of two coupled equations [19 p. 207] :

$$\frac{\partial A_x(z,t)}{\partial z}+\frac{\alpha^x}{2}A_x+\beta_1^x\frac{\partial A_x}{\partial t}+\frac{i}{2}\beta_2^x\frac{\partial^2 A_x}{\partial t^2}-\frac{1}{6}\beta_3^x\frac{\partial^3 A_x}{\partial t^3} = i\gamma\left(\left|A_x\right|^2A_x+\frac{2}{3}\left|A_y\right|^2A_x+\frac{1}{3}A_y{}^2A_x{}^*\right) \quad (1.2.103)$$

$$\frac{\partial A_y(z,t)}{\partial z}+\frac{\alpha^y}{2}A_y+\beta_1^y\frac{\partial A_y}{\partial t}+\frac{i}{2}\beta_2^y\frac{\partial^2 A_y}{\partial t^2}-\frac{1}{6}\beta_3^y\frac{\partial^3 A_y}{\partial t^3} = i\gamma\left(\left|A_y\right|^2A_y+\frac{2}{3}\left|A_x\right|^2A_y+\frac{1}{3}A_x{}^2A_y{}^*\right) \quad (1.2.104)$$

The procedure is similar to the one for the scalar case, which has been demonstrated in the subsection "Solving the Wave Equation for a Scalar Electrical Field" and in section 1.2.3.1. We observe that in equation (1.2.103) and (1.2.104) each polarization can be characterized by its own propagation constants β_n^x and β_n^y, and that different nonlinear terms occur containing combinations of the fields in *x*- and in *y*-polarization. An interpretation of these terms is given in section 1.2.4.2.

1.2.3.3 Solving the Propagation Equations

To solve the NLSE and the CNLSEs, usually the so-called split-step Fourier method (SSFM) is applied. To do so, the equations are first separated into a linear part and into a nonlinear part. In the more general case of the CNLSE this is done such that

$$\frac{\partial A_p(z,t)}{\partial z} = L^{(p)}(z,t) + N^{(p)}(z,t) \tag{1.2.105}$$

with the linear part being

$$L^{(p)} = -\frac{\alpha^{(p)}}{2} A_p - \beta_1^{(p)} \frac{\partial A_p}{\partial t} - \frac{i}{2}\beta_2^{(p)} \frac{\partial^2 A_p}{\partial t^2} + \frac{1}{6}\beta_3^{(p)} \frac{\partial^3 A_p}{\partial t^3} \tag{1.2.106}$$

and the nonlinear part being

$$N^{(p)} = i\gamma\left(\left|A_p\right|^2 A_p + \frac{2}{3}\left|A_q\right|^2 A_p + \frac{1}{3} A_q{}^2 A_p{}^* \right) \tag{1.2.107}$$

p and q with $p,q \in \{x,y\} \wedge p \neq q$ represent the two polarization components of the electrical field.

After this separation, the differential equations

$$\frac{\partial A_p(z,t)}{\partial z} = L^{(p)}(z,t) \tag{1.2.108}$$

and

$$\frac{\partial A_p(z,t)}{\partial z} = N^{(p)}(z,t) \tag{1.2.109}$$

are solved separately. For sufficiently small steps Δz, solving equations (1.2.108) and (1.2.109) alternately, and thus propagating in small, alternating linear and nonlinear steps through the fiber provides a sufficiently good approximation to the real solution of the NLSE and the CLNSEs [19 p. 52]. In the linear step, described by equation (1.2.106), the evolution of the field in one polarization p does not depend on the field in the orthogonal polarization q and so equation (1.2.108) can be solved independently for $p = x$ and $p = y$. The solution to equation (1.2.108) can be written as

$$A_p(z+\Delta z) = \exp\left(\Delta z \cdot \left(-\frac{\alpha^{(p)}}{2} - \beta_1^{(p)} \frac{\partial}{\partial t} - \frac{i\beta_2^{(p)}}{2} \frac{\partial^2}{\partial t^2} + \frac{\beta_3^{(p)}}{6} \frac{\partial^3}{\partial t^3} \right) \right) \cdot A_p(z), \tag{1.2.110}$$

and the exponential term can be evaluated in the frequency domain. By applying a Fourier transform, $i(\partial/\partial t)$ is replaced by ω and the term is computed at a given frequency $\omega = \omega_0$. Then the inverse Fourier transform is applied and the result is multiplied with the electrical field at the input of the linear step:

$$A_p(z+\Delta z) = FT^{-1}\left\{\Delta z \cdot \left(-\frac{\alpha^{(p)}}{2} + i\left(\beta_1^{(p)}\omega + \frac{\beta_2^{(p)}}{2}\omega^2 + \frac{\beta_3^{(p)}}{6}\omega^3\right)\right)\right\} \cdot A_p(z) \quad (1.2.111)$$

In contrast to the behavior in the linear step, the fields in both orthogonal polarizations influence each other during the nonlinear step given by equation (1.2.109). Hence, its solution is computed jointly for both polarizations using $N^{(x)}$ with $p = x$ and $p = y$, and using $N^{(y)}$ with $p = y$ and $q = x$. Applying the vectorial notation for the electrical field $\underline{A} = \left[A_x, A_y\right]^T$, the nonlinear step based on equations (1.2.107) and (1.2.109) can be rewritten as

$$\frac{\partial \underline{A}}{\partial z} = i\gamma\left(|\underline{A}|^2 \underline{A} - \frac{1}{3}\left(\underline{A}^{*T}\sigma_3 \underline{A}\right)\sigma_3 \underline{A}\right) \quad (1.2.112)$$

with σ_3 being the third Pauli matrix defined as

$$\sigma_3 = \begin{bmatrix} 0 & -i \\ i & 0 \end{bmatrix} \quad (1.2.113)$$

Finally, the solution to equation (1.2.112) for sufficiently short steps Δz is given by:

$$\underline{A}(z+\Delta z) = \exp\left(i\gamma\Delta z|\underline{A}|^2\right)\exp\left(-\frac{i\gamma\Delta z}{3}\left(\underline{A}^{*T}\sigma_3\underline{A}\right)\sigma_3\right)\cdot\underline{A}. \quad (1.2.114)$$

Please note that the argument in the first exponential is a scalar, whereas the argument in the second exponential is a *2x2*-matrix. Hence, the second "exp" operator represents the matrix exponential function.

The practical implementation of a simulation tool for propagation over an optical single mode fiber can be summarized as depicted in Fig. 1.2.6.

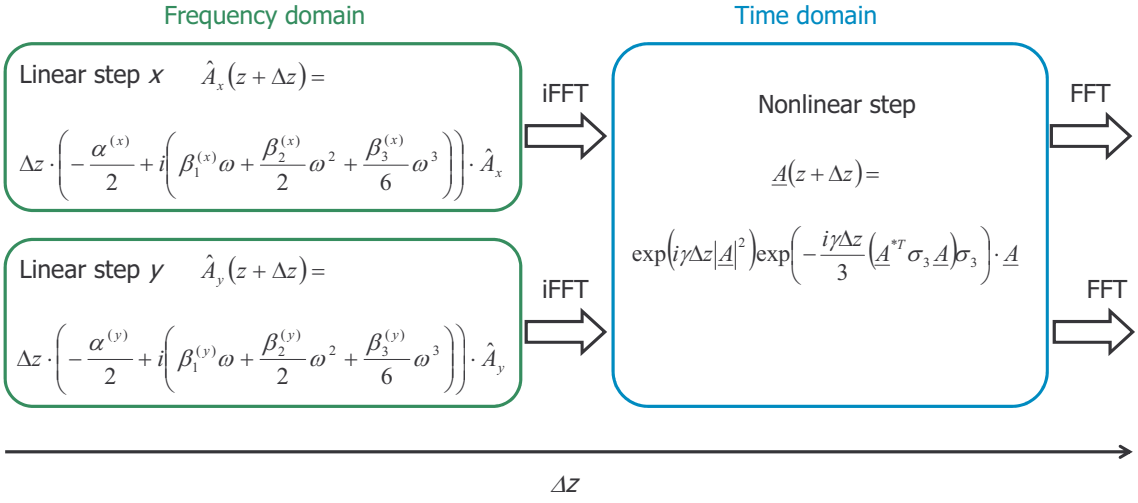

Fig. 1.2.6: Schematic visualization of the split-step Fourier method

In the case of the NLSE, the solution is done similarly, only with a single equation for the linear part and the nonlinear part. Additional effects such as polarization rotations can be included by additional calculation steps.

1.2.4 Physical Transmission Impairments in Single Mode Fibers

So far, in section 1.2, I described a mathematical derivation of a simplified theoretical model for signal propagation through an optical fiber. However, for a better understanding of the physical effects, it is useful to also have an intuitive interpretation of the mathematical expressions. So providing an intuitive description of the dominant physical phenomena that impact signal transmission in optical telecommunication systems, and linking them to the mathematical expressions presented before is the objective of this subsection 1.2.4. The transmission effects are described one by one, classified into the two categories "linear effects" and "nonlinear effects".

1.2.4.1 Linear Effects

The expression "linear effects" describes all transmission impairments that are independent of the signal itself and thus represent a linear transformation to the signal. Today, most of the linear transmission effects can be compensated for either physically or by appropriate algorithms in a digital signal processing (DSP) unit in the receiver.

Attenuation

Attenuation describes the loss of signal energy during propagation. In the theoretical model, attenuation originates from the imaginary part of the first order susceptibility $\tilde{\chi}^{(1)}(\omega)$ and is transferred into the attenuation parameter $\alpha(\omega)$ by equation (1.2.47). As already mentioned, nonlinear attenuation, originating in higher order susceptibility terms can be neglected in this work.

The solution of the CNLSE according to equation (1.2.110) indicates that the amplitude of the electrical field decreases exponentially with the transmission distance *z* following the rule

$$A(z,\omega) = A(0,\omega)\cdot\exp\left(-\alpha(\omega)/2\cdot z\right). \tag{1.2.115}$$

Hence, the signal power *P* follows an exponential decrease as well, but with a doubled argument in the exponential function:

$$P(z,\omega) = P(0,\omega)\cdot\exp\left(-\alpha(\omega)\cdot z\right) \tag{1.2.116}$$

If *z* is given in *km*, the dimension of $\alpha(\omega)$ is *1/km*. However, often values for signal power and attenuation are dealt with in a decibel (dB) scale and so the formula for the calculation of *P(z)* becomes

$$P_{dBm}(z,\omega) = P_{dBm}(0,\omega) - \alpha_{dB}(\omega)\cdot z\,. \tag{1.2.117}$$

The conversion between α and α_{dB} can be done straight forward leading to the relation

$$\alpha_{dB}(\omega) = \frac{10}{\ln(10)}\alpha(\omega). \tag{1.2.118}$$

Normally, attenuation is indicated by fiber manufacturers in *dB/km*, and is typically around *0.2 dB/km* for wavelengths near $\lambda = 1550nm$. Fig. 1.2.7 shows the attenuation in a typical optical fiber as a function of wavelength. For lower wavelengths, the main reasons for attenuation are Rayleigh scattering and impurities, notably the presence of OH^--ions leads to an absorption peak around $\lambda = 1390\ nm$. Then attenuation reaches a minimum around $\lambda = 1550nm$ before SiO_2 absorption becomes dominant and leads to an increasing loss for higher wavelengths. The minimum attenuation in the region around $\lambda = 1550nm$ is one of the reasons why today's optical telecommunication systems work mainly around this wavelength.

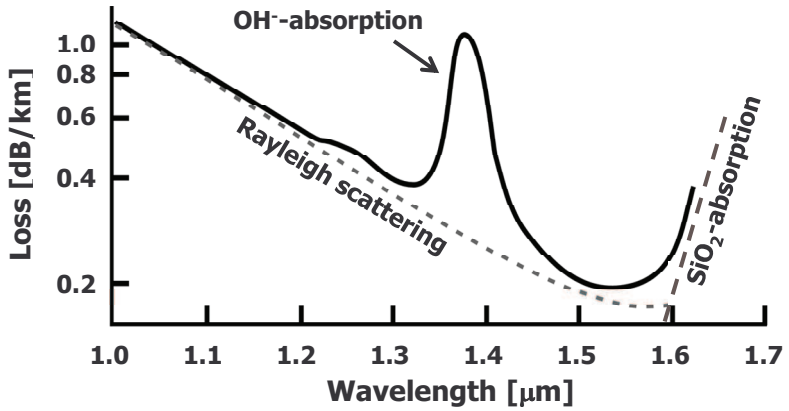

Fig. 1.2.7: Attenuation as a function of wavelength for a typical optical single mode fiber.

The historical evolution of attenuation over the last 50 years is impressive: In the early 1960s, attenuation of glass was above 100 dB/km, which is the attenuation of conventional window glass. Then in 1965, Kao and Hockham showed that the theoretical attenuation of an optical fiber could drop below 20 dB/km, a sufficiently low value to use optical fibers for data transmission [23]. Thanks to the technological progress during the 1970s providing much purer silica, loss could be reduced to ~0.2 dB/km. Today, the best published attenuation is at 0.148 dB/km using pure silica core fiber (PSCF) technology [24]. Here, the refractive index difference between core and cladding is obtained by doping the cladding with fluoride and allowing a core consisting of pure SiO_2 [25]. Whereas usually the refractive index difference is obtained by doping the core with GeO_2, leading to higher loss.

As a comparison to optical fiber loss, the attenuation of electrical cables with carrier frequencies below 100 MHz is in the range between 100 dB/km and 1000 dB/km [26].

Chromatic Dispersion and Dispersion Slope

The real part of the first order susceptibility $\tilde{\chi}^{(1)}(\omega)$ causes a phase shift of the propagating signal over the transmission distance. It is related to the linear refractive index $n(\omega)$ by equation (1.2.45), and as seen during the calculation of the propagation modes, $n(\omega)$ is linked to the propagation constant $\beta(\omega)$ by the wavenumber k_0 (equation (1.2.77)). Based on the Taylor series representation of $\beta(\omega)$, according to equation (1.2.86), each β_m term can be related to a different physical effect. As already mentioned in section 1.2.3.1, only the β_m terms for a maximum of $m = 3$ are relevant here. Of the remaining terms, β_0 and β_1 alone do not lead to any direct signal degradation during transmission, whereas β_2 is an important parameter for the design of optical transmission systems. It governs an effect called chromatic dispersion (CD) or group velocity dispersion (GVD). This effect describes the fact that different signal

components at different wavelengths (or equivalently at different frequencies) propagate with a different group velocity. Since the spectrum of a modulated signal is distributed over a certain frequency range, its frequency components propagate with a different velocity resulting in a signal deformation. The chromatic dispersion parameter *D* is defined as

$$D = \frac{d\beta_1}{d\lambda} = -\frac{2\pi c}{\lambda^2}\beta_2 \approx \frac{\lambda}{c}\frac{d^2 n}{d\lambda^2}, \tag{1.2.119}$$

and so it is directly linked to β_2. Its dimension is *ps/nm/km*, and it can be interpreted to indicate the number of picoseconds that two spectral components, whose wavelength differs by a nanometer, are delayed after transmission over one kilometer. Typical values for chromatic dispersion in different types of today's fibers are between -200 ps/nm/km and +22 ps/nm/km at a wavelength of $\lambda = 1550nm$. Fig. 1.2.8 visualizes the effect of chromatic dispersion on a single optical pulse (Fig. 1.2.8a) and on an optical signal consisting of a sequence of pulses (Fig. 1.2.8b).

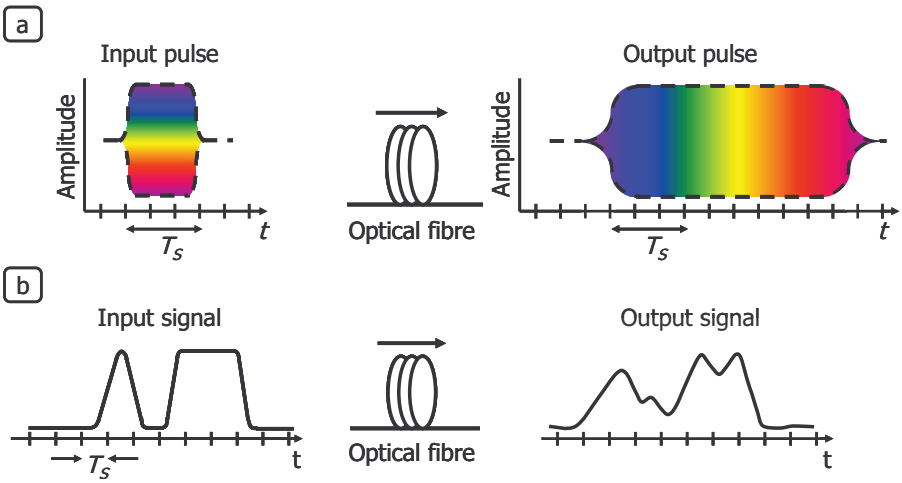

Fig. 1.2.8: Visualization of chromatic dispersion

If chromatic dispersion is not compensated, it rapidly causes severe signal degradations. This limitation led to the development of dispersion compensating modules (DCMs), which can be realized for example by special fibers being designed in order to have an opposite chromatic dispersion value compared to the line fiber (dispersion compensating fibers, DCFs) or by fiber Bragg gratings (FBGs). At the same time, it has been found that the interaction of chromatic dispersion with other transmission impairments can even improve the system performance. This led to the research field of "dispersion management", which is described in more detail in section 1.3.3.

Over a broad frequency band, as it is the case in WDM transmission systems, *D* is not constant but it varies as a function of the wavelength λ. The wavelength dependence of *D* is governed by the dispersion slope *D'*. It includes β_2 and β_3 and it is expressed in *ps/nm²/km*. It is defined through the following relation:

$$D' = \frac{dD}{d\lambda} = \frac{4\pi c}{\lambda^3}\left(\beta_2 + \frac{\pi c}{\lambda}\beta_3\right) \tag{1.2.120}$$

Differential Group Delay and Polarization Mode Dispersion

In a perfectly cylindrical fiber, the propagation constant $\beta(\omega)$ is independent of the polarization of the propagating electrical field. However, in reality a fiber always suffers from imperfections, which make perfect rotational symmetry virtually impossible and thus induce birefringence. Such imperfections can be caused for example during the fabrication process or by mechanical stress on the fiber. In order to include birefringence in our theoretical fiber model, the fiber is split into many short fiber sections. Each fiber section acts as a wave plate with two orthogonal principal axes of polarization *x* and *y*, along which the electrical fields propagate with different propagation constants $\beta^{(x)}$ and $\beta^{(y)}$. Equivalently this fact can be expressed by different values for $\tilde{\chi}_{xx}^{(1)}(\omega)$ and $\tilde{\chi}_{yy}^{(1)}(\omega)$. The concept is visualized in Fig. 1.2.9.

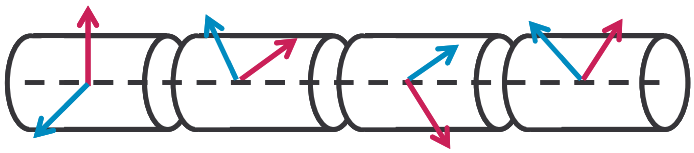

Fig. 1.2.9: Modeling birefringence by splitting the fiber into a concatenation of wave plates

A notable property of this model is that for any concatenation of wave plates with arbitrary principle axes of polarization and arbitrary degree of birefringence, there exist two so-called principle states of polarization (PSP). The pulses launched along both PSPs remain undisturbed by polarization dependent effects during propagation over the whole fiber link. However, due to the random nature of the wave plates, the PSPs cannot be predicted and have to be determined empirically if necessary. Moreover, they can change continuously because of environmental fluctuations such as mechanical stress or temperature fluctuations.

In order to characterize an optical fiber link with respect to its polarization dependent behavior, two parameters have been introduced: differential group delay (DGD) and polarization mode dispersion (PMD) [5 pp. 83, 84] .

The DGD is defined as the time delay $\Delta\tau$ between the two PSPs at the end of a link. Similar to the PSPs themselves it cannot be predicted and has to be measured for a concrete realization of a link. It varies over the time and follows a Maxwellian distribution [27]. Fig. 1.2.10 shows the experimental DGD measurement for a given fiber link over a period of 6 months.

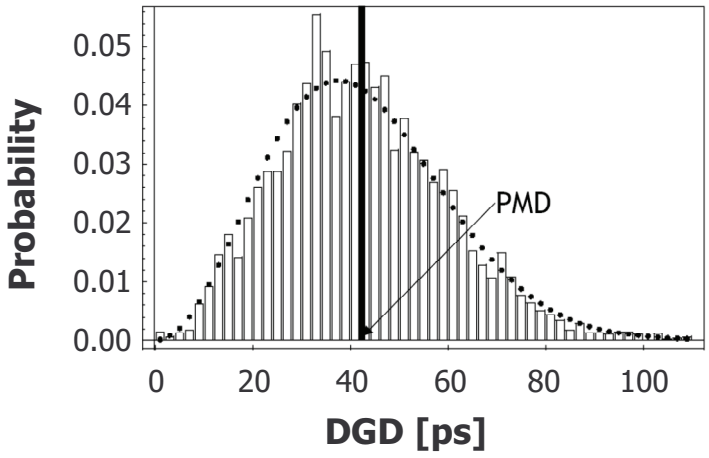

Fig. 1.2.10: Statistical distribution of DGD measured over 6 months in a fiber with PMD of 43 ps [28].

The PMD is defined as the mean value of the DGD as it is also illustrated in Fig. 1.2.10. It correlates with the square root of the transmission distance $\sqrt{z}$. Hence the so-called PMD coefficient or PMD link design value D_p is given in $ps/\sqrt{km}$ and the PMD can be calculated according to the following formula:

$$PMD \quad = \quad \langle DGD \rangle \quad = \quad D_p \sqrt{z}$$

Today, typical values for the PMD coefficient of new fibers are around 0.05 $ps/\sqrt{km}$ (see Table 1.3.2).

1.2.4.2 Nonlinear Effects

Other than with linear effects, the influence of nonlinear effects on the electrical field depends on the amplitude of the electrical field itself. Even though the material, which the optical fiber is made of (basically SiO_2) exhibits only little nonlinear behavior, high power densities and very long transmission distances lead to an important accumulation of nonlinear effects. And so today, signal distortions by nonlinear effects are one of the main limiting factors of long-haul optical transmission systems. Therefore it is important to analyze them as exactly as possible in order to develop strategies for their mitigation.

Nonlinear effects originate in the susceptibility terms $\chi^{(j)}$ for $j > 1$. In our model of the optical fiber, only third order nonlinearities are considered and all other higher susceptibility terms are neglected. Third order means that the polarization $\underline{P}$ correlates with a product of three electrical fields $\underline{E}$. Assuming $\underline{P}$ and $\underline{E}$ as 3-dimensional vectors, this results in a number of $3^4 = 81$ combinations between one dimension of the polarization $\underline{P}$ and one dimension of each of the three electrical field vectors. Furthermore, the nonlinear polarization has a non-instantaneous impulse response and thus, a complete description of third order nonlinearities is quite involved. However, as already mentioned in section 1.2.3.2, we can apply numerous simplifications concerning nonlinearities in the special case of optical fiber propagation using relatively long pulses compared to the impulse response of the nonlinear polarization.

It turns out that the dominant nonlinearities are caused by the so called Kerr-effect, which is the nonlinear contribution that has been maintained during the derivation of the propagation model in section 1.2.3. For a better understanding of the Kerr-effect, it has been further divided into several sub-categories. Historically, this categorization was first done based on a scalar model of the electrical field leading to the identification of self phase modulation (SPM), cross phase modulation (XPM) and parametric processes including for example four wave mixing (FWM) and third harmonic generation. Only in recent years the vectorial nature of the electrical field has been included leading to the introduction of cross polarization modulation (XpolM) [29], [30].

To identify the different nonlinear effects, the electrical field and the nonlinear electrical polarization can be written as a sum of N electrical fields at different carrier frequencies:

$$\boldsymbol{E}_{SM\_scalar}\left(\underline{r},t\right) \quad = \quad \frac{1}{2}\left[\sum_{n=1}^{N} E_n \exp\left(-i\omega_n t\right) + c.c.\right] \qquad (1.2.121)$$

$$\boldsymbol{P}_{NL}\left(\underline{r},t\right) = \frac{1}{2}\left[\sum_{n=1}^{N} P_{NL\_n}\exp\left(-i\omega_n t\right)+c.c.\right] \tag{1.2.122}$$

Calculating the nonlinear polarization with this approach for the electrical field using equation (1.2.32) gives an expression, which is a sum of numerous third order terms. To give an idea about the form of the expression, we write it down for *N = 2*:

$$\begin{aligned}\boldsymbol{P}_{NL} = & \frac{\varepsilon_0\chi^{(3)}_{xxxx}}{8}\left[E_1{}^3\exp\left(-i3\omega_1 t\right)+E_2{}^3\exp\left(-i3\omega_2 t\right)\ldots\right.\\ & + 3\cdot E_2{}^2E_1\exp\left(-i\left(2\omega_1+\omega_2\right)t\right)+3\cdot E_1{}^2E_2\exp\left(-i\left(2\omega_2+\omega_1\right)t\right)\ldots\\ & + 3\cdot E_2{}^2E_1^*\exp\left(-i\left(2\omega_1-\omega_2\right)t\right)+3\cdot E_1{}^2E_2^*\exp\left(-i\left(2\omega_2-\omega_1\right)t\right)\ldots\\ & \left.+\left(3\left|E_1\right|^2+6\left|E_2\right|^2\right)E_1\exp\left(-i\omega_1 t\right)+\left(3\left|E_2\right|^2+6\left|E_1\right|^2\right)E_2\exp\left(-i\omega_2 t\right)+c.c.\right]\end{aligned} \tag{1.2.123}$$

We see that even for *N = 2* the expression is already pretty bulky and so it is cumbersome to write it down for the general case of *N*. However, we can observe that several components at new frequencies are generated. If they are neglected, as it is often the case, equation (1.2.123) can easily be generalized for *N* becoming

$$P_{NL} = \frac{3\varepsilon_0\chi^{(3)}_{xxxx}}{4}\sum_{n}^{N}\left(\left|E_n\right|^2+\sum_{m,m\neq n}^{N}2\left|E_m\right|^2\right)E_n+c.c.. \tag{1.2.124}$$

With these new expressions for the nonlinear polarization, another propagation equation, similar to the NLSE (equation (1.2.94)) or the CNLSEs (equations (1.2.103) and (1.2.104)), can be derived. There, the nonlinear part $N^{(n)}$ for the calculation of the field around the carrier frequency ω_n, in analogy to equation (1.2.107), is

$$N^{(n)} = i\gamma\left(\left|A_n\right|^2+\sum_{m,m\neq n}^{N}2\left|A_m\right|^2\right)A_n\,. \tag{1.2.125}$$

And so the solution to the nonlinear step when applying the SSFM can be derived as:

$$A_n\left(z+\Delta z\right) = \exp\left(i\gamma\left(\left|A_n\left(z\right)\right|^2+\sum_{m,m\neq n}^{N}2\left|A_m\left(z\right)\right|^2\right)\Delta z\right)\cdot A_n\left(z\right) \tag{1.2.126}$$

In this simplified equation we can observe directly the consequence of the two most important scalar nonlinear effects namely SPM and XPM.

Self Phase Modulation

SPM originates from the product of A_n and $\left|A_n\right|^2$ in the nonlinear part of the propagation equation. The interpretation is that through SPM, the electrical field experiences a phase shift proportional to its own intensity (i.e. the square of the field's modulus). Since frequency is proportional to the phase change over time, SPM translates

into a frequency shift at the points where the phase shift increases or decreases. Fig. 1.2.11 shows this behavior schematically for a single optical pulse.

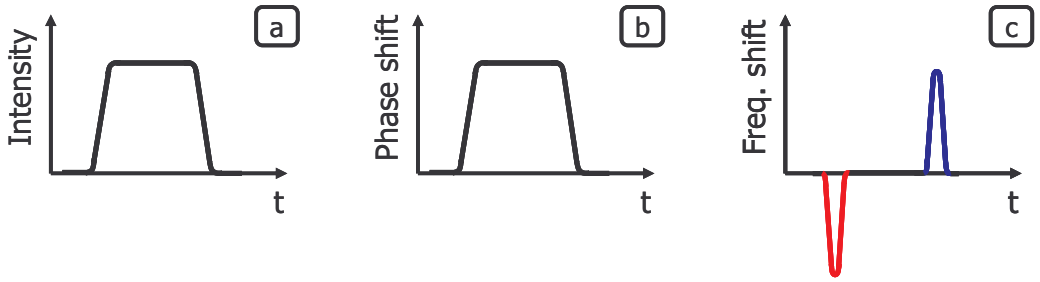

Fig. 1.2.11: Visualization of SPM

The accumulated phase shift induced by SPM after propagation over the distance *L* can be approximated by the following formula [19 p.18], [31]:

$$\phi_{SPM}(L) \approx \gamma L_{eff} |A_0|^2 = \gamma L_{eff} P_0 \qquad (1.2.127)$$

ϕ_{SPM} is given in rad, A_0 is the slowly varying envelope of the electrical field at the fiber input and so P_0 is the power at the fiber input. L_{eff} is the effective length of the propagation distance defined by

$$L_{eff} = \int_0^L \exp(-\alpha z)dz = [1-\exp(-\alpha L)]/\alpha \,. \qquad (1.2.128)$$

It accounts for the power decrease with the propagation distance caused by attenuation and the resulting decline of nonlinear effects.

The SPM phase shift ϕ_{SPM} calculated in this way can be used as a simple indicator for the SPM induced impairments of transmission quality. However, in order to get a more precise idea, the interplay with other propagation effects, such as XPM or CD has to be taken into account. This depends on the modulation format and a number of other system design parameters (see section 1.3.3). To account for these parameters, the impact of SPM on the system performance can either be estimated experimentally, by simulations, or by use of more sophisticated models that have been developed recently for transmission systems without in-line dispersion compensation [4], [32–35].

Cross Phase Modulation

XPM originates from the multiplication of A_n with the $\sum_{m,m\neq n}^{N} 2|A_m(z)|^2$ term in the nonlinear part of the propagation equation. Here, the slowly varying envelope A_n of the electrical field at carrier frequency ω_n experiences a phase shift, caused by the electrical fields around the other carrier frequencies ω_m propagating in the same optical fiber. The shift is proportional to the intensity of the neighboring channels. Furthermore, the factor of 2 in the mathematical expression indicates that for the same power per channel, XPM is two times stronger than SPM. Fig. 1.2.12 visualizes this behavior using the example of two co-propagating pulses on two different carrier wavelengths. The pulses depicted in Fig. 1.2.12a experience a phase shift depicted in Fig. 1.2.12a, which is proportional to the pulse on the other carrier wavelength.

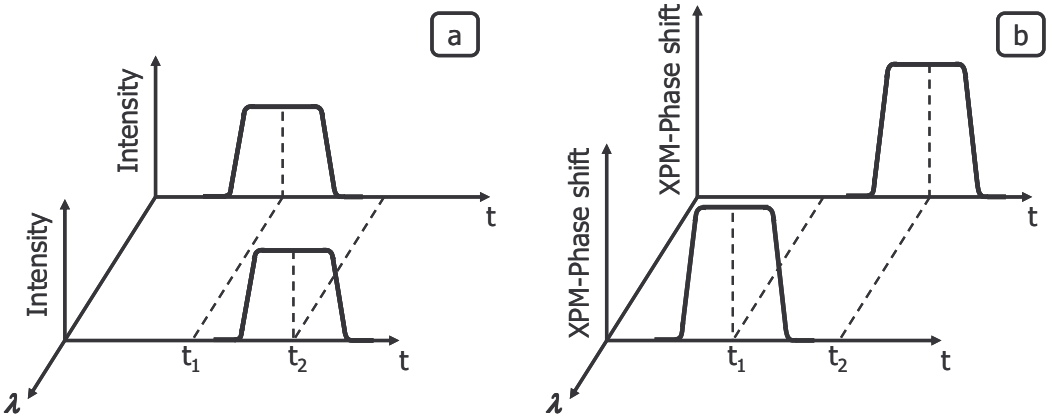

Fig. 1.2.12: Visualization of XPM

Parametric Processes

Several effects that generate new frequency components are grouped under the expression "parametric processes". Equation (1.2.123) gives a mathematical description about the origin of the different frequency components. In the general case, with incoming signals on more than two carrier wavelengths, new signals are generated at all frequencies that can be expressed as a sum of three existing frequencies with positive or negative sign.

Two concrete examples for parametric processes are the so-called third harmonic generation, where three times the same frequency sums up to generate a new frequency at the third harmonic, or four wave mixing (FWM), where three different frequencies are combined by any combination of summing or subtracting and thereby generate a fourth frequency.

Not all parametric processes occur with the same relevance, but they have in common, that they all require phase-matching. It becomes problematic in transmission systems using dispersion shifted fibers (DSF), where the chromatic dispersion of the considered wavelengths can be close to 0. However, in the optical transmission systems considered in this work the phase matching condition is virtually not fulfilled and so the phenomenon of parametric processes does not play an important role.

Cross Polarization Modulation

Cross polarization modulation (XpolM) describes a polarization dependent phase shift caused by intensity fluctuations in orthogonal polarization axes of neighboring channels resulting in a rotation of their state of polarization (SOP). In WDM systems, the large number of channels carrying unknown sequences makes XpolM essentially result in a random SOP scattering [36].

For a long time, nonlinear effects have only been investigated based on scalar models of the electrical field and so XpolM had been neglected. This worked pretty well until the advent of transmission systems that make use of both *x*- and *y*-polarization and thus require polarization sensitive detection. In this case, XpolM leads to sudden SOP changes in the received signal, which can be faster than the polarization tracking in the receiver and therefore result in significant performance degradations [37].

Including XpolM in a theoretical model requires a vectorial representation of the electrical field as it is the case in the CNLSEs (equations (1.2.103) and (1.2.104)). A detailed and comprehensive mathematical description of XpolM can be found in [29]. To give an idea of it, I would like to use the example of two co-propagating WDM signals $\underline{A_1}$

and $\underline{A_2}$ using each two linear polarizations *x* and *y*. In this scenario we can write the nonlinear parts of the CNLSEs according to the following expressions [36]:

$$N^{(x1)} = i\gamma\left\{\underbrace{\left(\left|A_{x1}\right|^2+\left|A_{y1}\right|^2\right)}_{SPM}A_{x1}+\frac{3}{2}\underbrace{\left(\left|A_{x2}\right|^2+\left|A_{y2}\right|^2\right)}_{XPM}A_{x1}\ldots\right.$$
$$\left.+\underbrace{\frac{1}{2}\left[\left(\left|A_{x2}\right|^2-\left|A_{y2}\right|^2\right)A_{x1}+A_{x2}A_{y2}^{*}A_{y1}\right]}_{XpolM}\right\} \quad (1.2.129)$$

$$N^{(y1)} = i\gamma\left\{\underbrace{\left(\left|A_{y1}\right|^2+\left|A_{x1}\right|^2\right)}_{SPM}A_{y1}+\frac{3}{2}\underbrace{\left(\left|A_{y2}\right|^2+\left|A_{x2}\right|^2\right)}_{XPM}A_{y1}\ldots\right.$$
$$\left.+\underbrace{\frac{1}{2}\left[\left(\left|A_{y2}\right|^2-\left|A_{x2}\right|^2\right)A_{y1}+A_{y2}A_{x2}^{*}A_{y1}\right]}_{XpolM}\right\} \quad (1.2.130)$$

Looking at equations (1.2.129) and (1.2.130) we observe that now, in the vectorial case, SPM and XPM also depend on the signals in the orthogonal polarization direction. However, the expressions are constant for both polarizations x and y because the '+' is commutative. The result is a phase shift independent of the polarization direction, and so SPM and XPM have no impact on the SOP.

In contrast, the non-commutative '-' in the first XpolM term results in a different phase shift for *x*- and *y*-polarization potentially causing a change of the SOP. This effect is increased by the second XpolM term, which can be considered as an FWM like effect.

Stimulated Raman Scattering and Stimulated Brillouin Scattering

By assuming an instantaneous impulse response of the nonlinear polarization, a number of effects caused by molecular vibrations are neglected. Among these effects the most important ones are stimulated Raman scattering (SRS) and stimulated Brillouin scattering (SBS). Both effects can be roughly described by an energy transfer between different frequencies and matter.

The impact of both effects on fiber propagation in today's optical transmission systems is much less important than the impact of the Kerr-effect. Nonetheless, for pulses with wide spectra, typically broader than 0.1 THz, the Raman effect can lead to an energy transfer from the higher frequencies of the spectral band to the lower ones. Since the spectra of WDM systems are usually several THz broad this phenomenon can play a role in certain configurations. To include the Raman effect in the theoretical fiber propagation model, the expression for the nonlinear polarization has to be maintained in its original form with the time delayed impulse responses of $\chi^{(3)}$ according to equation (1.2.25).
Then some more complicated steps are necessary for the further derivation of the theoretical model, which can be found in [19].

Besides its possible negative consequences, the energy transfer caused by the Raman effect can also be exploited in a positive way by constructing optical amplifiers [38–40](see section 1.3.3).

1.3 Practical Implementation of Optical Single Mode Transmission Systems

Starting from the general model of a digital transmission system presented in section 1.1, we are in this work particularly interested in the three "inner" blocks of Fig. 1.1.1 being modulator, channel and demodulator. All blocks before and after is accounted for by the fact that we have a sequence s_n at the input of our system, which we have to transmit and recover with a BER (respectively a Q^2-factor) below (respectively above) the FEC-threshold.

A typical set-up of an optical transmission system, realizing this functionality is depicted in Fig. 1.3.1. The elements "transmitter" and "receiver" comprise the modulation and demodulation blocks as well as some additional functionalities such as the generation of the optical carrier wave by a laser. WDM leads to the fact that several transmitters and receivers share the same transmission line, connected to it through a WDM-multiplexer (WDM-MUX) and a WDM-demultiplexer (WDM-DEMUX). The transmission line consists of the optical fiber transmission channel as well as elements to compensate for physical transmission impairments, notably optical amplifiers and dispersion compensation modules.

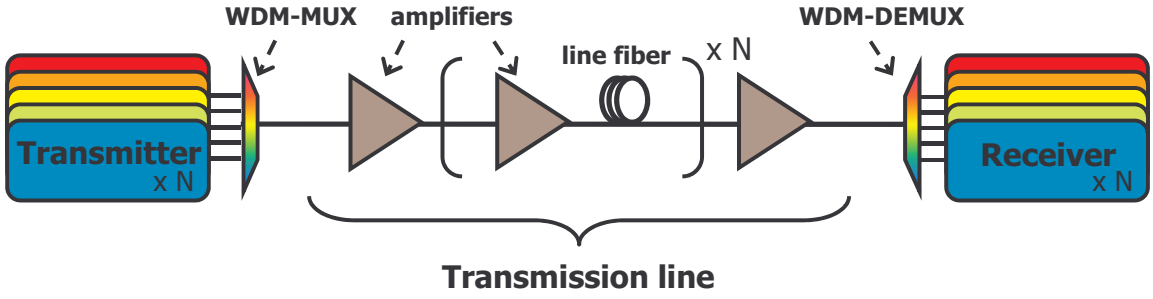

Fig. 1.3.1: Schematic representation of an optical transmission system.

In the following, I will describe the most common ways how these three parts are realized today and have been realized in the past, before I will discuss the – from my point of view – most important points concerning the performance of optical transmission systems.

1.3.1 Transmitter

It was explained in section 1.1.2 that from a theoretical point of view, choosing the appropriate modulation format can optimize the tradeoff between transmitted bits per symbol (capacity, spectral density) and robustness to transmission impairments. However, in practice, the choice for a modulation format also depends on the technical feasibility in both, transmitter (Tx) and receiver (Rx)

At the transmitter side, the basic elements for the generation of an optical signal are a laser source, in order to generate an optical carrier wave, followed by a modulator in order to encode the sequence that is to be transmitted onto this wave. Optionally, these two elements can be combined with devices for electronic or optical pulse shaping, for

example to improve the system performance [41–43] or to use the available channel bandwidth more efficiently [44].

In Fig. 1.3.2, some transmitter schemes, implementing carrier wave generation and modulation are shown. Historically, in the first available optical transmission systems, the laser was modulated directly by rapidly switching it on and off and thereby generating symbols with high and low intensity as it is depicted in Fig. 1.3.2a. The technology's drawbacks are that it allows only amplitude modulation and rather slow modulation rates. Therefore, nowadays, modulation in long-haul and ultra-long-haul transmission systems is mostly realized externally of the laser diode by so-called Mach-Zehnder modulators (MZMs). In Fig. 1.3.2b and c, commonly used transmitter schemes for the generation of BPSK and QPSK signals containing MZMs are depicted.

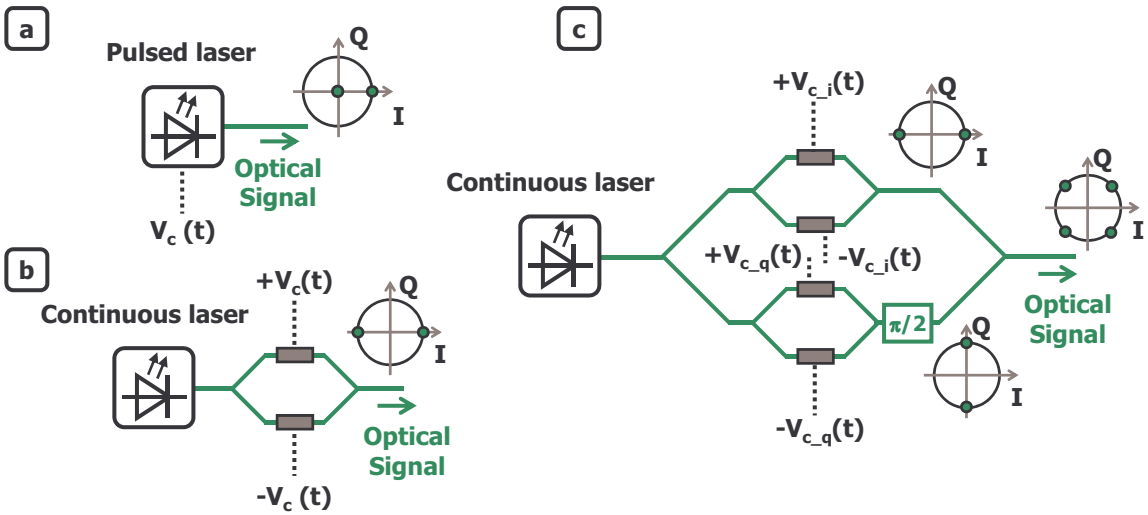

Fig. 1.3.2: Transmitter architectures for generation of (a) NRZ-OOK by direct modulation. (b) BPSK with an external MZM. (c) QPSK with an external nested MZM as I-Q-modulator.

MZMs are based on the interference between two waves with adjustable phase shifts. For this purpose, the incoming optical wave is split into two branches, which traverse an electro-optical material. There they can be phase shifted with respect to each other by applying an electrical voltage before the two branches are recombined. Depending on the relative phase-shift, the resulting output signal is phase modulated and/or amplitude modulated. A widely used variant of the MZM is the push-pull modulator, where the voltages applied to the two branches have the same moduli but opposite sign. Like this, the two waves are shifted by the same phase in opposite directions. If at the same time, the power is split equally into both branches, the phase of the output signal can only be shifted by either 0 or π and the modulation can be described by the graph plotted in Fig. 1.3.3.

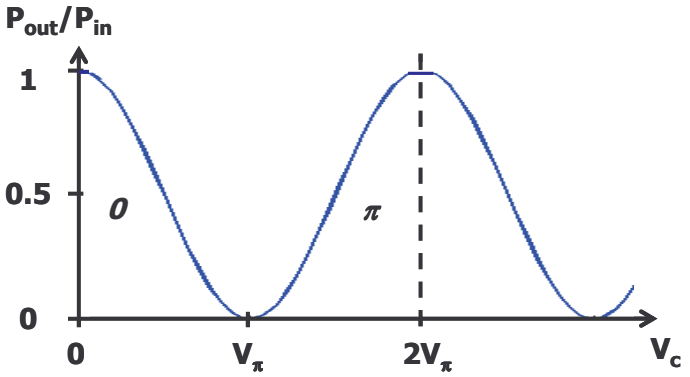

Fig. 1.3.3: Optical output power of an ideal push-pull MZM as a function of applied control voltage.

By using two MZMs combined into a "nested" MZM structure as in Fig. 1.3.2c, it is possible to modulate both the *I*- and the *Q*-component of an incoming wave, which is why this set-up is also called *I*-*Q*-modulator. *I*-*Q*-modulators are widely used for the generation of QPSK signals. Theoretically they can also be used for the generation of numerous other modulation formats, even though it is more challenging to operate the device in the steep regions of the function presented in Fig. 1.3.3. Generation of QAM modulation formats up to 1024-QAM has already been successfully demonstrated using *I*-*Q*-modulators [45].

In modern optical transmission systems, independent signals are transmitted over waves in both orthogonal polarization axes *x* and y in order to double the capacity per fiber. This technology is called polarization division multiplexing (PDM). Hence, in the transmitter, two optical signals are generated in parallel in the way just described. Then polarization multiplexing is done by combining the two signals in a polarization beam combiner before they are launched into the transmission fiber.

Wavelength Division Multiplexing

The available bandwidth of an optical transmission line is much higher than the spectral width of a commonly modulated signal. So in order to efficiently exploit the available bandwidth, wavelength division multiplexing (WDM) has become a key technology for optical transmission systems. The idea behind it is that several independent transmitters generate signals on different carrier wavelengths. The different signals, now also called "channels", are then combined in a WDM-multiplexer before being transmitted over the same transmission line.

It is important that the channels are spaced by a sufficiently high spectral distance in order to avoid crosstalk between them. If this is the case they can be demultiplexed at the receiver side without loss of information and are detected by independent receivers. In the context of optical networks it is also possible to add and drop different wavelength channels at certain nodes and to let them take different paths through the network.

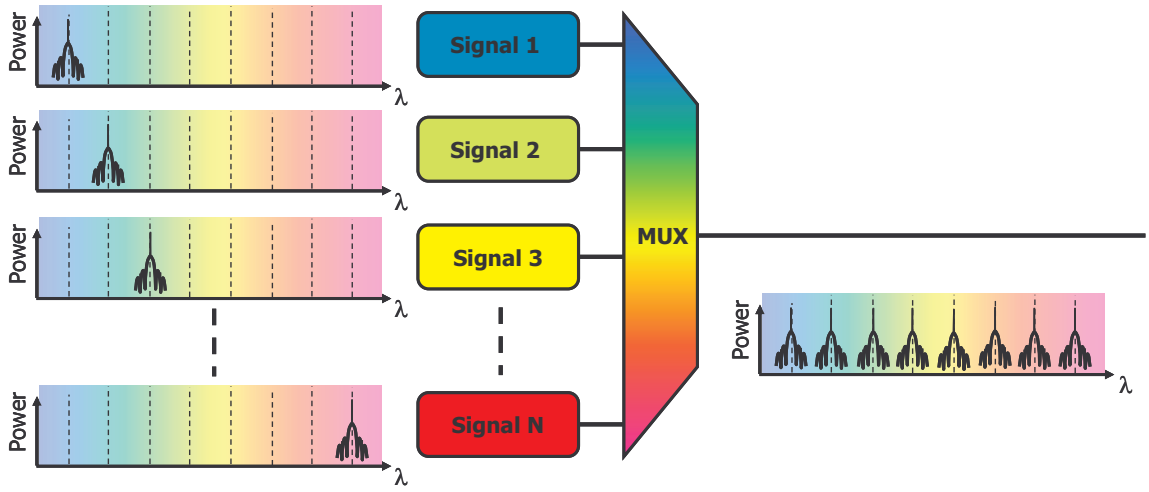

Fig. 1.3.4: Wavelength division multiplexing.

Today, the bandwidth of an optical transmission line is normally defined by the spectral gain window of erbium doped fiber amplifiers (EDFAs, see section 1.3.3). The most important wavelength band is the so-called C-band between $\lambda = 1530nm$ and $\lambda = 1565nm$ providing a bandwidth of 35nm, corresponding to ~4.4THz in this wavelength region. Other transmission bands defined by the International Telecommunication Union (ITU) are given in Table 1.3.1 [46]. Typical values for channel spacing are 100GHz or 50GHz resulting in up to ~80 channels in the C-band. In some submarine systems channel spacing is even reduced to 33GHz, allowing to further increase the number of channels in the C-band to ~120.

Table 1.3.1: ITU transmission bands in optical fiber communication systems [46].

Band	Description	Wavelength range
O-Band	original	1260 nm – 1360 nm
E-Band	extended	1360 nm – 1460 nm
S-Band	short wavelengths	1460 nm – 1530 nm
C-Band	conventional	1530 nm – 1565 nm
L-Band	long wavelengths	1565 nm – 1625 nm
U-Band	ultralong wavelengths	1625 nm – 1675 nm

1.3.2 Receiver

In the receiver (Rx) the incoming optical signal has to be converted back into an electrical one. This is done by a photodiode, which generates an electrical current *I(t)* proportional to the incoming optical power:

$$I(t) \propto |E(t)|^2 \tag{1.3.1}$$

Using one simple photodiode for signal detection followed by a decision gate in the electronic domain leads to the most basic receiver architecture. Its concept is known as direct detection and it is schematically depicted in Fig. 1.3.5a. As it is described by equation (1.3.1), the resulting photo-current gives only information about the intensity

of the optical field and so all information about the signal's phase is lost. In general, this solution provides a good fit to the directly modulated transmitter architecture since it is sufficient for detection of OOK modulated signals.

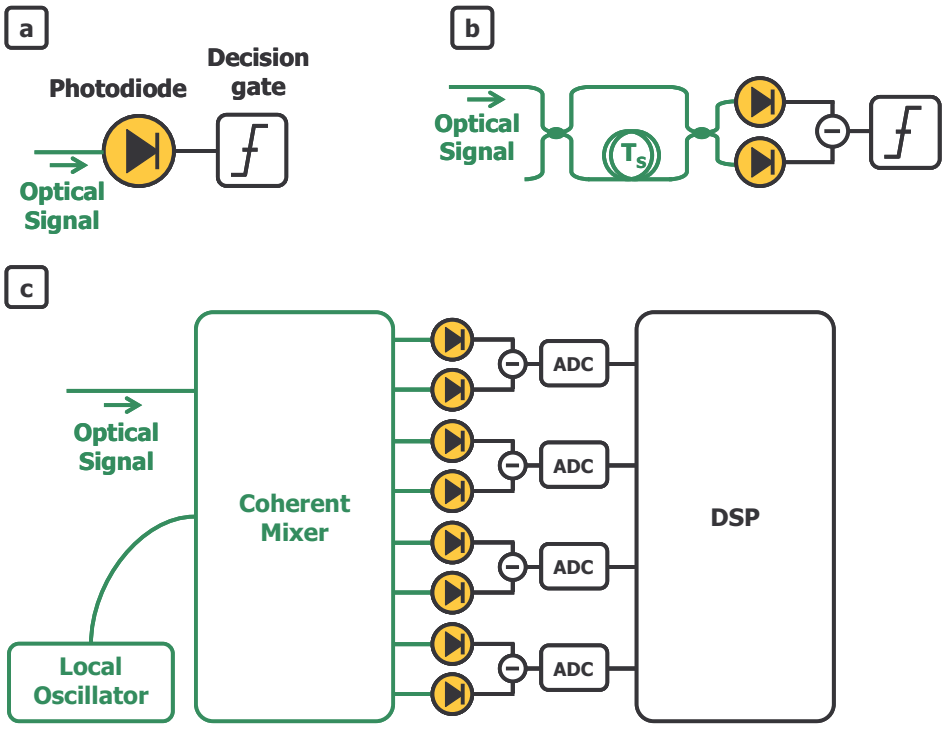

Fig. 1.3.5: Receiver architectures: (a) Direct detection. (b) Differential detection. (c) Coherent detection.

For achieving a given BER, the modulation format BPSK can tolerate an SNR that is 3dB lower than with OOK. However, in order to benefit from this advantage of phase shifted modulation formats, more sophisticated receiver architectures are necessary. One solution is the so-called differential detection as depicted in Fig. 1.3.5b, which allows the detection of the phase difference between two consecutive symbols. An example for a modulation format used with this technique is differential binary phase shift keying (DBPSK), where two possible phase shifts between subsequent symbols by *0* or by π are used to encode the bits "0" and "1". The reception is done with the help of a so called Mach-Zehnder delay interferometer (MZDI). At the input, the incoming signal E_{in} is split into two branches that are delayed by one symbol duration T_S with respect to each other. Then they are recombined into two outputs, one called "constructive" providing the optical field E_c and one called "destructive" providing the optical field E_d. The two fields can be calculated as:

$$E_c(t) = \frac{1}{2}\left[E_{in}(t) + E_{in}(t - T_S)\right] \tag{1.3.2}$$

and

$$E_d(t) = \frac{1}{2}\left[E_{in}(t) - E_{in}(t - T_S)\right]. \tag{1.3.3}$$

Then both optical signals are detected by a set of two photodiodes combined into a so-called balanced receiver, which means that the photo-currents are subtracted after detection. The resulting electrical current *I*, which is used for electrical decision about the received symbol, can be described as

$$I(t) \propto |E_c|^2 - |E_d|^2 = \begin{cases} +|E_{in}|^2 & for \quad E_{in}(t) = E_{in}(t - T_S) \\ -|E_{in}|^2 & for \quad E_{in}(t) = -E_{in}(t - T_S) \end{cases}. \tag{1.3.4}$$

Using differential detection, also higher order phase modulated signals, such as differential quadrature phase shift keying (DQPSK) can be detected.

Coherent Detection

The most complex but also the most powerful detection scheme is the so-called coherent detection, as it is depicted in Fig. 1.3.5c. It allows the detection of amplitude and phase of the incoming optical field. Moreover, it is usually used in a polarization diversity configuration and thus it allows detecting the signals in both orthogonal polarization axis of the transmission fiber. Today's coherent receivers are followed by analogue to digital converters (ADC) and digital signal processing (DSP) units. On the one hand, these units are necessary to compensate for intrinsic imperfections in the coherent receiver itself, but on the other hand they also allow for the compensation of other impairments that occur during transmission. It is standard that today's coherent receivers are able to compensate for large amounts of chromatic dispersion and PMD, and even efforts for compensation of nonlinear transmission impairments are made [47–49].

In order to better understand the coherent receiver, we divide the scheme of Fig. 1.3.5c into two blocks: the first one covering the coherent mixer and the photodiodes is depicted in Fig. 1.3.6. The second one, visualizing the different DSP steps is shown in Fig. 1.3.7.

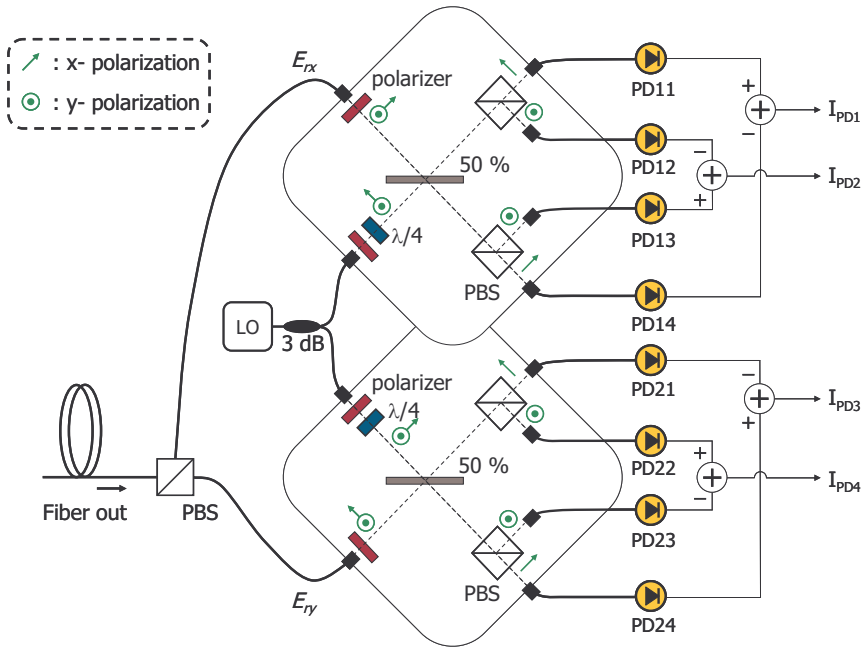

Fig. 1.3.6: Coherent mixer

At the input of the coherent mixer, the incoming signal is split into two orthogonal polarization components, which enter two equivalent mixer structures. In both, a second input is fed by an unmodulated laser, the so-called local oscillator (LO). By mixing signal and local oscillator with different relative phase shifts, the four photodiodes per polarization, which are only able to detect the optical power, receive optical powers containing information about the *I*- and *Q*-components of the optical field. Together with the polarization diversity provided by the two mixers in two orthogonal polarization axes all information about the incoming optical field can be recovered.

In order to describe the photocurrents mathematically, we first express the three incoming signals by

$$E_{rx} = A_{rx}\exp\left(i\left(\varphi_{rx}(t)-\omega_{rx}t\right)\right) \tag{1.3.5}$$

$$E_{ry} = A_{ry}\exp\left(i\left(\varphi_{ry}(t)-\omega_{ry}t\right)\right) \tag{1.3.6}$$

$$E_{LO} = A_{LO}\exp\left(i\omega_{LO}t\right) \tag{1.3.7}$$

For the calculation of the photocurrents we take into account that the polarizers at the input of each mixer are installed in a way that the incoming field is distributed equally into *x*- and *y*-axis. Then the $\lambda/4$-waveplate causes a shift of $\lambda/4$ (corresponds to a phase shift of $\pi/2$) for the *x*-polarization, and no phase-shift for the *y*-polarization. Besides, polarization beam splitters (PBS) and beam splitters cause a phase-shift of $\pi/2$ in the reflected (polarization) component and of *0* in the transmitted (polarization) component. At the photodiode *PD11*, the local oscillator wave is shifted by $\pi/2$ (at the $\lambda/4$-waveplate) and the signal is shifted by $\pi/2$ as well (reflection at beam splitter). This results in

$$\begin{aligned} I_{PD11} &\propto \left|E_{rx}\exp\left(i\frac{\pi}{2}\right)+E_{LO}\exp\left(i\frac{\pi}{2}\right)\right|^2 \\ &= \frac{1}{2}\left|A_{rx}\right|^2+\frac{1}{2}\left|A_{rx}\right|^2+A_{rx}A_{LO}\cos\left[\left(\omega_{rx}-\omega_{LO}\right)t+\varphi_{rx}(t)\right] \end{aligned} \tag{1.3.8}$$

At the photodiode *PD12*, the local oscillator wave is shifted by $\pi/2$ (reflection at PBS) and the signal is shifted by π (reflection at beam splitter and at PBS) leading to

$$\begin{aligned} I_{PD12} &\propto \left|E_{rx}\exp\left(i\pi\right)+E_{LO}\exp\left(i\frac{\pi}{2}\right)\right|^2 \\ &= \frac{1}{2}\left|A_{rx}\right|^2+\frac{1}{2}\left|A_{rx}\right|^2-A_{rx}A_{LO}\sin\left[\left(\omega_{rx}-\omega_{LO}\right)t+\varphi_{rx}(t)\right] \end{aligned} \tag{1.3.9}$$

Photodiode *PD13* receives the local oscillator shifted by π (reflection at beam splitter and at PBS) and the signal shifted by $\pi/2$ (reflection at PBS). The resulting photocurrent is

$$I_{PD13} \propto \left| E_{rx} \exp\left(i\frac{\pi}{2} \right) + E_{LO} \exp(i\pi) \right|^2 = \frac{1}{2}|A_{rx}|^2 + \frac{1}{2}|A_{rx}|^2 + A_{rx}A_{LO} \sin\left[(\omega_{rx} - \omega_{LO})t + \varphi_{rx}(t) \right] \quad (1.3.10)$$

And finally, at the photodiode PD14 the local oscillator is shifted by π ($\lambda/4$-waveplate and reflection at PBS) and the signal is shifted by *0*. The photocurrent is given by

$$I_{PD14} \propto \left| E_{rx} + E_{LO} \exp(i\pi) \right|^2 = \frac{1}{2}|A_{rx}|^2 + \frac{1}{2}|A_{rx}|^2 - A_{rx}A_{LO} \cos\left[(\omega_{rx} - \omega_{LO})t + \varphi_{rx}(t) \right] \quad (1.3.11)$$

Balanced detection is then used to filter out the DC-parts of the photo currents. Thus we obtain

$$I_{PD1} = I_{PD11} - I_{PD14} \propto \cos\left[(\omega_{rx} - \omega_{LO})t + \varphi_{rx}(t) \right] \quad (1.3.12)$$

and

$$I_{PD2} = I_{PD12} - I_{PD13} \propto \sin\left[(\omega_{rx} - \omega_{LO})t + \varphi_{rx}(t) \right]. \quad (1.3.13)$$

The photocurrents I_{PD3} and I_{PD4} can be calculated accordingly. Each of the four photocurrents I_{PD1}, I_{PD2}, I_{PD3} and I_{PD4} is then sampled by an ADC and passed into a DSP device. In this work, the DSP was done offline by a PC and the typical DSP steps used for signal recovery of a PDM signal are visualized in Fig. 1.3.7.

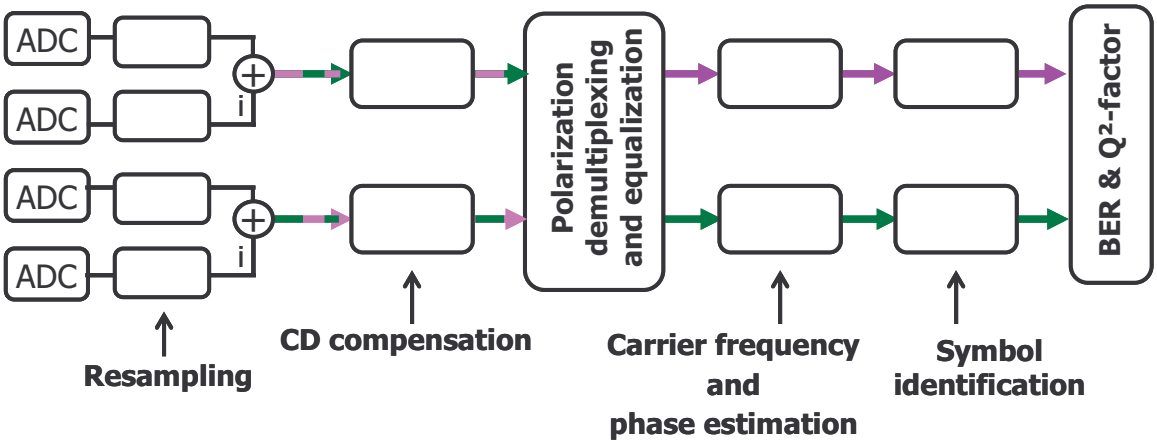

Fig. 1.3.7: DSP for coherent detection

Usually the sampling rate of the ADC is not synchronized to the modulation rate and so first, the four detected signals are resampled in order to obtain an integer number of samples per received symbol. In our case we work at 2 samples/symbol. After combining *cos* and *sin* terms of both polarizations as the real (*I*-) and the imaginary (*Q*-)

component of a complex signal, chromatic dispersion is compensated. This is done by a static finite impulse response (FIR) filter requiring information about the accumulated chromatic dispersion of the transmission line. The filter length is proportional to the amount of compensated chromatic dispersion [50].

The two polarization axes along which the incoming signal is separated into *x* and *y* at the input of the coherent mixer do generally not correspond to the two axes in which the two polarization tributaries of the signal have been modulated. Furthermore, signals suffer from channel perturbations, such as polarization dependent loss (PDL) or PMD. All these effect can be modeled by the Jones matrix $\underline{\underline{J}}$ of the transmission channel relating the optical fields before and after transmission (not taking into account CD, which has been dealt with separately):

$$\begin{bmatrix} E_{x\_Rx\_in} \\ E_{y\_Rx\_in} \end{bmatrix} = \underline{\underline{J}} \cdot \begin{bmatrix} E_{x\_Tx} \\ E_{y\_Tx} \end{bmatrix} \tag{1.3.14}$$

It is now the task of the DSP block "polarization demultiplexing and equalization" to invert the Jones matrix according to the following equation:

$$\begin{bmatrix} E_{x\_Rx\_out} \\ E_{y\_Rx\_out} \end{bmatrix} = \underline{\underline{J}}^{-1} \cdot \begin{bmatrix} E_{x\_Rx\_in} \\ E_{y\_Rx\_in} \end{bmatrix} = \underbrace{\begin{bmatrix} h_{xx} & h_{yx} \\ h_{xy} & h_{yy} \end{bmatrix}}_{\underline{\underline{H}}} \cdot \begin{bmatrix} E_{x\_Rx\_in} \\ E_{y\_Rx\_in} \end{bmatrix} \tag{1.3.15}$$

The filter configuration implementing this mathematical operation can be considered as a 2x2 multiple input multiple output (MIMO) filter with the butterfly structure depicted in Fig. 1.3.8.

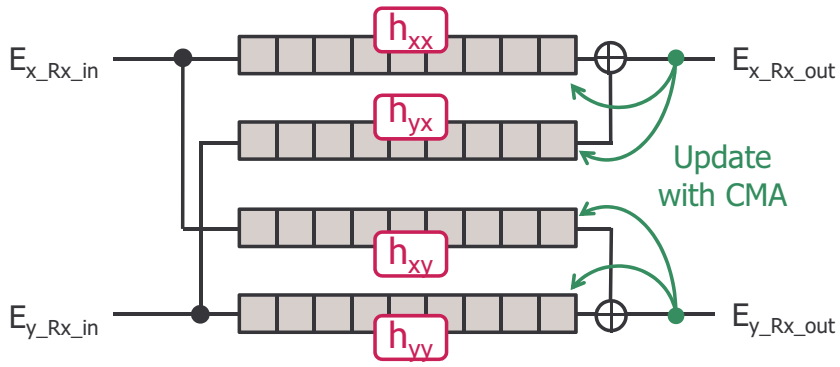

Fig. 1.3.8: Filter structure for polarization demultiplexing and equalization.

Each element of the matrix $\underline{\underline{H}}$ (h_{xx}, h_{yx}, h_{xy}, h_{yy}) is realized by an adaptive FIR filter with a number of *N* complex coefficients, called "taps". By setting *N* it is possible to define the memory length of the filter. In our case we use 2 samples per symbol, meaning that the taps are spaced by $T_S/2$. In our default configuration, *N* is set to 13 resulting in a memory of $6T_S$. A longer memory allows for the compensation of a larger amount of delayed impairments such as residual chromatic dispersion or PMD. On the other hand it requires more hardware resources and leads to a more complicated determination of the filter coefficients.

In our case, the filter works as a blind equalizer. The taps are initialized in the beginning and then permanently updated to follow fluctuations in the Jones matrix of

the transmission channel. For updating we use the so-called constant modulus algorithm (CMA) [51].

In order to detect the phase of the modulated signal, it is necessary that additional phase offsets between local oscillator and carrier wave are cancelled out. Reasons for such phase offsets are phase noise of both lasers used as LO and as carrier wave, or a frequency offset between the two lasers. Theoretically, the problem can be solved physically by phase locking both lasers. However, in practice it is much easier to compensate for phase and frequency offsets in the DSP unit. This is done by the steps carrier frequency estimation (CFE) and carrier phase estimation (CPE). The two steps are combined in order to provide a coarse correction of the frequency offset, done by the CFE, and afterwards a dynamic compensation of the fluctuating phase offset, done by the CPE [52], [53].

Finally symbols can be identified and in our case BER and Q^2-factor are calculated. If a coherent receiver is part of a complete digital communication system, symbol identification is followed by a channel decoder applying error correction through an FEC. In this case, another advantage of the coherent receiver is that it can provide information for so-called soft decision on the received symbols. Soft decision means that the determination of the detected symbols delivers not only the decision about one of the possible modulation states, but a more precise position in the complex plane. Taking this additional information into account can enable more powerful FEC codes [8], [54]

1.3.3 Transmission Line

A typical optical transmission channel consists of optical fiber spans in order to bridge the demanded transmission distance (in the following called "line fiber"), as well as elements to compensate for physical propagation effects. Notably these elements are amplifiers in order to compensate for loss and elements for the compensation of chromatic dispersion, if used. Fig. 1.3.9 shows schematic representations of a typical optical transmission line with dispersion compensation and without dispersion compensation.

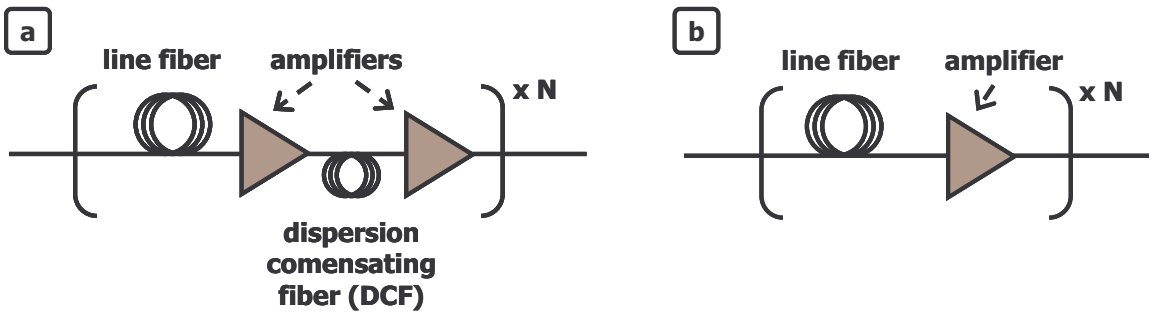

Fig. 1.3.9: Scheme of a periodic optical transmission line. (a) With dispersion compensation and dual stage amplifier. (b) Without dispersion compensation and with single stage amplifier.

The design of the transmission line is important for minimizing signal degradations. Since signal degradations typically get stronger with increasing distance and their effect is more severe at higher transmitted capacities (higher bit rate per channel, higher number of channels), line design is directly related to the maximization of capacity and reach. In the following, three aspects of line design are considered: the line fiber, amplifiers and dispersion management.

Properties of the line fiber

The importance of physical transmission impairments in an optical fiber presented in section 1.2.4 can be estimated using a set of parameters. These parameters can be influenced during fiber design and manufacturing, notably by the choice of the refractive index profile and by the use of well adapted materials. The most important parameters are listed in Table 1.3.2 together with values for different commercially available fibers.

Table 1.3.2: Key parameters of some commercially available fibers at λ = 1550nm [55–59]

	Prysmian **SM Light ("SMF")**	***Sumitomo*** **PureAdvance®**	***Corning*** **LEAF®**	***Corning*** **Vascade® EX2000**
Attenuation α *[dB/km]*	≤0.20	≤0.18	≤0.20	0.162
Chromatic Dispersion *D* *[ps/nm/km]*	≤18	≤18	3.4-5.8	20.4
PMD Link Design Value *[ps/km$^{1/2}$]*	≤0.06	<0.04	<0.04	≤0.05
Effective Area A_{eff} *[μm^2]*	~85	~85	~73	~112
Nonlinear Index Coefficient n_2 *[m^2/W]*	2.6x10^{-20}		2.7x10^{-20}	

Amplifiers

One of the key enabling technologies for the success of optical transmission systems is optical amplification. It avoids that the signal has to be converted into an electrical signal for amplification before being reconverted again into an optical one. Compared to that, optical amplification has several advantages such as reduced system complexity, latency or power consumption.

Today, the by far most important optical amplification technology is the erbium doped fiber amplifier (EDFA), which is schematically depicted in Fig. 1.3.10. The key element of the EDFA is an optical fiber doped with Erbium ions. The incoming signal is coupled into this fiber together with a so called pump signal at a wavelength of typically $\lambda = 980nm$ or $\lambda = 1480nm$. Pump signals can be injected from both sides into the erbium doped fiber (EDF) resulting in co- or contra-propagating pump signals (Fig. 1.3.10a). Inside the EDF, the pump photons at 980nm or 1480nm excite the erbium ions to a higher energy state. Then, the photons of the incoming signal at wavelengths around 1550nm can cause the erbium ions to return to the original lower energy state and thereby generating copies of the signal photons by stimulated emission (Fig. 1.3.10b).

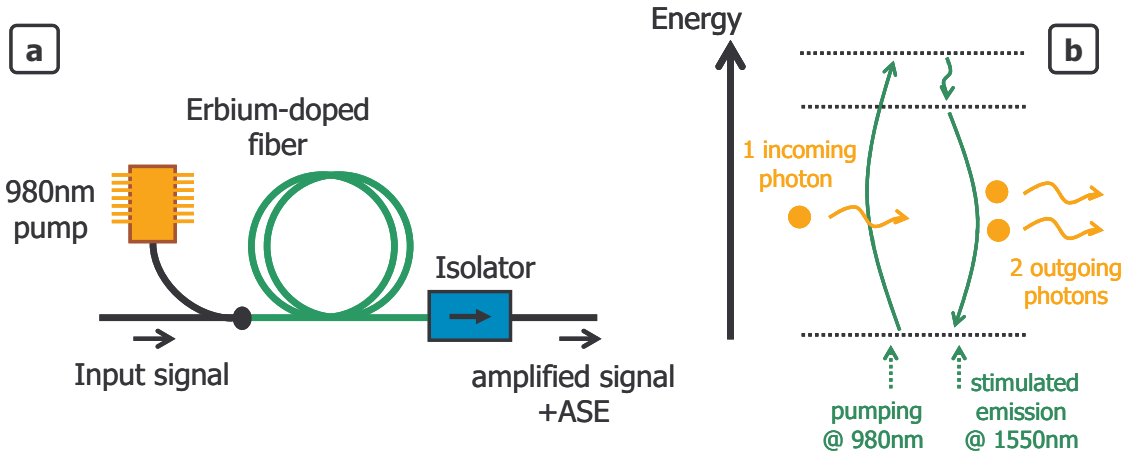

Fig. 1.3.10: (a) Scheme of an EDFA. (b) Principle of amplification in an erbium doped fiber.

At the same time, some erbium ions can "fall" back to their original energy level without stimulation by a signal photon, which is known as spontaneous emission. The photons generated by spontaneous emission are now amplified as well by the same mechanisms as the original signal photons. This phenomenon is called amplified spontaneous emission (ASE) and is the main noise source in optical amplifiers. The quality of an amplifier regarding the amount of generated ASE noise is given by the so-called noise figure (NF). It can be determined through a deeper analysis of the physical processes inside the amplifier [60]. For a single stage EDFA the NF is typically around 5dB, when pumped at a wavelength of 980nm, for pumping at 1480nm the NF is ~0.5dB worse.

Other mentionable optical amplification technologies besides the EDFA are the semiconductor optical amplifier (SOA) [61], [62] and the Raman amplifier [38], [39]. In long-haul transmission systems, the SOA is almost not used today since it has some important drawbacks compared to the EDFA such as polarization dependence, a higher NF and a fast gain response / nonlinear effects. Raman amplification is not very commonly used in commercially available systems due to its complexity and the high pump powers representing a risk for fiber fuse at fiber interconnections and furthermore requiring extensive eye safety procedures. However, in contrast to EDFA and SOA, Raman amplification provides distributed amplification over a fiber span and therefore allows reduced noise generation. This advantage has been exploited in laboratory experiments, where the combination of EDFA and Raman amplification has allowed achieving higher transmission distances than with only EDFA technology [63].

Dispersion Management

It has been found, that the tolerance to nonlinear effects is influenced by their interaction with chromatic dispersion [64–66]. This phenomenon has led to the research field of dispersion management. Here, the objective is to increase the tolerance to nonlinear effects of a transmission link by optimizing the evolution of chromatic dispersion along the transmission distance. This results in the so-called dispersion map, which indicates the accumulated dispersion as a function of distance. Fig. 1.3.11 shows three examples of typical dispersion maps.

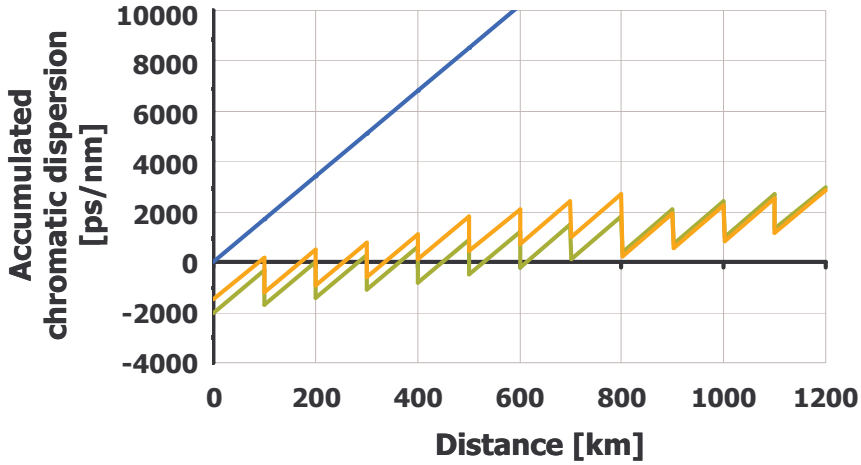

Fig. 1.3.11: Different dispersion maps: single periodic map, double periodic map (both comprising precompensation) and map without DCM

The optimum dispersion map depends on several parameters, such as the selected modulation format and the modulation rate [64–66]. Ways to practically implement different dispersion maps are mainly the use of fibers with different dispersion coefficients and the optimization of the location of dispersion compensating modules (DCMs) such as dispersion compensating fibers (DCFs) or fiber Bragg gratings. Nowadays, dispersion compensation can also be performed digitally in the DSP of a coherent receiver as already mentioned in section 1.3.2.

1.3.4 Performance Limits and Performance Evaluation

The practical implementation of Tx and Rx has a slightly worse performance then the theoretical optimum caused by limited bandwidth and other implementation imperfections [67]. This gap between theory and practice increases for higher modulation rates and for more complex modulation formats [45]. However, in most optical transmission systems the dominating signal impairments are caused in the transmission line. These impairments are mainly the physical propagation effects in the optical fiber presented in section 1.2.4, and the noise generated by ASE in the optical amplifiers.

It is of great interest for system design to separate the influence of the different effects on system performance in order to determine design rules and to predict performances of possible system configurations. An effect, which is relatively easy to quantify is the ASE noise. Its impact on system performance is linked by to so-called optical signal to noise ratio (OSNR), which is the ratio between signal power and noise power. Normally the OSNR is measured in a spectral band with a width of *0.1nm* and so it is given in *dB/0.1nm*.

For a concatenation of optical amplifiers with the same input power, as it is often the case in an optical transmission line, the OSNR in a reference bandwidth B_{ref} can be calculated according to the following formula [68]:

$$OSNR_{dB/B_{ref}} = -10\log_{10}\left(h\nu B_{ref}\right) + P_{inAmpli\_dBm} - NF_{dB} - 10\cdot\log_{10}\left(N_{Ampli}\right) \qquad (1.3.16)$$

$h\nu$ *is* the energy of a photon, given by the product of the Planck constant h and the photon's frequency ν. $P_{inAmpli\_dBm}$ is the input power of the amplifiers in dBm, NF_{dB} is the noise figure of the amplifiers in dB and N_{Ampli} is the number of concatenated amplifiers.

So for a wavelength around *1550nm* and a reference band of 0.1nm (corresponding to $B_{ref} \approx 12.5GHz$) the equation can be simplified to:

$$OSNR_{dB/0.1nm} \approx 58dBm + P_{inAmpli\_dBm} - NF_{dB} - 10 \cdot \log_{10}\left(N_{Ampli}\right) \quad (1.3.17)$$

In order to determine the quality of a combination of transmitter and receiver, a widely used criterion is its so-called back-to-back (BtB or B2B) performance as a function of the OSNR. To measure it, a transmitter and a receiver are connected directly, only by fibers of negligible length and by a device for noise generation, normally an optical attenuator followed by an optical amplifier. In this configuration, the signal is only impacted by transmitter and receiver degradations as well as by ASE noise. Fig. 1.3.12 shows the BtB performances, given by the Q²-factor, for different transmitter/receiver combinations using different modulation formats both obtained experimentally and by simulations.

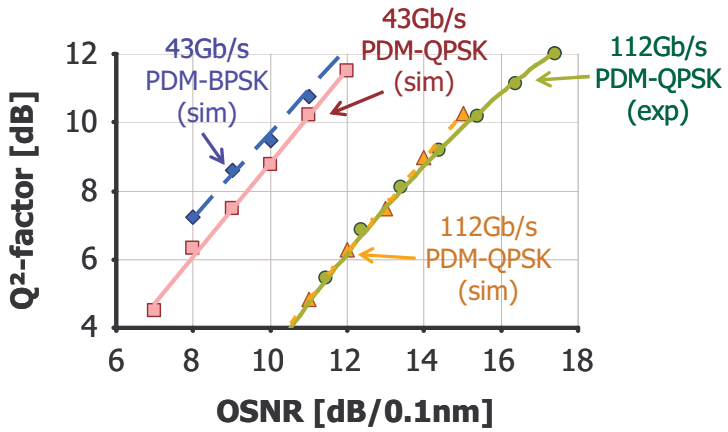

Fig. 1.3.12: Back to back performances for different modulation formats and different baud rates as function of OSNR for different modulation formats in simulations (sim) and experiments (exp).

Equations (1.3.16) and (1.3.17) indicate that the OSNR of a transmission system can be increased by simply increasing the input power, and it suggests that the performance can be improved in this way. This is true for systems that are limited by ASE noise. However, adding a transmission line causes additional limitations, particularly nonlinear effects. And so while it is desirable to increase the injected power in order to maximize the OSNR, a higher injected power also leads to stronger nonlinear effects that lead to signal degradations as well. This dilemma results in a tradeoff for the injected power at a point, where the OSNR is as high as possible without having to strong nonlinear impairments. As a consequence, we obtain the typical bell shaped curve for the Q²-factor as a function of injected power, as it is visualized in Fig. 1.3.13.

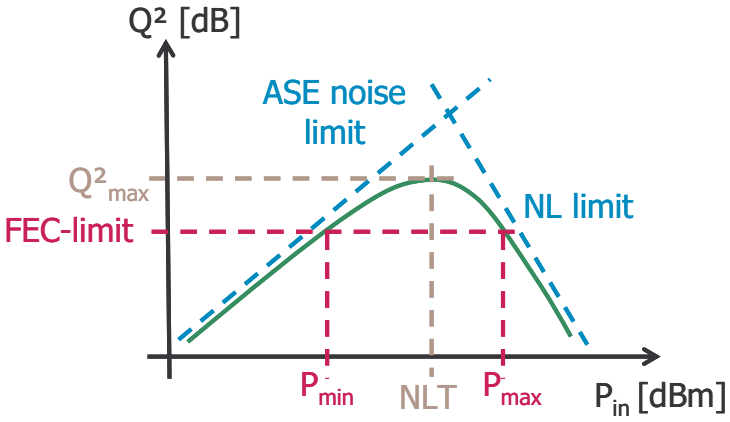

Fig. 1.3.13: Typical "bell shaped" curve for the Q²-factor as a function of input power after transmission. For low input powers, performance is limited by noise, for high input powers, performance is limited by nonlinear effects.

For low powers, in the so-called linear regime, the Q²-factor is limited by the OSNR and by linear transmission impairments, such as crosstalk for example, as we will see later in Chapter 3 and 4. Thus, the performance increases with increasing power up to the point, where nonlinear effects become dominant. The launch power at this point, which is also the point of optimum Q²-factor, is the so-called nonlinear threshold. For higher powers the Q²-factor decreases with increasing power due to the growing importance of nonlinear effects.

For a successful transmission, the received Q²-factor must be higher than a certain threshold, above which FEC is able to correct all received bit errors. We call this threshold the FEC-limit, as already mentioned in section 1.1.4. With increasing distance, the range of injected powers between P_{min} and P_{max} that permits staying above the FEC-limit gets smaller and smaller due to both, increased noise and increased nonlinear effects.

1.4 Conclusion of Chapter 1

In this chapter, I presented the generalities about optical transmission systems, which are useful for a better understanding of my work. I started with a general consideration of digital communication systems, without taking into account the particularities of optical data transmission. The basic objective of digital communication systems is providing the possibility to transmit a maximum of data from a given source to a given destination by making use of digital encoding of the signal. For this purpose, a transmission medium, the transmission channel, is required, which allows the propagation of physical signals, usually electromagnetic waves. The capacity of a digital communication system is on the one hand determined by the physical limitations of the channel, such as bandwidth or attenuation, and on the other hand by the applied technologies. Regarding the technologies, I gave a short overview over the most important basic concepts being namely modulation and demodulation as well as channel encoding and channel decoding. The actual realization of these concepts then depends on the concrete type of transmission system.

In order to set the focus on optical transmission, I started with the introduction of the optical fiber as a transmission channel. The optical transmission channel has the advantage of an extremely high bandwidth (around 4.5 THz in the C-band alone), since the guided electromagnetic waves are at a very high frequency (around ~200 THz). This

advantage in combination with relatively low attenuation (~0.2dB/km) makes optical transmission systems an unrivaled choice for nearly all world wide data traffic over long distances.

I presented the derivation of a theoretical model for the optical fiber, as it is commonly used today. Based on this model I pointed out the main physical limitations in optical transmission systems, which can be categorized into linear effects and nonlinear effects. The most important linear effects are attenuation, chromatic dispersion and polarization mode dispersion. The most important nonlinear effects are self phase modulation, cross phase modulation and cross polarization modulation. Today, system performance is limited by the compromise between nonlinear effects and noise, since linear effects can be compensated either physically or by digital signal processing.

Finally I introduced the typical set-up of optical transmission systems today, as well as its most important components. They are typically separated into three categories: transmitter, receiver and transmission line. Even though the functionality of each of these categories can be dealt with independently it is crucial to consider the interplay of these three blocks in order to optimize the system performance. Introducing a certain modulation format, for example, requires not only the possibility to generate it in the transmitter, but also the possibility to recover the encoded information in the receiver. So it was the improvement in both, transmitter and receiver technologies that allowed the progress from the most simple modulation format, NRZ-OOK, to more complex modulation formats such as QPSK or 16-QAM in combination with PDM as they are used today. Finally, also the design of the transmission line plays an important role. Different modulation formats cause different interactions with physical transmission impairments and so the optimum line design changes. Here an important topic is the so called dispersion management, which deals with the interplay of chromatic dispersion and nonlinear effects. It was found that by intelligently choosing where which amount of chromatic dispersion is compensated for, the impact of nonlinear effects can be reduced. In recent optical transmission systems using coherent detection, it has been found that the best nonlinear performance is achieved, when using no in-line DCMs and instead compensating for all chromatic dispersion in the Rx.

Chapter 2: The Increasing Demand for Capacity and Possible Concepts to Cope with It

2.1 Evolution of Network Traffic and Capacity of Optical Transmission Systems

Over the last decades, capacity demand for telecommunication systems has grown dramatically, driven by various new technologies and by new applications notably in the fields of file sharing, web browsing and video streaming [69], [70] . Fig. 2.1.1 shows the evolution of worldwide data traffic via internet protocol (IP) between 2006 and 2015 according to the Cisco Visual Networking Index [69], [70].

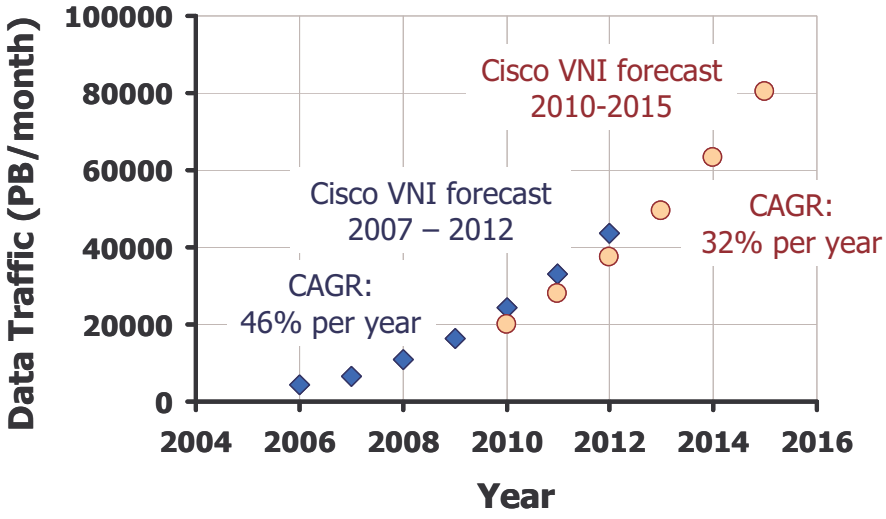

Fig. 2.1.1: Forecast of the worldwide IP-traffic in petabytes per month, according to the Cisco Visual Networking Index [69], [70].

We observe an exponential growth with a compounded annual growth rate (CAGR) of 46% per year for the prediction between 2006 and 2012 and with an estimated CAGR of

32% per year for the prediction between 2010 and 2015, which corresponds to a growth by a factor of 4 over this period. Although the CAGR has declined according to these two studies, the growth is still exponential and there is no reason to believe that the demand for new capacity will end abruptly. Providing the infrastructure in order to satisfy this demand in an economically attractive way, and thereby allowing continuing the traffic growth is a tremendous challenge for telecommunication operators, equipment vendors, developers and researchers.

As already mentioned in the introduction and in chapter 1, optical data transmission plays a key role in the worldwide telecommunication network, as it is by far the most appropriate known technology in order to transmit the required amount of data over long haul and ultra-long haul distances. Hence, economically worthwhile capacity growth in optical transmission systems is a key enabler for further overall traffic growth.

Since the advent of optical telecommunication systems, their capacity has already been increased tremendously, boosted by several key enabling technologies. Fig. 2.1.2 shows the evolution of the capacity x distance product over a single optical fiber between 1988 and 2012. This criterion is a good measure for the technological limit in optical transmission systems, since for the same technology, an increased capacity leads to a reduced transmission distance and vice versa. It can be observed, that since the first WDM experiment in the early 1990s, the capacity x distance product could be increased by a factor of 1000. Another factor of 100 has been gained by the introduction of WDM.

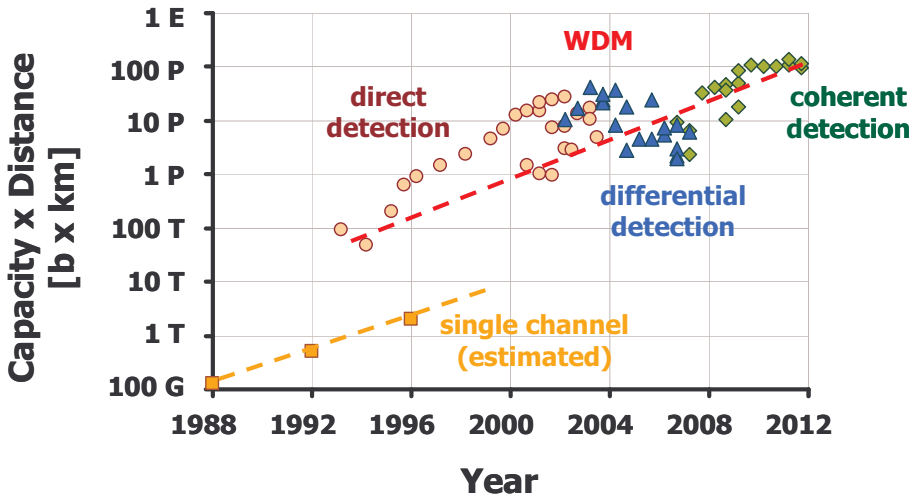

Fig. 2.1.2: Evolution of the capacity x distance product over a single optical fiber in research experiments between 1988 and 2012 on a logarithmic scale.

Fig. 2.1.3 shows the evolution of the capacity in commercially available optical transmission systems over a single fiber. Looking at this graph, we can underline more clearly than with results from the laboratory that the evolution was regularly approaching saturation before a new technological breakthrough allowed a further increase. During the late 1990s and the early 2000s, EDFA and WDM technology with channel spacing at 100 GHz allowed the transmission of ~40 channels at 2.5 Gb/s leading to an overall capacity of ~100 Gb/s. The introduction of FEC in optical transmission systems allowed an increase of the bitrate per channel to 10 Gb/s and together with dense WDM (DWDM), which reduced channel spacing to 50 GHz, overall capacities of ~1 Tb/s could be obtained. A further increase of the channel rates could then be obtained thanks to phase modulation and dispersion management, which both helped increasing the tolerance to noise and transmission impairments. Finally, the

introduction of coherent detection in combination with DSP nowadays allows the commercial use of PDM-QPSK at a channel rate of 100 Gb/s leading to an overall capacity of approximately 10 Tb/s.

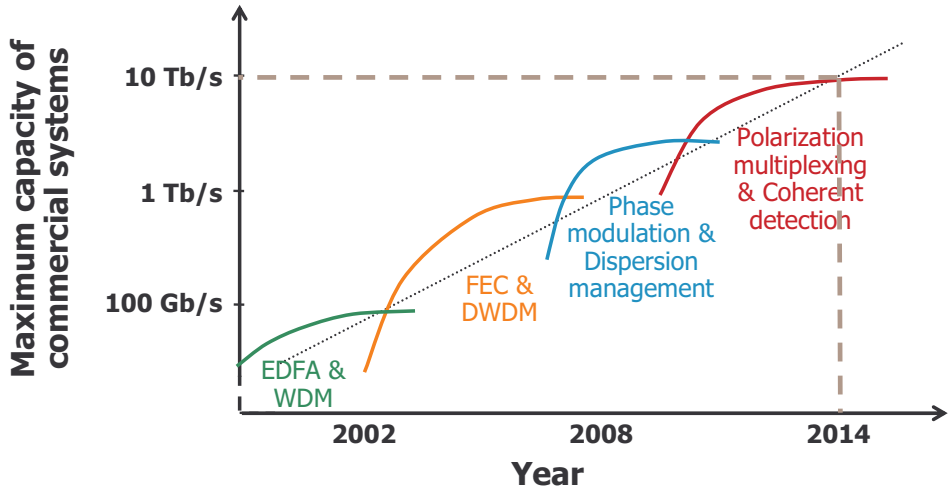

Fig. 2.1.3: Capacity evolution of commercially available optical transmission systems over a single optical fiber on a logarithmic scale.

The existing state of the art PDM-QPSK transmission systems with coherent detection are still subject to research, and it is supposed that they contain some more potential for optimization and thus for onward capacity growth. Areas of improvement can be for example pulse shaping/filtering and further reduced channel spacing [41], [42], [44], [71], advanced FEC technology [8], [9], [43] or digital mitigation of transmission impairments (MAP, MLSE, or NL-compensation) [42], [47], [72].

A part of my work was dedicated to the optimization of PDM-QPSK transmission systems with coherent detection. Two milestone transmission experiments are described in the following section in order to give examples how an incremental enhancement of the capacity x distance product could be achieved. At the same time, Fig. 2.1.3 suggests that more substantial technological progress will be needed soon, if optical transmission systems shall be able to continue to follow the exponential growth of traffic demand. Several possible solutions are discussed in the research community at the moment, which I will present in section 2.3. One of these solutions is mode division multiplexing (MDM), on which I will then focus during the rest of this manuscript.

2.2 Record Transmission Experiments with State of the Art Technology

The two experiments presented in the following were led by my colleague Massimiliano Salsi. I contributed in big parts to the installation of the set-up, the measurements and the evaluations of the data. The description of the experiments in the sections 2.2.1 and 2.2.2 are very similar to the published articles [63] and [43].

2.2.1 155 x 100 Gb/s Transmission over 7200 km using C + L-Band with a Combination of EDFA and Raman Amplification

Background

At the time of the experiment, in August 2009, commercial undersea cables had been relying on WDM at 10Gbit/s channel rate for almost 10 years, but a new generation of cables was then in sight, using channels at 40Gbit/s. Moreover, research had shown how to further increase the capacity of ultra-long haul systems by using 100Gbit/s per channel [73], [74]. In this work, we extended previous results [74] by employing a different fiber type, and combined C+L band amplification supporting a total of 155 channels. An overall capacity of 15.5Tbit/s was sent over a distance of 7200km in a single fiber. This was the first report of a capacity x distance product in excess of 100Pbit/s·km.

Experimental Set-Up

The test-bed is schematized in Fig. 2.2.1. It involves 155 distributed feedback (DFB) lasers spaced by 50GHz, ranging from 1531.51nm to 1562.64nm in the C-Band and from 1571.24nm to 1602.74nm in the L-Band. The even and odd channels of each band are combined into two spectrally-interleaved wavelength combs. Both combs are modulated independently at 100Gbit/s in separate QPSK modulators, fed with 2^{15}-1 bit-long sequences at 28Gbit/s, taking into account 7% FEC and protocol overheads. The output from each modulator is split into two polarization-maintaining fiber (PMF) paths in a 3dB coupler. The QPSK data along one path are delayed by some hundreds of symbols in a PMF, before being polarization-multiplexed with the QPSK data along the other path by a polarization beam combiner. This scheme produces PDM-QPSK channels at 112Gbit/s. The odd and even channels are then spectrally interleaved through a 50GHz interleaver, and boosted by a C-band or an L-band EDFA, whichever applies. The output of the C- and L-EDFA boosters are combined thanks to a C/L multiplexer and injected into the recirculating loop.

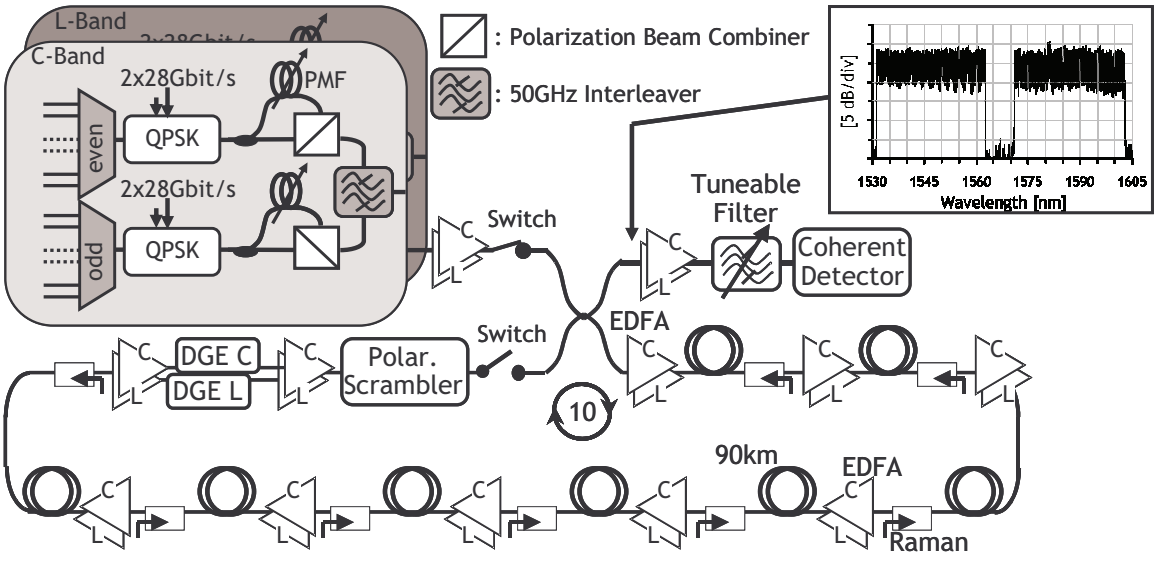

Fig. 2.2.1: Experimental set-up for transmission of 155x100 Gb/s over 7,200 km.

The loop consists of eight 90-km-long spans of Enhanced Pure Silica Core Fiber (E-PSCF) [75], which is the Z-PLUS Fiber™ provided by Sumitomo and characterized by 110μm² effective area, 0.168dB/km average loss, <0.1ps/√km polarization mode dispersion. No dispersion-compensating fiber is used here. Fiber loss is compensated for by hybrid Raman-erbium optical repeaters, depicted in Fig. 2.2.2. Each repeater incorporates a C-band EDFA and an L-band EDFA operating in parallel and a Raman pre-amplifier. The pre-amplifier is designed to provide ~10dB on-off gain, thanks to backwards-directed laser diodes at wavelengths 1432nm, 1457nm and 1487nm. It is spliced to the set of EDFAs via a gain-flattening filter (GFF), which equalizes the power distribution across the multiplex. Further power adjustment is performed thanks to a pair of dynamic gain equalizers (DGE), inserted at the end of the recirculating loop. The loop also incorporates a low speed (~1 kHz) polarization scrambler which ensures that the PMD conditions vary from one loop to the next. It is filled and emptied using two acousto-optic switches, triggered by time-delay generators, synchronously with the BER measurement equipment.

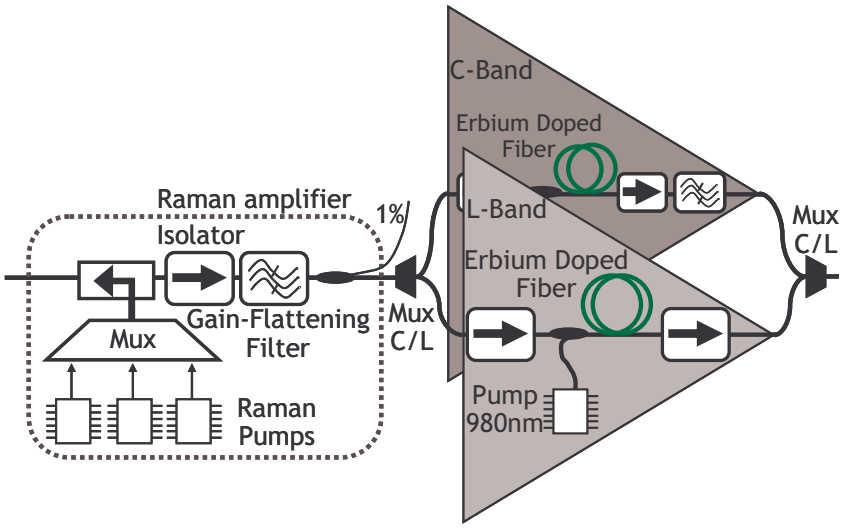

Fig. 2.2.2: Scheme of hybrid Raman-Erbium repeaters.

At the receiver end, each channel can be isolated from the rest of the multiplex by a tunable filter and is sent to the dual-polarization coherent mixer together with a 100 kHz line-width DFB laser as local oscillator. The mixer feeds four balanced photodiodes, connected to a real time sampling oscilloscope working at 50GSamples/s. A computer collects the oscilloscope's waveforms and performs offline signal processing for recovering the original bit streams [76]. All the chromatic dispersion accumulated within the transmission line (up to 170,000ps/nm in the L-band) is compensated numerically by a digital filter.

Experimental Results

Four sets of 2 million samples are used to calculate the BER of each one of the 155 channels. The BERs are converted into Q²-factors and depicted versus wavelength after 10 loop round-trips, i.e. after 7,200km, in Fig. 2.2.3a. The average Q²-factor is 9.7dB, while the minimum Q²-factor is never lower than 9.1dB. Assuming today's commercial FEC code with 7% overhead, this minimum Q²-factor is still 0.5dB above the threshold leading to a BER of 10^{-13} after FEC.

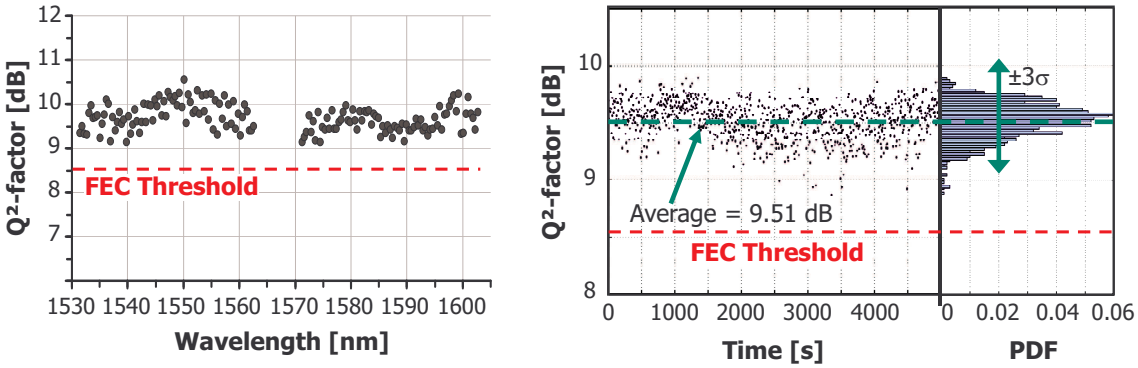

Fig. 2.2.3: Experimental results. (a) Q²-factor vs. wavelength after 7200km; all the results are above FEC threshold. (b) Statistical distribution of Q²-factor for the channel at 1584.95nm; Average value= 9.51dB.

We now investigate the Q²-factor stability by performing 1,000 consecutive Q²-factor measurements of a typical channel, at 1584.95nm. Each measurement is extracted out of 0.5M samples, every 5s. In Fig. 2.2.3b the Q²-factors are reported as a function of time. The probability density function is also shown on the right. The interval corresponding to three times the standard deviation σ is [10.2, 9.1]dB, with an average Q²-factor of 9.51dB. The presence of the polarization scrambler in the loop grants that each recording corresponds to a different polarization condition. However, the small Q²-factor fluctuations are mainly attributed to loop-specific effects and the worst points never fall below the FEC threshold of 8.5dB.

Conclusion

We reported here an experimental demonstration of 15.5Tbit/s over 7,200km. Even though the margins shown by the experimental results did not satisfy industrial requirements, this experiment was an important milestone towards the potential of coherent-based solutions for ultra-long haul applications. With the technologies reported here, the capacity of undersea systems were having the potential to increase by a factor of 10 (×5 from the higher spectral efficiency and ×2 from the doubling of the amplifier bandwidth), compared to at that time commercial state of the art 10Gbit/s submarine systems.

2.2.2 Transmission of 96×100 Gb/s with 23% Super-FEC Overhead over 11,680 km, using Optical Spectral Engineering

Background

The experiment was realized in August 2010 and published in March 2011 [43]. Preceding publications had shown the possibility of covering transoceanic distances with coherent-based modulation formats at 100Gb/s [41], [63], [73], [74]. A large majority of them had used Raman amplification to provide an OSNR over the extremely long distances. However, Raman amplification has not yet been implemented in any commercial submarine cable, where well-mastered, reliable technologies are mandatory.

We used here only EDFAs, similarly to other works published around that time [41], [77]. We transmitted 96 channels at 100Gb/s with polarization-division multiplexed quadrature phase-shift keying (PDM-QPSK), for a cumulative capacity of 9.6Tb/s, over 11,680km in a recirculating loop based on 50km ultra-large effective area fiber spans. We therefore matched the best reported capacity × distance product to date (112Pb/s·km) [63], but without costly L-band or Raman amplification [63] and by relying on standard receiver algorithms, free of complex detection schemes such as maximum a posteriori probability (MAP) estimation [41]. We showed that this performance can be obtained with optical spectral engineering and super FEC.

With the advent of coherent systems, the field of FEC had gained some more interest. Up to then, the most common FEC code in wavelength-division multiplexed (WDM) transmission systems at 10Gb/s and 40Gb/s bit rates used a concatenated code with hard-decision, having 7% overhead and a net coding gain (NCG) of ~8.5dB, leading to an FEC threshold at a BER of $4 \cdot 10^{-3}$ [7]. An alternative hard-decision code, with 25% overhead, was also in operation over some commercial submarine cables at 10Gb/s allowing a correction of a BER of 1.3 10^{-2} (7dB Q²-factor). By comparison, a super FEC code using soft-decision could achieve more than 10dB of NCG. With a comparable overhead (23.6%) [8], [9], such an FEC code could correct BERs up to $2 \cdot 10^{-2}$ (6.25dB Q²-factor). It was demonstrated experimentally at 10Gb/s in 2003 [8], and realized in CMOS VLSI technology in 2006 [9]. The super FEC requires complex analog-to-digital converters at the receiver, which helpfully are included in all coherent receivers. However, the benefits of super FEC cannot be evaluated only through the NGC and the maximum BER that can be corrected. They can be undermined by the increase of overhead, resulting in impairments from electronic components and in greater linear and nonlinear crosstalk from WDM channel neighbors.

In our experiment, we assessed the impact of these impairments by operating at 128 Gb/s and 112 Gb/s to emulate super FEC and conventional FEC with 7% and 23% coding and protocol overheads respectively. Despite the very narrow channel spacing (37.5GHz), we successfully performed a transmission over a transpacific distance.

Experimental Set-Up

Our test-bed is depicted in Fig. 2.2.4. It contains 96 distributed feedback (DFB) lasers, ranging from 1533.47nm to 1561.83nm, spaced 37.5GHz apart, which are combined into two spectrally-interleaved wavelength combs. The two combs are passed into two separate QPSK modulators, fed with 2^{15}-1 bit-long sequences at 32Gb/s, emulating 23%-FEC overhead and protocol overhead. A 3dB coupler splits the output of each modulator into two polarization-maintaining fiber paths, which are delayed by several hundreds of

symbols, before being recombined through a polarization beam combiner (PBC). This produces PDM-QPSK data at 128 Gb/s. The odd and even channels are spectrally interleaved through a commercially available 37.5GHz optical interleaver with programmable transfer function. After the interleaver the optical comb is boosted by a dual-stage EDFA and is injected into the recirculating loop.

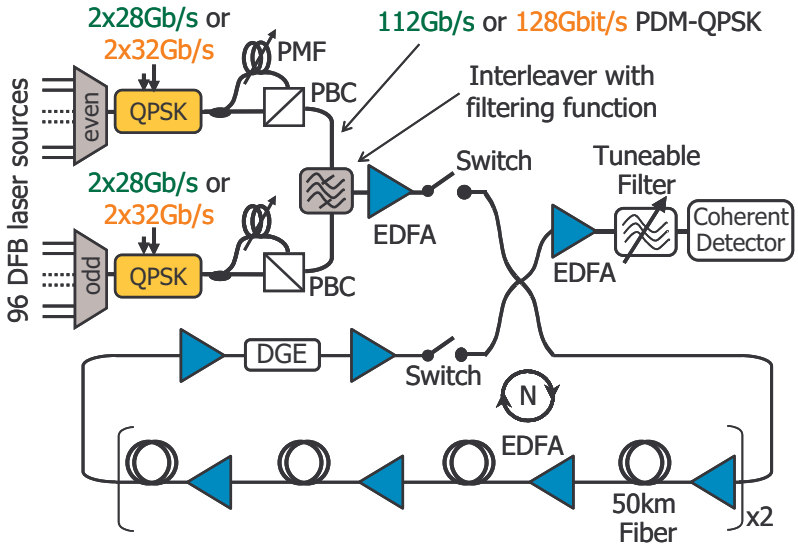

Fig. 2.2.4: Experimental set-up for transmission of 96x100 Gb/s over 11,680 km.

The loop consists of eight 50km spans of a new prototype fiber from Draka with an ultra-large effective area of 155μm², an attenuation of 0.185dB/km at 1550nm, and a chromatic dispersion of 21.7ps/nm·km at 1550nm. No dispersion-compensating fiber is used in the experiment. The loss of each span is compensated for by a single stage 980-nm pumped EDFA followed by a gain-flattening filter for channel-to-channel equalization. Further adjustment is performed with a dynamic gain equalizer, located between two EDFAs. Filling and emptying of the loop is controlled by two acousto-optic switches, triggered by time-delay generators, synchronously with the BER measurement equipment.

At the receiver end, the signal is pre-selected with a narrowband tunable optical filter and sent to the dual-polarization coherent receiver. The receiver is based on a real-time 50GSamples/s sampling scope with 16GHz bandwidth, interfaced with a computer for offline processing [78]. Chromatic dispersion of up to 295ns/nm is digitally compensated for.

Waveform engineering is undoubtedly a promising field for performance improvement. We focused here on spectral engineering, targeting the largest filling ratio of the 37.5GHz channel grid with 32Gbaud signals. This suggests reshaping the spectrum of each channel to a square-like profile [79]. We adjust our programmable optical filter with 34GHz bandwidth at 25dB (i.e. with the steepest leading and trailing edges achievable with our equipment), while the top of the intensity response is engineered to follow a quadratic intensity profile of variable depth in dB.

Experimental Results

We measure the Q^2-factor of one typical channel in a back to back configuration with all WDM neighbors and normalize it to the reference Q^2-factor of the same channel without filter (actually, passed in a large noise-rejecting optical filter which causes no noticeable signal truncation). This yields the so-called Q^2-gain, reported in Fig. 2.2.5.

The gain is measured when the filter center depth is varied, whether the channel is surrounded by neighbors or not. It can be seen that the Q^2-factors are almost unchanged when the neighboring channels are removed, which shows that channel-to-channel crosstalk is well-contained in all filter configurations investigated here. Fig. 2.2.5 also depicts a few typical spectral profiles and the corresponding eye-diagrams of one polarization tributary, when surrounded by neighbors. One conclusion that can be drawn from the measurements is that the narrow profile of the standard flat-top filter is found responsible for 0.5dB penalty with respect to the no-filter reference. Engineering the spectral response according to a quadratic profile with variable depth enhances the power of the spectral components which are farther from the carrier frequency, and the Q^2-factor can become larger than that of a single channel without optical filter. Interestingly, the optimum depth (at 6dB) was found identical in the back-to-back configuration of Fig. 2.2.5 and after transmission. We therefore chose this setting in the rest of the paper.

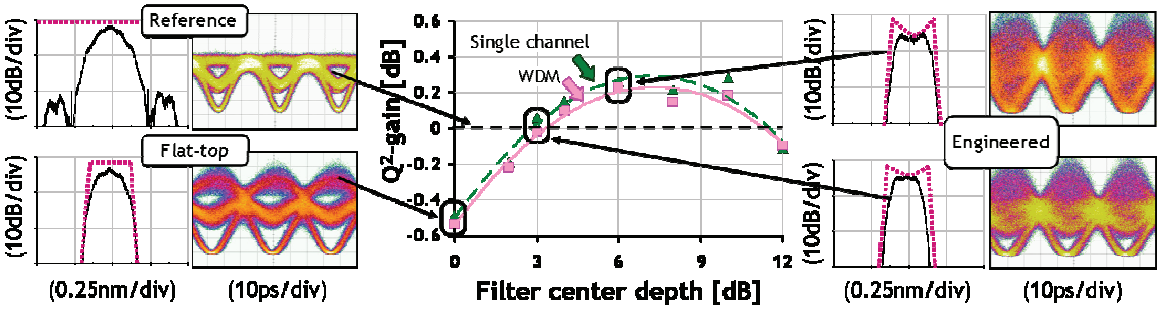

Fig. 2.2.5: Benefits of optical spectral engineering. In the insets, measured signal spectra (1pm resolution), filter power responses and eye-diagrams along one polarization

We feed the recirculating loop with the above signal at 18, 23, 28 and 33 loop round-trips corresponding to 7,250 km, 9,270 km, 11,280 km and 13,300 km. To evaluate the impact of the increased FEC overhead the measurements have been taken at 28 GBaud and 32 GBaud at these distances. We report in Fig. 2.2.6a the average performance (over a dozen channels) in the middle of the EDFA band versus distance at 112 Gb/s (green circles) and 128 Gb/s (red squares). A point at 11,280 km (gray diamond) indicates the Q^2-factor with a simple flat top filter at 128 Gb/s. The average Q^2-factor is 9.85 dB and 10.95 dB respectively at 128 Gb/s and at 112 Gb/s after 7,250 km. It decreases down to 7.57 dB and 8.75 dB respectively after 13,300 km. The impact of an FEC overhead increase from 7% to 23% is therefore in the range of 1 dB, to be compared with the 0.6 dB line rates ratio ($10 \cdot \log(128/112)$). This Q^2-factor degradation stays within acceptable limits despite the narrow channel spacing. Hence, the reduction of the Q^2-factor FEC threshold (2.2 dB) stemming from the use of 23%-overhead super FEC clearly outweighs the degradations due to crosstalk and propagation impairments. Note that no BER could be recorded after transmission without optical pre-filtering. Besides, the fine optical spectral engineering of Fig. 2.2.5 is found to provide a 1 dB Q^2-factor improvement at 11,280 km distance. By simply extrapolating the curves of Fig. 2.2.6a, this improvement can be translated here into a valuable ~2500 km gain in propagation distance.

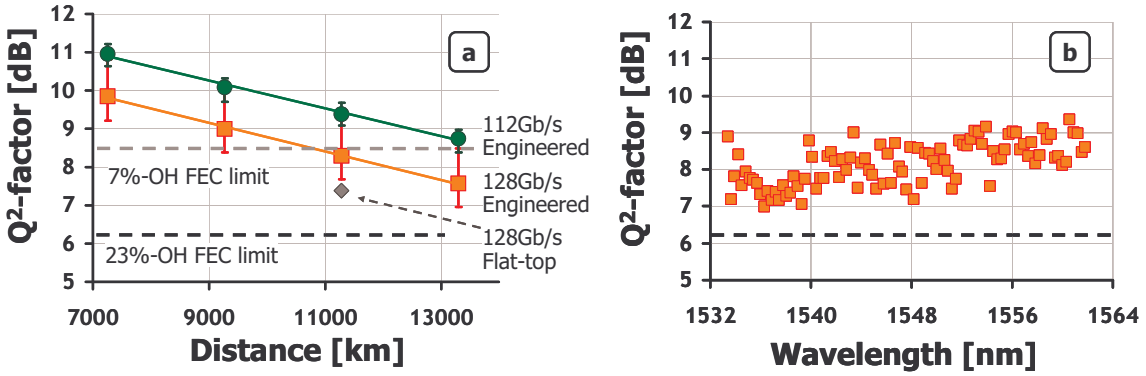

Fig. 2.2.6: (a) Impact of FEC overhead on performance versus distance. (b) Q^2-factors of all the 96 channels after 11,680km.

Fig. 2.2.6a shows the results obtained at 11,680km, where all the 96 channels have been measured. The average Q^2-factor is 8.1dB and the worst Q^2-factor across the WDM comb is 7.0dB, still 0.75dB above the FEC threshold. In Fig. 2.2.7, we reported the statistics of Q^2-factor recordings over 4000s for a typical channel, namely at 1547.31nm. The measurements are found to be very stable, with standard deviation below ±0.25dB.

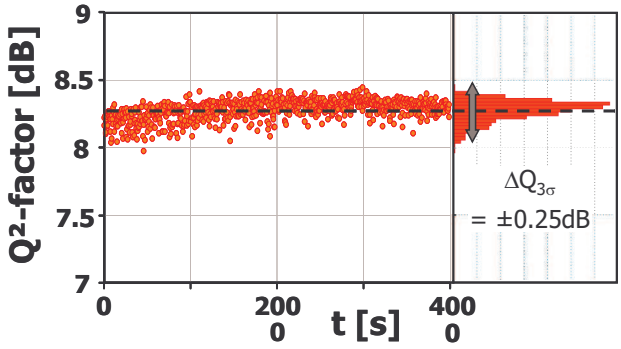

Fig. 2.2.7: Statistics of Q^2-factor over 4000s at 1547.31nm after 11,680km.

Conclusion

We have demonstrated a transmission of 96 x 100 Gb/s 37.5 GHz-spaced channels over 11,680 km. We used coherent detection, polarization multiplexing, QPSK modulation format and an ultra-large effective area fiber. The combination of 23%-overhead-FEC and optical spectral engineering enabled the high spectral information density of 2.7 b/s/Hz with minimal increase of propagation impairments. Therefore our experiment matched the best reported capacity times distance product (112 Pb/s·km) at that time while employing only C-band EDFAs.

2.3 Ways to Continue the Capacity Growth

The crucial resource that limits the capacity in digital communication systems is the exploitable spectral bandwidth of the physical transmission channel. So capacity increase over an optical fiber, as over any other digital transmission channel, can be achieved in two ways: firstly by increasing the exploitable spectral bandwidth and secondly by using the spectral bandwidth more efficiently. If both of these solutions cannot provide the capacity that is demanded to be transmitted between two points, additional physical transmission channels must be added. In other words the signals have to be spatially multiplexed and so this technique is referred to as space division multiplexing (SDM). All of these three mentioned directions for capacity increase are subject to research at the moment. Although I have not worked in detail on most of the topics, I'm now going to present a brief overview about the possibilities for capacity growth in order to facilitate the positioning of my work in this context.

2.3.1 Increasing the Exploitable Spectral Bandwidth

Today, the exploitable bandwidth in optical transmission systems is limited by the amplification band of the EDFA, which has a width of ~35nm. Compared to that, the band of low attenuation in an optical fiber is much broader, as it can be observed in Fig. 1.2.7 and in Table 1.3.1. Consequently, there is the possibility to make use of a larger part of this band by applying other amplification techniques. Fig. 2.3.1 shows two possibilities to do so: the first one depicted in Fig. 2.3.1a represents the approach of combining C-band and L-band EDFAs allowing doubling the exploitable bandwidth. This technology is already available, as demonstrated in the transmission experiment of section 2.2.1, but it leads to increased complexity and so it is questionable if it is also of interest for commercial systems. A second possibility, depicted in Fig. 2.3.1a, could be to apply amplifier concepts being completely different from the EDFA technology and having a broader amplification band. Such technologies could be based on Raman amplification, improved SOA devices or parametric amplification.

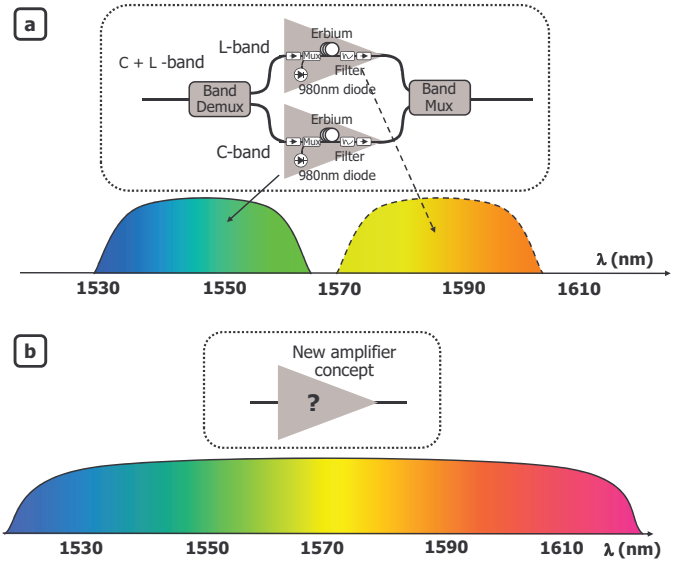

Fig. 2.3.1: Possibilities to increase the exploitable bandwidth.

2.3.2 Increasing the Spectral Efficiency

Much more attention in research is paid to the second approach though, the increase of the so-called spectral efficiency (SE). It is defined as the number of transmitted bits per second in a frequency interval of 1 Hz; hence its unit is *bits/s/Hz*. So far, SE was enhanced either by increasing the modulation rate per WDM channel at constant channel spacing, by packing WDM channels more densely or by using higher order modulation formats. The three approaches are visualized in Fig. 2.3.2. Today channel spacing has become very close to the symbol rate and only little potential is left for gaining SE in this direction.

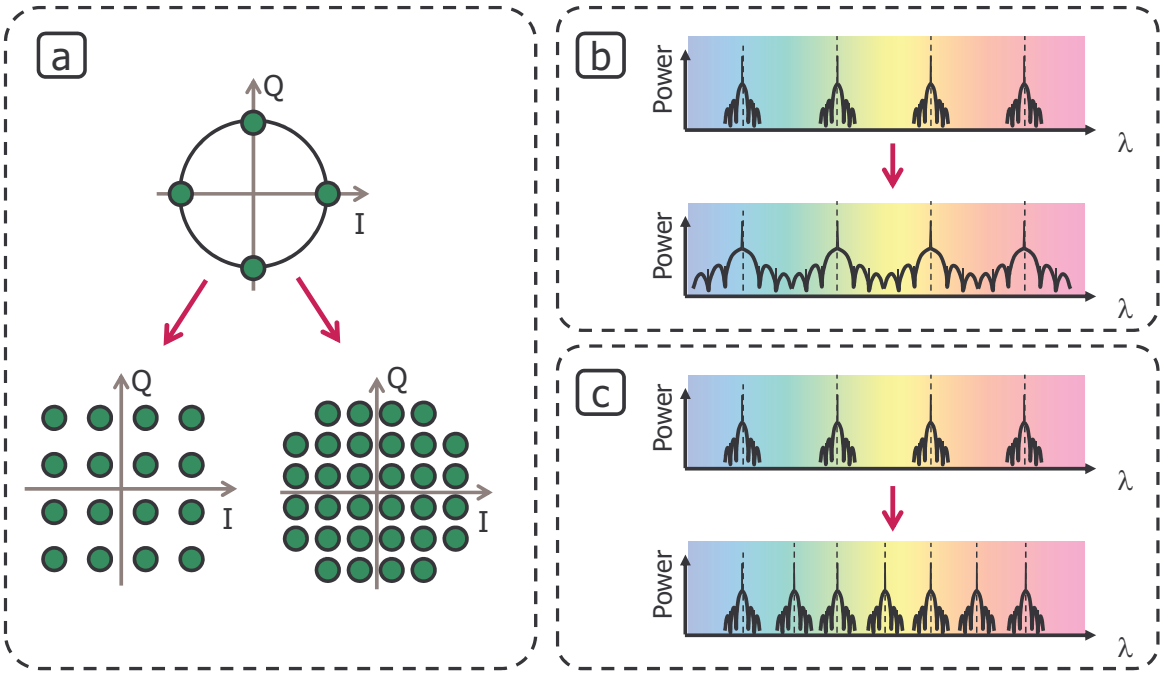

Fig. 2.3.2: Ways to increase spectral efficiency (packing denser, modulation formats, higher bitrate per channel).

The Shannon limit formulated in equation (1.1.1) shows that the maximum capacity for constant bandwidth, which is equivalent to the spectral efficiency, scales logarithmically with the SNR. Moreover, in state-of-the-art optical transmission systems without in-line dispersion compensation, the so-called effective SNR, accounting for both noise and nonlinear effects, is inversely proportional to the transmission distance [34], [80]. This has the consequence that increasing the spectral efficiency leads to a dramatically reduced transmission reach. Fig. 2.3.3, which has been taken from [11], shows how the maximum transmission reach declines as a function of SE based on the theoretical limit for the nonlinear optical fiber channel [2] and on published experimental results in single channel or WDM systems.

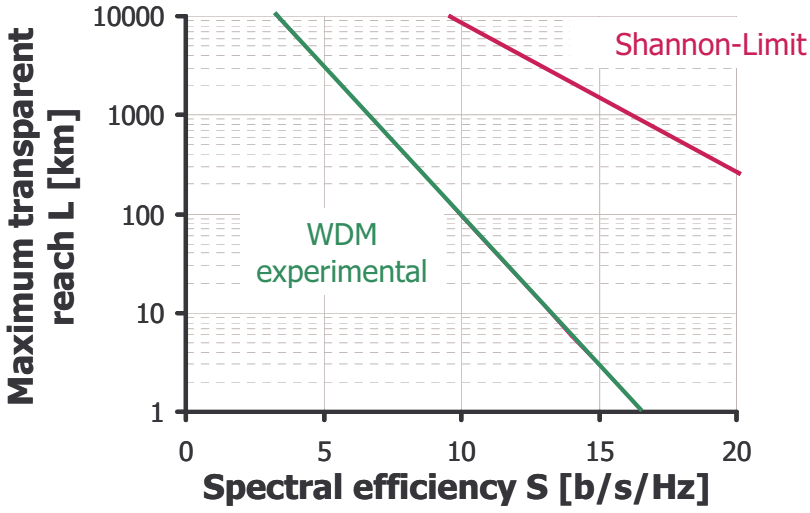

Fig. 2.3.3: Maximum reach without electrical regeneration for increasing spectral efficiency. Theoretical limit (Shannon-limit), estimations based on published experimental results for both single channel and WDM transmissions.

Taking a transmission reach of 1000 km as a reference, we can observe from Fig. 2.3.3, that the experimental results for WDM systems have reached an SE of ~6.5 b/s/Hz compared to an SE of ~16.5 b/s/Hz at the Shannon-limit. Hence the theoretically possible maximum capacity gain at this point is a factor of ~2.5. Comparing this limited potential to the predicted traffic growth by a factor of 4 between 2010 and 2015 alone, as it is presented in Fig. 2.1.1, makes it clear that other solutions for capacity increase must be considered as well.

2.3.3 Spatial Division Multiplexing

Concerning the practical realization of SDM, I will distinguish between four different approaches that have been proposed so far. Their difference is based on the applied fiber type, which leads to consequences for the whole system design. Of course, it is desirable to have a maximum of synergies between the different spatial channels in order to reduce the required space of an SDM system and mainly to reduce the costs for system deployment and operation. Synergies can be imagined in all parts of the system: Tx/Rx, fiber and amplifiers. At the same time, it is crucial to minimize performance limiting interactions between the different spatial channels and the propagating signals. Based on these criteria, all approaches come along with different potentials and challenges. In the following we will describe them briefly:

SMF-Bundle

The trivial solution when capacity over a single fiber is not sufficient is simply deploying a higher number of fibers in parallel. From a theoretical point of view, this solution can be considered as a form of SDM. Optical fibers have the advantage that there is no crosstalk between two fibers when putting them close to each other, as it is the case with copper wires for example. This results in the positive aspect, that deploying SMF-bundles leads to no additional transmission impairments compared to transmission over a single fiber and so the achievable performance is the same. However, this approach allows for no synergies in the fiber itself, whereas synergies in amplifiers and Tx/Rx are imaginable.

Uncoupled Multicore Fiber

Transmission over uncoupled multicore fibers is supposed to allow propagation of independent signals through different cores of the same fiber. By doing so, the advantage of having no significant crosstalk as it is the case in the SDM solution "fiber bundle", shall be combined with a higher level of integration in the line fiber. However, in order to avoid crosstalk between the different signals, the cores have to be spaced sufficiently far from each other [81]. An example of an uncoupled multicore fiber design is shown in Fig. 2.3.4.

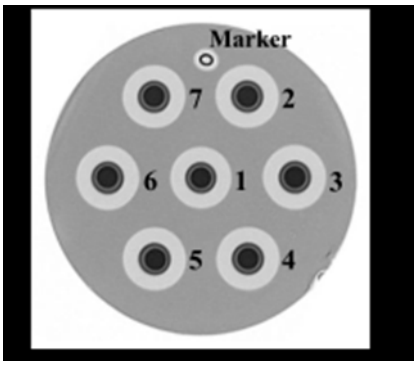

Fig. 2.3.4: Cross section of a trench-assisted uncoupled 7-core fiber [81].

So far, transmission of 7 x 10 x 128 Gb/s using an uncoupled 7-core fiber has been demonstrated over 2688 km, claiming a record SE x distance product per fiber of 40,320 km·b/s/Hz [82]. However, amplification was done here by splitting the signals of each core into independent SMFs and by amplifying them separately before reinjecting them into the multicore fiber. The transmission experiment with the highest number of cores has been presented using a 19-core fiber and transmitting 19 x 100 x 172 Gb/s over 10.1 km without inline amplification [83]. Independently, multicore amplification has also been demonstrated using 7-core EDFs [84], [85].

In general, design and manufacturing of multicore fibers is much more complicated than it is the case for single mode fibers. Hereby, key issues in addition to coupling between the cores are also the control of bending loss and the maximization of the effective areas in the different cores, which are typically around $80\mu m^2$ at the moment [81]. Furthermore, it will be crucial to master efficient coupling into the multicore fiber and out of the multicore fiber, as well as multicore amplification in order to take advantage of this technology.

Coupled Multicore Fiber

In this approach, the cores of the employed multicore fiber are closer to each other than in an uncoupled multicore fiber as it is depicted in Fig. 2.3.5a. This leads to stronger coupling between the signals propagating through the different cores, forming so-called "supermodes" that are illustrated in Fig. 2.3.5b. Compared to uncoupled multicore fibers, coupled multicore fibers impose less constraints concerning fiber design and manufacturing, but in exchange, they require MIMO DSP in the Rx for the decoupling of the supermodes.

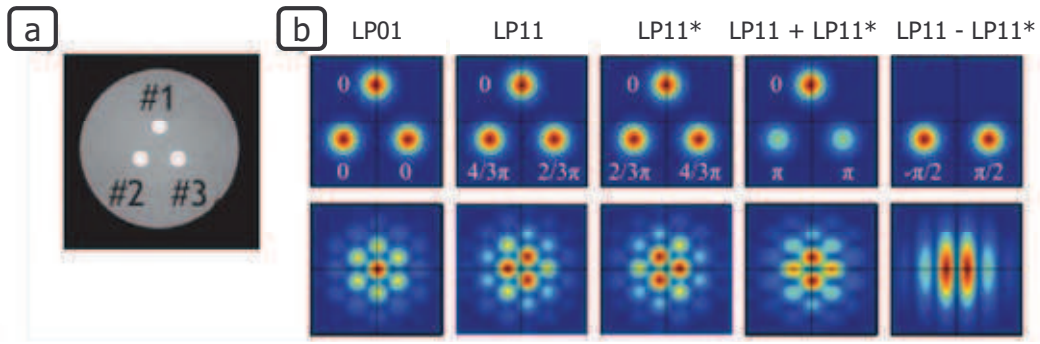

Fig. 2.3.5: (a) Cross section of a coupled multicore fiber. (b) Super modes [86].

Coupled multicore transmission using supermodes has been investigated recently based on numerical studies [87], and experimental demonstrations using three cores achieving transmission distances of 1200 km [86] and 4200 km [88] have been presented in the postdeadline sessions of ECOC 2011 and OFC 2012. Decoupling of the supermodes, which were modulated at 20 GBaud was done by a 6x6 MIMO processing taking into account the signals transmitted in the 2 polarization modes in each fiber core. In both mentioned demonstrations of coupled multicore transmission experiments, amplification has been done by splitting the signals of each core into independent SMFs and by amplifying them separately, as it was done in the uncoupled multicore experiments.

Compared to the uncoupled multicore approach, constraints on fiber design are less strict and so parameters can be tuned more easily to allow better transmission properties. This is manifested for example when looking at the relatively high effective areas of $\sim 130 \mu m^2$ per core in [88]. Moreover, the accomplished transmission distance of 4200 km is the highest for all types of SDM so far. Hence, coupled multicore transmission seems to be a promising approach, even though transmission over a number of cores higher than 3 has not been demonstrated yet.

Strongly Coupled and Weakly Coupled Mode Division Multiplexing

The idea behind mode division multiplexing (MDM) is to use an optical fiber, which allows the propagation of several spatial modes through a single core. Since all spatial modes in one fiber are orthogonal with respect to each other it is theoretically possible to modulate independent signals onto each spatial mode, transmit them over the same fiber and to recover the signals after transmission without any loss of information. As a consequence, the capacity per fiber can be multiplied by the number of spatial modes. This is in analogy to the aforementioned SDM systems, where the system-capacity can be multiplied by the number of fibers or fiber cores.

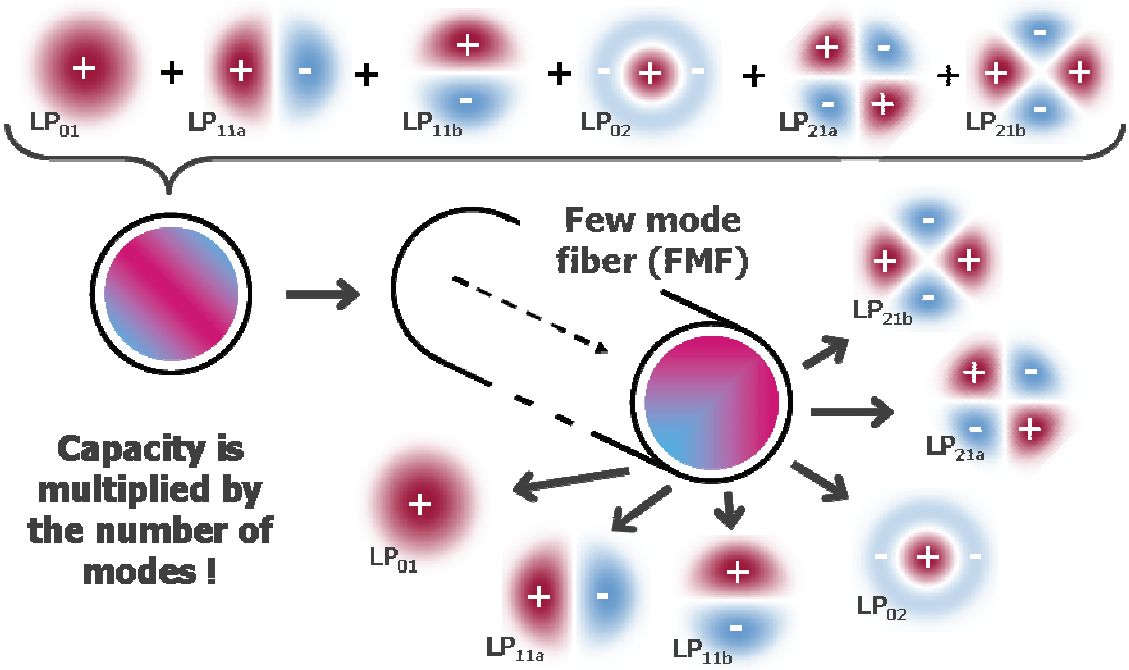

Fig. 2.3.6: Concept of mode division multiplexing

MDM was already subject to research in 1982 [89] but there has never been a lot of attention paid to this technology until almost 30 years from then. So the first experimental MDM demonstrations have been presented at OFC 2011 [90–93] accomplishing a record distance of 10 km when using 3 spatial modes modulated at 14 GBaud PDM-QPSK [93], and of 40 km when using 2 spatial modes modulated at 28 GBaud PDM-QPSK [92]. All of the first MDM demonstrations made use of only one single wavelength channel per spatial mode and of no few-mode amplification. Mode demultiplexing was enabled by a 6x6- respectively 4x4-MIMO DSP taking into account the two polarization modes of each spatial mode used for signal propagation.

Since then, we have witnessed numerous improvements. Without amplification, the transmission distance for 3-mode experiments has been increased to 33 km [94] and 96 km [95], and the maximum number of exploited modes has been increased to 5, by successfully using them for a transmission over 40 km [96]. This experiment was the only one so far that successfully relied on purely physical demultiplexing without joint MIMO-processing of all applied spatial modes. We call this approach "weakly coupled" MDM compared to the "strongly coupled" approach relying on joint DSP for all modes. I will introduce the two MDM system design strategies more in detail in section 3.1.2.

A next important step was the realization of few-mode amplification. After several theoretical and numerical studies on it [97–101], first experimental results have been presented at ECOC 2011. In one experiment, few-mode Raman amplification was used for transmission of three spatial modes over 137 km [102], and in another experiment a few-mode EDFA was used together with the first combined demonstration of WDM and MDM [103]. In this experiment, 88 x 3 x 112 Gb/s were transmitted over 50 km of 3-mode fiber. A second realization of a few-mode EDFA was presented without associated transmission experiment [104].

Recently a record transmission distance for MDM has been presented by transmitting 6 x 20 GBaud modulated with QPSK using 3 modes over 1200 km [105]. Amplification was done similarly to the record transmission experiments with multicore fibers, by demultiplexing the signals into SMFs for amplification and then multiplexing them again

into the FMF. However, an interesting novelty of this experiment is that two different FMF types were used in order to equalize group velocity differences between the modes.

Comparison of the Presented SDM Techniques

To end this chapter I would like to compare the presented approaches for SDM according to the technological challenges and their potential benefits. The evaluation is summarized in Table 2.3.1. In all categories I defined the already existing solution "SMF-bundle" as reference. Thus, possible synergies in this solution have been taken into account when evaluating the potential of the four alternatives.

Starting with amplification, both multicore and MDM seem to have potential for synergies by shared pumping equipment. However, it has been suggested in [97], [98], [100], [101] that the MDM approach is even more promising from this point of view. On the other hand, technological challenges are tremendous. It is hard to say if the problems of multicore amplification, such as fabrication of an appropriate amplifier fiber or the correct pump injection, are harder to overcome than the problems of MDM amplification. These are mainly modal gain and NF equalization as well as mode coupling, which represents a much bigger handicap for the weakly coupled MDM approach since it can't be compensated for by DSP in the receiver.

At first sight, the perspective of using a common fiber instead of several SMFs in parallel is an attractive perspective. However, especially in the uncoupled multicore approach it is possible that challenges during fiber design and fiber fabrication turn this potential benefit into a drawback. In coupled multimode fibers, design constraints should be less strict because coupling between the supermodes is no problem. Few-mode fibers have even higher potential, since the realization of a single core is much more efficient than the realization of multiple cores. Here the main challenges are reduction of differential mode group delay (DMGD, see section 3.1.1) in the strongly coupled approach and the reduction of linear mode coupling in the weakly coupled approach. The practical limits of DMGD and linear mode coupling are hard to predict, and they are supposed to be a decisive argument when choosing between the two design approaches.

Table 2.3.1: Comparison of SDM techniques

		SMF-Bundle	Multicore		Mode Division Multiplexing	
			Uncoupled	*Coupled*	*Weakly coupled*	*Strongly coupled*
Amplifiers	**Potential**	0	+	+	+ +	+ +
	Technical challenges	0	−	−	− −	−
Fiber	**Potential**	0	+	+	+ +	+ +
	Technical challenges	0	− −	−	− −	− −
MUX-/DEMUX		0	0 ?	0 ?	− −	−
Connectors		0	−	0 −	−	0 −
Nonlinearities		0	−	?	+ ?	+ ?
MIMO-DSP complexity		0	0	−	0 −	− −

Another important aspect of new fiber types is how light can be injected into it. Signals coming from multiple sources have to be multiplexed into the multicore fiber respectively into the few-mode fiber, and after transmission, signals have to be demultiplexed. In multicore transmission, so far pretty complex structures have been used for this purpose [83], and so this represents additional complexity. However, it is imaginable to integrate multiple sources especially adapted to the multicore fiber, and so one day this could even lead to synergies with respect to the SMF-bundle solution. MDM systems additionally require mode conversion, which makes multiplexing/demultiplexing more complicated compared to the fiber injection in multicore transmission, especially when thinking of higher order modes with complicated profiles (see Fig. 1.2.5). In the weakly coupled MDM approach the required precision is higher than in the strongly coupled since no DSP is intended to be used for crosstalk compensation.

A second important way to inject light into the considered fibers is by interconnection between two fibers. Concerning this aspect, the coupled multicore approach and the weakly coupled MDM approach are easier to handle, since potential mode coupling can be compensated by MIMO-DSP and therefore represents no big problem. The uncoupled multicore approach and the weakly coupled MDM approach demand very low coupling between the different cores or modes, and thus both solutions require very high precision.

Concerning nonlinear transmission impairments, uncoupled multicore fibers are penalized by their relatively small effective area. For 7-core fibers, published values have been around 80 μm^2 at $\lambda = 1550nm$ [81] and for the published 19-core experiment the effective area of each core has even been smaller at ~72 μm^2 at $\lambda = 1550nm$ [83]. The fiber used for demonstrations of coupled multicore transmission in [86], [88] had a much higher effective area of ~130 μm^2 at $\lambda = 1550nm$. However, nonlinear interactions between different supermodes have not been studied sufficiently to exclude an important negative impact, especially given the fact that modes propagate with very similar propagation constants. In few-mode fibers, the effective areas vary between one spatial mode and another, but they tend to be higher than in single mode fibers [106], [107]. At the same time, the different propagation constants of different modes are supposed to diminish nonlinear interactions between modes significantly, as it will be presented by numerical results later on in this work (section 3.2.1). However, this hypothesis remains to be confirmed experimentally.

The last point that I would like to take into account is the MIMO-DSP complexity in the receiver. The uncoupled multicore solution requires no MIMO-DSP and has therefore the same complexity as the SMF-bundle solution. Coupled multicore and strongly coupled MDM approach require *NxN* MIMO processing for transmission over *N* cores respectively *N* modes. Hence, the complexity per MIMO input scales with *N* (see section 3.5.2). Besides, the MIMO filter length (number of taps) is proportional to the accumulated group delay between the jointly processed signals, and therefore scales with the transmission distance and the DMGD coefficients of the fiber. Here, the coupled multicore solution has the advantage of lower group delays. Finally, the weakly coupled MDM approach uses MIMO-DSP only for polarization demultiplexing and for demultiplexing of two degenerate spatial modes. Thus the maximum MIMO order is *4x4* and the complexity per MIMO input is constant, independently of *N*. Furthermore, DMGD between polarizations and between degenerate spatial modes is lower than between non-degenerate modes, having a positive influence on filter length.

2.4 Conclusion of Chapter 2

Chapter 2 was dedicated to the historical evolution of worldwide data traffic, to the simultaneous progress in capacity of optical transmission systems and to possible new technologies in order to continue this growth.

Since the early 2000s we've witnessed an exponential growth of world wide data traffic and this growth is supposed to continue at least for a few more years. In order to cope with this growing bandwidth demand, data transmission technology has to evolve. The objective is to lower the cost per bit and thereby keeping the costs per user at an affordable level when traffic per user is growing.

Optical transmission systems already played a key role in the progress of modern telecommunication networks by providing an enormous growth of transmission capacity over long distances compared to earlier technologies. And in addition they have steadily been improved enabling further traffic increase. Since the late 1990s alone, capacity per fiber in commercially available systems increased by a factor of ~100 from ~100 Gb/s to ~10 Tb/s. This evolution was enabled by regularly upcoming breakthrough technologies such as the EDFA, WDM, FEC, dispersion management or the coherent detection in combination with advanced modulation format, allowing pushing the capacity limits further and further.

Today, the limits of the state-of-the-art technology seem not far from being reached and so new, disruptive solutions are once more needed. In this chapter I presented an overview over the main research directions currently pursued for this objective. I classified them into three categories: increasing the exploitable bandwidth, increasing the spectral efficiency, and using several spatial channels by SDM.

Focusing on space division multiplexing, I identified five different approaches to realize it: transmission over a bundle of standard SMFs, transmission over uncoupled multicore fibers, transmission over coupled multicore fibers ("supermodes"), weakly coupled MDM transmission, and strongly coupled MDM transmission. The solution that is the least challenging to realize is the SMF-bundle but it also offers the least potential for possible synergies. MDM in contrast requires the solution of numerous challenges but also promises to offer the highest synergies, if the challenges can be mastered one day. Multicore transmission, especially coupled multicore transmission, seems to be a promising compromise between synergies and technical complexity.

Chapter 3: Realization of a Mode Division Multiplexed Optical Transmission System and its Key Elements

Moving from single mode transmission to MDM transmission requires some fundamental changes. A number of completely new components have to be included into the optical transmission system being notably a new fiber type allowing few-mode propagation, devices for multiplexing and demultiplexing the spatial modes into and out of this fiber, few-mode amplifiers, as well as a receiver architecture incorporating an appropriate DSP unit. During my PhD studies I worked on all of these four elements, and in this chapter I will introduce them in the sections 3.2 to 3.5 after some more general considerations on the whole MDM system in section 3.1. The work was done in the frame of the "STRADE" project, supported by the French government. So most of the results presented in the following could be obtained thanks to the fruitful collaboration with our project partners from Kylia, Prysmian (formerly Draka), the IRCICA laboratory at the Université Lille 1, Télécom SudParis and IRISA.

3.1 System overview

Fig. 3.1.1 shows schematically, how a single mode transmission system could be extended to an MDM transmission system. The new elements are marked in blue. On the transmitter side everything remains unchanged up to the output of the WDM-MUX. Then several WDM combs are injected into a mode-MUX, where they are spatially modulated and combined into a few-mode fiber (FMF). In order to take advantage of the potential synergies of MDM transmission, it is crucial to be able to amplify all of the MDM signals at the same time without having to separate the modes. This is done during transmission by special amplifiers. At the FMF output, the WDM combs modulated on different spatial modes are separated by a mode-DEMUX and reinjected into an SMF each. There, the different WDM channels are demultiplexed and sent into optical receivers. In our case, we work with coherent receivers allowing us to perform digital signal processing. It comprises the same blocks as in single mode transmission systems, and in addition, it can be used to process jointly the signals transmitted on several modes in order to decouple them.

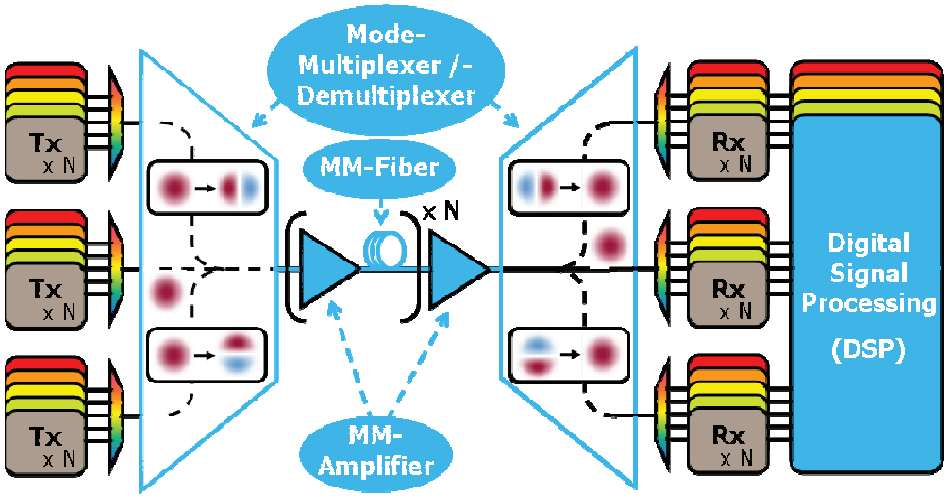

Fig. 3.1.1: Architecture of a mode division multiplexed transmission system.

3.1.1 Additional Performance Limiting Factors in MDM Systems

In addition to the limitations of optical single mode long-haul transmission systems, MDM also leads to new challenges that limit the transmission performance. These challenges occur because of interactions between the spatial modes. In the following, the most important additional limitations of MDM systems are described:

Intermodal Crosstalk through Linear Mode Coupling

Intermodal Crosstalk describes crosstalk between signals, which are modulated on different propagation modes. For signals modulated on the same wavelength it can be modeled as in-band crosstalk [18] according to the description in section 1.1.5.1.

At the origin of intermodal crosstalk is an energy transfer from one mode to another, which we call mode coupling. On the one hand, local, "concentrated" mode coupling takes place at discrete points in the transmission systems where light propagation conditions change abruptly. This can be the case in the mode-MUX and –DEMUX, at splices/connectors between different FMF sections or in the FM-amplifier. On the other hand, during propagation through the FMF itself, imperfections and mechanical stress can cause relatively weak mode coupling at numerous points, which adds up to a kind of "distributed" mode coupling. We will deal with the intermodal crosstalk occurring in each of the mentioned elements in the section dedicated to them.

Without compensation by digital signal processing, intermodal crosstalk is the main limiting factor of MDM transmissions as we will see by the experimental results presented in chapter 4 of this work. Thus, it is of great interest to know its impact on performance. Recently, Winzer et al. proposed a simple but accurate model to estimate SNR-penalties from in-band crosstalk [18]. It leads to the results depicted in Fig. 3.1.2. Theoretically, the SNR-penalties also depend on the relative phase-between measured and interfering channel. However, today in all practical systems, propagation constants differ by such high values that the relative phase changes constantly and very quickly. Hence, considering an average value for the SNR penalty as a function of crosstalk is sufficient.

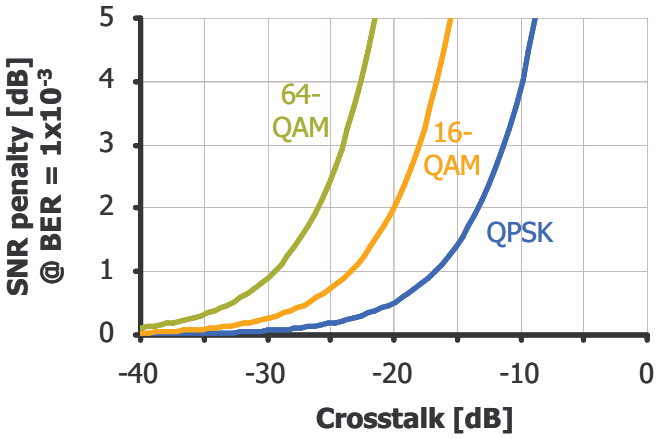

Fig. 3.1.2: Penalties from in-band crosstalk at a BER of 10^{-3} for different modulation formats. Results have been taken from [18].

In this work we will have to deal with systems, where a channel *i* suffers crosstalk from more than one co-propagating channel. For these cases, we generalize the crosstalk definition from equation (1.1.13) to obtain

$$Crosstalk_i = \frac{\sum_j P_{j\to i}}{P_{signal\_i}}. \tag{3.1.1}$$

Hence, instead of considering the transferred power coming from one interfering channel, we now simply consider the sum over the transferred powers to channel *i* coming from each interfering channel [14], [16], [17].

To describe the quality of a component concerning linear mode coupling we can use a table of the form of Table 3.1.1a. It describes the relative transferred powers $P_{j\to i}/P_{in\_j}$ from each input *j* to each output *i*. In some cases later on, I normalized the lines with respect to the power transferred to the desired output mode (element in the main diagonal) to better see the ratio between the "useful" powers and the "perturbing" powers coming from one input. However, in this representation, information about attenuation of the component is lost. This second variant is illustrated in Table 3.1.1b.

Table 3.1.1: Concept of the tables used to describe linear mode coupling of investigated elements.

a		Power measured at output		
		1	2	3
Power injected into input…	1	$P_{1->1}/P_{in\_1}$	$P_{1->2}/P_{in\_1}$	$P_{1->2}/P_{in\_1}$
	2	$P_{2->1}/P_{in\_2}$	$P_{2->2}/P_{in\_2}$	$P_{2->3}/P_{in\_2}$
	3	$P_{3->1}/P_{in\_3}$	$P_{3->2}/P_{in\_3}$	$P_{3->3}/P_{in\_3}$

b		Power measured at output		
		1	2	3
Power injected into input…	1	1	$P_{1->2}/P_{1->1}$	$P_{1->3}/P_{1->1}$
	2	$P_{2->1}/P_{2->2}$	1	$P_{2->3}/P_{2->2}$
	3	$P_{3->1}/P_{3->3}$	$P_{3->1}/P_{3->3}$	1

The values in the two tables can be obtained experimentally by measuring the output powers $P_{j\to i}$ at all outputs *i* when successively injecting signals in all inputs *j*, always one at a time. Alternatively, this description can also be used for the evaluation of numerical results.

Finally the values in the tables can be linked to intermodal crosstalk at the different outputs *i* by taking into account the input powers P_{in_j} to calculate the resulting output powers $P_{j\to i}$ and by applying equation (3.1.1) together with the fact that

$$P_{signal\_i} = P_{i->i} \tag{3.1.2}$$

At this point I would like to underline that the amount of mode coupling is a property of the considered device, independent of the injected powers (at least in the linear regime). In contrast, intermodal crosstalk depends on the injected powers and therefore can be adjusted, for example in order to equalize it among the different modes, even when the mode coupling properties of the considered device are asymmetric. This idea is used in the experiment presented in section 4.2 for example.

Differential Mode Group Delay

Each propagation mode has its own propagation constant $\beta(\omega)$, which can be described by a Taylor series according to equation (1.2.86). The difference in group velocity β_1 between two modes is what we call differential mode group delay ($\Delta\beta_1$ or DMGD). In contrast to the DGD between two polarizations of the same spatial mode, which occurs due to fiber imperfections, DMGD is an intrinsic property even of a perfectly symmetric few-mode fiber. Therefore, DMGD per km can be predicted and isn't a random value for each link as it is DGD. DMGD also increases linearly with the transmission distance and takes much higher values than DGD. Depending on fiber design and on considered modes, it can be between ~30ps/km and >10ns/km. Realizing fibers with low DMGD values for several combinations of spatial modes is quite

challenging, and at the same time, the amount of DMGD is roughly inversely proportional to the amount of mode coupling during fiber propagation.

Mode Dependent Loss and Mode Dependent Amplifier Gain

Different propagation modes in an MDM system can also have different attenuation coefficients α. We call this phenomenon mode dependent loss (MDL), and especially after transmission over long distances including multiple amplifications it becomes a major limitation since it makes it impossible to work at optimum power for each transmitted signal. The effect of mode dependent loss can be either counteracted or even increased by mode dependent gain in few-mode amplifiers. The problem is similar to the problem of wavelength dependent loss and wavelength dependent amplifier gain in WDM systems, where gain flattening filters are applied to mitigate it.

Intermodal nonlinear effects

In optical single mode transmission systems we already identified nonlinear interactions of a frequency tributary with itself (SPM), between different frequency components in a WDM system (XPM) and between signals in the two orthogonal polarization axes (XpolM). In an MDM system, an additional property is added namely the spatial propagation mode. Consequently, we identify intermodal nonlinear effects as the nonlinear interactions between signals that are modulated on different spatial modes. A first study on intermodal nonlinear effects is presented in section 3.2.1.

3.1.2 Design Strategies

As already mentioned in the very beginning of this work (section 1.1.1) digital telecommunication systems are usually designed around their transmission channel. In MDM transmission systems, the crucial properties of the transmission channel are the interplay between intermodal crosstalk and the DMGD. It turned out that in the first experimental demonstrations two fundamentally different design approaches have been presented, which differ with respect to these two parameters. The first approach, which we call "strongly coupled", allows an almost arbitrarily high amount of intermodal crosstalk all over the transmission system and compensates for it by making use of a multiple input multiple output (MIMO) DSP equalizer in the Rx [93], [94], [102], [103], [108]. This approach offers relaxed specifications for the amount of mode coupling in the components of the transmission system, such as mode-MUX/-DEMUX, FMF or FM-amplifier. However, it brings along the drawback of potentially high DSP complexity. The complexity per mode of the MIMO equalizer is proportional to the number of modes and proportional to the amount of accumulated DMGD over the transmission link. Hence, for this approach, priority in fiber design is on reducing the DMGD per km between all guided modes, whereas mode coupling properties of the fiber are less important. Until today, experimental demonstrations using this approach have been limited to the simultaneous transmission of no more than 3 spatial modes.

The second approach, called "weakly coupled" is based on the idea that intermodal crosstalk can be reduced to a minimum so that the spatial modes can be physically demultiplexed and recovered by independent coherent receivers. The only exceptions are pairs of degenerate modes, which are considered as always suffering from strong mode coupling. Thus, they are detected by a common receiver block using a MIMO DSP equalizer to separate them [96]. Accordingly, the MIMO equalizer in this case never deals with more than two spatial modes, and at the same time, the DMGD between these two degenerate spatial modes is relatively small. Using the model of the LP-modes, they have exactly the same propagation constant and so the DMGD between

them is *0*. In a more detailed model, modes are not exactly degenerate, leading to a DMGD in the order of magnitude of ~25ps/km. Altogether, the equalizer complexity is supposed to remain much lower than in the strongly coupled approach. Moreover, DMGD between all modes but two degenerate ones is no critical parameter leaving more freedom for fiber design, and so increasing the number of transmitted spatial modes might be easier in this case. However, the big drawback of the weakly coupled solution is the extremely strict requirement in terms of mode coupling in all components of the transmission system. In this work we chose to work on the weakly coupled approach and so in the following, the problem of crosstalk in the particular components will play an important role.

3.2 The few-mode fiber

In today's optical single mode transmission systems, the performance is limited by the compromise between OSNR and the tolerance to nonlinear effects as it was explained in section 1.3.4. Thanks to modern digital signal processing, linear impairments such as PMD or chromatic dispersion can be quasi perfectly compensated inside a certain range (see section 1.3.2). The consequence for fiber design is that the crucial parameters are those impacting OSNR and tolerance to nonlinear effects. These parameters are notably the fiber loss α, which is directly related to the OSNR, the effective area A_{eff} and the nonlinear refractive index n_2, which are directly related to nonlinear effects, as well as the chromatic dispersion D, which has an indirect impact on the nonlinear tolerance as described in section 1.3.3.

If we now move on to an MDM system, the additional limitations mentioned in section 3.1.1 appear, and so in the FMF, which replaces the formerly used SMF, new parameters become crucial. First of all, the parameters that impact linear mode coupling and DMGD are of great interest, since at the moment, the combination of these two effects is the decisive limitation in MDM systems, at least in the "weakly coupled" design approach used in this work. Secondly, also nonlinear interactions between the various spatial modes might additionally limit the system performance one day. Given the fact that in single-mode transmission systems, the actual performance limit is set by nonlinear effects, it is important to investigate the potential concerning nonlinear tolerance in MDM systems, as well as to identify key parameters that can influence the nonlinear behavior.

In this section we give an insight into linear mode coupling and into nonlinear interactions between spatial modes. The linear effects are hereby investigated both numerically and experimentally by making use of a prototype FMF, whereas the nonlinear effects are investigated numerically.

3.2.1 Numerical investigation on intermodal nonlinear effects

As already mentioned in section 1.2.1, the optical fiber is a very slightly nonlinear medium. As a consequence, nonlinear effects can only be observed when the input power is sufficiently high and/or the transmission distance is sufficiently long. Both conditions are currently still hardly to fulfill in experimental few-mode transmission set-ups, mainly because the transmission distance is currently limited by other problems such as intermodal crosstalk, missing amplifier technologies or simply not enough available fiber and missing few-mode components for the construction of a recirculating fiber loop. Thus, we developed a theoretical model for a first evaluation of intermodal

nonlinear effects, taking into account two spatial modes at a time so far, and carried out numerical investigations to assess their importance.

3.2.1.1 Theoretical model

Extending the Fiber Propagation Model for Two-Mode Propagation

In order to evaluate the impact of intermodal nonlinear effects, we extended the CNLSE system to a system of four equations that describes the propagation of the two polarizations of two spatial modes. In existing work, propagation models for several spatial modes in one wave guide had already been proposed, however not in the context of optical long-haul transmission systems [109], [110]. As a consequence, these models were more general, whereas in our case, it is crucial to use an adapted model that contains all relevant effects, but is not too complex in order to keep the computational effort reasonable.

As a starting point, we use the multi-mode generalized NLSE (MM-GNLSE) proposed in [109]. In the linear part, we keep only the terms containing β_1 and β_2 and we add the term containing α, since in [109] attenuation was included in the complex valued β_0. In the nonlinear part we neglect Raman-terms and fast oscillating terms for the reasons already mentioned in sections 1.2.1 and 1.2.4.2. Then the MM-GNLSE for the mode *p* becomes:

$$\begin{aligned}\frac{\partial A_p(z,t)}{\partial z} &= -\frac{\alpha^{(p)}}{2}A_p - \beta_1^{(p)}\frac{\partial A_p}{\partial t} - \frac{i}{2}\beta_2^{(p)}\frac{\partial^2 A_p}{\partial t^2} \\ &+ i\frac{n_2\omega_0}{c}\sum_{l,m,n}\left(Q_{plmn}^{(1)}\cdot 2\cdot A_l\cdot A_m\cdot A_n^{*} + Q_{plmn}^{(2)}\cdot A_l^{*}\cdot A_m\cdot A_n\right)\end{aligned} \tag{3.2.1}$$

Every mode *p,l,m* and *n* stands for one polarization mode of one spatial mode. Hence, the total number of modes in this model is two times the number of spatial modes. The terms $Q_{plmn}^{(1)}$ and $Q_{plmn}^{(2)}$ are measures for the strength of the nonlinear interactions between the modes *p,l,m* and *n*. They are calculated based on the mode functions *F(x,y)* of the concerned modes, which can be determined as explained in section 1.2.2. We assume the mode functions to be real valued and so it is [109]

$$Q_{plmn}^{(1)} = Q_{plmn}^{(2)} = Q_{plmn} \tag{3.2.2}$$

with [109]

$$Q_{plmn} = \begin{cases}\frac{1}{3}f_{pq} & : \quad p=l\wedge m=n=q \\ 0 & : \quad p\neq l\vee m\neq n\end{cases}. \tag{3.2.3}$$

f_{pq} is called the overlap integral between the modes *p* and *q*. It is defined by the following equation [19 p.263]:

$$f_{pq} = \frac{\iint \left|F_p(x,y)\right|^2 \left|F_q(x,y)\right|^2 dxdy}{\iint \left|F_p(x,y)\right|^2 dxdy \iint \left|F_q(x,y)\right|^2 dxdy} \tag{3.2.4}$$

For $p = q$, the overlap is the inverse of the effective area of either mode p or mode q (called $A_{eff,p}$ or $A_{eff,q}$), which is already well known from single mode transmission systems and has been introduced in equation (1.2.93). It provides a measure of how the energy is distributed along the fiber cross-section. Consequently, we generalize this definition for all combinations of two spatial modes such that

$$A_{eff,pq} = \frac{1}{f_{pq}}. \tag{3.2.5}$$

If $p \neq q$, we call $A_{eff,pq}$ the "intermodal effective area" between two spatial modes p and q. Like the effective area is inversely proportional to the nonlinear effects within one spatial mode, the intermodal effective area is inversely proportional to the intermodal nonlinear effects between two spatial modes.

The adapted MM-GNLSE (equation (3.2.1)) is solved numerically using the SSFM similarly to the solution of the standard NLSE and the CNLSEs. To do so, it is first separated into a linear part and into a nonlinear part according to equation (1.2.105) resulting in the linear step

$$L^{(p)} = -\frac{\alpha^{(p)}}{2} A_p - \beta_1^{(p)} \frac{\partial A_p(z,t)}{\partial t} - \frac{i}{2} \beta_2^{(p)} \frac{\partial^2 A_p}{\partial t^2} = \frac{\partial A_p}{\partial z} \tag{3.2.6}$$

and in the nonlinear step

$$N^{(p)} = i\frac{n_2 \omega_0}{c} \sum_{l,m,n} \left(Q_{plmn}^{(1)} \cdot 2 \cdot A_l \cdot A_m \cdot A_n^{\,*} + Q_{plmn}^{(2)} \cdot A_l^{\,*} \cdot A_m \cdot A_n \right) = \frac{\partial A_p}{\partial z}. \tag{3.2.7}$$

Then the two equations are solved alternately for short steps Δz.

Again, the linear step can be solved independently for each mode p, exactly as it is the case for the CNLSEs. This means that so far no linear mode coupling is included in this model. The solution to the linear step can be obtained in the same way as described in section 1.2.3.3 for the CNLSEs. Linear mode coupling could subsequently be included with little extra effort: for example by adding simple linear coupling steps between some linear and nonlinear steps in the SSFM algorithm. The linear coupling steps can have the form:

$$A_{p\_out} = \sum_n k_n A_{n\_in} \tag{3.2.8}$$

Numerical investigations of linear mode coupling have for example been done in [111–114].

Solving the nonlinear step is a little bit more complicated. Our objective is to convert equation (3.2.7) into a vectorial equation of the form

$$\frac{\partial}{\partial z}\begin{bmatrix} A_1 & A_2 & \cdots & A_N \end{bmatrix}^T = \frac{\partial}{\partial z}\underline{A} = \underline{\underline{M}} \cdot \underline{A}, \tag{3.2.9}$$

so that its solution for small steps Δz can be computed by

$$\underline{A}(z+\Delta z) = \exp\left(\underline{\underline{M}} \cdot \Delta z\right) \cdot \underline{A} \tag{3.2.10}$$

with "exp" standing for the matrix exponential operator in this case.

Hence, in order to keep the complexity of the matrix $\underline{\underline{M}}$ as low as possible, we focus on the case of four modes for the derivation of this first model. Please remember that four modes stand for two spatial modes with two polarization modes each. In this case we can write down equation (3.2.7) explicitly for each value of *p = 1, 2, 3 or 4*, while making use of equations (3.2.2) to (3.2.5) . For *p = 1* this results in

$$\begin{aligned} N^{(1)} \quad = \quad & \left(\gamma_{11}\left|A_1\right|^2 + \frac{2}{3}\gamma_{12}\left|A_2\right|^2 + \frac{2}{3}\gamma_{13}\left|A_3\right|^2 + \frac{2}{3}\gamma_{14}\left|A_4\right|^2\right)\cdot A_1 \\ & + \frac{1}{3}\left(\gamma_{12}{A_2}^2 + \gamma_{13}{A_3}^2 + \gamma_{14}{A_4}^2\right)\cdot {A_1}^* \end{aligned}, \tag{3.2.11}$$

with

$$\gamma_{pq} = \frac{n_2\omega_0 f_{pq}}{c} = \frac{n_2\omega_0}{cA_{eff,pq}}. \tag{3.2.12}$$

We call γ_{pq} the intermodal nonlinear coefficient in analogy to the well-known nonlinear coefficient γ introduced in section 1.2.3.1. For the derivation of equation (3.2.11) we neglected terms that account for what could be called "intermodal four wave mixing" and similar to classical FWM, they have only to be taken into account, when the phase matching condition is fulfilled. Thus, given that β_0 and β_1 varies significantly from one mode to another neglecting these terms is justified.

Now we can transform equation (3.2.11) into a form similar to the form of the CNLSE-nonlinear step containing the third Pauli Matrix expressed in equation (1.2.112). To do so, we first rearrange the elements of equation (3.2.11) in the following way:

$$\begin{aligned} N^{(1)} &= \left(\gamma_{11}\left|A_1\right|^2 + \gamma_{12}\left|A_2\right|^2 + \gamma_{13}\left|A_3\right|^2 + \gamma_{14}\left|A_4\right|^2\right)\cdot A_1 \\ &- \frac{1}{3}\left[\gamma_{12}\left(\left|A_2\right|^2 A_1 - {A_2}^2 {A_1}^*\right) + \gamma_{13}\left(\left|A_3\right|^2 A_1 - {A_3}^2 {A_1}^*\right) + \gamma_{14}\left(\left|A_4\right|^2 A_1 - {A_4}^2 {A_1}^*\right)\right] \end{aligned}$$

Then we use the identity

$$\begin{aligned} \left|A_q\right|^2 A_p - {A_q}^2 {A_p}^* \quad &= \quad \underbrace{\left[{A_p}^* {A_q}^*\right]\sigma_3\begin{bmatrix} A_p \\ A_q \end{bmatrix}}_{s_{3,pq}} \cdot \left(-iA_q\right) \\ &= \quad \underbrace{2\left(\mathrm{Re}\{A_p\}\cdot\mathrm{Im}\{A_q\} - \mathrm{Im}\{A_p\}\mathrm{Re}\{A_q\}\right)}_{s_{3,pq}} \cdot \left(-iA_q\right) \end{aligned}$$

and so we obtain

$$N^{(1)} = \left(\gamma_{11}\left|A_1\right|^2 + \gamma_{12}\left|A_2\right|^2 + \gamma_{13}\left|A_3\right|^2 + \gamma_{14}\left|A_4\right|^2\right)\cdot A_1 + i\frac{1}{3}\left(\gamma_{12}s_{3,12}A_2 + \gamma_{13}s_{3,13}A_3 + \gamma_{14}s_{3,14}A_4\right) .$$

This equation can be generalized for all the four considered modes ($p,q \in \{1,2,3,4\}$) by

$$N^{(p)} = \left[\sum_{q=1}^{N}\gamma_{pq}\left|A_q\right|^2\right]A_p + \frac{i}{3}\sum_{\substack{q=1\\q\neq p}}^{N}\gamma_{pq}s_{3,pq}A_q$$

Finally the matrix $\underline{\underline{M}}$ can be obtained using

$$\begin{bmatrix} N^{(1)} \\ N^{(2)} \\ N^{(3)} \\ N^{(4)} \end{bmatrix} = \underline{\underline{M}}\cdot\underline{A} . \tag{3.2.13}$$

It can be written as:

$$\underline{\underline{M}} = \begin{bmatrix} m_{main,1} & m_{side,12} & m_{side,13} & m_{side,14} \\ m_{side,21} & m_{main,2} & m_{side,23} & m_{side,24} \\ m_{side,31} & m_{side,32} & m_{main,3} & m_{side,34} \\ m_{side,41} & m_{side,42} & m_{side,43} & m_{main,4} \end{bmatrix} \tag{3.2.14}$$

with

$$m_{main,p} = \left[\sum_{q=1}^{N}\gamma_{pq}\left|A_q\right|^2\right]A_p \tag{3.2.15}$$

and

$$m_{side,pq} = i\cdot s_{3,pq}\frac{\gamma_{pq}}{3} = -m_{side,qp} . \tag{3.2.16}$$

It turns out that with the given assumptions, this formalism can be applied to an arbitrary number of modes, using essentially the equations (3.2.10) and (3.2.14) to (3.2.16) .

3.2.1.2 Discussion

We started our investigation by identifying the parameters that are relevant for intermodal nonlinear effects. These parameters are mainly those, which contain information about the relation between different spatial modes, and which are similar to the parameters that are already well known to be important for nonlinear effects in single mode transmission systems. This reasoning led us to the intermodal effective area

$A_{eff,pq}$, the differential mode group delay *DMGD* or $\Delta\beta_1$ and the differential chromatic dispersion ΔD as the most interesting parameters to investigate.

After having identified these parameters, we used the numerical model just described in section 3.2.1.1 to perform simulations in order to investigate their importance. In a first step, we assigned to them some hypothetical combinations of values. These values are not necessarily supposed to occur in a real system configuration, but instead give a good idea about the order of magnitude of each parameter's impact, and help setting upper and lower bounds.

In a second step, we assumed the set of parameters for a realistic step-index FMF. Using this scenario, we assessed the nonlinear potential of an MDM system under realistic conditions.

Since our theoretical model emulates the propagation of two spatial modes at a time, all simulation results represent the pair wise impact of intermodal nonlinear effects between exactly two spatial modes.

3.2.1.3 Simulations with a Hypothetical Parameter-Set

Simulation Set-Up

On each spatial mode we simulated 7 WDM channels modulated at 112Gb/s PDM-QPSK (including overhead for forward error correction) and filtered by an ideal 50GHz band-pass filter before multiplexing them into a 50GHz grid, centered on a carrier wavelength of 1550nm. The initial state of polarization and the temporal alignment of each channel were randomly chosen and kept constant for all simulations. The transmitted data were modeled using quaternary De Bruijn sequences with a length of 4096 symbols.

The transmission line consisted of 12x100km of the bimodal fiber implementing the model described above in section 3.2.1.1 with the parameters shown in Table 3.2.1 and of a noiseless, spectrally flat, bimodal amplifier after each span compensating exactly for the span loss. Ideal compensation of chromatic dispersion and group delay between modes as well as noise loading to obtain the desired bit error rate (BER) were performed after transmission. The attenuation was assumed to be mode independent, thus the OSNR at the end was the same for all modes. In all results presented in the following, the amount of noise added by noise loading corresponded to a noise figure of 10dB at a span loss of 22dB.

At the receiver side, the two spatial modes were processed separately by independent coherent detectors [3], where the BERs of each mode's central WDM channel were measured, averaged over both polarizations of both modes and finally converted into Q^2-factors.

Table 3.2.1: Fiber parameters of SMF-based few-mode fiber.

	LP01	LP02
α_{dB} [dB/km]	0.22	0.22
DGD [ps/km]	-	0
DMGD [ns/km]	-	From 0 to 10
D [ps/nm/km]	17	17 and 27
Intramodal A_{eff} [μm^2]	80	80
Intermodal $A_{eff,12}$ [μm^2]	107	
n_2 [m^2/W]	2.7e-20	2.7e-20

Results

As explained in section 3.2.1.2, we investigated the intermodal nonlinear behavior as a function of the parameters *DMGD*, ΔD and $A_{eff,12}$.

Fig. 3.2.1 shows the Q²-factor averaged over all modes versus injected power P_{in} per channel per spatial mode for different intermodal effective areas $A_{eff,12}$. The case "realistic mode overlap" is the one with the $A_{eff,12}$ of Table 3.2.1. This value was calculated using equations (3.2.4) and (3.2.5) for a bimodal fiber containing the modes LP01 and LP02 with $A_{eff} = 80\ \mu m^2$ each. The cases "single mode PDM" and "full mode overlap" (LP01 and LP02 have exactly the same mode function) represent theoretical upper and lower bounds with $A_{eff,12} = \infty$ and $A_{eff,12} = A_{eff} = 80\mu m^2$ respectively. In this figure both *DMGD* and ΔD are chosen to be zero in order to simulate what is expected to be a theoretical worst case scenario. Regarding the maximum Q²-factors, this case demonstrates that intermodal NL effects can add up to 1dB of penalties in our set-up.

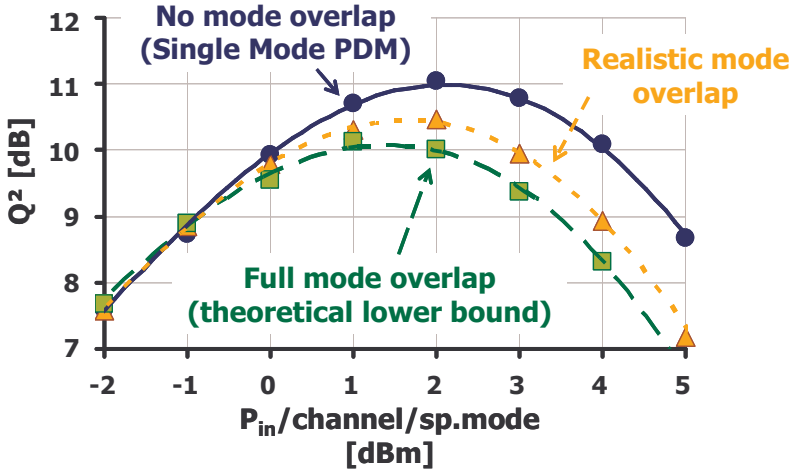

Fig. 3.2.1: Impact of different overlap integrals between spatial modes when DMGD and ΔD are artificially set to zero.

In contrast, Fig. 3.2.2 shows the performances for more realistic values of *DMGD* and ΔD estimated based in discussions with our STRADE project partners. In Fig. 3.2.2a, we used $\Delta D = 10ps/nm/km$ and $DMGD = 0$. It can be observed that the curves for realistic and full mode overlap approach the single mode PDM curve. This can be explained by the decorrelation between the signals of the different spatial modes induced by the differential chromatic dispersion. It can also be observed that the performance of the

single mode PDM configuration is slightly increased, where a decorrelation between the spatial modes should actually have no impact. This improvement is however due to the fact that the chromatic dispersion of one spatial mode increases and so does its robustness to classic intramodal nonlinear effects.

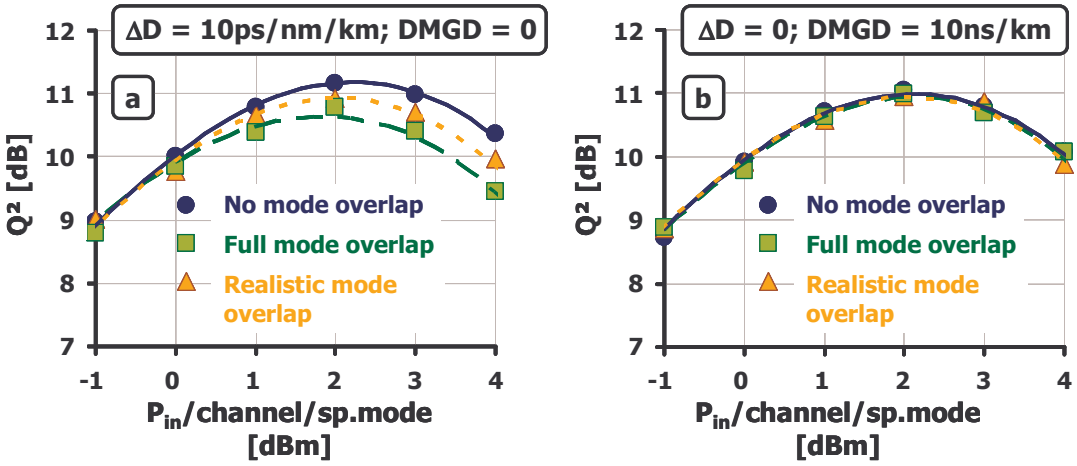

Fig. 3.2.2: Influence of DMGD and ΔD.

In Fig. 3.2.2b we set *ΔD = 0* and *DMGD = 10 ns/km*, which means that in a 28Gbaud transmission, the spatial modes are shifted by about 300 symbols with respect to each other every kilometer. As a consequence, we observe a complete suppression of intermodal nonlinear effects. However, such a huge delay could pose some problems for the detection algorithms if the signals transmitted over two spatial modes are processed jointly in a MIMO DSP unit. To overcome this drawback it would be interesting to lower the *DMGD* value down to the lowest point where the induced decorrelation still allows to significantly reducing the impact of nonlinear effects. In Fig. 3.2.3, we show the penalties on the maximum Q²-factor with respect to the single mode PDM case as a function of *DMGD*, keeping *ΔD = 0*. It can be seen that with *DMGD = 100ps/km* the penalties are still around *0 dB* for both configurations.

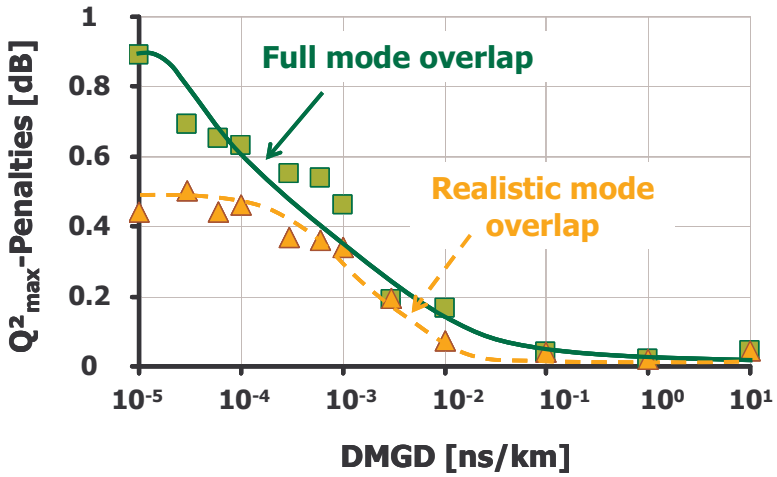

Fig. 3.2.3: Penalties on maximum Q²-factor as a function of DMGD for two different mode overlaps (respectively intermodal effective Area).

3.2.1.4 Investigating a Concrete MDM-Scenario

Considering the relation between two spatial modes, we can distinguish between two fundamentally different cases:

1. The relation between two degenerate spatial modes (modes of the same order)
2. The relation between two spatial modes of different order

Classifying any couple of two spatial modes into these two cases allows us to exploit some notable properties concerning $A_{eff,pq}$ and *DMGD*, which have been shown to be the most important parameters with respect to intermodal nonlinear effects in section 3.2.1.3.

Let us first consider $A_{eff,pq}$ in the case of two degenerate spatial modes. Since both modes have the same radial dependence and their angular dependence is shifted by a quarter of a period $2\pi/k$, their mode functions can be written as the following:

$$F_p(r,\theta) = g_p(r)\cdot h_p(\phi) = g(r)\cdot\cos(k\phi) \quad k \in N \tag{3.2.17}$$

$$F_q(r,\theta) = g_q(r)\cdot h_q(\phi) = g(r)\cdot\sin(k\phi) \quad k \in N \tag{3.2.18}$$

Now the intermodal effective area can be calculated and compared to the individual effective area of both modes:

$$\begin{aligned} A_{eff,pq} &= \frac{\iint\left|F_p(x,y)\right|^2 dxdy \iint\left|F_q(x,y)\right|^2 dxdy}{\iint\left|F_p(x,y)\right|^2\left|F_q(x,y)\right|^2 dxdy} \\ &= \frac{\iint\left|F_p(r,\phi)\right|^2\cdot r\cdot drd\phi \iint\left|F_q(r,\phi)\right|^2\cdot r\cdot drd\phi}{\iint\left|F_p(r,\phi)\right|^2\left|F_q(r,\phi)\right|^2\cdot r\cdot drd\phi} \\ &= \frac{\int g(r)^2\cdot r\cdot dr\int\cos^2(k\phi)d\phi\int g(r)^2\cdot r\cdot dr\int\sin^2(k\phi)d\phi}{\int g(r)^4\cdot rdr\int\cos^2(k\phi)\sin^2(k\phi)d\phi} \\ &= \frac{\int g(r)^2\cdot r\cdot dr\int g(r)^2\cdot r\cdot dr\int\cos^2(k\phi)d\phi\int\sin^2(k\phi)d\phi}{\int g(r)^4\cdot rdr\int\cos^2(k\phi)\sin^2(k\phi)d\phi} \end{aligned} \tag{3.2.19}$$

$$\begin{aligned} A_{eff,p} &= \frac{\int g(r)^2\cdot r\cdot dr\int\cos^2(k\phi)d\phi\int g(r)^2\cdot r\cdot dr\int\cos^2(k\phi)d\phi}{\int g(r)^4\cdot rdr\int\cos^4(k\theta)d\theta} \\ &= \frac{\int g(r)^2\cdot r\cdot dr\int g(r)^2\cdot r\cdot dr\int\cos^2(k\phi)d\phi\int\cos^2(k\phi)d\phi}{\int g(r)^4\cdot rdr\int\cos^4(k\phi)d\phi} \end{aligned} \tag{3.2.20}$$

As the parts with radial dependence are equivalent, they can be cancelled when calculating the ratio between $A_{eff,pq}$ and $A_{eff,p}$:

$$\begin{aligned}\frac{A_{eff,pq}}{A_{eff,p}} &= \frac{\int\cos^2(k\phi)d\phi\int\sin^2(k\phi)d\phi\int\cos^4(k\phi)d\phi}{\int\cos^2(k\phi)\sin^2(k\phi)d\phi\int\cos^2(k\phi)d\phi\int\cos^2(k\phi)d\phi} \\ &= \frac{\int\cos^4(k\phi)d\phi}{\int\cos^2(k\phi)\sin^2(k\phi)d\phi} \\ &= 3\end{aligned} \tag{3.2.21}$$

Finally we can keep in mind the simple relation

$$A_{eff,pq} = 3\cdot A_{eff,p} = 3\cdot A_{eff,q}\,. \tag{3.2.22}$$

In the second case, where there are two modes of different order, $A_{eff,pq}$ has to be calculated explicitly for each combination of modes by using the relevant mode functions.

Considering *DMGD* under the assumption of being in the weakly guiding limit, as explained in section 1.2.1, it takes the value *0* for two degenerate modes. Although the weakly guiding limit assumption is not exactly fulfilled in reality, setting *DMGD = 0* is a worst case scenario with respect to nonlinear effects according to section 3.2.1.3 and therefore does not lead to unrealistic performance improvement. For two modes of different order, it is, as for the intermodal effective Area $A_{eff,pq,}$ not trivial to give a general prediction of the *DMGD* value. However, our simulation results indicate that with a very good statistical reliability, *DMGD* values are sufficiently high that their precise value doesn't play a major role concerning nonlinear effects. The two cases that have just been discussed are illustrated and summarized in Fig. 3.2.4.

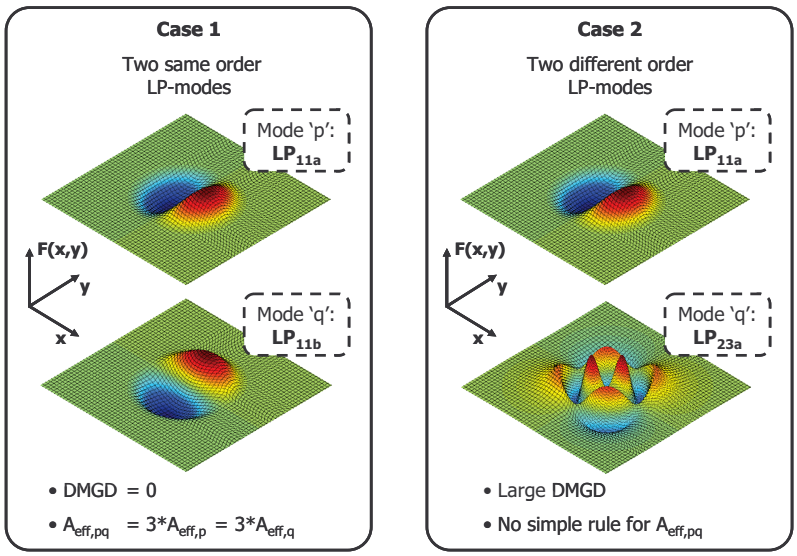

Fig. 3.2.4: Different kind of relations between two spatial modes.

Simulation Set-Up

Transmitter and receiver were kept the same as described in section 3.2.1.3. We only changed the transmission line using now 24 x 100 km of another few-mode fiber with again a noiseless, spectrally flat, few-mode amplifier after each span compensating exactly for the span loss.

The values for the key parameters concerning intermodal nonlinear effects were obtained by modeling a few-mode fiber with the following properties: a step-index fiber with a core radius $a = 15\mu m$, a refractive index in the core of $n_{co} = 1.454$ and an index difference between core and cladding of $\Delta n = 0.0102$, both at a wavelength $\lambda = 1550nm$. Such a fiber would allow the propagation of 30 spatial modes (4 non-degenerate modes plus 13 times two degenerate modes). By solving Maxwell's equations with their boundary conditions in the weakly guided limit as described in section 1.2.1 we computed the mode functions $F(x,y)$ and the propagation constants β from which the parameters of interest, $A_{eff,pq}$ and $DMGD$ were derived. All other parameters take the following values, based on the values for standard single mode fibers: attenuation $\alpha = 0.22\ dB/km$; chromatic dispersion $D = 17\ ps/nm/km$; nonlinear index coefficient $n_2 = 2.7e\text{-}20\ m^2/W$.

In order to obtain similar Q^2-factors as before, the changed configuration of the transmission line required a different amount of loaded noise, being now the equivalent to a noise figure of 6 dB in every amplifier at a span loss of 27 dB.

Results

First we take a look at the nonlinear behavior of two degenerate modes. In Fig. 3.2.5, we show the Q^2-factor after propagation as a function of the input power per channel and per spatial mode for the degenerate spatial modes with the lowest (LP13 mode, $A_{eff} = 300\mu m^2$) and the highest effective area (LP23 mode, $A_{eff} = 450\mu m^2$). Our two criteria to evaluate the performance are the maximum Q^2-factor and the nonlinear threshold (NLT), which is the input power at this maximum Q^2-factor. The impact of intermodal nonlinear effects can be seen by the difference between the solid curves, where only one spatial mode is transmitted, and the dashed curves, where both degenerate modes propagate together. For both LP13 and LP23 mode, the difference in maximum Q^2-factor and in NLT is around 0.2dB. We also observe a performance difference between the modes LP23 and LP13 of ~1.2dB of Q^2-factor and NLT, due to the different effective areas.

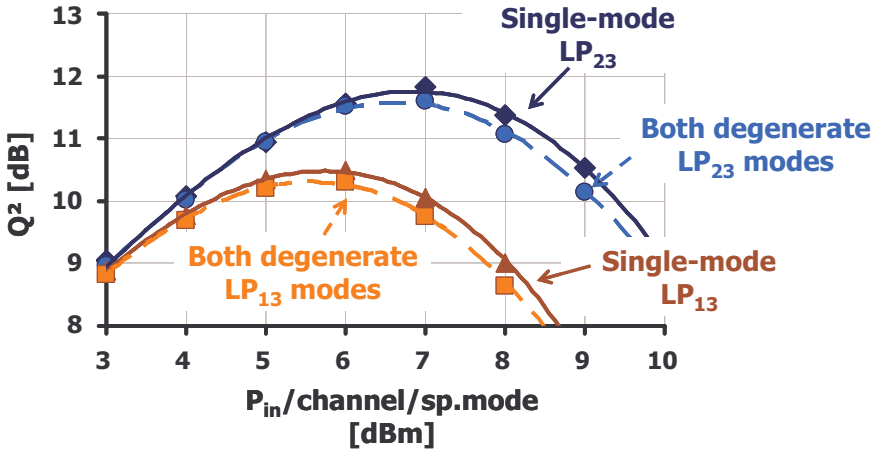

Fig. 3.2.5: Q²-factors as a function of input power for degenerate modes with highest (LP23, A_{eff} = 450μm²) and lowest (LP13, A_{eff} = 300μm²) effective area in the emulated fiber.

As the effective area is the only variable parameter in our model that changes the impact of nonlinear effects when transmitting any pair of degenerate modes, we can generalize our observations by plotting the NLT as a function of the effective area. In Fig. 3.2.6, we plot the NLTs obtained after propagating a PDM-signal through our fiber on every single spatial mode at a time, and on every pair of degenerate spatial modes at a time. The results are two sets of points along two straight lines, one line for the transmission over a single spatial mode and one line for the transmission over two degenerate modes. Both lines are superposed, which shows that the penalties due to intermodal nonlinear effects remain negligible for all couples of degenerate modes.

Moreover, Fig. 3.2.6 shows the NLT at the highest effective area of commercially available single mode fibers. It is ~2.5dB lower than the NLT of the worst performing mode in the simulated few-mode system. This amounts to the potentially better robustness to nonlinearities in MDM transmission systems as a result of the highly increased effective areas compared to systems using single mode fibers.

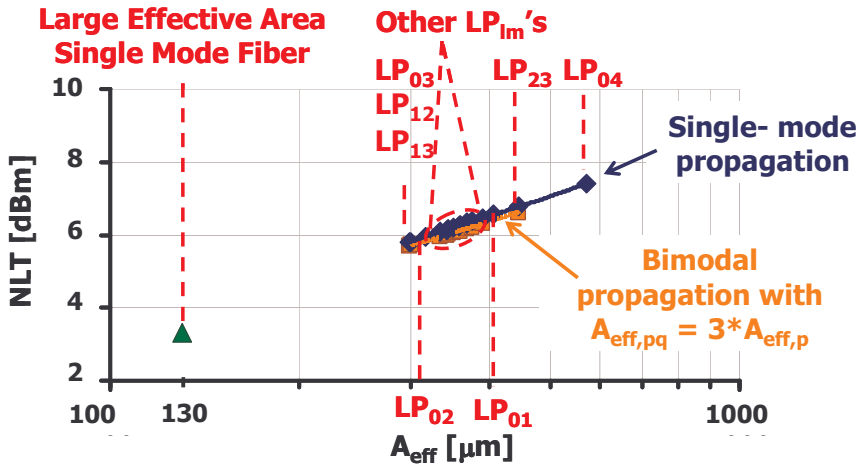

Fig. 3.2.6: Nonlinear threshold after single mode PDM propagation of all spatial modes and after bimodal PDM propagation of all degenerate spatial modes.

In the case of two non-degenerate modes, $A_{eff,pq}$ can be significantly lower than $3*A_{eff,p}$ but the occurring *DMGD* mitigates its impact as shown in the previous section (3.2.1.3). In Fig. 3.2.7a, we present some results similar to the ones plotted in Fig. 3.2.3, applying an unrealistic but worst case, in which $A_{eff,pq} = A_{eff,p} = A_{eff,q}$. We plot the

penalties on maximum Q²-factor due to intermodal nonlinear effects for varying *DMGD*. The dashed vertical line at *DMGD = 50ps/km* indicates the minimum *DMGD* value, from which on intermodal nonlinear effects become negligible.

In order to figure out if it is possible to fulfill this condition in practice, we calculated all *DMGD* values for the fiber described in the subsection "Simulation Set-Up" and plotted the results in Fig. 3.2.7b. For 17 modes with different β, there exist 136 DMGD values (taken only the positive ones, calculated by *17/2*(17-1)*) and in our case all lie above the defined threshold.

Thus, it has been shown that a few-mode fiber with *DMGD* values higher than *50ps/km* can exist and would provide almost "linear" performance with respect to a present single mode fiber thanks to an increased NLT. Interestingly, the additional inter-modal nonlinear effects of the FMF are negligible for both degenerate (due to the factor of 3 in the $A_{eff,pq}$) and non-degenerate (due to the large *DMGD*) cases. Hence, we define a few-mode fiber with large *DMGD* values a "quasi-linear few-mode fiber".

In our example, the maximum *DMGD* (difference between the highest and the lowest β_1) is at *44ns/km*. Taking this as a guiding value and comparing it to β_1 values that are spaced by the minimum of *50ps/nm* in order to fulfill the quasi linear few-mode fiber condition, a difference by three orders of magnitude indicates that this condition is very unlikely to compromise fiber design.

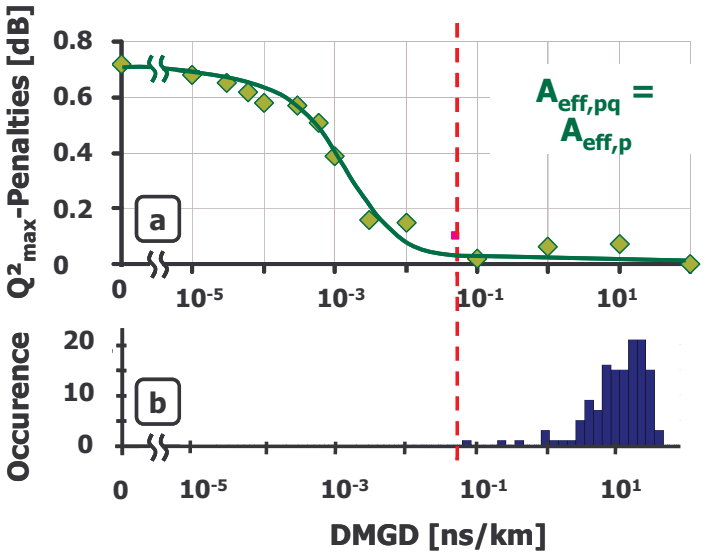

Fig. 3.2.7: (a) Penalties on maximum Q²-Factor due to intermodal nonlinear effects as a function of DMGD between two spatial modes with 100% overlap (theoretical worst case). (b) Distribution of all DMGD values in simulated 17-mode-fiber.

3.2.2 Practical Realization of a Few-Mode Fiber

In the frame of the STRADE project, an FMF was realized by our project partner Prysmian [106]. Besides a very slightly bimodal fiber (cutoff wavelength $\lambda_c \approx 1650$ *nm*) used as pigtail in one of the mode-MUX/-DEMUX realizations, this was the only FMF used in any of our experimental set-ups up to this point. Hence it was a key element for my work, and so I will describe it in this section, even though I didn't contribute to its design and to its fabrication.

For the fiber, an optimized step-index profile has been chosen, as it is depicted in Fig. 3.2.8a. It offers simplicity in terms of fabrication and good compatibility with standard

step-index single-mode fibers, also supported by the fact that its cladding diameter is the same as in all common types of SMFs (125μm). The core has a radius of 7.5μm and an index difference with the cladding of Δn = (n_{core} - $n_{cladding}$) = $9.7 \cdot 10^{-3}$ at 1550nm, leading to a normalized frequency V of 5.1 that ensures the guidance of the first four modes (the fundamental LP01 mode and the higher-order LP11, LP21 and LP02 modes) in the whole C-band, while cutting off the next higher-order modes. This is illustrated in Fig. 3.2.8b, where the normalized propagation constant $B = \left(n_{eff,lm}^2 - n_{cladding}^2\right) / \left(n_{core}^2 - n_{cladding}^2\right)$, with $n_{eff,lm}$ as the effective index of the LP*lm* mode, is plotted as a function of V and it can be seen that for the given value of V = 5.1, the first four modes, LP01, LP11, LP21 and LP02, take positive values for B. In Fig. 3.2.9, the spatial distributions of the four guided modes are depicted, which we obtained through simulations with the according fiber parameters. All of these four guided modes have low macro-bend losses (<10dB/turn at 10mm radius at 1550nm), as well as large effective-index differences (>0.8·10-3) between each other, which ensures low mode couplings [115], [116]. Furthermore they have large differential mode group delays (DMGD) (between 1 and 9ps/m for all modes and 4.35ps/m between LP01 and LP11) and large effective areas A_{eff} (between 118 and 133μm² depending on modes), which ensures small inter- and intra-modal non-linear effects. They also exhibit low losses (<0.22dB/km), which should differ by a maximum of 0.01dB/km between the guided modes according to predictions of Prysmian. More detailed characteristics about the fiber can be found in [106].

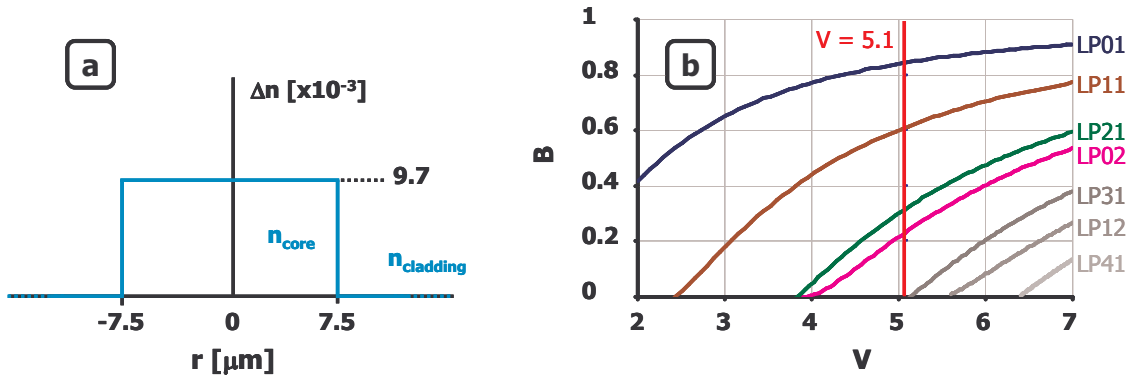

Fig. 3.2.8: Fiber characteristics of FMF: (a) Selected step-index profile. (b) Normalized propagation constant B, as a function of normalized frequency, V.

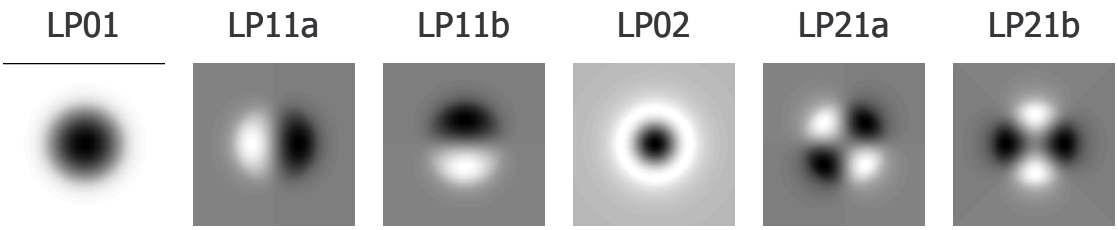

Fig. 3.2.9: Spatial field distribution, orthogonal to the propagation direction of all guided modes in our FMF.

3.2.3 Linear Mode-Coupling

In a perfectly cylindrical FMF, no linear mode coupling should occur. So again, similar to PMD for example, this is a phenomenon which is due to imperfections such as bending or mechanical pressure on the fiber. According to theoretical models, linear mode coupling inside an FMF or inside a multimode fiber (MMF) correlates with the effective index differences between the considered spatial modes [115]. In other words, in order to minimize linear mode coupling between the modes *p* and *q*, the expression $\left|n_{eff,p} - n_{eff,q}\right|$ has to be maximized [106]. However, recent experimental tests in our laboratory with two different types of FMF gave unexpected results and suggested that the amount of linear mode coupling must also strongly depend on other design parameters. The analysis on this subject is still ongoing, and so is the characterization of the intermodal crosstalk in the FMF used in this work.

A very interesting information would be a parameter of the type "mode coupling per fiber length". This information can be obtained by measuring mode coupling after transmission over fiber spans of different lengths while keeping all other system parameters unchanged. Here, we had several FMF spools of 20 km length and so we could change the overall transmission length in two ways. The first possibility was a destructive test using a single spool and cutting it shorter and shorter. The drawback of this solution, besides the irreversible shortening of the fiber, is the limited maximum transmission distance. The second possibility was a non-destructive test, connecting more and more FMF spools through splices. The problem with this method is that the splices might add mode coupling as well and so it is problematic to attribute the measured overall mode coupling to its correct origin, splices or fiber propagation.

For this reason I started to investigate the mode coupling at fiber interconnections, not only through splices, but also through optical connectors. With the knowledge about the impact of splices, mode coupling in the fiber can then be studied much easier. Furthermore, the complexity of interconnections is also an important issue for the practical interest in MDM systems.

3.2.3.1 Linear Mode Coupling at Splices and Connectors

For the practical applicability of MDM, it is required to be able to interconnect fibers without causing considerable penalties on system performance at the interconnections. In optical single mode transmission systems, interconnections are normally realized by splices or by specially designed connectors, and their impact on performance is mainly characterized by additional loss. According to specifications and experimental measurements, the connector loss is typically lower than 0.2 dB and the loss of a well-executed splice is in the order of magnitude of 0.01 dB. The main reason for these losses is a slight misalignment Δr between the two fiber ends as it is depicted in Fig. 3.2.10. Thanks to the rotational invariance of an optical fiber, the direction of the misalignment has no impact on the result, apart from the relative energy distribution between two degenerate modes in an FMF or MMF. So in the following, the misalignment was chosen to be applied in y-direction, that's why we can say that $\Delta r = \Delta y$.

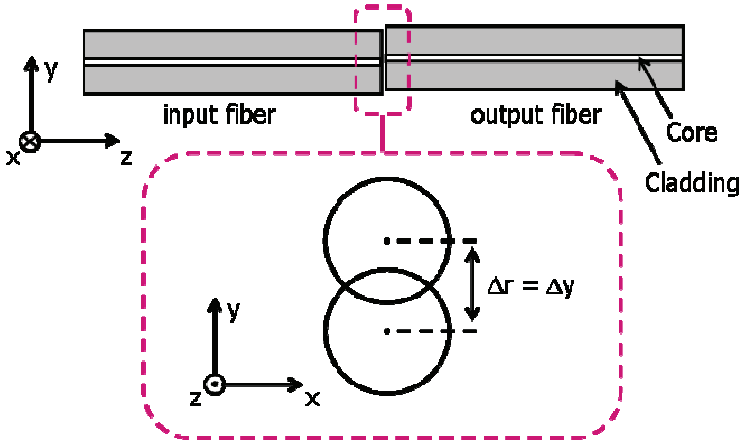

Fig. 3.2.10: Modeling of misalignment at splices or connectors.

If the same connection techniques are used with FMFs instead of SMFs, a misalignment leads not only to loss, but also to coupling of energy between the different spatial modes of the input and the output fiber. To calculate the energy that is lost or transferred between the different modes of input and output fiber, I calculated the scalar products of the mode function F_{in} of the input mode and the mode functions $F_{out,n}$ of all possibly guided output modes, which are shifted by the distance and in the direction of the fiber misalignment. The mode functions were normalized so that the square of each of these scalar products resulted in the relative output energy of the respective output mode with respect to the power of the input mode. In mathematical terms, this can be described according to

$$P_{out\_rel,n}(\Delta x,\Delta y) = \left\langle \frac{F_{out,n}(x-\Delta x, y-\Delta y)}{\|F_{out,n}\|}, \frac{F_{in}}{\|F_{in}\|} \right\rangle^2 \tag{3.2.23}$$

with '$\langle\ \rangle$' standing for the scalar product and

$$\|f\| = \sqrt{\langle f, f\rangle} \tag{3.2.24}$$

being used for normalization.

If no energy was lost between input and output, the sum of all relative output powers would be *1*. Thus the missing part is identified as relative loss and we can write

$$P_{out\_rel,1}(\Delta x,\Delta y)+\ldots+P_{out\_rel,N}(\Delta x,\Delta y)+Loss = 1. \tag{3.2.25}$$

Connectors

Using this method, I first simulated the interconnection of two SMFs in order to find out which misalignment distance corresponds to a loss of 0.2dB representing a connector. The result is the curve "SMF-SMF" referenced to the right ordinate in Fig. 3.2.11. We observe that the value of interest, and so the misalignment that we have to expect from a connector, is 1.4μm. Thanks to the fact that FMF and SMF have the same cladding diameter, the same connector-types can be used for both, and so it can be assumed, that a realistic connector between FMFs has the same misalignment. The three other curves in Fig. 3.2.11, "LP11", "LP02" and "LP21", show the relative transferred

power into the respective mode with respect to the LP01 mode as a function of the fiber misalignment, when interconnecting an SSMF with an FMF as specified in section 3.2.2. Here, "LP11" respectively "LP21" stand for the sum of LP11a and LP11b respectively for the sum of LP21a and LP21b. The vertical red dashed line indicates the realistic misalignment of a standard connector and its intersection with the curves gives the resulting crosstalk when using the mentioned connector type. It can be found that while for the LP02 and the LP21 mode, the mode coupling might still be acceptable, the mode coupling to the LP11 mode is at about -14dB. For the same input powers in all modes this translates into a crosstalk of -14dB in the LP11 mode, resulting in OSNR penalties of ~2.5 dB at a BER of 1e-3 for QPSK modulation, according to Fig. 3.1.2 [18].

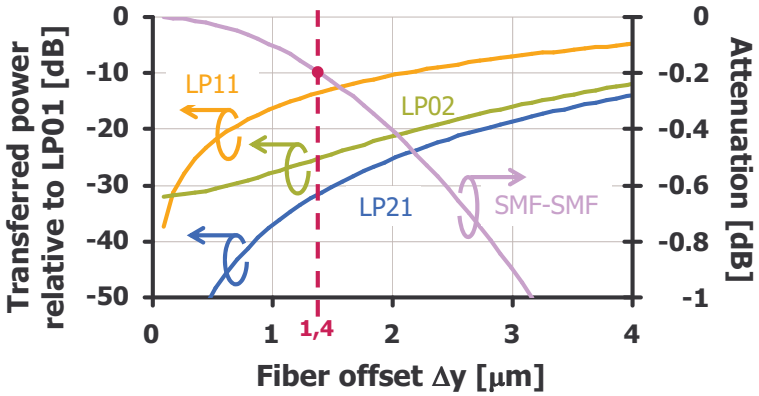

Fig. 3.2.11: Impact of fiber misalignment on attenuation when interconnecting SMF-SMF (right axis), or on transferred power relative to LP01 when interconnecting SMF-FMF (left axis).

I did the same tests for an interconnection between two FMFs of the same type, where now not only several possible modes of the output fiber can be excited, but also different modes guided by the input fiber can be injected. As a consequence, the result for every misalignment distance can be represented in a table as it has been described in section 3.1.1 "Intermodal Crosstalk through Linear Mode Coupling", showing the relative power that is coupled into each guided mode of the output fiber for any guided mode of the input fiber. Table 3.2.2 shows the matrix for a misalignment in *y*-direction by 1.4μm. The first line is very similar to the results presented in Fig. 3.2.11, but not exactly the same, since now, the LP01 mode of the incoming FMF differs slightly from the incoming mode in the before-used SMF. In addition, we can see the crosstalk values, when injecting other modes than LP01. One important aspect is the symmetry of the matrix. That is, the energy coupled from mode *p* of the input fiber into mode *q* of the output fiber is the same as the energy coupled from mode *q* of the input fiber into mode *p* of the output fiber. Furthermore, Table 3.2.2 shows that for any injected mode, at least one output mode suffers from an intolerable amount of transferred power being less than 13dB lower than the desired mode. Hence, we can conclude that the use of standard connectors does not provide sufficiently high precision in order to guarantee the required crosstalk values, especially when thinking of a concatenation of several connectors.

Table 3.2.2: Relative output powers [dB] for all combinations of guided modes at input FMF and output FMF, applying a fiber misalignment of Δy = 1.4μm.

in \ out	LP01	LP11a	LP11b	LP02	LP21a	LP21b
LP01	-0.26	----------	-13.06	-35.60	----------	-33.97
LP11a	----------	-0.31	----------	----------	-12.04	----------
LP11b	-13.06	----------	-0.96	-11.30	----------	-12.36
LP02	-35.60	----------	-11.30	-1.14	----------	-21.79
LP21a	----------	-12.04	----------	----------	-1.09	----------
LP21b	-33.97	----------	-12.36	-21.79	----------	-1.07

Splices

Using splices to interconnect two fiber sections is less convenient than using connectors, but in exchange it provides much higher precision. To get a first impression about the generated intermodal crosstalk by splices, we can assume the aforementioned loss of 0.01 dB and use Fig. 3.2.11 for the same analysis as we did for the case of connectors. Based on this method, the vertical red dashed line would be on the very left of the diagram and so the generated crosstalk with all modes would be below -30dB.

To confirm this positive result we went on to do experimental tests. We started with an analysis on the reproducibility of a splice. To do so, we used the same experimental set-up as it will be described in section 4.2.1 containing a mode-MUX/DEMUX connected by two 20 km FMF spools. Then we repeatedly cut the connection between the spools, spliced them together again and each time did power measurements to fill out a table as described in Table 3.1.1b. The 6 elements of the table, which are not equal to 1, are plotted in Fig. 3.2.12 for seven different splices.

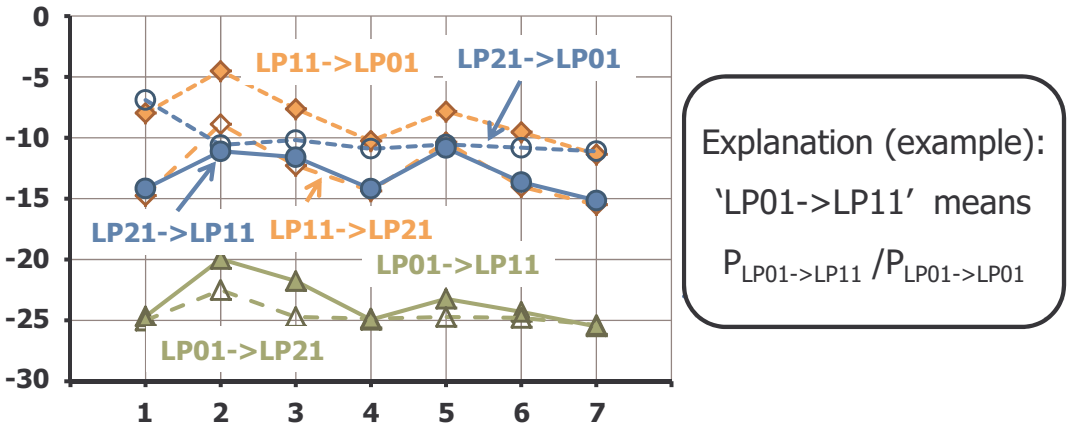

Fig. 3.2.12: Relative transferred powers after MDM transmission over 40 km including on splice, which was reproduced 7 times.

Looking at the results we can first of all observe a big difference between the transferred powers coming from the LP01 mode and the transferred powers coming from the two other modes. We mainly attribute this to asymmetric mode coupling during fiber transmission since we observed that this effect gets stronger with increasing transmission distance (see Table 4.2.1). Moreover, we can see fluctuations in the

transferred powers of ~5dB for the different splices. Hence, subsequent to this study we tried to establish a splicing procedure which can provide a more constant splicing quality, followed by further investigations with the objective to precisely determine the mode coupling generated in a splice. After the end of my work, this study is now continued by my colleagues.

3.3 Mode-Multiplexer and Mode-Demultiplexer Including Mode-Converters

Mode-multiplexer (mode-MUX) and mode-demultiplexer (mode-DEMUX) are depicted in Fig. 3.3.1. They contain several functionalities. In the multiplexer, the incoming signals arrive through SMFs on their fundamental modes with the mode function F_{SMF}. After entering the mode-multiplexer, each mode is converted into a different guided mode of the FMF F_{FMF_n}. Then all converted modes are combined together and injected into the FMF.

At first sight, mode-demultiplexing seems more complicated than mode-multiplexing since there is not only one mode that has to be converted, but a superposition of several modes which also have to be separated. However, it turns out that the same set-up can be used, only operated in the inverse direction [117], [118]. At the input of the mode-DEMUX, the output beam of the FMF is split into a number of identical beams consisting of a superposition $\underline{F}$ of all modes that were propagating through the FMF. Each of these beams then hits a conversion device. Here, the mode F_{FMF_n} containing the signal that is to be extracted is projected onto the guided mode of the output SMF, and all the other modes being part of the beam are projected on orthogonal mode components. Then the modified beam $\underline{F}_{FMF\_n\text{-}SMF}$ is injected into the output SMF, which filters out all but the desired signal tributary being now on the guided mode of the SMF F_{SMF}.

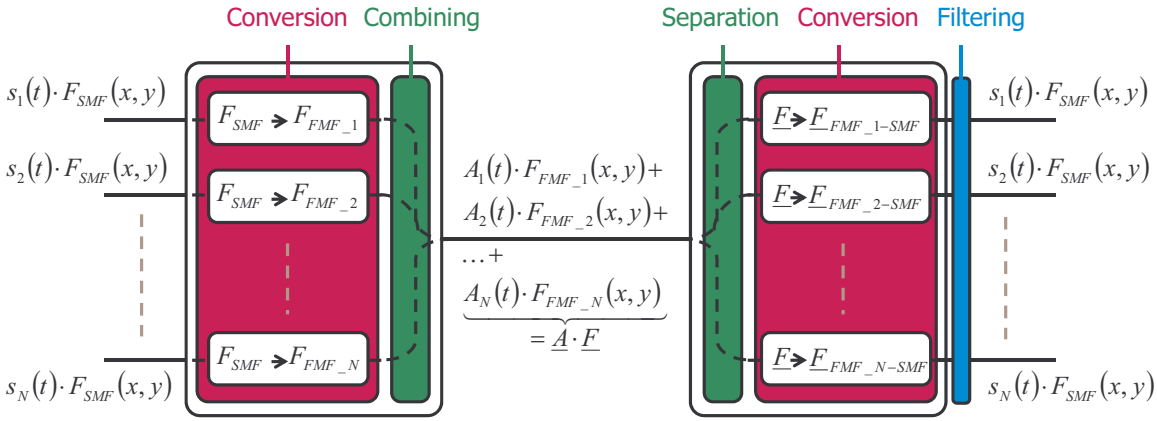

Fig. 3.3.1: Scheme of mode-multiplexer and mode-demultiplexer.

In our approaches, the combining- or separation-part is realized with standard beam-combiners / -splitters so its realization is straight forward and it is not necessary to dedicate a lot of attention to this subject. All necessary explanations will be given in section 3.3.3, when presenting the two concrete mode-MUX/-DEMUX realizations. The more interesting part is the mode conversion, where several techniques have been proposed in literature [90], [91], [117], [119], [120]. I will describe the theoretical background of our solution for mode conversion in section 3.3.1.

For future generations of mode-multiplexers and mode-demultiplexers it might be preferable to combine the steps of separation/combination and conversion into one

single step, which would highly reduce the insertion loss thanks to the fact that the 3dB loss at every beam splitter would fall away. Such a solution is theoretically possible [119], [121] but it requires a very sophisticated optical design and extremely high precision in the manufacturing process. Recently a first experimental realization of this idea has been published [122].

3.3.1 Mode Conversion Using Fourier Optics

3.3.1.1 Optical Basic Concept

Our mode converting unit is based on Fourier optics, with the basic set-up depicted in Fig. 3.3.2. The input fiber is collimated by a lens, whose distance to the fiber output corresponds to its focal length f_1. As a result, the spatial light distribution in the input-fiber $F_{in}(x,y)$ becomes its two-dimensional, spatial Fourier transform (FT) $\breve{F}_{in}(k_x,k_y)$ exactly after free-space propagation over another f_1 [123]. The two dimensional FT is defined as

$$\breve{F}(k_x,k_y) \;=\; FT\{F(x,y)\} \;=\; \iint F(x,y)\exp\left[-j2\pi(k_x x+k_y y)\right]dxdy \qquad (3.3.1)$$

with k_x and k_y being referred to as spatial frequencies. Here, in the so-called Fourier plane, $\breve{F}_{in}(k_x,k_y)$ can be modulated by a multiplicative mask $\breve{m}(k_x,k_y)$ in order to obtain the Fourier transform of the desired output mode $\breve{F}_{out}(k_x,k_y)$. To perform the inverse Fourier transform and to inject the light with the correct spatial distribution $F_{out}(x,y)$ into the output fiber, it is sufficient to use a similar assembly as at the input, consisting of a collimated fiber with a lens that is spaced by the same distance f_2 between the Fourier plane and the output-fiber. The two dimensional inverse Fourier transform (FT^{-1}) is defined as

$$F(x,y) \;=\; FT^{-1}\left\{\breve{F}(k_x,k_y)\right\} \;=\; \iint \breve{F}(k_x,k_y)\exp\left[j2\pi(k_x x+k_y y)\right]dxdy\,. \qquad (3.3.2)$$

We see that inverse Fourier transform and Fourier transform are realized by almost the same operation, only differing in the "-" sign in the exponential.

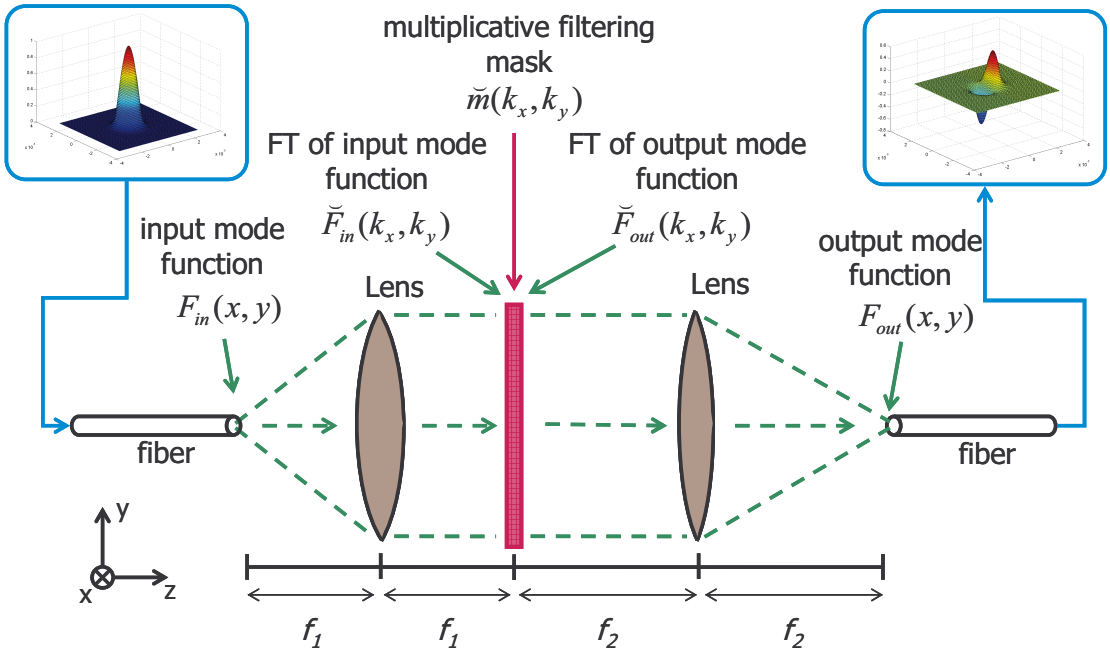

Fig. 3.3.2: Concept of a Fourier optics set-up.

The resulting field distribution in the output fiber can be calculated by applying the inverse Fourier transform to the product of mask and incoming Fourier transform:

$$F_{out}(x,y) = FT^{-1}\left\{FT\left\{F_{in}(x,y)\right\}\cdot m(k_x,k_y)\right\} \tag{3.3.3}$$

Equation (3.3.3) points out that under ideal conditions, the calculation of all light propagation in free-space is reduced to two simple Fourier transforms. We will exploit this property in order to establish a numerical model for the design of the phase mask, which is the key element of our mode conversion set-up, and to assess the impact of different imperfections such as size- or position-mismatch. However, to simulate imperfections that change the properties of the model, such as a phase mask offset in the propagation direction *z*, the explicit calculation of light propagation in free-space is required.

3.3.1.2 Conversion in the Fourier Plane

By rewriting equation (3.3.3), the ideal multiplicative mask for a given input mode with mode function $F_{in}(x,y)$ and a desired output mode with mode function $F_{out}(x,y)$ can be calculated straight forward in the following way:

$$\breve{m}_{ideal}(k_x,k_y) = \frac{FT\left\{F_{out}(x,y)\right\}}{FT\left\{F_{in}(x,y)\right\}} = \frac{\breve{F}_{out}(k_x,k_y)}{\breve{F}_{in}(k_x,k_y)} \tag{3.3.4}$$

In general, $\breve{m}_{ideal}(k_x,k_y)$ can be a complex-valued function, since already $F_{in}(x,y)$ and $F_{out}(x,y)$, as well as $\breve{F}_{in}(k_x,k_y)$ and $\breve{F}_{out}(k_x,k_y)$ can be complex-valued. However, in the special case of the fiber modes in the weakly guiding limit, the mode functions are real valued and either purely odd or purely even functions. Hence, their Fourier transforms are either purely real or purely imaginary.

Now we can decompose $\breve{m}_{ideal}\left(k_x,k_y\right)$ into an amplitude term and into a phase term leading to:

$$\breve{m}_{ideal}\left(k_x,k_y\right)=\breve{A}_m\left(k_x,k_y\right)\cdot\breve{\theta}_m\left(k_x,k_y\right) \tag{3.3.5}$$

Since the applied mask is supposed to be a passive device, the condition $A_m\left(k_x,k_y\right)\le 1 \quad \forall\left(k_x,k_y\right)$ has to be fulfilled in practice, which is usually not the case when following the straight forward approach of (3.3.4). Furthermore, the resulting phase mask $\breve{m}_{ideal}\left(k_x,k_y\right)$ can have singularities when the incoming mode function has zero crossings. With these constraints it is quasi impossible to realize an ideal phase- and amplitude-mask. As a consequence, the possibility to do mode conversion using only a phase mask seems interesting having additionally the positive effect of reduced implementation complexity.

The easiest way to calculate the required phase mask is to use the phase term out of the straight forward approach from equation (3.3.5) so that:

$$m_{sf}\left(k_x,k_y\right)=\theta_m\left(k_x,k_y\right) \tag{3.3.6}$$

As it will be shown in the following section 3.3.2, this approach already provides satisfying conversion ratios for several relevant combinations of spatial modes. However, using sophisticated optimization algorithms the design of the pure phase masks for mode conversion can strongly be improved [121], [124]. In this work I won't give any further details on such techniques, since the modes that we used in the experimental part could be generated with a sufficiently good quality by using the straight forward approach, compared to other dominating sources of mode coupling in the transmission system such as imperfections in the free-space optics part of the mode-MUX/-DEMUX or some tens of kilometers of transmission fiber. Nonetheless, to further improve the conversion ratios, reduce the insertion loss while at the same time increasing the number of modes, phase masks closer to the optimum will certainly be needed.

3.3.2 Numerical Modeling and Mode Coupling Estimations

In order to design phase masks for the generation of the desired modes and in order to assess the quality of mode conversion with these masks we developed a simulation tool for mode conversion. Moreover, the tool was used to get an idea of the tolerance to possible imperfections in a real mode converter, such as phase mask offsets in *x*- or *y*-direction or size changes.

In the top of Fig. 3.3.3, the concept of the simulation set-up is shown. First of all, the mode functions of all guided modes in input fiber and output fiber were calculated. Since both fibers that we used in experimental works, our prototype FMF and the standard SMF, are step index fibers, we limited the simulation tool to the calculation of mode functions in step index fibers. This was done by the procedure described in section 1.2.2.2. In a second step, the phase mask was generated: either by applying equations (3.3.4) to (3.3.6) or by manually defining an arbitrary phase pattern. Then the behavior of the incoming modes was tested one by one. First, the phase mask was applied by transforming the incoming mode into the spatial Fourier domain and by multiplying the result with the phase mask. Afterwards the product was retransformed into the original domain. Finally, loss and crosstalk between resulting mode function and the guided modes of the output fiber were calculated. To do so, a procedure similar to the one

already described in section 3.2.3.1 was applied. By calculating the scalar product of the newly generated, modified incoming mode with any of the guided modes of the output fiber, we obtained the relative power, injected into each of these modes. In the bottom of Fig. 3.3.3 the fiber parameters are given, and two examples for the calculated straight forward phase masks are shown. Below the masks, the mode shapes are depicted as they had to look like directly after the mask for a perfect injection into the output fiber. This corresponds to the FT of the respective mode functions in the FMF. Please note that here we simulated only the mode conversion aspect of the mode-MUX/-DEMUX, and in order to completely characterize the whole device, potential loss differences in the different paths during combining / separation must be taken into account.

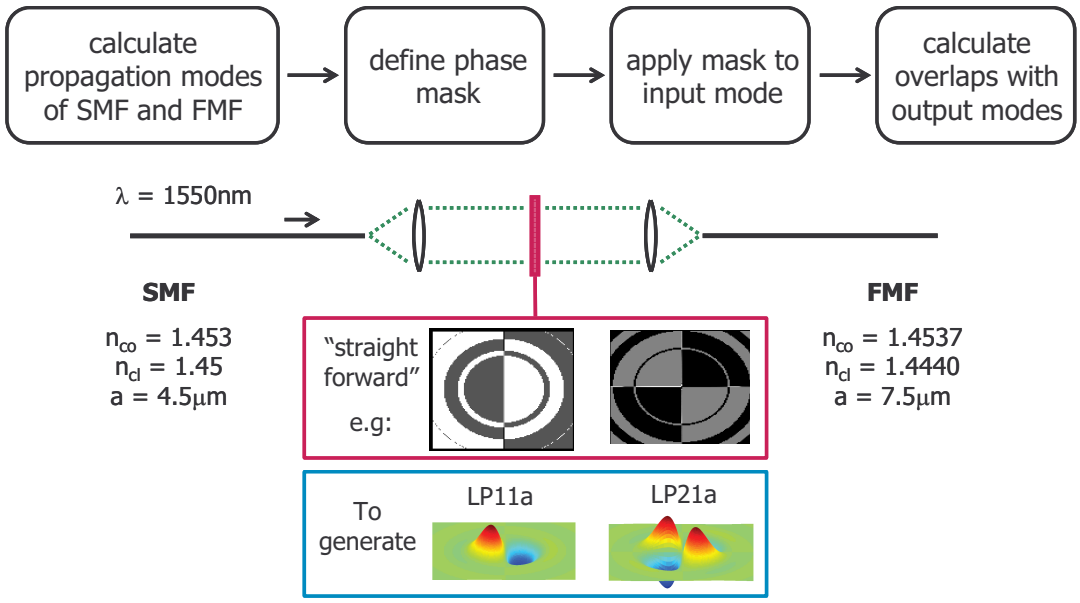

Fig. 3.3.3: Concept of the simulation tool and simulation set-up for mode conversion with straight forward masks.

First, we used the described model to test the quality of mode conversion into the modes of the prototype FMF when injecting the fundamental mode of an SMF and using straight forward phase masks. Table 3.3.1 shows the relative powers injected into each of the guided modes of the output FMF. The green cells in the main diagonal of the table show the value that is to be maximized, since it is the mode that is desired to be injected. All other values shall be minimized since they cause intermodal crosstalk. A good measure for the conversion quality of a mask is the difference between the value in the main diagonal and the other values in the same line. The higher the difference in dB, the higher is the ratio of useful power over power that disturbs the signals on other modes. We can observe that this value is critical when applying the mask for generation of the LP02 mode. In this case, the relative transferred power to the LP01 mode is only ~5dB lower than the power injected into the LP02 mode. For all other conversions, the relative power is at least 20dB higher in the desired mode than in the second strongest mode. Please note that the differences in the lines for application of the LP21a mask and the LP21b mask result from numerical imprecisions caused by the rotation of 45° with respect to each other. Furthermore, when applying the mask for the generation of a mode with an odd mode function, such as LP11a/b or LP21a/b, symmetry aspects suggest that the energy transferred to modes with even mode functions is *0* (or *-∞* in a dB scale). I attribute the different results from Table 3.3.1 to numerical problems, mainly

with the modeling of the phase jumps in the center of the mask and with the exact alignment of the mask to the center of the Fourier transform of the incoming mode.

Table 3.3.1: Relative power in *dB* transferred into the different output modes of the FMF, when using "straight forward" phase masks.

		Relative power into output mode…					
		LP01	**LP11a**	**LP11b**	**LP02**	**LP21a**	**LP21b**
Mask to generate mode…	**LP01**	-0.17	----------	----------	-22.9	----------	----------
	LP11a	-24.4	-3.31	----------	-30.9	----------	-33.9
	LP11b	-24.4	----------	-3.31	-30.9	----------	-33.9
	LP02	-8.74	----------	----------	-3.9	----------	----------
	LP21a	-28.2	-44.9	-56.7	-30.0	-6.18	-28.1
	LP21b	-25.2	-47.8	-44.5	-27.9	-32.6	-6.17

Another important property for mode conversion is the conversion loss of the desired modes. With a maximum of roughly 6 dB for the two LP21 modes it is pretty high here. However, in our design approach for MDM systems, loss in a mode-MUX/-DEMUX is less important than conversion quality. This is because system performance is mainly limited by intermodal crosstalk and it is sufficient to compensate for the relatively high loss in the mode-MUX/-DEMUX by strong amplification in the single mode part of the MDM system directly before the input of the mode-MUX. However, when designing an MDM system with the highly mode coupled approach, the situation can be different: If intermodal crosstalk is compensated by DSP and no few-mode amplification is used, the performance will be limited by the OSNR, which is then mainly determined by the input power of the single mode EDFAs at the output of the mode-DEMUX. Hence, in this case it is important to minimize the loss in mode-MUX and mode-DEMUX.

For the practical manufacturing of the phase masks it is beneficial to use a phase pattern that is as simple as possible. Considering the phase masks for conversion from LP01 to LP11a/b and from LP01 to LP21a/b, the most important features are the π-phase jumps in the center of the masks. All other phase jumps are in regions where very little energy hits the masks. Hence, I tested phase masks consisting only of the central phase jump in order to confirm this hypothesis. The results for the application of these simplified phase masks are presented in Table 3.3.2.

It can be observed that the performance is very similar compared to the performance with the straight forward phase masks. Only the power transfer to the LP11a mode when applying the mask for the LP21a mode has significantly increased. But given the negligible power transfer to the LP11b mode in this case, I attribute this to problems in terms of numerical imprecisions and quantification.

Table 3.3.2: Relative power in *dB* transferred into the different output modes of the FMF, when using simplified phase masks for generation of LP11a/LP11b and LP21a/LP21b.

		Relative power into output mode…					
		LP01	**LP11a**	**LP11b**	**LP02**	**LP21a**	**LP21b**
Mask to generate mode…	**LP11a**	-24.4	-3.3	----------	-30.9	----------	-33.8
	LP11b	-24.4	----------	-3.3	-30.9	----------	-33.8
	LP21a	-25.6	-28.4	----------	-33.2	-6.2	----------
	LP21b	-29.2	-42.18	-42.18	-37.4	-36.8	-6.2

Finally I did simulations to estimate the tolerance to a shift of the phase mask inside the *x*-*y*-plane. For these tests, the configuration differed slightly from the preceding set-ups: now the incoming beam was modeled as the LP01 mode of the FMF, not the LP01 of an SMF. The rest remained unchanged and I applied the straight forward phase mask for LP11a generation. I shifted the phase mask in *x*-direction (that is orthogonal to the central phase jump) and calculated the relative powers transferred into the different output modes for varying shifting distances. The results are presented in Table 3.3.3. We observe that the ratio between the power injected into the LP11a mode and the power injected into the second strongest mode (in this case always the LP01 mode) drops rapidly. Already a shift by 2% of the beam diameter causes a drop from ~22 dB to ~15 dB. Assuming a beam diameter of ~500 μm, which is realistic based on our experimental work, this corresponds to a shift of ~10 μm. This gives an idea about the required precision for the practical implementation of a mode converter. When further increasing the mask misalignment, the power ratio between LP11a and LP01 decreases more and more slowly but nevertheless, at a shift of ~10% the LP01 mode gets even stronger than the LP11a mode.

Table 3.3.3: Relative power in *dB* transferred into the different output modes of the FMF for varying phase mask shifts in x-direction using mask for generation of LP11a.

Relativ mask shift w.r.t. beam diameter	**Relative power into output mode…**						**Power ratio between LP11a and second strongest mode**
	LP01	**LP11a**	**LP11b**	**LP02**	**LP21a**	**LP21b**	
0 %	-24.5	-2.6	--------	-32.9	-32.4	--------	21.9
2 %	-17.5	-2.7	--------	-25.8	-25.4	--------	14.8
4 %	-12.3	-3,0	--------	-20.6	-20.3	--------	9.3
6 %	-9.1	-3.5	--------	-17.6	-17.3	--------	5.6
8 %	-6.9	-4.2	--------	-15.7	-15.4	--------	2.7
16%	-2.4	-10.0	--------	-12.8	-12.9	--------	-7.6

3.3.3 Practical Realization of Mode-Multiplexers and Mode-Demultiplexers

We designed and constructed two sets of mode-multiplexers and mode-demultiplexers, whose key difference was based on the realization of the multiplicative mask. The first one used a programmable Liquid Crystal on Silicon (LCoS) panel working in a reflective mode, whereas the second one used static, transparent phase plates. In the following, I describe these two devices:

3.3.3.1 Mode-Multiplexer and Mode-Demultiplexer using Programmable Liquid Crystal on Silicon Technology

The employed LCoS device is a panel of 1920x1080 pixels, which can all be programmed independently to produce a phase shift between 0 and 2π. This offers the possibility to obtain a huge number of mode shapes with high precision, limited by the resolution inside the area hit by the modulated light beam. Using sophisticated algorithms the attribution of the pixels' phase values can be optimized [120]. However, according to the simulations presented in section 3.3.2, already very simple mask designs can provide sufficiently good mode conversion when taking into account the limited number of guided modes in the applied FMF. The LCoS device operates in reflective mode and it works only along one polarization axis, which leads to additional complexity in the optical free-space design.

Based on these constraints imposed by the LCoS panel our STRADE project partner Kylia constructed a 4x1 mode-converter and a 2x1 mode-converter. Both devices can be operated in both directions and so they can arbitrarily be applied as multiplexer or demultiplexer. Their structure is depicted in Fig. 3.3.4. In the 4x1 multiplexer, all four inputs enter the free-space device through a collimated SMF pigtail. Then, three of them are spatially modulated as it is depicted in the grey box in the upper left of Fig. 3.3.4. The light of each of them is split along two optical paths by a polarization beam splitter (PBS), and one of the two resulting beams passes by a half-wave plate in order to rotate it by 90° and to align both beams along the correct polarization axis of the LCoS. After passing a lens to slightly refract them, the beams hit the LCoS panel on two of six possible spots on its upper half (see Fig. 3.3.4. in the upper right). The refraction by ~0.2° is necessary to allow the beam not to hit the components of the input path after reflection at the LCoS. The spots on the LCoS device count approximately 80x80 pixels and are programmed with one of the three phase masks depicted in the center of Fig. 3.3.4, which give the light beam the shape of either LP01, LP11a or LP11b mode from then on. After spatial modulation, each light beam is sent back through a comparable assembly of lens, half-wave plate and PBS in order to put the two polarization tributaries back together. Finally, the three spatially modulated beams are combined with the fourth, unchanged input beam and are collimated into the FMF. At the receiver end, the 2x1 converter is designed similarly, but with only two SMF-fiber pigtails, which can both be spatially modulated, making use of four spots on the lower half of the LCoS panel for programming the phase masks.

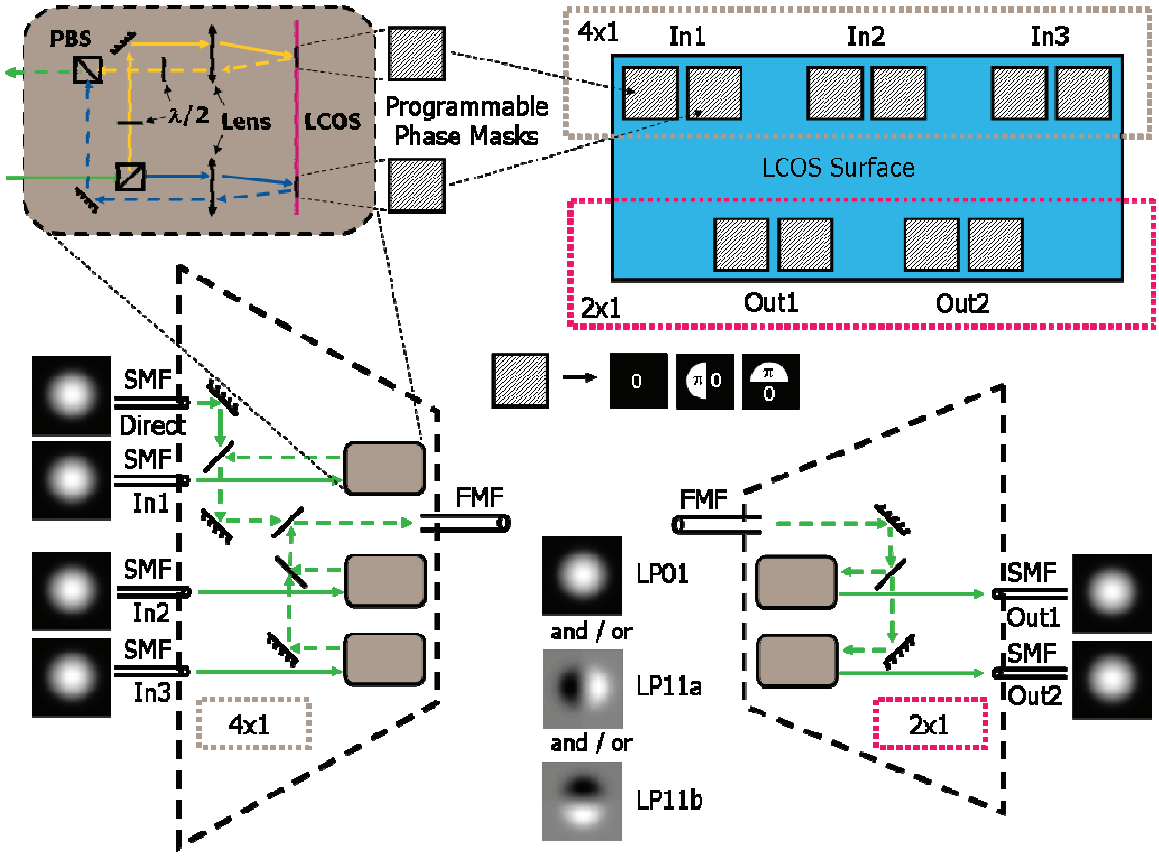

Fig. 3.3.4: Design of LCoS based mode-multiplexer and mode-demultiplexer as we used it in our laboratory.

Characterization and optimization of the mode-multiplexer and –demultiplexer were difficult for several reasons:

- The devices were developed in collaboration with our project partner Kylia and assembled by them both together in one packaged "black box" (a photograph of the device is shown in Fig. 3.3.5). Hence, the only changes that we could apply to the set-up without risking its destruction were through the programming of the LCoS and by cutting/splicing the FMF pigtails in order to lengthen or shorten the transmission distance between mode-Mux and -DEMUX.
- The only points to access for measurements were the SMF fibers at the input of the mode multiplexer and at the output of the mode demultiplexer, or the FMF after cutting it. But in this case it would have been hard to discriminate between the portions of the various spatial modes and so we didn't make use of this possibility.
- At the time when the mode-multiplexer and –demultiplexer was packaged, the final FMF wasn't available yet and so we had to use another type of fiber as FMF pigtail, which had to be definitively connected to the 4x1 and the 2x1 device. This fiber guided only the fundamental mode and the LP11 mode, but the latter with an estimated attenuation of ~3dB/m. Furthermore, it made it necessary to include two splices between the two types of FMF, one after the mode-multiplexer and one before the mode-demultiplexer.
- The overall performance of the device was never good enough to work in a regime, where mathematical simplifications could be made in the calculations thanks to the mode power of one mode being dominant, and others being negligible.

- The LCoS pixels were refreshed with a frequency of 60 Hz translating into a "dithering" in the reflected optical power. This also impacted the performance negatively.

So finally, for every measurement taken at the SMF outputs, the light had to pass through two phase masks in the mode multiplexer (for the two polarizations), the FMF pigtails, two splices, the transmission FMF and two phase masks in the mode demultiplexer (again for the two polarizations), all while the quality of the LCoS panel was very limited.

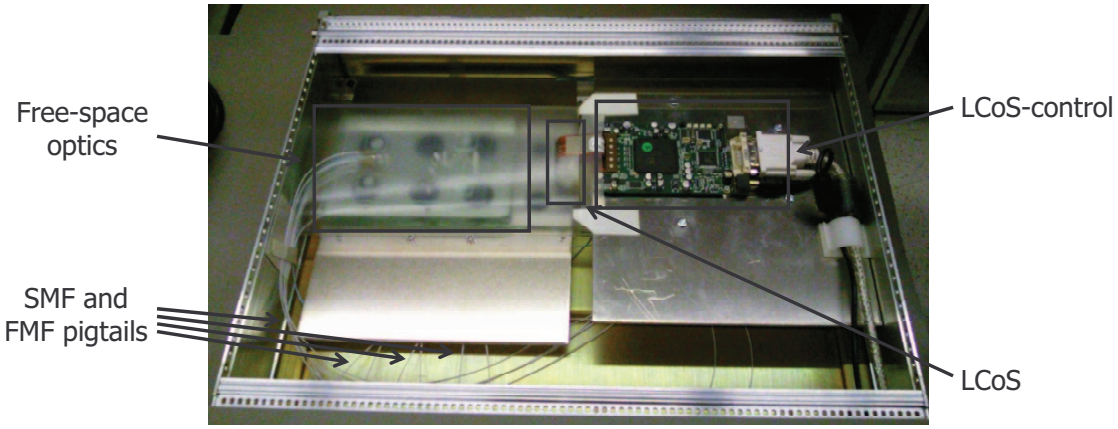

Fig. 3.3.5: Realization of LCoS based mode-multiplexer and –demultiplexer.

Nonetheless, we made a lot of efforts to optimize and to characterize the whole system, and the major results have been published in [92], [118], [125–127].

3.3.3.2 Mode-Multiplexer and Mode-Demultiplexer using Static Phase Plates

Our second generation mode-multiplexer and –demultiplexer, based on transparent phase plates, was realized in free-space optics using micro-mechanical building blocks in order to finely tune the alignment of all the optical subparts. On the one hand, this made it possible to optimize any geometrical parameter, but on the other hand, the set-up had to be regularly readjusted because it was not satisfyingly stable.

In Fig. 3.3.6a, the design of the 5x1 mode-converter is depicted. Again, the device can be operated in both directions, and so it can be used as either mode-multiplexer or mode-demultiplexer, only depending on the direction in which it is connected. Along its five input paths, the spatial profiles of the optical beams are either unchanged or converted to the profiles of the LP11a, LP11b, LP21a, and LP21b modes. Mode conversion of each beam is again based on the principle of the 4f configuration as described in section 3.3.1. For this purpose, the multiplicative masks are realized by 4-quadrant phase plates, which were realized in-house out of two superimposed horizontal and vertical π-phase steps. The quality of the phase step was carefully controlled to guarantee high mode-to-mode rejection ratio. By now sending each beam onto the appropriate location on one of these phase plates, as schematized in Fig. 3.3.6b, the desired mode conversion can be performed.

Finally, the five beams corresponding to the five exploited fiber modes are combined with standard beam combiners, and coupled into an FMF pigtail.

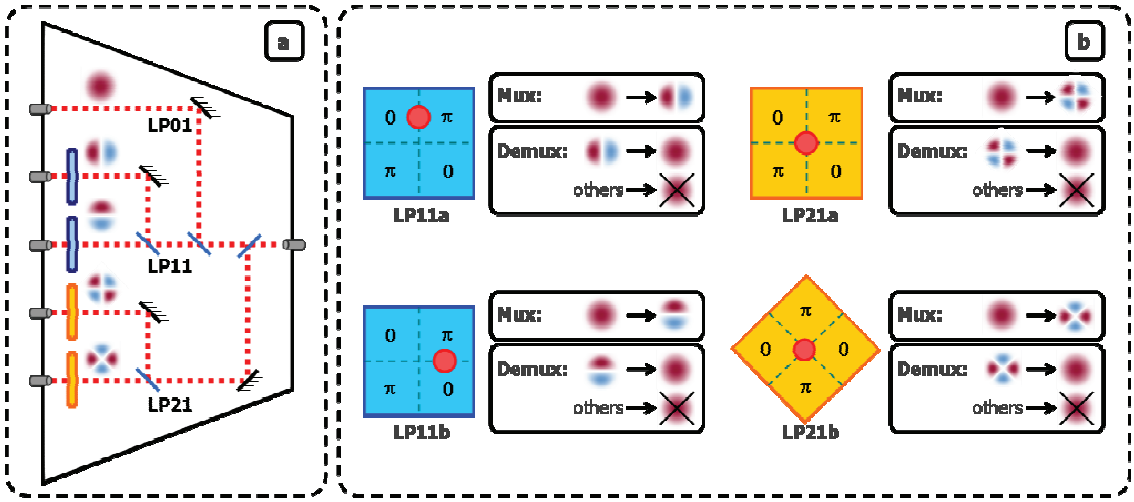

Fig. 3.3.6: Design of our second generation mode-multiplexer and mode-demultiplexer based on transparent phase plates. (a) Scheme of the entire device. (b) Use of phase plates.

In order to characterize this type of 5x1 mode converter, that is to determine the generated intermodal crosstalk, we connected two of them with a small section of FMF (~10m) so that one worked as mode-multiplexer and the other one as mode-demultiplexer. Subsequently, we performed a series of power measurements.

For each input mode / pair of degenerate input modes at the mux side we firstly obtained a reference output power when extracting the same mode / pair of degenerate modes at the DEMUX side. Then we measured the output power when extracting the other modes at the DEMUX side and noted the ratio with respect to the reference output power. The ratios in dB are shown in Table 3.3.4. Note that the modes LP11a and b as well as the modes LP21a and b were injected and extracted together to obtain a result that is independent of possible rotations of the spatial field distribution. The relative input powers of two degenerate modes had been adjusted previously for identical output powers, in order to account for the slightly different losses in each of the optical paths inside our device.

Table 3.3.4: Crosstalk ratios measured with two 5x1 mode convertors based on phase plates and realized in free-space optics, connected by ~10m of FMF.

	LP01	LP11a +LP11b	LP21a+ LP21b
LP01	0	-22.3	-20.2
LP11a+b	-23.6	0	-16.1
LP21a+b	-28	-16.1	0

Taking a look at Table 3.3.4, we observe that the worst case can give a relative transferred power of up to -16.1 dB, which is the case between the modes LP11 and LP21. Furthermore, it can be observed that the relative transferred power between LP11 and LP21 as well as between LP01 and LP11 take at least similar values in both directions whereas the relative transferred power between LP01 and LP21 differs by ~8dB, depending on in which direction it is measured. We attribute this asymmetry mainly to imperfections as a consequence of differently well-adjusted paths and instabilities between the measurements.

Since stability was a critical point for this device, we investigated it by performing a series of measurements over a longer period of time. In a first step, we measured the crosstalk between the modes LP01 and LP11 every 4 to 5 minutes, while at the same time we measured the Q²-factors for the signals transmitted on these two modes. Hereby, the system was in back to back configuration and the OSNR in both modes was >20dB/0.1nm, leading to no measurable BER without crosstalk. The crosstalk was measured in the same way as we did it to obtain the results in Table 3.3.4 and the Q²-factors were measured with the receiver set-up described later in section 3.5.

In Fig. 3.3.7, both Q²-factors (y-axis scale on the left) and crosstalk values (y-axis scale on the right) are plotted as a function of time. First of all, it can be observed that the crosstalk from LP01 to LP11 takes better values than the crosstalk from LP11 to LP01, whereas in Table 3.3.4 they were symmetric. Again, this can be attributed to imperfections in the fine-tuning of the mode-MUX and –DEMUX. Furthermore, the crosstalk from LP11 to LP01 also degrades faster than the one from LP01 to LP11, and as a consequence the Q²-factor of LP01 degrades much faster than the Q²-factor of LP11. Both Q²-factors start around 13 dB and reach ~10 dB, respectively ~11.5 dB after ~110 min. Then we continued the measurements with a much lower frequency, as we supposed an ongoing monotonic decrease of the performance. However, when we took the next measurements, after a total of ~210 min we observed an improvement of all performance indicators, Q²-factors and crosstalk values, which even continued at the following measurement at ~250 min.

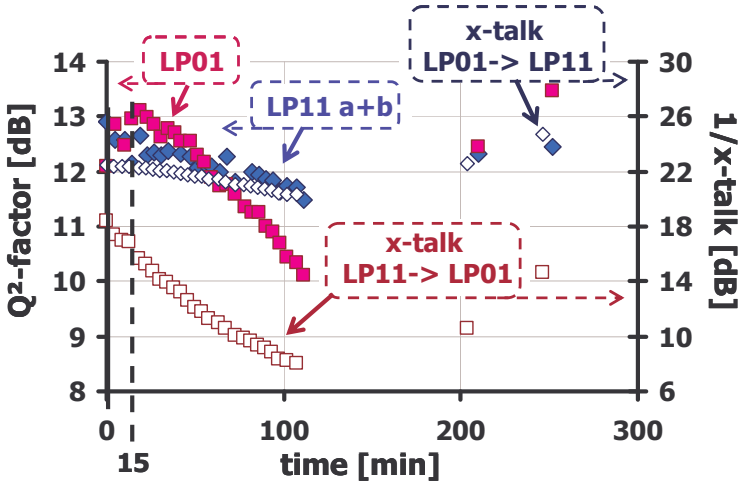

Fig. 3.3.7: Stability measurements of free-space mode-multiplexer and mode–demultiplexer, over a period of 5 hours by measuring crosstalk values and Q²-factors.

Hence, we started a new series of measurements over a longer time period in order to observe potential performance fluctuations and if there could be a convergence towards a stable point of operation. Since during all measurements in Fig. 3.3.7 Q²-factors and crosstalk levels correlated very well, we decided, for practical reasons, to measure only the Q²-factors.

The measurements were taken over a weekend during approximately three days and the results are presented in Fig. 3.3.8. Indeed, we can observe a strong Q²-factor fluctuation, especially regarding the LP01 mode. Starting at a Q²-factor of 14 dB it drops down to 8 dB after ~11 h and reaches 14 dB again after ~19 h, passing through several local minima and maxima in the meantime. However, from that moment on, the tendency is strongly negative and after 30 h, the LP01 Q²-factor is already down to ~7 dB, fluctuates between ~7 dB and ~2 dB until a total measurement duration of

~50 h, before it eventually drops below 0 dB. In comparison, the LP11 mode performs more stably. During the first ~30 h its Q²-factor decreases from ~12 dB to ~10 dB, while fluctuating by ~1 dB over indeterminably short time frames, indicated by the thickness of the point-set. From then on, these fluctuations get much smaller and after 50 h, the Q²-factor is still at 10 dB, having passed through two local minima at ~8dB at ~35 h and ~40 h. Starting at 50 h of measurement time, the Q²-factor drops fast down to around 4 dB and remains in this region until the end of the measurements.

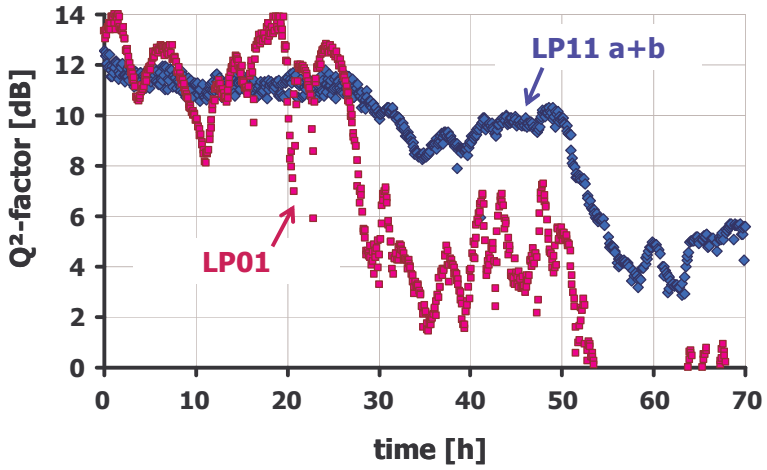

Fig. 3.3.8: Stability measurements of free-space mode-multiplexer and mode–demultiplexer, over a period of 3 days by measuring Q²-factors only.

So through the longer term measurements, it was confirmed that the performance of this mode-multiplexer and mode-demultiplexer doesn't just monotonically decrease with time, but there are also heavy fluctuations. Especially the behavior regarding the LP01 mode, allows only a short time frame of stable measurements. Based on the Q²-factors in Fig. 3.3.7 and depending on the required tolerance, this is typically around 15 min. The general performance decline, which is superposed to these fluctuations, makes it necessary to completely readjust the device on a daily basis.

3.4 The Few-Mode Amplifier

Similar to amplification in single mode systems, also in MDM systems, different candidate technologies exist. Recently, few-mode optical amplifiers have been described, based either on erbium doped fiber amplification [103], [104] or on distributed Raman amplification [102].

For the same reasons as in single mode transmission systems, the EDFA technology seems to be the most attractive one and so we decided to work on this approach in the frame of the STRADE project. The key component, the few mode erbium doped fiber (FM-EDF) was designed and realized by our STRADE project partners from the IRCICA laboratory at the Université Lille 1 according to our jointly defined specifications.

3.4.1 Amplifier Design

Our few-mode amplifier is schematized in Fig. 3.4.1. The signal coming from the FMF is collimated by a lens with a focal length of 3mm, sent towards a free space isolator to prevent unwanted reflections and then coupled with a high power pump at λ = 980 nm through a dichroic mirror. Both the modulated signal and the pump are coupled into a

4m-long prototype erbium doped fiber (EDF). This fiber is highly doped with erbium and exhibits an absorption of 16dB/m at λ = 1530nm (if excited through SMF-28 and a pump at λ = 980 nm), with a 10µm core diameter.

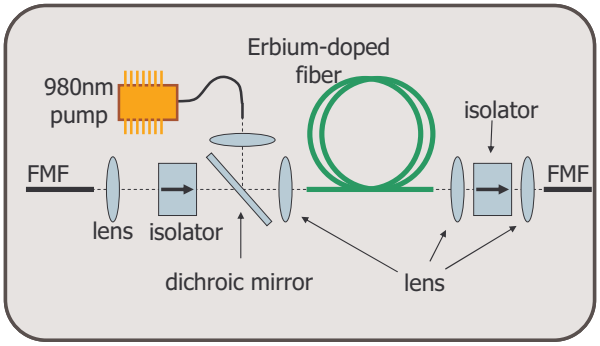

Fig. 3.4.1: Scheme of the few-mode erbium doped fiber amplifier.

Besides the "traditional" challenges in optical amplifiers, that are obtaining high gain at low noise figure, the key challenges in few-mode optical amplifiers are reducing mode coupling and providing similar gains across the various optical modes. To deal with these challenges, the principle fiber design parameters that can be adjusted are the refractive index profile (similar to the design of a non-doped optical fiber) and the profile of the erbium doping concentration. In addition, when constructing the amplifier around the FM-EDF, its behavior can be influenced by the spatial power distribution of the injected pump light wave.

In both [102], [103], gain equalization was addressed by pre-converting the pump power distribution into a higher order mode (LP21) before feeding it into the amplifying fiber or by injecting the fundamental mode with an offset [104]. Here, we pursue another approach for our few mode erbium doped fiber amplifier (FM-EDFA) as also suggested in [104]. Instead of adding complexity by using higher order pump modes, we send the pump along the fundamental mode and tailor the erbium concentration profile such that the gain excursion is reduced across the exploited modes.

We therefore decided to use a distribution of erbium dopants in a ring form when looking at the transverse plane of the fiber. In order to optimize the ring geometry, we used a numerical model of our EDF that accounted for the overlap integrals over the guided modes. Now, the outer diameter of the ring was set to match the core diameter, while the inner diameter was varied. The expected amplifier gain inside the EDF for mode groups LP01, LP11 and LP21 was then computed and is reported in Fig. 3.4.2a. As the doping profile moves away from uniform step-like distribution (ring diameter of 0), the gain along the fundamental mode LP01 continuously drops, while the gains along the LP11 and the LP21 mode groups reach a maximum before decreasing as the inner ring diameter approaches the outer ring diameter. Initially lower, the LP21 gain catches up and matches the LP11 gain at 3.5µm inner ring radius. At this radius, the LP01 mode is expected to experience 2dB lower gain than LP11/LP21. However, in our particular case we voluntarily designed our prototype FM-EDF with an inner radius of 3.5µm since the LP01 mode suffers lower coupling loss between FMF and EDF, as well as lower loss in mode-MUX and –DEMUX since it does not require loss causing phase masks (see section 3.3.3.2).

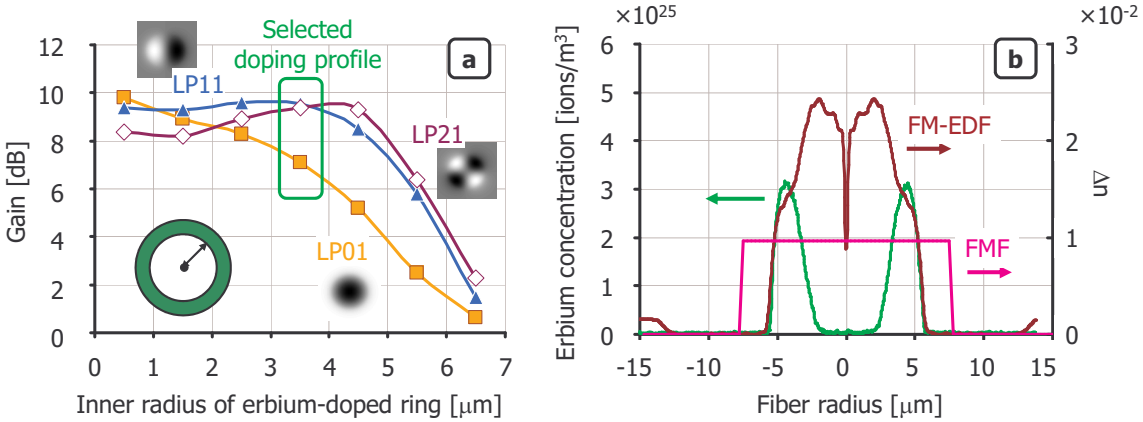

Fig. 3.4.2: (a) Simulated gain of different modes for varying doping ring radius at 1550nm. (b) Refractive index profile of FM-EDF and FMF together with doping profile of EDF.

Fig. 3.4.2b represents the erbium concentration profile of the realized FM-EDF together with its refractive index profile and the refractive index profile of the FMF line fiber described in section 3.2.2. Concerning the erbium concentration, we can observe that the inner radius of the doped ring corresponds to the 3.5μm that were defined after simulations. However, we can also observe that our FM-EDF fabrication method induces transitions between the doped zones and the non-doped zones that take place over a radius of another ~2μm at each side of the ring.

The refractive index profile of the FM-EDF has been chosen with two main objectives: The first objective was matching the propagation modes of the FM-EDF to the ones of the non-doped FMF. This shall minimize mode coupling at the transition between the two fiber types at the input and at the output of the amplifier. The second objective was providing high gain with a low noise figure, which requires a rather small core diameter. Hence, the resulting refractive index profile of the FM-EDF is based on a step index profile with a smaller core diameter and a higher refractive index difference between core and cladding (Δn) compared to the FMF. However, as we can see from Fig. 3.4.2b, the shape of the refractive index step is compromised by the impact of the erbium doping on the refractive index.

3.4.2 Amplifier Characterization

Experimental Set-Up

In our transmission set-up, depicted in Fig. 3.4.3, we employ twenty modulated laser sources ranging from 1530 to 1560nm. They are decorrelated by several hundreds of symbols using standard single mode fiber (SMF) patch-cords, and fed to five optical amplifiers, connected to the five inputs of the 5×1 mode multiplexer (MUX).

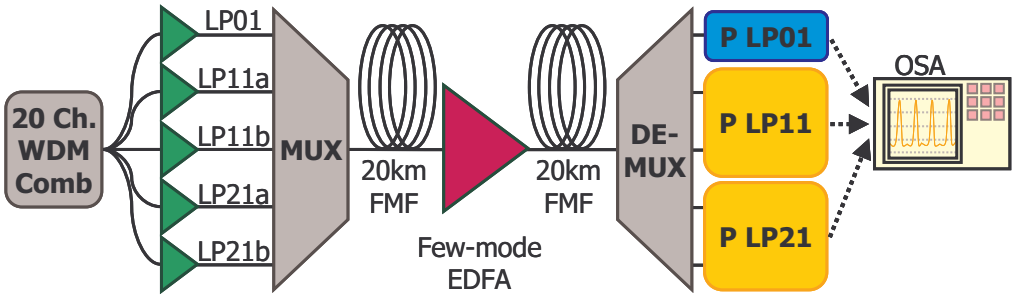

Fig. 3.4.3: Experimental set-up for FM-EDFA characterization.

The MUX is realized in free-space optics using micro-mechanical building blocks, in order to finely tune the alignment of all the optical subparts. Along its five input paths, the spatial profiles of the optical beams are either unchanged or converted to the profiles of LP11a, LP11b, LP21a, and LP21b modes, where a and b refer to the two spatially degenerate modes. Mode conversion is performed by sending each beam onto the appropriate location of 4-quadrant phase plates. The five beams corresponding to the five modes are combined and coupled into a 20km-long FMF which ends in the FM-EDFA described before.

The output of the few-mode EDFA is then coupled to the next 20km of FMF as depicted in Fig. 3.4.1. The signal is then demultiplexed by a 1×5 mode demultiplexer (DEMUX) having the same structure as the MUX, but operated in the reverse direction. The outputs of the DEMUX are connected to single mode fibers that lead to power meters and an optical spectrum analyzer (OSA).

Experimental Results

Twenty wavelengths, regularly spaced in the C-band and of equal power, are sent into each input port of the MUX. The power per spatial mode at the FM-EDFA input is set to -13dBm per mode, and the pump power is adjusted to 400mW. The optical spectrum is measured with a resolution of 0.1nm at the output of the DEMUX, and the amplifier gain profile is plotted in Fig. 3.4.4a for the LP01 mode, the LP11a+b modes (called LP11 group) and the LP21a+b (LP21 group). All the three mode groups present a relatively flat gain with an excursion between minimum and maximum of ~5dB each (it should be noted that no gain flattening filter is present in the setup). The gain in the middle of the C-band of the three mode groups is 17.1dB, 22.9dB, and 16.9dB respectively for LP01, LP11, and LP21. In this configuration the LP11 mode group experiences ~6dB more gain than the other modes, which makes the maximum differential mode group gain about 1dB higher than the maximum wavelength dependent gain excursion.

Noise figure (NF) as a function of wavelength is also calculated and plotted in Fig. 3.4.4b for the three mode groups. We observe a flat NF as a function of wavelength and mode (maximum excursion of ~2dB). Nevertheless, NF values are clearly worse than the ones measured for standard single mode EDFAs. We attribute this to a non-optimum signal coupling from the FMF into the EDF, in particular for the LP21 mode group. The EDF has also a much larger core diameter (10μm) compared to standard EDFs for single mode operation in order to ensure multi-mode compatibility but at the expense of EDFA noise performance.

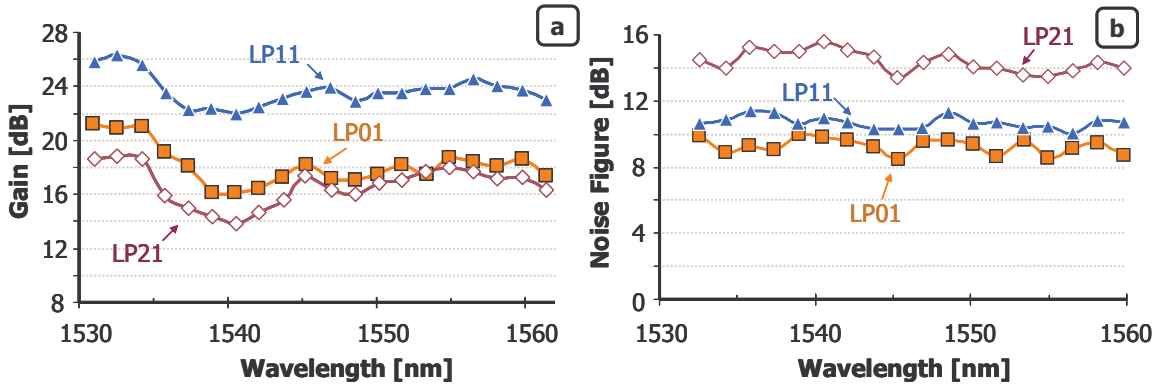

Fig. 3.4.4: Experimental results for FM-EDFA characterization. (a) Noise figure in dB as a function of wavelength. (b) Gain in dB as a function of wavelength.

In a second experiment, we remove 4 channels from the WDM comb that is injected into all the input ports of the MUX. We replace them by 5 other channels, which are now injected into only one of the 5 ports of the MUX through an additional coupler (not reported in Fig. 1 for clarity). This manipulation provides straightforward access to modal cross-talk with the help of the OSA. Fig. 3.4.5 reports the spectrum of the amplified signal at the output of the LP01 port of the DEMUX. The ratios between the peak powers at each port of the DEMUX, averaged when applicable over the two degenerate contributions, give the cross-talk levels. These levels have been measured without and with the amplifier, and are reported in Table 3.4.1a and in Table 3.4.1b, respectively. Please note that the precision was limited to integer dB values by the accuracy of the OSA. It appears clearly that all the modes suffer from a large amount of additional cross-talk due to the insertion of the amplifier in the line. In particular, the LP21 mode group tributaries show more power leaking from the LP11 mode group tributaries than from the LP21 tributaries themselves. We believe that one very important source of performance degradation (including reduced gain and large NF) for the LP21 mode is the anamorphosis induced by angled cleavings at both ends of the EDF. Flat cleavings would have prevented the phenomenon, but they would have triggered detrimental lasing of the cavity thereby created inside the FM-EDFA.

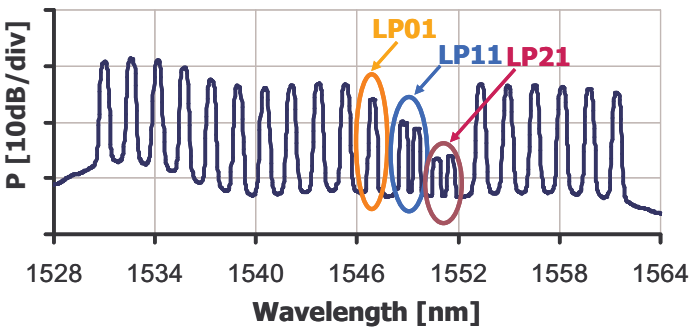

Fig. 3.4.5: Output spectrum of the amplified signal at the LP01 port of the DEMUX. The 5 channels in the middle are injected on one mode only for cross-talk measurements.

Table 3.4.1: (a) Crosstalk [dB] of the 40km line. (b) Crosstalk [dB] of the 40km line including few-mode amplifier in line.

a		Output		
		LP01	LP11	LP21
Input	LP01	0	-26	-25
	LP11	-11	0	-13
	LP21	-12	-15	0

b		Output		
		LP01	LP11	LP21
Input	LP01	0	-10	-9
	LP11	-2	0	+1
	LP21	-7	-6	0

Conclusions

We have reported a few-mode amplifier compatible with 5-mode operation. The 5 modes are the LP01, the two degenerate LP11 modes, and the two degenerate LP21 modes. The performance of the LP21 mode group is below theoretical expectations in terms of both gain and noise figure. The modal cross-talk has also been measured to be high. To allow for system experiments where modes are primarily demultiplexed in the optical domain, further progress is needed concerning this key parameter.

3.5 The Few-Mode Receiver

3.5.1 Receiver Front-End

Our receiver concept for MDM transmission is based on coherent. After the output of the mode-DEMUX, possibly followed by pre-amplification and filtering, each single mode fiber containing the signal of one spatial mode is injected into a coherent mixer. Depending on the design approach and on the spatial modes used for transmission of the respective signal, the electrical outputs of the coherent mixers can be used for joint digital signal processing in order to compensate for linear mode coupling resulting in intermodal crosstalk. Fig. 3.5.1 depicts the receiver architectures for the weakly coupled MDM approach (Fig. 3.5.1a) and for the strongly coupled MDM approach (Fig. 3.5.1b) using the example of 5 spatial modes (1 non degenerate mode and 2 times 2 degenerate modes).

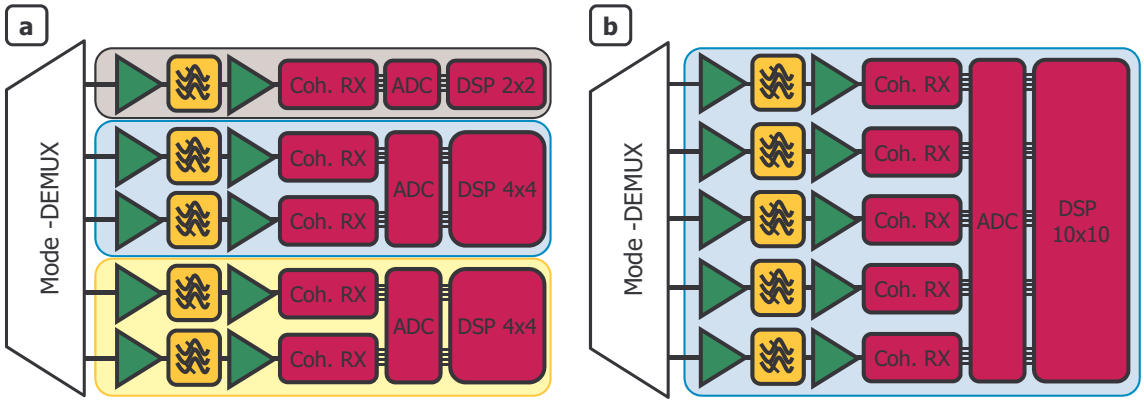

Fig. 3.5.1: Receiver architectures for MDM systems using (a) the weakly coupled approach and (b) the strongly coupled approach.

The coherent receivers are state-of-the-art coherent receivers as described in section 1.3.2. Subsequently, the analog to digital converters (ADCs) have to be synchronized for the modes that are intended to be processed by a joint DSP device. As a consequence, in our example, the weakly coupled approach results in three completely independent receiver chains, whereas in the strongly coupled approach all ADCs have to be synchronized and the digital signals are processed in a single 10x10 MIMO DSP device.

3.5.2 Digital Signal Processing

Most of the DSP blocks for MDM reception remain the same as the ones in the single mode coherent receiver described section 1.3.2 and depicted in Fig. 1.3.7. Resampling, chromatic dispersion compensation, carrier frequency estimation (CFE) and carrier phase estimation (CPE), and symbol identification can be performed individually for each polarization of each spatial mode. The main difference is in the block formerly called "polarization demultiplexing and equalization". It can now be used for decoupling not only the two polarizations but also the spatial modes, if physical demultiplexing cannot assure a sufficiently low level of intermodal crosstalk.

As mentioned in section 1.3.2, the polarization demultiplexing device can be considered as a 2x2 MIMO processor. For allowing mode-separation, MIMO processing has to be generalized to the order N, with N being 2 times the number of processed spatial modes. The factor of 2 originates from the fact that each spatial mode contains 2 polarization modes. Fig. 3.5.2 depicts the extension of the filter structure from 2x2 MIMO to 4x4 MIMO. The principle remains unchanged: each MIMO input is injected into N finite impulse response (FIR) filters. Then N FIR filter outputs, one coming from each input, are summed up to form N MIMO outputs. The filter taps of the FIR filters are continuously updated in order to adapt to dynamic changes of the transmission channel, such as polarization rotations or rotations of the degenerate modes with respect to each other. For our case using 4x4 MIMO with relatively short FIR filters (~15 taps) we found that the updating algorithm of the filter taps can remain the same as for simple polarization demultiplexing being the constant modulus algorithm (CMA). However, it should be noted that the CMA tends to converge to the more powerful signal tributaries. In particular, in presence of multiple inputs it is necessary to correctly initialize the filter taps for allowing the detection of all the polarization/mode tributaries. Failing to do so would cause different outputs converging to the same input. We employed a 1-tap blind source separation algorithm [128], and we confirmed the correct detection by identifying the different polarization/mode tributaries based on the injected bit patterns.

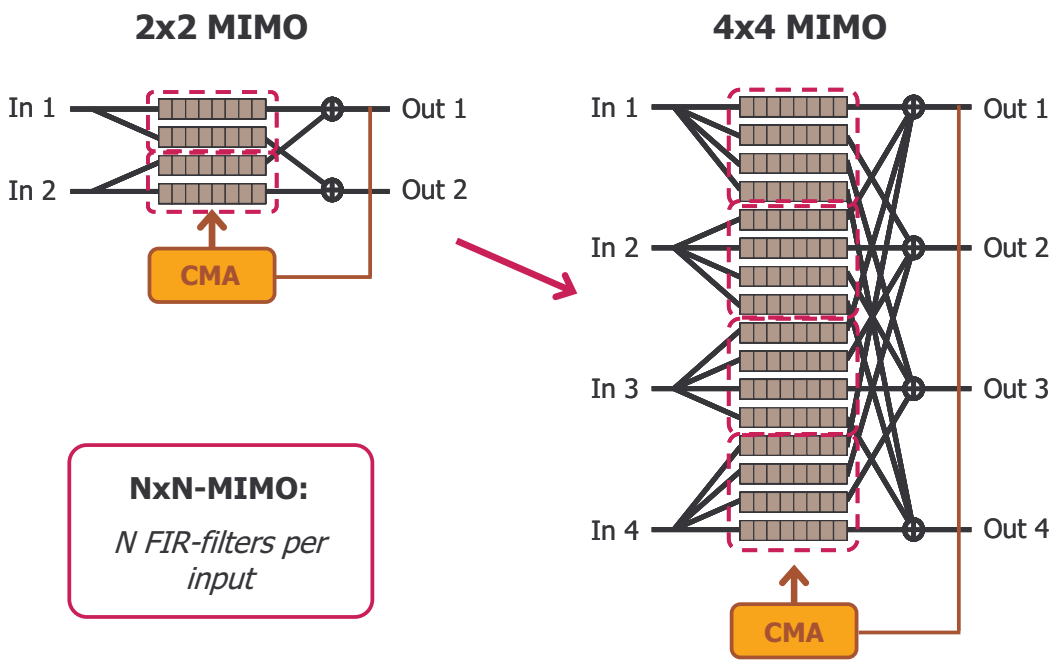

Fig. 3.5.2: Increasing MIMO order

MIMO processing is required for the separation of two degenerate spatial modes, for the same reason as it is required for polarization demultiplexing. Degenerate modes are rotated in an unpredictable, fluctuating way during transmission, whereas the physical mode-DEMUX can only separate them along two static spatial axes. Therefore, 4x4 MIMO processing can be used to compensate for rotations of two degenerate spatial modes and for rotations of their respective two polarization components at the same time. Furthermore, it has been demonstrated that MIMO processing is also very powerful for the separation of spatial modes that are not degenerate [94], [108], [129].

The main problem, when extending the order of MIMO processing is the increasing calculation complexity. The increasing number of FIR filters can be deduced from Fig. 3.5.2. For 2x2 MIMO it is *4* for 4x4 MIMO it is *16* and so it grows continuously with N to a total number of N^2 FIR filters. N^2 filters for the whole MIMO DSP device correspond to N filters per MIMO input. In other words, total MIMO DSP complexity scales quadratically with capacity and so the complexity per bit scales linearly with the capacity.

Beside the number of FIR filters, also the length of each filter is an important point to consider. The required minimum filter length is proportional to the highest accumulated DMGD between the jointly processed modes [94], [108], [129]. Thus it scales linearly with the transmission distance and with the DMGD coefficient between two modes. Generally, the DMGD between two modes of different order can be a lot higher than the DMGD between two degenerate modes (see section 3.2.1.4). Hence, considering the two design approaches presented in section 3.1.2, it can be noted that extending the MIMO processing to the non-degenerate modes not only increases the number of FIR filters, but also leads to a significant increase of the filter length. It remains to be seen how far DMGD can be decreased for a higher number of modes, in order to reduce this effect. Another interesting approach to deal with the problem of FIR filter length has been presented in [105]. Here two different FMF types with opposite DMGD coefficients are concatenated and so the accumulated DMGD is reduced resulting in a shorter filter length.

Using the model of the LP-modes, two degenerate modes have exactly the same propagation constant, and so for demultiplexing FIR filter length is no problem at all.

However, in more detailed models, the propagation constant of two modes that are considered degenerate in the LP-model is slightly different, leading to a DMGD in the order of magnitude of ~25ps/km. For 100Gb/s PDM-QPSK systems, this corresponds to a delay of ~1 symbol per km. Compared to the current lengths of ~10 FIR filter taps in the polarization demultiplexing block of a single mode coherent receiver this requires a tremendous increase in FIR filter length for the envisaged transmission distances of at least several hundreds of kilometers. However, some of our experimental studies have produced astonishing results. We measured the Q²-factor as a function of the number of taps in the FIR filters, first for a reference single mode signal in back to back configuration and then for two signals modulated on two degenerate modes (LP11a+b) and transmitted over 40 km of FMF. The results are depicted in Fig. 3.5.3. Interestingly both curves are very similar with a slight optimum at 9, respectively 11 taps, and with an almost constant Q²-factor between 9 and 15 taps (the taps were spaced by $T_S/2$). We already double checked these results for longer FIR filter lengths and for longer transmission distances. But until now, we couldn't find any hint for a performance improvement with a higher tap count, even after transmission over 80 km. Hence, the subject is still under investigation by my colleagues.

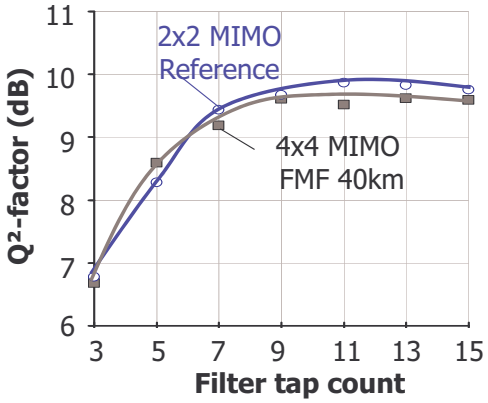

Fig. 3.5.3: Q²-factor as a function of the FIR filter length for a single mode back to back reference (2x2 MIMO) and for a transmission of two degenerate modes (LP11a+b) over 40 km of FMF (4x4 MIMO)

3.6 Conclusion of Chapter 3

In chapter 3 I described the architecture of an MDM transmission system, its main newly arising limitations, as well as the most important new elements compared to a "classical" single mode transmission system. These elements are the FMF, the mode-MUX/-DEMUX, the few-mode amplifier and the few-mode receiver. Each of them was investigated in this work using theoretical and experimental methods.

Concerning the system design it can be observed that two approaches have been developed to deal with the problematic combination of linear mode coupling and DMGD. The so-called "strongly coupled" approach tries to lower the DMGD in order to be able to compensate for mode coupling by MIMO DSP with acceptable complexity. The so-called "weakly coupled" approach tries to minimize mode coupling in order to be able to demultiplex modes mainly physically without extensive use of DSP. In this work we followed the weakly coupled approach since it relaxes the constraints on fiber design concerning DMGD and thus might be more easily scalable to a higher number of modes.

The FMF was investigated concerning its nonlinear behavior with numerical simulations using a newly developed theoretical model. The simulations led to the promising result that DMGD is supposed to highly suppress nonlinear interactions between different modes. Afterwards, a practical realization of an FMF has been presented (the fiber was realized by our STRADE project partner Prysmian) followed by some studies on linear mode coupling. However, experimentally characterizing a fiber with respect to linear mode coupling is quite involved and so this topic remains open for further investigations.

Then I addressed the mode-MUX and –DEMUX. First I explained the theoretical concept of mode multiplexing and demultiplexing based on mode conversion with Fourier Optics. Afterwards I showed some numerical estimations about the potential performance of such a device. Finally, I presented two practical realizations of a mode-MUX/-DEMUX; one based on programmable, reflective phase masks on an LCoS panel realized by our STRADE project partner Kylia, and another one based on static, transparent phase plates realized by ourselves at Bell Labs.

A few-mode amplifier has been realized in cooperation with our STRADE project partners from the Université Lille 1, making use of a few mode erbium doped fiber with a special ring-doped profile. We characterized the amplifier concerning gain, noise figure and mode coupling. It turned out that optimizing all of these parameters at the same time was not possible yet and that additional efforts have to be made to better understand the occurring phenomena and to improve the performance.

Finally I addressed the receiver architecture for MDM transmission systems looking at its key novelty, the MIMO DSP device. It can be very powerful in the demultiplexing of different spatial modes. However its complexity and thus its hardware requirements for potential real-time processing are critical, especially when increasing the number of modes and/or the transmission distance.

Chapter 4: Mode Division Multiplexed Transmission Experiments

During my work for this thesis our group performed several pioneer mode division multiplexed transmission experiments, which were also the results of the successful collaboration with our project partners from the "STRADE" project, exactly as the work presented in Chapter 3. Together with my colleague Massimiliano Salsi, I was mainly in charge of these experiments and conducted a major part of the work. In this final chapter I will describe the experiments and discuss their results.

4.1 Two-Mode Transmission over 40km using Programmable Mode-Converter based on Liquid Crystal on Silicon Technology

Our first MDM transmission experiment was realized in January 2011 and published at the postdeadline session of the optical fiber conference (OFC) 2011 as one of the first experimental MDM demonstrations together with [90], [91], [93]. We made use of 40 km of the FMF described in section 3.2.2 and of the LCoS based mode-MUX/-DEMUX described in section 3.3.3.1, which theoretically could allow us to transmit up to 4 modes at a time and to detect 2 of them. However, because of insufficient quality in mode conversion we only achieved a successful transmission of 2 spatial modes at a time, namely the LP11a and the LP11b mode.

In a second step, we inverted mode-MUX and –DEMUX allowing us only injecting two spatial modes, but in exchange using an additional coherent receiver for higher order MIMO processing. In this way we could confirm that high mode coupling in mode-MUX and DEMUX was a main reason for the poor performance.

4.1.1 Experimental Set-Up

In our set-up, depicted in Fig. 4.1.1, the light from a laser at 1533.47nm is passed into an integrated transmitter. The transmitter uses a serializer to produce four 28Gb/s electrical pseudo-random signals of length 2^{15}-1, each shifted by 8192 bits, which feed a quad-driver and a polarization-multiplexed nested Mach-Zehnder modulator. It generates a data stream modulated at 112 Gb/s PDM-QPSK, including 12% protocol and FEC overhead. This stream is replicated along two fiber paths decorrelated by several thousands of symbols using an SMF patch-cord, and fed to two optical amplifiers,

connected to two of the four inputs of a mode multiplexer where they are converted into the LP11a and LP11b modes. Another independent PDM-QPSK transmitter is used for the generation of the signal transmitted on the fundamental mode LP01 and connected to another port of the mode multiplexer. However, not more than two transmitters are used at once.

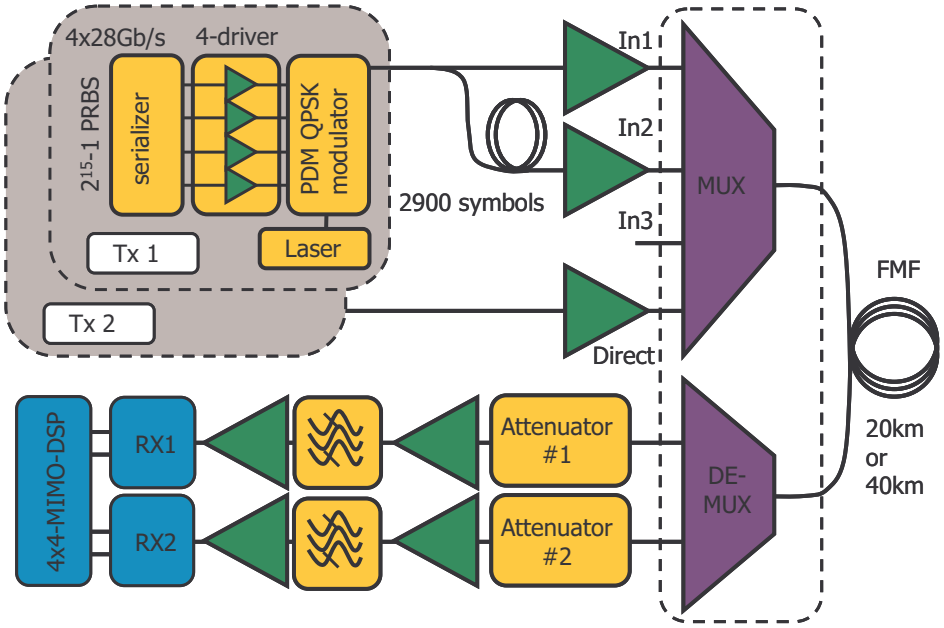

Fig. 4.1.1: Experimental Set-up of first mode-division multiplexed transmission using LCOS based mode-multiplexer and –demultiplexer.

The mode-multiplexer and -demultiplexer used in this experiment was the LCoS based one described in section 3.3.3.1. As already mentioned, its output was realized by using a pigtail fiber supporting up to 3 modes (LP01 as well as the two degenerate LP11 modes 'a' and 'b') for practical reasons. This pigtail was spliced to either 20 km or 40 km of the prototype FMF described in section 3.2.2. After transmission, the output of the FMF is connected to the mode demultiplexer, again by splicing it to a pigtail of the same type as at the output of the mode multiplexer. In the mode demultiplexer, two arbitrary modes of the FMF can be extracted and converted back into LP01 before they are injected into two SMFs.

With this setup we investigated several configurations: single mode transmissions (LP01 only) and MDM transmission (LP11a + LP11b or LP01+LP11b). In all configurations, the power into each receiver is varied using dedicated attenuators in order to adjust the optical signal to noise ratio (OSNR) when measuring the performance. The power at the outputs of these attenuators is from now on called "received power".

The coherent receivers incorporate optical preamplifiers and four balanced photodiodes in a polarization diversity configuration. Sampling is performed with two real-time oscilloscopes (one per receiver), which have an analog bandwidth of 16GHz and are synchronously triggered. When the LP01 mode is detected a constant phase mask and a single receiver are used. Whereas, when the phase masks are set to select LP11a and LP11b, two receivers are used to perform joined signal processing. The receiver set-up is described more in detail in section 3.5.

4.1.2 Results

The first experimental results have been recorded after transmission over 20km of FMF fiber. To ease comparisons, we chose to focus on the same received power in all configurations namely -31dBm. In Fig. 4.1.2a, the fundamental mode LP01 shows 1.1dB Q^2-factor penalty after 20km compared to the reference back-to-back performance measured before with the same Tx and Rx in a pure single mode set-up. After the same distance, the average Q^2-factor of the LP11a + LP11b modes detected with the 4x4 MIMO receiver is reduced by another 0.6dB with respect to the LP01 mode. After 40km of FMF, the modes LP11a + LP11b are further degraded, but by no more than 1.1dB. The values represented in Fig. 4.1.2a are averaged over all the received mode/polarization tributaries (2 for the LP01 and 4 for the LP11). Fig. 4.1.2b depicts the actual performance of all mode/polarization tributaries of LP11. The Q^2-factors of mode LP11a-polarization X appear significantly lower (by typically 2.5dB) than the other Q^2-factors. This is attributed to degraded characteristics of our mode-MUX/-DEMUX along one polarization. This degradation increased over the measuring time, which gets very clear by the fact that the point at a received power of -31.6 dBm was the first to be measured before increasing power until -27.6 dBm and then restarting at -34.6 dBm and again increasing received power up to -32.6 dBm.

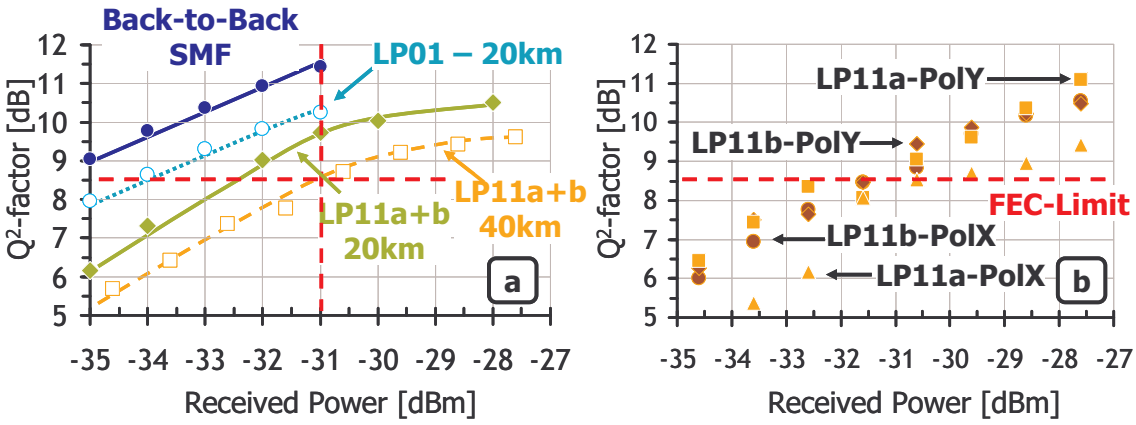

Fig. 4.1.2: Experimental performances for separated transmission over either the LP01 mode or over the LP11a+b modes as a function of received power. (a) Comparison between different configurations. (b) Detailed performance measurements of all polarization and degenerate mode components for LP11a+b transmission over 40km.

Further insight on intermodal crosstalk can be obtained when propagating both LP01 and LP11b modes, as depicted in Fig. 4.1.3. We kept the LP11b power constant at -32dBm at the receiver and varied the power of the LP01 mode. When the LP01 mode reaches -36dBm, 1dB Q^2-factor penalty can already be observed as a result of linear crosstalk. The LP01 mode should reach a received power of -19dBm to yield a reasonable 10dB Q^2-factor, i.e. a 12dB higher power than without the LP11b mode (see the straight line "LP01 only" in Fig. 4.1.3). This result suggests that three-mode propagation involving LP01, LP11a, and LP11b would require progress on the key components such as mode-MUX and –DEMUX or FMF.

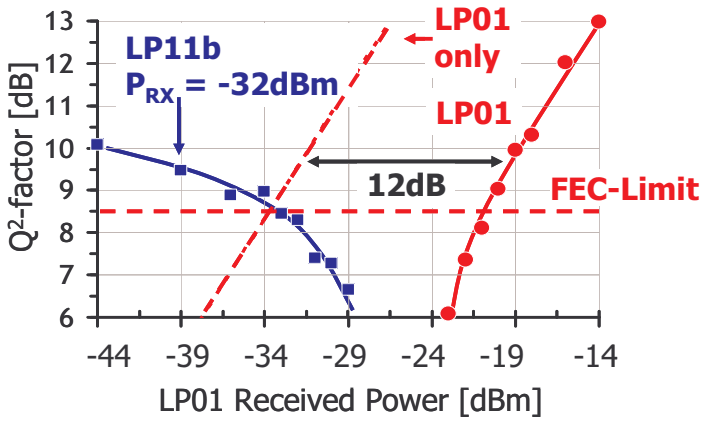

Fig. 4.1.3: Experimental performance for simultaneous transmission over the LP01 mode and over the LP11a+b modes as a function of received power.

4.1.3 Intermodal Crosstalk Mitigation using DSP

The most likely reason for the transmission penalties observed in the few-mode configurations compared to the single mode configuration is intermodal crosstalk / linear mode-coupling. Intermodal crosstalk, in turn, can either occur during transmission through the few-mode fiber or in the mode-MUX/-DEMUX. Since theory predicted low mode coupling in our FMF, we supposed the mode-MUX/-DEMUX to be the main source of intermodal crosstalk.

In order to verify this hypothesis and to find a way to mitigate the impact of intermodal crosstalk, we described our transmission system by the model depicted in Fig. 4.1.4a. In this model we consider the case, that two signals shall be transmitted over the two modes LP11a and LP11b. Hence, in the mode-MUX, two signals coming from SMF inputs are spatially converted into LP11a and LP11b modes and combined into the FMF. However, due to imperfect mode conversion, some energy is also coupled into the LP01 mode of the FMF. This signal component propagates faster than the LP11a and LP11b modes and so it arrives earlier at the mode-DEMUX. There, the signal on each of the three spatial modes shall be decomposed into a separate SMF, but also during this step, imperfections in the device make that the desired signal in each output is mixed with disturbing energy from the other propagated modes.

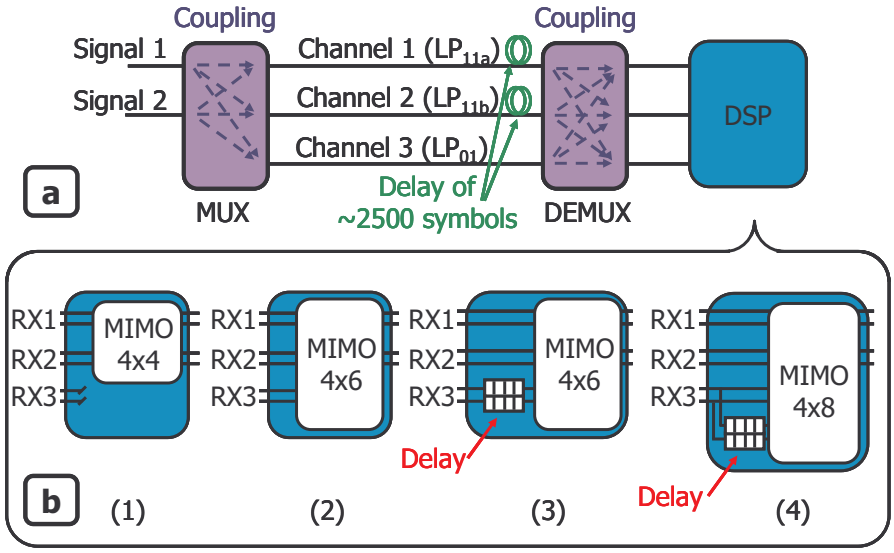

Fig. 4.1.4: (a) Simplified system model for mode coupling in mode-multiplexer and –demultiplexer. (b) Different DSP schemes for intermodal crosstalk mitigation.

Taking this model as a basis, it is obvious that the results for LP11a+b transmission in Fig. 4.1.2a suffer from penalties compared to single mode transmission, since only a maximum of two receivers was used to acquire data for digital signal processing. Hence, the information transferred to the third propagated mode was lost. However, adding a third coherent receiver would allow to recover the energy of all propagated modes and to see if appropriate DSP algorithms can benefit from this energy and improve the system performance. Possible DSP structures are depicted in Fig. 4.1.4b. The first one, "MIMO 4x4", is the same as already used before, taking only into account the received signals at the mode-DEMUX output coming from the LP11a and LP11b modes. The second and third one use MIMO 4x6 equalizers, thereby additionally benefitting from the signal of the newly added third coherent receiver. At this point, it is important to remember that the propagation on the fundamental mode is faster, leading to a DMGD of ~2500 symbol times between the modes LP01 and LP11 after 20km. This is why we propose two different 4x6 MIMO equalizers - one with and one without a digitally-implemented delay in this range at their inputs, which means that the cross-talk generated respectively at the receiver or at the transmitter is considered. The fourth and last configuration contains a 4x8 MIMO equalizer where both cases with and without delay are exploited at the same time, thus taking into account cross-talk terms generated in both mode-MUX and mode -DEMUX.

In order to realize these concepts, we slightly modified the experimental set-up of Fig. 4.1.1 and the new set-up is depicted in Fig. 4.1.5. We essentially used the configuration for transmission over 20 km of FMF but inverted mode-MUX and mode-DEMUX and so having now the possibility to inject only a maximum of two SMF signals into the mode-MUX but to receive up to four signals from the mode-DEMUX. This allowed us to add a third coherent receiver chain and to use the three received signals in offline processing implementations of the four described DSP structures. Hereby all MIMO algorithms are based on the principle of the algorithm explained in detail in sections 3.5.2 and 1.3.2. The 4x6 and the 4x8 equalizers are 6x6 and 8x8 equalizers using only 4 outputs. Passing from 4x4 MIMO two 6x6 MIMO and to 8x8 MIMO can be done straight forward in analogy to the transition from 2x2 MIMO to 4x4 MIMO.

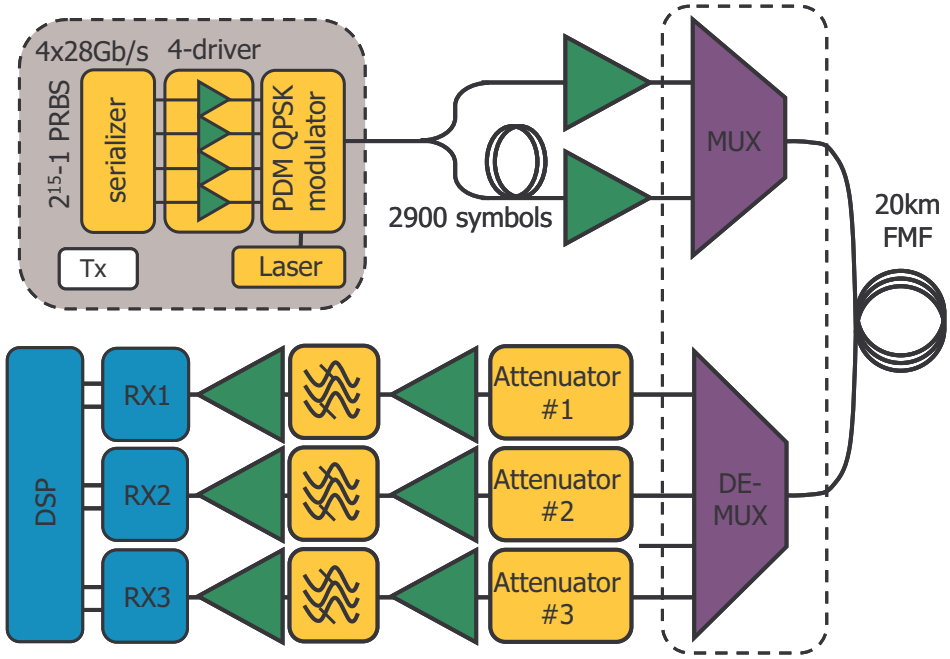

Fig. 4.1.5: Experimental Set-up for MDM transmission using LCOS based mode-multiplexer and –demultiplexer and a third coherent receiver in order to apply digital mitigation of intermodal crosstalk.

We then tested the different MIMO configurations described in Fig. 4.1.4b. In Fig. 4.1.6a we can observe the resulting Q^2-factors of the standard 4x4 case, which is a replica of the curve "LP11a+b 20km" in Fig. 4.1.2a, the Q^2-factors of two 4x6 MIMO algorithms using the third input of the demultiplexer with and without the digitally-generated delay, carefully tuned for optimal Q^2-factor, and the Q^2-factors of the 4x8 case using at the same time the third receiver's sequences with and without delay. The results show that increasing the number of detectors for the MIMO algorithm can improve the performance. The two 4x6 MIMO cases have similar Q^2-factors, which suggests that the amounts of inter-modal cross-talk generated at the transmitter and at the receiver are comparable. Finally, the 4x8 MIMO algorithm gives the best performance, especially for higher received powers where the cross-talk impact is more evident because of the higher signal to noise ratio. Compared to the 4x4 case, the use of 8 DSP-inputs increases the Q^2-factor by 1dB. This proves that the additional imperfections coming from the mode conversion employed in the MDM case can be mitigated by post-processing, at the cost of additional hardware and a more complex signal processing.

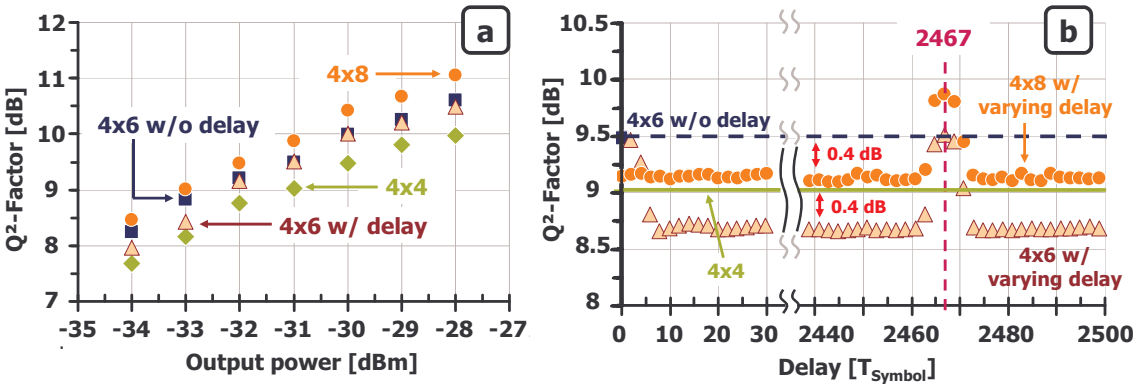

Fig. 4.1.6: Experimental performances for transmission over the LP11a+b modes with third coherent receiver and higher order MIMO DSP. (a) Performances for different MIMO DSP structures for varying output power. (b) Performances for different MIMO DSP structures for varying length of digital delay compensation.

Each FIR filter in the MIMO equalizer has a fixed number of taps (13 T/2-spaced taps in our case, see section 3.5.2 for more details), which in our case using a 112Gb/s PDM-QPSK signal corresponds to ~200ns and lets us tolerate a delay between different inputs inferior to this duration. But since the accumulated DMGD is much higher, the last two cases of Fig. 4.1.4b employ a digital delay line before the input of the MIMO equalizer, in order to combine signal parts that exceed this tolerable delay. We tested the dependence of the Q²-factor on the delay value in the DSP for the 4x6 and the 4x8 case at -31dBm received power and report the results in Fig. 4.1.6b. In the 4x6 case, there are two delay values which maximize the performance, namely zero and 2467 symbols. When departing from these two values by more than 5 symbols, the Q²-factor drops to a constant minimum value, which is even below the Q²-factor in the 4x4 case. The existence of these two optimum delay values indicates that there is meaningful information in the signal portions that have leaked into the LP01 mode at two local cross-talk sources being the mode converters at the receiver (delay around 0 symbols) and at the transmitter (delay around 2467 symbols). By providing the correct timing alignment, the MIMO algorithm can exploit the information contained in the third input and the Q^2-factor can be improved by 0.5dB. If, however, the timing alignment is too imprecise, the equalizer cannot work correctly and the additional input even generates penalties of ~0.4dB. We finally varied the delay for the 4x8 MIMO case where we confirmed that a delay of 2467 symbol times corresponds to the DMGD between the modes LP01 and LP11, as it maximizes the performance. Interestingly, comparing the 4x8 case to the two optimized 4x6 cases shows the same relation as when comparing 4x6 case and 4x4 case: a maximum Q²-factor gain of 0.5dB and Q²-factor penalties of 0.4dB at misalignment.

4.2 Five-Mode Transmission over 40km with Low DSP-Complexity using High Performance Mode Converters

New challenges arise as the number of modes grows: on the one hand, the increased number of modes leads to a higher number of potential sources for linear or nonlinear mode coupling, and on the other hand, the higher order modes that need to be used in

this case have a more complex spatial distribution making them harder to generate. Here, we report the first successful transmission over five spatial modes.

One important concern when expanding MDM transmission over a larger number of modes is the scalability of digital signal processing. Single-mode coherent receivers use 2x2 MIMO to handle polarization diversity. In transmission systems over *N* modes, MDM receivers need 2Nx2N MIMO to achieve mode demultiplexing, if mode coupling is high and is to be compensated digitally. This can rapidly require tremendous processing power (scaling quadratically with *N*). Here, we assume and make sure that mode coupling is contained, such that only 4x4 MIMO is needed regardless of the value of *N>3*, to handle polarization diversity and mode degeneracy only. Low mode coupling is achieved during transmission by employing the FMF described in section 3.2.2 having high differential mode group delay and large effective index differences between any two non-degenerate modes, and during mode-multiplexing and -demultiplexing thanks to phase plates designed specifically to operate with five modes.

4.2.1 Experimental set-up

In the first part of our set-up, depicted in Fig. 4.2.1, the light from a laser at 1542.54nm is passed into an integrated Polarization Division Multiplexed Quadrature Phase Shift Keying (PDM-QPSK) transmitter. It generates a data stream at 112Gb/s, including 12% protocol and FEC overhead, which is replicated along five fiber paths into five streams referred to as mode channels in the following. They are decorrelated by several hundreds of symbols using standard SMF patch-cords, and fed to five optical amplifiers, connected to the five inputs of the mode-MUX.

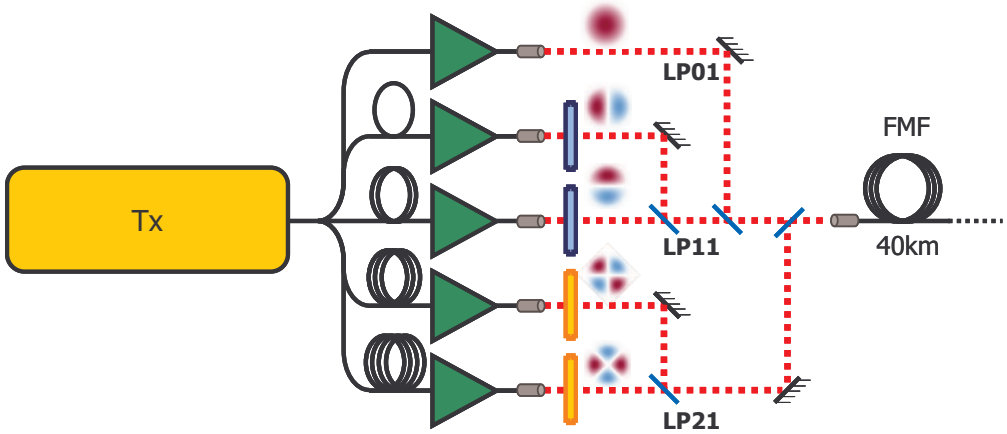

Fig. 4.2.1: Experimental Set-up for 5-mode MDM transmission using mode-multiplexer and –demultiplexer with transparent phase plates, transmitter side.

The mode-MUX was realized in free-space optics with transparent phase plates for mode conversion as described in section 3.3.3.2. Along its five input paths, the spatial profiles of the optical beams are either unchanged or converted to the profiles of LP11a, LP11b, LP21a, and LP21b modes, where a and b refer to the two spatially degenerate modes. The five beams corresponding to the five modes are then combined and coupled into 40km of the FMF described in section 3.2.2. This prototype FMF supports up to 6 modes (LP01, LP02 and the four aforementioned modes) with low attenuation (0.22dB/km) and large effective area (>120μm^2). The differential mode group delay (DMGD) per unit length between LP01 and LP11 is 4.35ps/m (4872 symbols after 40km at 28GBaud) and 8.7ps/m between LP01 and LP21, while the effective-index difference

is $>10^{-3}$, which minimizes mode coupling [106]. At the receiver side the FMF is connected to the DEMUX as depicted in Fig. 4.2.2.

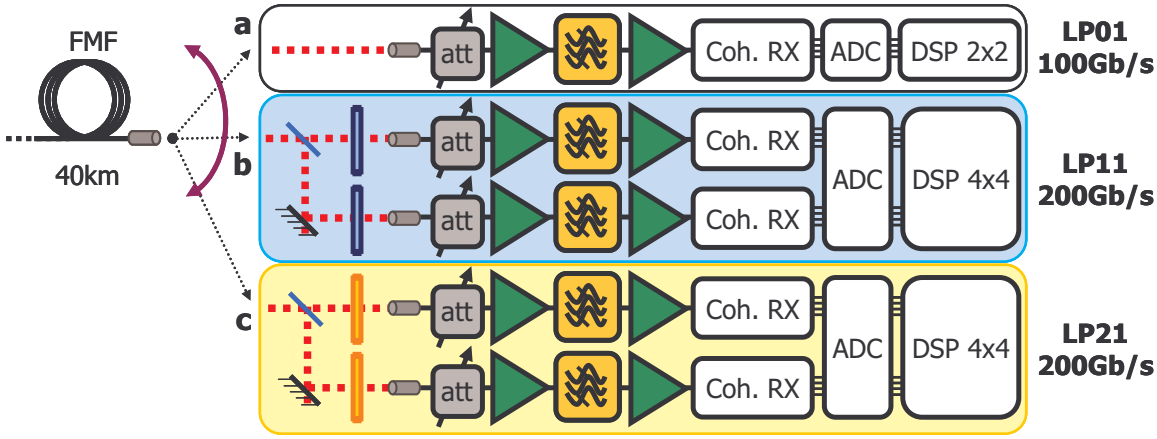

Fig. 4.2.2: Experimental Set-up for 5-mode MDM transmission using mode-multiplexer and –demultiplexer with transparent phase plates, receiver side.

The DEMUX was also based on free-space optics. After a beam-splitter, two phase-plates, similar to those of the MUX, could be inserted to filter out the desired (degenerate) modes. The plates convert the full set of modes from the FMF to another set, depending where they were hit by the light beam coming through. However, out of all the converted modes, only the one which matches the LP01 mode can propagate further in the collimated SMF pigtails that follow, and is therefore filtered out. After demultiplexing, the two remaining optical signals were passed through variable attenuators, dual-stage amplifiers incorporating band-pass filters, and sent into a pair of coherent mixers, attached to balanced photodiodes. The photodiodes were connected to two real-time oscilloscopes (16GHz bandwidth) with synchronized triggers, delivering four complex data series which were processed off-line in a computer. The data series were processed jointly in order to discriminate between the degenerate mode channels and the two polarization tributaries using a 4x4 MIMO equalizer. In contrast, the LP01 channel required only one input of the mode DEMUX and a 2x2 MIMO to discriminate the polarization tributaries. The equalizers were the same as described in section 3.5.2 based on the CMA. After detection, we performed identification of polarizations and of modes by comparing the delays of the different tributaries, in order to ensure that the four modes were correctly recovered. We then counted errors, computed the bit error ratio and converted it into Q^2-factors.

By detecting the modes sequentially under the same conditions, we emulated the reception of all 5 modes by 5 receivers at the same time. The difference to a fully equipped system is visualized in Fig. 4.2.3. There, two additional beam splitters would be required in the DEMUX for extracting all the modes at once. Hence, the received power would be lower by 3 to 6dB with respect to our lab setup, depending on the number of additional beam splitters in the path of the respective mode. We therefore provisioned 6dB margin in received power for claiming a successful 5-mode transmission.

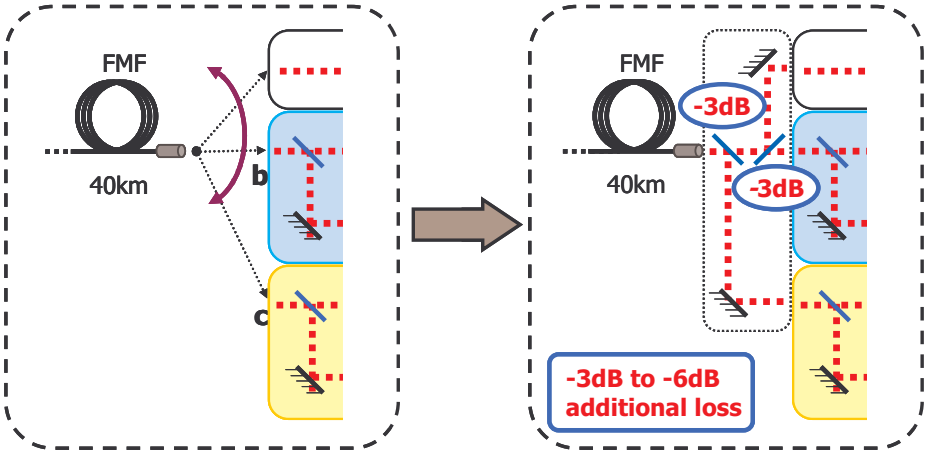

Fig. 4.2.3: Origin of additional loss in mode-demultiplexer when using 5 mode-outputs at the same time.

4.2.2 Results

The first experiments have been carried out with a small section of FMF (~10m) between mode-MUX and mode-DEMUX to characterize these two devices in a back-to-back configuration. To do so, we determined the amount of linear mode coupling in our setup by performing a series of power measurements. For each input mode / pair of degenerate input modes at the MUX side we firstly obtained a reference output power when extracting the same mode / pair of degenerate modes at the DEMUX side. Then we measured the output power when extracting the other modes at the DEMUX side and noted the ratio with respect to the reference output power. The ratios in dB are shown in Table 4.2.1a (which is actually the same as Table 3.3.4). Note that the modes LP11a and b as well as LP21a and b were injected and extracted together to obtain a result that is independent of possible rotations of the spatial field distribution. Their relative power had been adjusted previously for identical output power. Taking a look at Table 4.2.1a, we observe that the worst case can give a crosstalk up to -16.1 dB. The same measurements have then been repeated with 40km of FMF and measurement results are reported in Table 4.2.1b. By comparing these numbers with the back-to-back results of Table 4.2.1a we can estimate the mode coupling added by the transmission fiber and the splices, observing that the worst transferred power value goes up from -16.1dB to -10.5dB.

Table 4.2.1: Intermodal crosstalk ratios in dB. (a) Measured with mode-MUX/-DEMUX only (connected through ~10 m of FMF). (b) Measured with mode-MUX/-DEMUX and 40 km of FMF in between.

a **MUX/DEMUX only**

Tx \ Rx	LP01	LP11a+ LP11b	LP21a+ LP21b
LP01	0	-22.3	-20.2
LP11a+b	-23.6	0	-16.1
LP21a+b	-28	-16.1	0

b **MUX/DEMUX + 40km FMF**

Tx \ Rx	LP01	LP11a+ LP11b	LP21a+ LP21b
LP01	0	-18.3	-23
LP11a+b	-15.1	0	-13.3
LP21a+b	-16	-10.5	0

The transmission experiment over 40km has been performed by sending all 5 mode channels into the mode-MUX. A first important step was to adjust the relative input powers of the different signals so as to equalize their performance. The Q^2-factors of all 5 mode channels have been measured for numerous combinations of input powers and the optimum combination was defined as the set of reference input powers. Here again, the power ratio between the pairs of degenerate modes remained constant. We plotted the Q^2-factors for every mode channel, when varying the input power of either only LP01 (Fig. 4.2.4a), only LP11 (Fig. 4.2.4b) or only LP21 (Fig. 4.2.4c) from -4dB to +4dB around the reference power. We observe that each mode channel's Q^2-factor increases when increasing its input power whereas the other Q^2-factors decrease. Furthermore, the slopes of the decreasing curves correlate with the crosstalk values of Table 4.2.1b. E.g., when increasing the input power of the LP01 mode channel, the Q^2-factors of the other mode channels in Fig. 4.2.4a decrease slower than the decreasing Q^2-factors in Fig. 4.2.4b and Fig. 4.2.4c since the crosstalk values in line one of Table 4.2.1b are the lowest in the system.

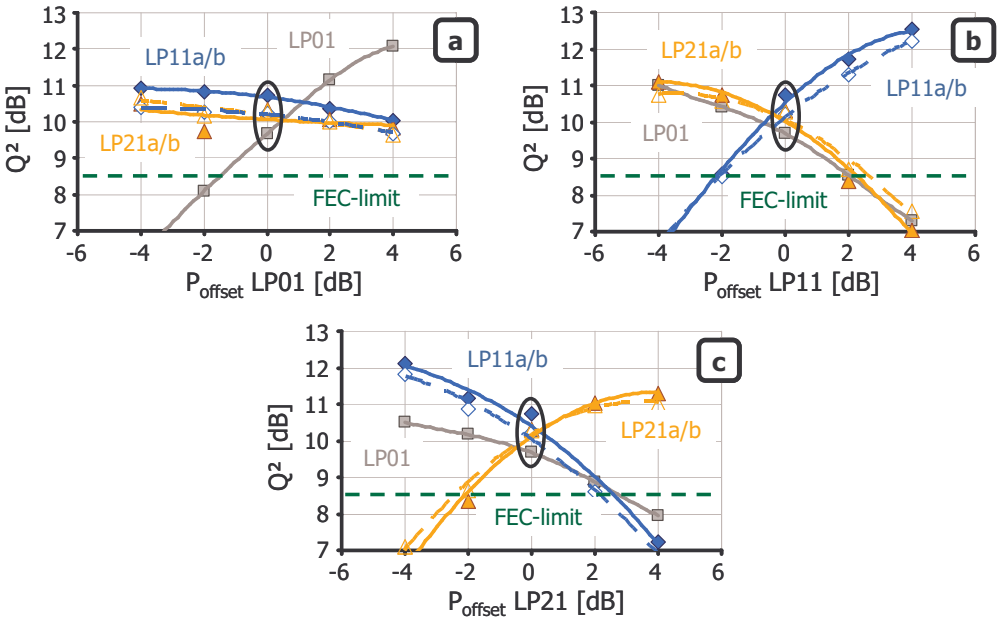

Fig. 4.2.4: Q^2-factor measurement of the modes LP01, LP11 and LP21 for varying input power. (a) Of the LP01 mode. (b) Of the LP11 modes, and (c) Of the LP21 modes.

The set of reference input powers for the mode channels has then been selected to measure Q^2-factors for all modes as a function of received power. It is measured at the outputs of the attenuators directly after the DEMUX and it is proportional to the received OSNR. Q^2-factors for the 2 polarization tributaries of the 5 mode channels LP01, LP11a, LP11b, LP21a and LP21b are plotted in Fig. 4.2.5. For very low input power (around -36dBm), a steep curve is observed because ASE noise degradation becomes the predominant limitation. It is almost parallel to the reference back to back performance with an OSNR-penalty of ~4dB. For higher receiver power, Q^2-factor improvement versus received power becomes much reduced because the system performance becomes limited by intermodal crosstalk.

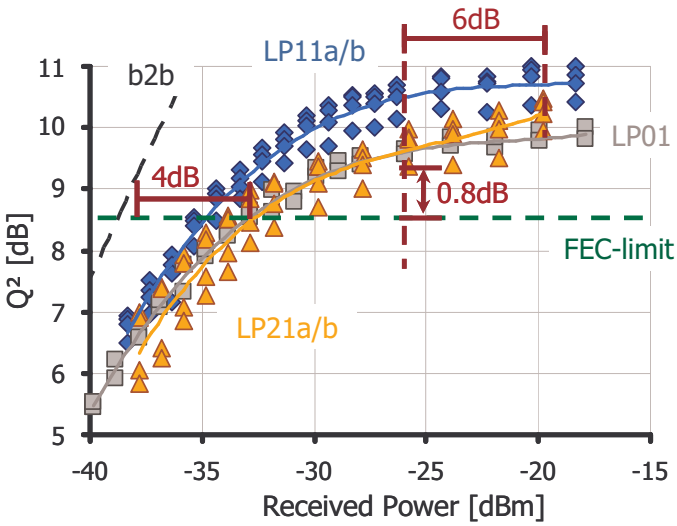

Fig. 4.2.5: Q^2-factor measurement of the modes LP01, LP11 and LP21 for varying receiver power at the optimized input power combination.

After 40km transmission, Q^2-factors above the FEC limit at 8.5dB are measured simultaneously for mode LP01, LP11 and LP21. Even when taking into account the 6dB OSNR-margin to allow the simultaneous reception of all 5 mode channels, the worst polarization tributary is still 0.8dB above the FEC limit. This shows that error free transmission could be obtainable after FEC decoding.

4.3 Mode division multiplexed transmission over 40 km including in-line few-mode amplification

During the FM-EDFA design presented in section 3.4, we were facing the problem of reflections at the input and at the output of the EDF, as it can also occur in single mode EDFAs. The reflections transform the fiber into a structure similar to a laser cavity and as soon as the gain in the EDF exceeds the outgoing power at each end of the EDF, the amplifier starts lasing and normal operation is impossible. Even at slightly lower gain values, performance is already penalized by this effect. Hence, we had to find a way to suppress reflections at EDF input and output. In single mode fibers, this can easily be realized by cleaving the EDF with an angle other than 90° with respect to the propagation axis. Therefore we also applied this technique in our FM-EDFA but as observed in Table 3.4.1, this induced very strong intermodal crosstalk. Other possibilities such as antireflection treatment of both fiber ends are imaginable but were not available to us at that time.

So in order to do a transmission experiment with crosstalk values that allow Q^2-factors around the FEC limit we had to find a compromise between reflections at the EDF ends and between intermodal crosstalk originating at the angled cuts. In Fig. 4.3.1 the resulting FM-EDFA design is depicted.

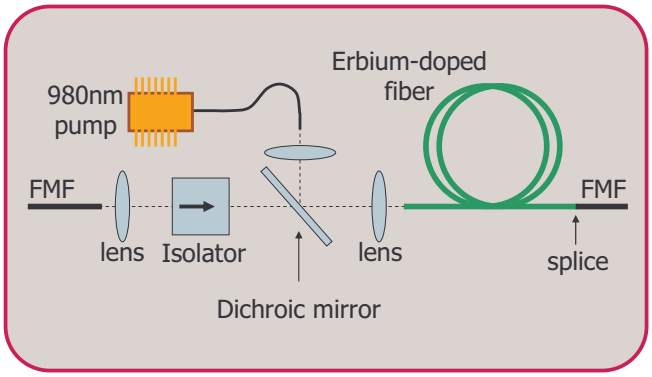

Fig. 4.3.1: Scheme of the few-mode erbium doped fiber amplifier designed as a compromise between intermodal crosstalk and gain/NF.

Instead of two angled cleavings at both sides of the FM-EDF as in the design of Fig. 3.4.1, we used an angled cleaving at the input and a splice between FM-EDF and FMF at the output. The results show that the splice effectively induced less crosstalk but indeed enforced the lasing in the FM-EDF. The angled cleaving at the input was necessary to avoid an even stronger lasing. We also tested a flat cleaving but this allowed almost no gain without lasing.

4.3.1 Experimental set-up

In our transmission set-up, depicted in Fig. 4.3.2, the light from a tunable laser is passed into an integrated Polarization Division Multiplexed Quadrature Phase Shift Keying (PDM-QPSK) transmitter. It generates a data stream at 128Gb/s, including 25% protocol and forward error correction (FEC) overhead, which is replicated along five fiber paths into five streams referred to as mode channels in the following. They are decorrelated by several hundreds of symbols using standard single mode fiber (SMF) patch-cords, and fed to five optical amplifiers, connected to the five inputs of the 5×1 mode multiplexer (MUX).

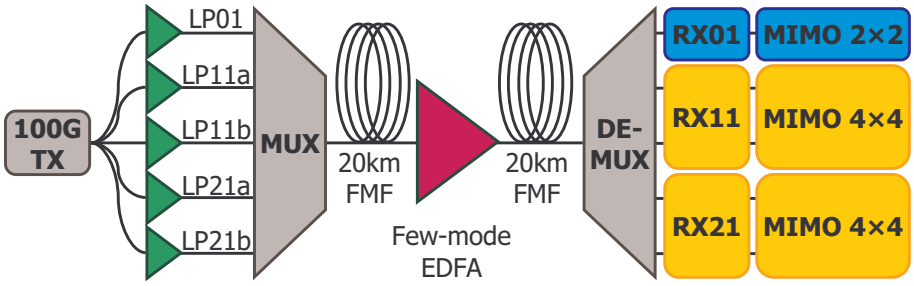

Fig. 4.3.2: Experimental set-up for MDM transmission including FM-EDFA

The MUX is realized in free-space optics using micro-mechanical building blocks, in order to finely tune the alignment of all the optical subparts. Along its five input paths, the spatial profiles of the optical beams are either unchanged or converted to the profiles of LP11a, LP11b, LP21a, and LP21b modes, where a and b refer to the two spatially degenerate modes. Mode conversion is performed by sending each beam onto the appropriate location on 4-quadrant phase plates, as described in section 3.3.3.2. The five beams corresponding to the five modes are combined and coupled into a 20 km-long FMF which ends in the FM-EDFA depicted in Fig. 4.3.1 and described in detail in section 3.4.

The output of the few-mode EDFA is spliced to another 20 km of FMF before the signal is demultiplexed by a 1×5 mode demultiplexer (DEMUX) having the same structure as the MUX, but is operated in the inverse direction. The outputs of the DEMUX are connected to single mode optical pre-amplifiers and then to coherent receivers. The signal transmitted on the LP01 mode is detected by a standard single mode coherent receiver, while the signals transmitted on the LP11a/b modes and on the LP21a/b modes are detected by a pair of synchronously triggered coherent receivers and processed with a 4x4 MIMO processor as described in section 3.5.2.

4.3.2 Results

First we measured gain and NF as with the amplifier configuration of section 3.4. To do so, twenty wavelengths, regularly spaced in the C-Band and of equal power, were sent into each input port of the MUX. The power per spatial mode at the FM-EDFA input was set to -10dBm and the pump power was adjusted to 120mW. For higher pump power or lower signal input power the amplifier would have started lasing in this configuration. The optical spectrum was measured with a resolution of 0.1nm at the output of the mode-DEMUX, and the amplifier gain profile is plotted in Fig. 4.3.3a for the LP01 mode, the LP11a+b modes (called LP11 group) and eventually the LP21a+b (LP21 group). The LP01 gain appears relatively flat over the C-Band, with an average gain of 12dB. But the gains for LP11 and LP21 exhibit a clear tilt, with lower gain for shorter wavelengths. This can be attributed to a lower inversion of erbium ions for these modes, at this pump power. The higher pump power of 400mW in combination with the 3dB lower input power of the signals used in the preceding amplifier configuration presented in section 3.4 has been shown to be effective to reduce the tilts in the gain profiles (see Fig. 3.4.4a) and to increase the overall gain. Here we observe gains between ~4 dB and ~14 dB, whereas in Fig. 3.4.4a, gains between ~14 dB and ~26 dB can be observed. It should also be noted that here, the LP01 mode experiences the highest gain, whereas in Fig. 3.4.4a, the LP11 mode group's gain is by ~4 dB higher than the gain of the two other modes / mode groups.

The NF as a function of wavelength was calculated and plotted in Fig. 4.3.3b for the LP01, LP11 and LP21 mode groups. We here measured a flat NF as a function of wavelength and mode, despite the variation of the gain. Nevertheless, NF values are clearly worse than the one measured for standard single mode EDFAs and also between ~1 dB (LP21) and ~4dB (LP01 and LP11) worse than the NF's presented in Fig. 3.4.4b, which had been measured with the first amplifier configuration. We attribute these additional NF degradations to the reduction of pump power from 400mW to 120mW and to the 3 dB higher signal input power. As already mentioned in section 3.4.2, the NF degradations compared to single mode operation are mainly attributed to non-ideal signal coupling into the FM-EDF and to the FM-EDF's much larger core diameter (10µm) necessary for ensuring multi-mode compatibility.

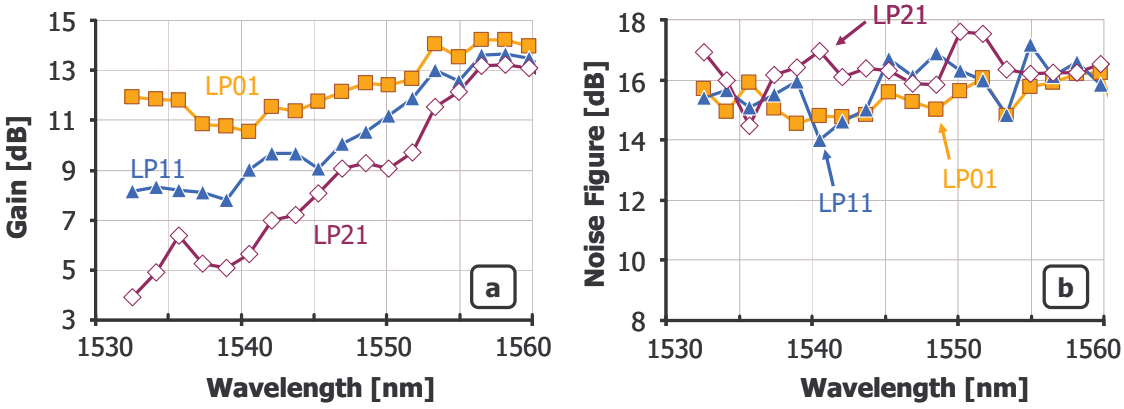

Fig. 4.3.3: Experimental results for MDM transmission including FM-EDFA. (a) Noise figure in dB as a function of wavelength. (b) Gain in dB as a function of wavelength.

Finally we measured the Q²-factors of the five exploitable mode channels for different transmission configurations and the results are reported in Fig. 4.3.4. To do so, we set the tunable laser to 1559.8nm, the FM-EDFA input power per spatial mode was set to -9 dBm and the pump power was set to 100 mW. We started by injecting each group of spatial modes independently, first the LP01 mode alone, then the LP11 group and eventually the LP21 group. The three bars on the left in Fig. 4.3.4 demonstrate that the mode channels' Q²-factors differ by a maximum of 0.3 dB. However, they are limited to ~12 dB whereas transmission over the same set-up, but without FM-EDFA, would allow Q²-factors above 14 dB (no error counted within 40µs). Then we injected all three combinations of modes of two different groups into the FMF (LP01+LP11, LP01+LP21, or LP11+LP21). The colored bars indicate the performance of the mode channels after transmission through the set-up with FM-EDFA and the surrounding frame indicates the performance without FM-EDFA. We observe that the two combinations involving the LP01 mode are penalized by 2-4 dB caused by the FM-EDFA but reach Q²-factors well above the FEC limit. The combination of LP11 and LP21 is detected with lower Q²-factors but also provides 33% more capacity than any combination with the LP01 mode. In this case, the penalty induced by the FM-EDFA on the LP11 mode channels (resp. LP21) is relatively large at 4dB (resp. ~6dB), which can be attributed to heavier mode crosstalk between LP11 and LP21. Finally, we injected the combination of all three mode groups (LP01+LP11+LP21). In contrast to the preceding configurations, where the LP01 mode channel had ~2dB lower Q²-factors than the LP11 mode channels and ~1dB lower Q²-factors than the LP21 mode channels, the LP01 mode channel is now the best performing one. It exhibits Q²-factor penalties of ~3.5dB compared to the set-up without FM-EDFA, whereas the LP11 and LP21 mode channels sustain Q²-factor penalties of ~4.5dB and ~5dB. This confirms the previous observation that intermodal crosstalk between LP11 and LP21 is predominant.

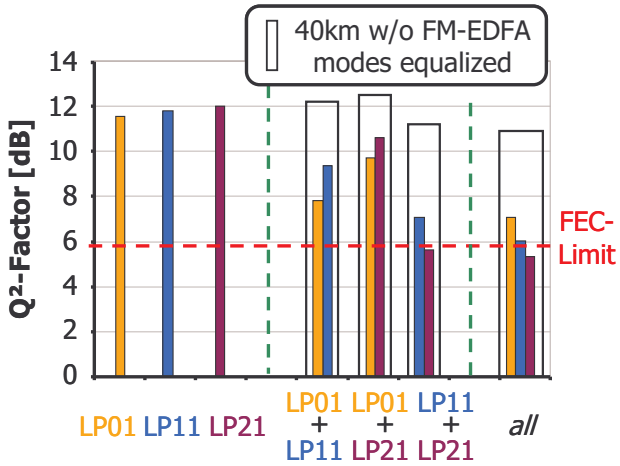

Fig. 4.3.4: Q²-factors for different mode input configurations

Even though the measured Q²-facors are strongly penalized by adding the FM-EDFA, Q²-factors at worst ~0.5 dB below the FEC limit have been obtained when transmitting five modes. In configurations with three modes (LP01+LP11 or LP01+LP21 respectively) Q²-factors are even well above the FEC limit (by a minimum of ~2dB or by a minimum of ~4dB respectively). Compared to the crosstalk values for the first FM-EDFA configuration presented in Table 3.4.1, this confirms the assumption that removing the angled fiber cleavings can improve intermodal crosstalk significantly. At the same time it has also been confirmed that this measure severely degrades gain and NF of the FM-EDFA. Hence, finding a solution that avoids reflections inside the FM-EDF without at the same time adding intermodal crosstalk offers very interesting potential.

4.4 Conclusion of Chapter 4

Chapter 4 was dedicated to the pioneer MDM transmission experiments, realized in the frame of this work. In the beginning of 2011 we were among the first teams in the world to present a successful MDM transmission. It was realized by using two degenerate modes, the so-called LP11a and LP11b modes, and by transmitting independent 100Gb/s signals modulated on each of the two modes over 40km. The performance was limited by intermodal crosstalk, and so we were not able to transmit a higher number of modes than two. We showed afterwards that the main source for intermodal crosstalk was the mode-MUX/DEMUX and that performance could be improved by partially compensating for it with an appropriate DSP design.

Using a second experimental set-up, we realized another mode-MUX/DEMUX providing much less linear mode coupling and thus much better intermodal crosstalk ratios. It allowed us to realize the first mode division multiplexed transmission over more than three modes. We successfully transmitted five 100 Gb/s PDM-QPSK signals modulated on five spatial modes over 40km. The five signals were demultiplexed optically with a sufficiently high quality so that only the degenerate modes had to be jointly processed in a DSP unit for subsequent decoupling. This is a very positive aspect regarding the evolution of computational complexity with the number of modes. However, it requires very low mode coupling and there are doubts that this condition can be fulfilled for longer transmission distances and especially when inserting optical few-mode amplification.

Optical few-mode amplification was the key novelty in the third and last transmission experiment. In a preceding FM-EDFA configuration, we had decided to reduce reflections

at input and output of the doped fiber by angled cleavings. This however degraded the intermodal crosstalk significantly. As a consequence we then constructed a second amplifier with only one angled cleave at the input and a direct splice to the FMF line fiber at the output. Using this FM-EDFA configuration in combination with a higher FEC overhead we realized a 40km MDM transmission with the amplifier at half the transmission distance. The achieved Q^2-factors were at least 2 dB above the FEC limit for transmission of three modes and ~0.5 dB below the FEC limit for transmission of 5 modes. This represented a significant improvement in terms of crosstalk compared to the set-up with two angled cleaves at the expense of lower gains and higher NFs.

Conclusion and Perspective

In this thesis I presented the concept of optical mode division multiplexed transmission systems. The continuously increasing demand for worldwide data traffic requires new, disruptive technologies in optical transmission systems, and mode division multiplexing (MDM) is one of the candidates currently drawing a lot of attention from the worldwide research community.

MDM is a special form of space division multiplexing (SDM) and it has been shown that compared to other SDM techniques, MDM offers a relatively high potential for synergies, but at the same time, it also comes along with the highest amount of uncertainty of all SDM solutions concerning its feasibility (section 2.3.3). It requires fundamental changes in system design, based on four new key elements: the few-mode fiber (FMF), the mode-multiplexer and –demultiplexer (mode-MUX and –DEMUX), the few-mode amplifier and the few-mode receiver with multiple input multiple output (MIMO) digital signal processing (DSP). Since MDM is a newly arising subject on which only little information had been published at the beginning of my work, my objective was to provide a broad view over the whole system rather than focusing on a single aspect and studying it in detail. Hence I conducted investigations on all of the four mentioned key elements and I also addressed the use of these elements in the system design.

MDM systems come along with new design parameters and with new transmission limiting effects compared to systems relying on single mode fiber (SMF). Right now, the biggest challenge is linear mode coupling leading to intermodal crosstalk in combination with a high differential mode group delay (DMGD) between different spatial modes. The penalties caused by intermodal crosstalk do not depend on the DMGD, but without DMGD, intermodal crosstalk could be compensated for by MIMO DSP in a relatively easy way. The presence of high DMGD values however leads to an explosion of the DSP filter length and makes crosstalk compensation through MIMO DSP too costly in a potential real-time detection unit This dilemma has led to two design approaches for MDM systems: the first one, the strongly coupled approach, tries to reduce the DMGD in order to be able to compensate intermodal crosstalk with DSP filters of reasonable complexity. The second one, the weakly coupled approach, tries to keep intermodal crosstalk sufficiently low in order to be able to separate the signals on the different modes physically, needing the support of MIMO DSP only for demultiplexing of two degenerate spatial modes. This results in a maximum required MIMO order of 4x4 (two spatial modes with two polarizations each). During this thesis I worked on the weakly coupled approach and so it was crucial to reduce linear mode coupling in any part of the MDM system. On the other hand, constraints concerning DMGD are relaxed in this approach and the solution seems to be easier scalable for a higher number of modes.

In the frame of the "STRADE" project, partially funded by the French government, we realized one FMF, and experimental investigations showed that in this FMF mode coupling was low compared to fibers used in other published works, but nevertheless it limited the transmission distance to 40 km for an MDM transmission of 5 modes.

Besides linear mode coupling, also nonlinear interactions between different spatial modes are expected to occur in an FMF. At the time of my thesis it was not possible to investigate intermodal nonlinear effects experimentally. Therefore, we developed a theoretical model and studied the phenomenon numerically. The results of this study indicate that intermodal nonlinear effects are almost completely mitigated by the high amount of DMGD. These promising results are to be confirmed in further numerical and experimental investigations.

In the mode-MUX and –DEMUX, the main performance indicators that we focused on were linear mode coupling and loss. To estimate the potential of a mode-MUX/-DEMUX with our given technological possibilities I first made a numerical evaluation. It indicated that for the modes LP01, LP11a+b and LP21a+b, mode conversion can be realized with a sufficiently high quality. However, a first practical realization of a mode-MUX/-DEMUX based on programmable phase masks realized in LCoS technology could not meet the specifications. The result was significantly improved with a second-generation mode-MUX/-DEMUX using static phase plates. This device provided mode conversion ratios in accordance with the numerical predictions for the modes LP01, LP11a+b and LP21a+b.

Few-mode amplification requires a sophisticated design to optimize gain and noise figure over the whole spectrum for all considered spatial modes. At the same time, linear mode coupling has to be minimized. It can originate from the few-mode erbium doped fiber (FM-EDF) itself but also from the unavoidable transitions between FM-EDF and FMF line fiber. Another challenge is the fact that these transitions generate internal reflections, and in combination with the active medium that the FM-EDF consists of this can create a laser cavity, which strongly limits the maximum amplifier gain. To address these issues we realized a first prototype few mode erbium doped fiber amplifier (FM-EDFA) based on a special ring-doped FM-EDF. However, amplifier performance hasn't been satisfying yet and requires further investigations.

In the weakly coupled MDM approach, the few-mode receiver does not require many innovations. After optical demultiplexing, each of the output signals is received by a standard single mode coherent receiver. The two receivers dealing with signals coming from two degenerate spatial modes are synchronized and share a common DSP unit. Here, the degenerate modes are decoupled by a 4x4 MIMO DSP. Similar to polarization demultiplexing in single mode systems, demultiplexing of degenerate modes must be assisted by DSP since the spatial orientation of the spatial modes in the transverse plane of the fiber is unknown at the mode-DEMUX and detection is done along two arbitrary axes. DSP is then used to decouple the two received modes.

In the last part of this manuscript, I presented three MDM transmission experiments that we realized with systems consisting of a combination of the above mentioned devices. The first of these experiments was realized in the beginning of 2011 using the LCoS based mode-MUX/-DEMUX. The rather poor performance of this device limited the experiment to the transmission of two 100Gb/s PDM-QPSK signals using two modes (LP11a+b) over 40 km. Nonetheless, with this experiment we succeeded to be among the first teams worldwide to present a successful MDM transmission at the Optical Fiber Communication Conference and Exhibition (OFC) 2011.

The improved mode-MUX/-DEMUX allowed us to realize the transmission of five 100Gb/s PDM-QPSK signals using five spatial modes (LP01, LP11a+b, LP21a+b) over 40km in a second experiment. This result, presented at the European Conference and Exhibition on Optical Communication (ECOC) 2011, is still the only published experiment demonstrating MDM using more than three spatial modes for transmission of independent signals.

The third and last transmission experiment presented in this work contained few-mode amplification. We successfully transmitted three 100Gb/s PDM-QPSK signals using three

spatial modes over 40 km with a few-mode amplifier after 20 km. Transmission over five modes led to Q^2-factors slightly below the FEC limit. Altogether, the tradeoff between high gain, low noise figure and low mode-coupling in the FM-EDFA could not yet be solved in a satisfying way.

The research on optical MDM transmission systems is still at the beginning and there are open questions in numerous directions. After several experimental demonstrations have shown successfully that the concept can be realized, it is now required to go deeper into the analysis and into the optimization of the individual components. With the number of fundamental changes that MDM requires compared to single mode transmission systems, it is clear that it can only be a success if the number of modes is higher than in the experimental demonstrations that have been published so far. It is hard to give a concrete number but maybe around 10 modes should at least be envisaged. So scalability for a higher number of modes is a key issue.

Investigations on FMFs should give further insight into the practical limits concerning linear mode coupling and DMGD especially when increasing the number of guided modes. This information will play a major role concerning the evaluations of the two design strategies "strongly coupled" and "weakly coupled" MDM.

The physical mode-MUX/-DEMUX technology already works quite well; here the focus could not only be on further increasing the number of modes, but also on reducing insertion loss and on integration in order to reduce the size of a potential commercially used device.

A very delicate subject is Few-mode amplification. From an economic point of view, it is crucial for the success of MDM, since here most of the synergies can be gained. On the other hand it poses extremely difficult problems, such as gain and NF equalization over the whole C-band for all modes and linear mode coupling. It might be here, where the strongly coupled design approach has the decisive advantage over the weakly coupled approach: if mode coupling during few-mode amplification cannot be avoided, joint MIMO processing of all the received modes gets indispensable and very low mode coupling in all the other elements of the system becomes practically useless.

Bibliography

[1] J. G. Proakis, *Digital Communications*, 4th ed. New York, NY: McGraw-Hill, 2001.

[2] R.-J. Essiambre, G. Kramer, P. J. Winzer, G. J. Foschini, and B. Goebel, "Capacity Limits of Optical Fiber Networks," *J. Lightw. Technol.*, vol. 28, no. 4, pp. 662–701, Feb. 2010.

[3] C. E. Shannon, "A Mathematical Theory of Communication," *Bell System Technical Journal*, vol. 27, pp. 379–423,623–656, 1948.

[4] E. Grellier, "Etude des effets non-!inéaires à l'oeuvre dans les systèmes de transmissions optiques fortement dispersifs," Université de Franche-Comté, 2011.

[5] G. P. Agrawal, *Lightwave Technology Telecommunication Systems*. Hoboken, NJ: John Wiley & Sons, Inc., 2005.

[6] M. Abramowitz and I. A. Stegun, *Handbook of Mathematical Functions*. Dover, NY: , 1970.

[7] "ITU-T G.975.1, Forward error correction for high bit rate DWDM submarine systems." 2003.

[8] T. Mizuoshi, K. Ouchi, T. Kobayashi, Y. Miyata, K. Kuno, H. Tagami, K. Kubo, H. Yoshida, M. Akita, and K. Motoshima, "Experimental Demonstration of Net Coding Gain of 10.1 dB using 12.4 Gb/s Block Turbo Code with 3-bit Soft Decision," in *Proc. OFC 2003, Postdeadline Papers*, 2003, p. PD21.

[9] D. Ouchi, K. Kubo, T. Mi, Y. Miyata, H. Yoshida, H. Tagami, K. Shimizu, T. Kobayashi, K. Shimomura, K. Onohara, and K. Motoshima, "A fully integrated block turbo code FEC for 10 Gb/s optical communication systems," in *Proc. OFC 2006*, 2006, p. 3 pp.

[10] G. Li and X. Liu, "Focus Issue: Space Multiplexed Optical Transmission," *Optics Express*, vol. 19, no. 17, pp. 16574–16575.

[11] P. J. Winzer, "Energy-Efficient Optical Transport Capacity Scaling Through Spatial Multiplexing," *IEEE Photonics Technology Letters*, vol. 23, no. 13, pp. 851–853, Apr. 2011.

[12] T. Zami, L. Noirie, F. Bruyere, and A. Jourdan, "Crosstalk-induced degradation in an optical-noise-limited detection system," in *Proc. OFC 1999*, San Diego, CA, 1999, pp. 255–257.

[13] T. Zami, B. Lavigne, and E. Balmefrezol, "Crosstalk analysis applied to wavelength selective switches," in *Proc. OFC 2006*, Anaheim, CA, 2006, p. 3 pp.

[14] T. Zami, B. Lavigne, E. Balmefrezol, M. Lefrancois, and H. Mardoyan, "Comparative Study of Crosstalk Created in 50 GHz-Spaced Wavelength Selective Switch for Various Modulation Formats at 43 Gbit/s," in *Proc. ECOC 2006*, Cannes, France, 2006, pp. 1–2.

[15] M. Filer and S. Tibuleac, "Estimating system penalties of spectrally-shaped crosstalk on wide-bandwidth DWDM signals," in *Proc. IEEE Phot. Soc.2010*, Denver, co, 2010, pp. 690–691.

[16] M. Filer and S. Tibuleac, "Generalized weighted crosstalk for DWDM systems with cascaded wavelength-selective switches," in *Proc. OFC 2012*, Los Angeles, California, 2012.

[17] Y.-T. Hsueh, A. Stark, M. Filer, T. Detwiler, S. Tibuleac, G.-K. Chang, and S. E. Ralph, "In-Band Crosstalk Transmission Penalties on 112-Gb/s PDM-QPSK Optical Links," *IEEE Photonics Technology Letters*, vol. 23, no. 11, pp. 745–747, Jun. 2011.

[18] P. J. Winzer, A. H. Gnauck, A. Konczykowska, F. Jorge, and J.-Y. Dupuy, "Penalties from in-band crosstalk for advanced optical modulation formats," in *Proc. ECOC 2011*, Geneva, Switzerland, 2011.

[19] G. P. Agrawal, *Nonlinear Fiber Optics*, 3rd ed. San Diego, CA: Academic Press, 2001.

[20] B. E. A. Saleh and I. John Wiley & Sons, *Fundamentals of Photonics (Second Edition)*. Wiley-Interscience, 1991.

[21] R. W. Boyd, *Nonlinear Optics*. San Diego, CA: Academic Press, 1992.

[22] M. A. Duguay, "An Ultrafast Light Gate," *Applied Physics Letters*, vol. 15, no. 6, p. 192, 1969.

[23] K. C. Kao and G. A. Hockham, "Dielectric-Fiber Surface Waveguides for Optical Frequencies," *Proc of Institution of Electrical Engineers*, vol. 113, no. 7, pp. 1151–1158, Jul. 1966.

[24] K. Nagayama, M. Kakui, M. Matsui, T. Saitoh, and Y. Chigusa, "Ultra-Low-Loss (0.1484 dB/km) Pure Silica Core Fibre and Extension of Transmission Distance," *Electronics Letters*, vol. 38, no. 20, pp. 1168–1169, Sep. 2002.

[25] Y. Chigusa, Y. Yamamoto, T. Yokokawa, T. Sasaki, T. Taru, M. Hirano, M. Kakui, M. Onishi, and E. Sasaoka, "Low-loss pure-silica-core fibers and their possible impact on transmission systems," *Journal of Lightwave Technology*, vol. 23, no. 11, pp. 3541–3550, Nov. 2005.

[26] M. Lefrancois, "Etude de technologies avancées pour l'optimisation des systèmes de transmission optique multiplexés en longueur d'onde au débit de 40 Gb/s," Université Paris-sud 11, 2007.

[27] C. D. Poole, J. H. Winters, and J. A. Nagel, "Dynamical equation for polarization dispersion," *Optics Letters*, vol. 16, no. 6, p. 372, Mar. 1991.

[28] Y. Frignac, "Contribution à l'ingénierie des systèmes de transmission terrestres sur fibre optique utilisant le multiplexage en longueur d'onde de canaux modulés au débit de 40 Gb/s," Ecole Nationale Supérieure des Télécommunications, 2003.

[29] M. Winter, C.-A. Bunge, D. Setti, and K. Petermann, "A Statistical Treatment of Cross-Polarization Modulation in DWDM Systems," *Journal of Lightwave Technology*, vol. 27, no. 17, pp. 3739–3751, Sep. 2009.

[30] M. Winter, D. Setti, and K. Petermann, "Cross-Polarization Modulation in Polarization-Division Multiplex Transmission," *IEEE Photonics Technology Letters*, vol. 22, no. 8, pp. 538–540, Apr. 2010.

[31] J.-C. Antona, S. Bigo, and J.-P. Faure, "Nonlinear cumulated phase as a criterion to assess performance of terrestrial WDM systems," in *Proc. OFC 2002*, Anaheim, CA, 2002, pp. 365–367.

[32] P. Poggiolini, A. Carena, V. Curri, G. Bosco, and F. Forghieri, "Analytical Modeling of Nonlinear Propagation in Uncompensated Optical Transmission Links," *IEEE Photonics Technology Letters*, vol. 23, no. 11, pp. 742–744, Jun. 2011.

[33] E. Torrengo, R. Cigliutti, G. Bosco, A. Carena, V. Curri, P. Poggiolini, A. Nespola, D. Zeolla, and F. Forghieri, "Experimental validation of an analytical model for nonlinear propagation in uncompensated optical links," *Optics Express*, vol. 19, no. 26, p. B790, Dec. 2011.

[34] F. Vacondio, O. Rival, C. Simonneau, E. Grellier, A. Bononi, L. Lorcy, J.-C. Antona, and S. Bigo, "On nonlinear distortions of highly dispersive optical coherent systems," *Optics Express*, vol. 20, no. 2, p. 1022, Jan. 2012.

[35] A. Carena, V. Curri, G. Bosco, P. Poggiolini, and F. Forghieri, "Modeling of the Impact of Nonlinear Propagation Effects in Uncompensated Optical Coherent Transmission Links," *Journal of Lightwave Technology*, vol. 30, no. 10, pp. 1524–1539, May 2012.

[36] O. Bertran-Pardo, "On coherent detection for optical transmissions at 40 Gb/s and 100 Gb/s," Télécom ParisTech.

[37] B. C. Collings and L. Boivin, "Nonlinear polarization evolution induced by cross-phase modulation and its impact on transmission systems," *IEEE Photonics Technology Letters*, vol. 12, no. 11, pp. 1582–1584, Nov. 2000.

[38] R. H. Stolen, "Raman Oscillation in Glass Optical Waveguide," *Applied Physics Letters*, vol. 20, no. 2, p. 62, 1972.

[39] J. Hegarty, N. A. Olsson, and L. Goldner, "CW pumped Raman preamplifier in a 45 km-long fibre transmission system operating at 1.5 μm and 1 Gbit/s," *Electronics Letters*, vol. 21, no. 7, p. 290, 1985.

[40] A. J. Stentz, S. G. Grubb, C. E. Headley, J. R. Simpson, T. Strasser, and N. Park, "Raman amplifier with improved system performance," in *Proc. OFC 1996*, San Jose, CA, 1996, pp. 16–17.

[41] J.-X. Cai, Y. Cai, C. R. Davidson, D. G. Foursa, A. Lucero, O. Sinkin, W. Patterson, A. Pilipetskii, G. Mohs, and N. S. Bergano, "Transmission of 96x100G pre-filtered PDM-RZ-QPSK channels with 300% spectral efficiency over 10,608km and 400% spectral efficienxy over 4,368km," in *Proc. OFC 2010, Postdeadline Papers*, San Diego, CA, 2010, p. PDPB10.

[42] Y. Cai, J. X. Cai, C. R. Davidson, D. Foursa, A. Lucero, O. Sinkin, A. Pilipetskii, G. Mohs, and N. S. Bergano, "High spectral efficiency long-haul transmission

with pre-filtering and maximum a posteriori probability detection," in *Proc. ECOC 2010*, Torino, Italy, 2010, pp. 1–3.

[43] M. Salsi, C. Koebele, P. Tran, H. Mardoyan, E. Dutisseuil, J. Renaudier, M. Bigot-Astruc, L. Provost, S. Richard, P. Sillard, S. Bigo, and G. Charlet, "Transmission of 96×100Gb/s with 23% Super-FEC Overhead over 11,680km, using Optical Spectral Engineering," in *Proc. OFC 2011, Paper OMR2*, Los Angeles, California, 2011.

[44] J. Renaudier, O. Bertran-Pardo, L. Pierre, P. Tran, H. Mardoyan, G. Charlet, and S. Bigo, "Nonlinear tolerance of ultra-densely spaced 100Gb/s coherent PDM-QPSK channels," in *Proc. ECOC 2010*, Torino, Italy, 2010, pp. 1–3.

[45] M.-F. Huang, D. Qian, and E. Ip, "50.53-Gb/s PDM-1024QAM-OFDM transmission using pilot-based phase noise mitigation," in *Proc. OECC 2011*, Kaohsiung, Taiwan, 2011.

[46] "ITU-T G.Sup39, Optical System Design and Engineering Considerations." Feb-2006.

[47] E. Ip and J. M. Kahn, "Compensation of Dispersion and Nonlinear Impairments Using Digital Backpropagation," *Journal of Lightwave Technology*, vol. 26, no. 20, pp. 3416–3425, Oct. 2008.

[48] E. Ip, "Nonlinear Compensation Using Backpropagation for Polarization-Multiplexed Transmission," *Journal of Lightwave Technology*, vol. 28, no. 6, pp. 939–951, Mar. 2010.

[49] A. Ghazisaeidi and L. A. Rusch, "On the Efficiency of Digital Back-Propagation for Mitigating SOA-Induced Nonlinear Impairments," *Journal of Lightwave Technology*, vol. 29, no. 21, pp. 3331–3339, Nov. 2011.

[50] S. J. Savory, "Digital filters for coherent optical receivers," *Optics Express*, vol. 16, no. 2, p. 804, 2008.

[51] S. J. Savory, A. D. Stewart, S. Wood, G. Gavioli, M. G. Taylor, R. I. Killey, and P. Bayvel, "Digital Equalisation of 40Gbit/s per Wavelength Transmission over 2480km of Standard Fibre without Optical Dispersion Compensation," in *Proc. ECOC 2006*, Cannes, France, 2006, pp. 1–2.

[52] A. Leven, N. Kaneda, U.-V. Koc, and Y. K. Chen, "Feed-Forward Phase and Frequency Estimation in Coherent Digital and Analog Photonic Links Using Digital Signal Processing," in *Proc. IMS 2007*, Honolulu, HI, 2007, pp. 1511–1514.

[53] A. Leven, N. Kaneda, U.-V. Koc, and Y.-K. Chen, "Frequency Estimation in Intradyne Reception," *IEEE Photonics Technology Letters*, vol. 19, no. 6, pp. 366–368, Mar. 2007.

[54] A. Leven, F. Vacondio, L. Schmalen, S. Brink, and W. Idler, "Estimation of Soft FEC Performance in Optical Transmission Experiments," *IEEE Photonics Technology Letters*, vol. 23, no. 20, pp. 1547–1549, Oct. 2011.

[55] Prysmian Cables and Systems, "SM Light Single Mode Fiber, Datasheet." 2008.

[56] Sumitomo Electric, "Sumitomo Fiber Specification SE-12** PureAdvance® Single-Mode Fiber." Jan-2012.

[57] Corning Incorporated, "Corning® LEAF® Optical Fiber, Product Information." Dec-2011.

[58] Corning Incorporated, "Corning® Vascade® Optical Fibers, Product Informations." Aug-2010.

[59] R. Mishra, S. Ten, and R. Rukosueva, "Ultra Low Loss and Large Effective Area Fiber for Next Generation Submarine Networks," *Voice of the Industry, submarine telecoms Forum*, p. September 2010.

[60] E. Desurvire, *Erbium-Doped Fiber Amplifiers*. Wiley-Interscience, 1994.

[61] N. A. Olsson, "Semiconductor optical amplifiers," *Proceedings of the IEEE*, vol. 80, no. 3, pp. 375–382, Mar. 1992.

[62] M. Connelly, *Semiconductor Optical Amplifiers*. Kluwer Academic Publishers, 2002.

[63] M. Salsi, H. Mardoyan, P. Tran, C. Koebele, E. Dutisseuil, G. Charlet, and S. Bigo, "155x100Gbit/s coherent PDM-QPSK transmission over 7200km," in *Proc. ECOC 2009, Postdeadline Papers, Paper PD 2.5*, Vienna, Austria, 2009.

[64] A. Sano, Y. Miyamoto, S. Kuwahara, and H. Toba, "A 40-Gb/s/ch WDM transmission with SPM/XPM suppression through prechirping and dispersion management," *Journal of Lightwave Technology*, vol. 18, no. 11, pp. 1519–1527, Nov. 2000.

[65] Y. Frignac, J.-C. Antona, S. Bigo, and J.-P. Hamaide, "Numerical optimization of pre- and in-line dispersion compensation in dispersion-managed systems at 40 Gbit/s," in *Proc. OFC 2002*, Anaheim, CA, pp. 612–613.

[66] A. G. Striegler and B. Schmauss, "Compensation of Intrachannel Effects in Symmetric Dispersion-Managed Transmission Systems," *Journal of Lightwave Technology*, vol. 22, no. 8, pp. 1877–1882, Aug. 2004.

[67] C. Koebele, M. Salsi, G. Charlet, O. Bertran-Pardo, J. Renaudier, H. Mardoyan, P. Tran, and S. Bigo, "Impact of Transmitter Bandwidth on Transmission Performance of Coherent 112-Gb/s PDM-QPSK Systems," *IEEE Photon. Technol. Lett.*, vol. 22, no. 24, pp. 1859–1861, Oct. 2010.

[68] G. Charlet, "Etude des formats de modulation et des méthodes de détéction pour les transmissions multiplexées en longueur d'onde sur fibre optique au débit de 40Gb/s et 100Gb/s," Université Paris-sud 11, 2011.

[69] "Cisco Visual Networking Index - Forecast and Methodology, 2007-2012," Cisco Systems, Inc., Jun. 2008.

[70] "Cisco Visual Networking Index - Forecast and Methodology, 2010-2015," Cisco Systems, Inc., Jun. 2011.

[71] J.-X. Cai, Y. Cai, Y. Sun, C. R. Davidson, D. G. Foursa, A. Lucero, O. Sinkin, W. Patterson, A. Pilipetskii, G. Mohs, and N. S. Bergano, "112 x 112 Gb/s transmission over 9,360 km with channel spacing set to the baud rate (360% spectral efficiency)," in *Proc. ECOC 2010, Postdeadline Papers*, Torino, Italy, 2010, pp. 1–3.

[72] Y. Cai, J.-X. Cai, A. Pilipetskii, G. Mohs, and N. S. Bergano, "Spectral efficiency limits of pre-filtered modulation formats," *Optics Express*, vol. 18, no. 19, p. 20273, Sep. 2010.

[73] G. Charlet, M. Salsi, P. Tran, M. Bertolini, H. Mardoyan, J. Renaudier, O. Bertran-Pardo, and S. Bigo, "72×100Gb/s transmission over transoceanic

distance, using large effective area fiber, hybrid Raman-Erbium amplification and coherent detection," in *Proc. OFC 2009, Postdeadline Papers*, San Diego, USA, 2009, p. PDPB6.

[74] H. Masuda, E. Yamazaki, A. Sano, T. Yoshimatsu, T. Kobayashi, E. Yoshida, Y. Miyamoto, S. Matsuoka, Y. Takatori, M. Mizoguchi, K. Okada, K. Hagimoto, T. Yamada, and S. Kamei, "13.5-Tb/s (135 × 111-Gb/s/ch) no-guard-interval coherent OFDM transmission over 6,248 km using SNR maximized second-order DRA in the extended L-band," in *Proc. OFC 2009, Postdeadline Papers*, San Diego, USA, 2009, p. PDPB5.

[75] T. Kato, M. Hirano, M. Onishi, and M. Nishimura, "Ultra-low nonlinearity low-loss pure silica core fibre for long-haul WDM transmission," *Electronics Letters*, vol. 35, no. 19, p. 1615, 1999.

[76] J. Renaudier, G. Charlet, M. Salsi, O. B. Pardo, H. Mardoyan, P. Tran, and S. Bigo, "Linear Fiber Impairments Mitigation of 40-Gbit/s Polarization-Multiplexed QPSK by Digital Processing in a Coherent Receiver," *Journal of Lightwave Technology*, vol. 26, no. 1, pp. 36–42, Jan. 2008.

[77] M. Salsi, C. Koebele, P. Tran, H. Mardoyan, S. Bigo, and G. Charlet, "80x100-Gbit/s transmission over 9,000km using erbium-doped fibre repeaters only," in *Proc. ECOC 2010, Paper We.7.C.3*, Torino, Italy, 2010.

[78] J. Renaudier, G. Charlet, O. Bertran-Pardo, H. Mardoyan, P. Tran, M. Salsi, and S. Bigo, "Transmission of 100Gb/s Coherent PDM-QPSK over 16x100km of Standard Fiber with all-erbium amplifiers," *Optics Express*, vol. 17, no. 7, pp. 5112–5117, Mar. 2009.

[79] G. Gavioli, E. Torrengo, G. Bosco, A. Carena, V. Curri, V. Miot, P. Poggiolini, M. Belmonte, F. Forghieri, C. Muzio, S. Piciaccia, A. Brinciotti, A. La Porta, C. Lezzi, S. Savory, and S. Abrate, "Investigation of the impact of ultra-narrow carrier spacing on the transmission of a 10-carrier 1Tb/s superchannel," in *Proc. OFC 2010*, San Diego, CA, 2010, p. OThD3.

[80] F. Vacondio, C. Simmoneau, L. Lorcy, J.-C. Antona, A. Bononi, and S. Bigo, "Experimental characterization of Gaussian-distributed nonlinear distortions," in *Proc. ECOC 2011*, Geneva, Switzerland, 2011.

[81] T. Hayashi, T. Taru, O. Shimakawa, T. Sasaki, and E. Sasaoka, "Design and fabrication of ultra-low crosstalk and low-loss multi-core fiber," *Optics Express*, vol. 19, no. 17, p. 16576, Aug. 2011.

[82] S. Chandrasekhar, A. H. Gnauck, X. Liu, P. J. Winzer, Y. Pan, E. C. Burrows, B. Zhu, T. F. Taunay, M. Fishteyn, M. F. Yan, J. M. Fini, E. M. Monberg, and F. V. Dimarcello, "WDM/SDM Transmission of 10 x 128-Gb/s PDM-QPSK over 2688-km 7-core Fiber with a per-Fiber Net Aggregate Spectral-Efficiency Distance Product of 40,320 km·b/s/Hz," in *Proc. ECOC 2011, Postdeadline Papers, Paper Th.13.C.4*, Geneva, Switzerland, 2011.

[83] J. Sakaguchi, B. J. Puttnam, K. Werner, Y. Awaji, N. Wada, A. Kanno, T. Kawanishi, K. Imamura, H. Inaba, K. Mukasa, R. Sugizaki, T. Kobayashi, and M. Watanabe, "19-core fiber transmission of 19x100x172-Gb/s SDM-WDM-PDM-QPSK signals at 305Tb/s," in *Proc. OFC 2012, Postdeadline Papers, Paper PDP5C.1*, Los Angeles, California, 2012.

[84] K. S. Abedin, T. F. Taunay, M. Fishteyn, M. F. Yan, B. Zhu, J. M. Fini, E. M. Monberg, F. V. Dimarcello, and P. W. Wisk, "Amplification and noise properties of an erbium-doped multicore fiber amplifier," *Optics Express*, vol. 19, no. 17, p. 16715, Aug. 2011.

[85] Y. Tsuchida, K. Maeda, Y. Mimura, H. Matsuura, R. Miyabe, K. Aiso, and R. Sugizaki, "Amplification Characteristics of a Multi-core Erbium-doped Fiber Amplifier," in *Proc. OFC 2012*, Los Angeles, California, 2012.

[86] R. Ryf, A. Sierra, R.-J. Essiambre, A. H. Gnauck, S. Randel, M. Esmaeelpour, S. Mumtaz, P. J. Winzer, R. Delbue, P. Pupalaikis, A. Sureka, T. Hayashi, T. Taru, and T. Sasaki, "Coherent 1200-km 6 x 6 MIMO Mode-Multiplexed Transmission over 3-core Microstructured Fiber," in *Proc. ECOC 2011, Postdeadline Papers, Paper Th.13.C.1*, Geneva, Switzerland, 2011.

[87] C. Xia, N. Bai, I. Ozdur, X. Zhou, and G. Li, "Supermodes for optical transmission," *Optics Express*, vol. 19, no. 17, p. 16653, Aug. 2011.

[88] R. Ryf, R.-J. Essiambre, A. H. Gnauck, S. Randel, M. A. Mestre, C. Schmidt, P. J. Winzer, R. Delbue, P. Pupalaikis, A. Sureka, T. Hayashi, T. Taru, and T. Sasaki, "Space-Division Multiplexed Transmission over 4200 km 3-Core Microstructured Fiber," in *Proc. OFC 2012, Postdeadline Papers, Paper PDP5C.2*, Los Angeles, California, 2012.

[89] S. Berdagué and P. Facq, "Mode division multiplexing in optical fibers," *Applied Optics*, vol. 21, no. 11, p. 1950, Jun. 1982.

[90] N. Hanzawa, K. Saitoh, T. Sakamoto, T. Matsui, S. Tomita, and M. Koshiba, "Demonstration of mode-division multiplexing transmission over 10 km two-mode fiber with mode coupler," in *Proc. OFC 2011*, Los Angeles, California, 2011.

[91] A. Li, A. Al Amin, X. Chen, and W. Shieh, "Reception of Mode and Polarization Multiplexed 107-Gb/s CO-OFDM Signal over a Two-Mode Fiber," in *Proc. OFC 2011, Postdeadline Papers, Paper PDPB8*, Los Angeles, California, 2011.

[92] M. Salsi, C. Koebele, D. Sperti, P. Tran, P. Brindel, H. Mardoyan, S. Bigo, A. Boutin, F. Verluise, P. Sillard, M. Astruc, L. Provost, F. Cerou, and G. Charlet, "Transmission at 2x100Gb/s, over Two Modes of 40km-long Prototype Few-Mode Fiber, using LCOS-based Mode Multiplexer and Demultiplexer," in *Proc. OFC 2011, Postdeadline Papers, Paper PDPB9*, Los Angeles, California, 2011.

[93] R. Ryf, S. Randel, A. H. Gnauck, C. A. Bolle, R.-J. Essiambre, P. J. Winzer, D. W. Peckham, A. McCurdy, and R. Lingle, "Space-division multiplexing over 10 km of three-mode fiber using coherent 6 x 6 MIMO processing," in *Proc. OFC 2011, Postdeadline Papers, Paper PDPB10*, Los Angeles, California, 2011.

[94] S. Randel, R. Ryf, A. Sierra, P. J. Winzer, A. H. Gnauck, C. A. Bolle, R.-J. Essiambre, D. W. Peckham, A. McCurdy, and R. Lingle, "6x56-Gb/s mode-division multiplexed transmission over 33-km few-mode fiber enabled by 6x6 MIMO equalization," *Optics Express*, vol. 19, no. 17, pp. 16697–16707, Aug. 2011.

[95] R. Ryf, S. Randel, A. H. Gnauck, C. Bolle, A. Sierra, S. Mumtaz, M. Esmaeelpour, E. C. Burrows, R.-J. Essiambre, P. J. Winzer, D. W. Peckham, A. H. McCurdy, and R. Lingle, "Mode-Division Multiplexing Over 96 km of Few-Mode Fiber Using

Coherent 6 x 6 MIMO Processing," *Journal of Lightwave Technology*, vol. 30, no. 4, pp. 521–531, Feb. 2012.

[96] C. Koebele, M. Salsi, L. Milord, R. Ryf, C. A. Bolle, P. Sillard, S. Bigo, and G. Charlet, "40km Transmission of Five Mode Division Multiplexed Data Streams at 100Gb/s with low MIMO-DSP Complexity," in *Proc. ECOC 2011, Postdeadline Papers, Paper Th.13.C.3*, Geneva, Switzerland, 2011.

[97] P. M. Krummrich and K. Petermann, "Evaluation of potential optical amplifier concepts for coherent mode multiplexing," in *Proc. OFC 2011*, Los Angeles, California, 2011.

[98] P. M. Krummrich, "Optical amplification and optical filter based signal processing for cost and energy efficient spatial multiplexing," *Optics Express*, vol. 19, no. 17, p. 16636, Aug. 2011.

[99] N. Bai, E. Ip, T. Wang, and G. Li, "Multimode fiber amplifier with tunable modal gain using a reconfigurable multimode pump," *Optics Express*, vol. 19, no. 17, p. 16601, Aug. 2011.

[100] P. M. Krummrich, "Optical amplification for capacity increase in long haul transmission systems by spatial multiplexing," 2011, pp. 585–586.

[101] P. M. Krummrich, "Optical Amplifiers for Multi Mode / Multi Core Transmission," in *Proc. OFC 2012*, Los Angeles, California, 2012.

[102] R. Ryf, A. Sierra, R.-J. Essiambre, S. Randel, A. H. Gnauck, C. Bolle, M. Esmaeelpour, P. J. Winzer, R. Delbue, P. Pupalaikis, A. Sureka, D. W. Peckham, A. McCurdy, and R. Lingle, "Mode-equalized distributed Raman amplification in 137-km few-mode fiber," in *Proc. ECOC 2011, Postdeadline Papers, Paper Th.13.C.3*, Geneva, Switzerland, 2011.

[103] E. Ip, N. Bai,, Y.-K. Huang, E. Mateo, F. Yaman, M.-J. Li, S. Bickham, S. Ten, J. Linares, C. Montero, X. Prietu, V. Tse, K. Man Chung, A. Lau, H.-Y. Tam, C. Lu, Y. Luo, G.-D. Peng, and G. Li, "88x3x112-Gb/s WDM Transmission over 50 km of Three-Mode Fiber with Inline Few-Mode Fiber Amplifier," in *Proc. ECOC 2011, Postdeadline Papers, Paper Th.13.C.2*, Geneva, Switzerland, 2011.

[104] Y. Yung, S. Alam, Z. Li, A. Dhar, D. Giles, I. Giles, J. Sahu, L. Grüner-Nielsen, F. Poletti, and D. J. Richardson, "First demonstration of multimode amplifier for spatial division multiplexed transmission systems," in *Proc. ECOC 2011, Postdeadline Papers, Paper Th.13.K.4*, Geneva, Switzerland, 2011.

[105] S. Randel, R. Ryf, A. H. Gnauck, M. A. Mestre, C. Schmidt, R.-J. Essiambre, P. J. Winzer, R. Delbue, P. Pupalaikis, A. Sureka, Y. Sun, X. Jiang, and R. Lingle, "Mode-Multiplexed 6x20-GBd QPSK Transmission over 1200-km DGD-Compensated Few-Mode Fiber," in *Proc. OFC 2012, Postdeadline Papers, Paper PDP5C.5*, Los Angeles, California, 2012.

[106] P. Sillard, M. Bigot-Astruc, D. Boivin, H. Maerten, and L. Provost, "Few-Mode Fiber for Uncoupled Mode -Division Multiplexing Transmissions," in *Proc. ECOC 2011, Paper Tu.5.LeCervin.7*, Geneva, Switzerland, 2011.

[107] C. Koebele, M. Salsi, G. Charlet, and S. Bigo, "Nonlinear Effects in Mode Division Multiplexed Transmission over Few-Mode Optical Fiber," *IEEE Photon. Technol. Lett.*, vol. 23, no. 18, pp. 1316–1318, Jun. 2011.

[108] S. Randel, M. Magarini, R. Ryf, R.-J. Essiambre, A. H. Gnauck, P. J. Winzer, T. Hayashi, T. Taru, and T. Sasaki, "MIMO-based signal processing of spatially multiplexed 112-Gb/s PDM-QPSK signals using strongly-coupled 3-core fiber," in *Proc. ECOC 2011*, Geneva, Switzerland, 2011.

[109] F. Poletti and P. Horak, "Description of ultrashort pulse propagation in multimode optical fibers," *J. Opt. Soc. Am. B*, vol. 25, no. 10, pp. 1645–1654, Sep. 2008.

[110] T. Chaipiboonwong, P. Horak, J. D. Mills, and W. S. Brocklesby, "Numerical study of nonlinear interactions in a multimode waveguide," *Optics Express*, vol. 15, no. 14, Jul. 2007.

[111] M. B. Shemirani, W. Mao, R. A. Panicker, and J. M. Kahn, "Principal Modes in Graded-Index Multimode Fiber in Presence of Spatial- and Polarization-Mode Coupling," *Journal of Lightwave Technology*, vol. 27, no. 10, pp. 1248–1261, May 2009.

[112] M. B. Shemirani and J. M. Kahn, "Higher-Order Modal Dispersion in Graded-Index Multimode Fiber," *Journal of Lightwave Technology*, vol. 27, no. 23, pp. 5461–5468, Dec. 2009.

[113] J. Vuong, P. Ramantanis, A. Seck, D. Bendimerad, and Y. Frignac, "Understanding discrete linear mode coupling in few-mode fiber transmission systems," in *Proc. ECOC 2011*, Geneva, Switzerland, 2011.

[114] F. Yaman, E. Mateo, and T. Wang, "Impact of Modal Crosstalk and Multi-Path Interference on Few-Mode Fiber Transmission," in *Proc. OFC 2012*, Los Angeles, California, 2012.

[115] R. Olshansky, "Mode Coupling Effects in Graded-Index Optical Fibers," *Applied Optics*, vol. 14, no. 4, pp. 935–945, Apr. 1975.

[116] F. Yaman, N. Bai,, Y. K. Huang, M. F. Huang, B. Zhu, T. Wang, and G. Li, "10 x 112Gb/s PDM-QPSK transmission over 5032 km in few-mode fibers," *Optics Express*, vol. 18, no. 20, pp. 21342–21349, Sep. 2010.

[117] R. Ryf, "Optical coupling components for spatial multiplexing in multi-mode fibers," in *Proc. ECOC 2011*, Geneva, Switzerland, 2011.

[118] C. Koebele, M. Salsi, D. Sperti, P. Tran, P. Brindel, H. Mardoyan, S. Bigo, A. Boutin, F. Verluise, P. Sillard, M. Astruc, L. Provost, F. Cerou, and G. Charlet, "Two mode transmission at 2x100Gb/s, over 40km-long prototype few-mode fiber, using LCOS-based programmable mode multiplexer and demultiplexer," *Optics Express*, vol. 19, no. 17, pp. 16593–16600, Aug. 2011.

[119] G. Stepniak, L. Maksymiuk, and J. Siuzdak, "Increasing multimode fiber transmission capacity by mode selective spatial light phase modulation," in *Proc. ECOC 2010*, Torino, Italy, 2010, pp. 1–3.

[120] J. Carpenter and T. D. Wilkinson, "Holographic Mode-Group Division Multiplexing," in *Proc. OFC 2011, Paper OThN3*, Los Angeles, California, 2011.

[121] J.-F. Morizur, "Quantum protocols with transverse spatial modes," Université Pierre et Marie Curie / The Australian National University, Paris / Canberra, 2011.

[122] R. Ryf, S. Randel, C. Schmidt, R.-J. Essiambre, P. J. Winzer, R. Delbue, P. Pupalaikis, A. Sureka, Y. Sun, X. Jiang, D. W. Peckham, A. H. McCurdy, and R. Lingle, "Low-Loss Mode Coupler for Mode-Division-Multiplexed transmission in Few-Mode Fiber," in *Proc. OFC 2012, Postdeadline Papers, Paper PDP5B.5*, Los Angeles, California, 2012.

[123] J. W. Goodman, *Introduction to Fourier Optics*, 2nd ed. McGraw-Hill, 1996.

[124] J. Carpenter and T. D. Wilkinson, "All Optical Mode-Multiplexing Using Holography and Multimode Fiber Couplers," *Journal of Lightwave Technology*, vol. 30, no. 12, pp. 1978–1984, Jun. 2012.

[125] D. Sperti, M. Salsi, C. Koebele, P. Tran, H. Mardoyan, S. Bigo, A. Boutin, P. Sillard, and G. Charlet, "Experimental Investigation of Modal Crosstalk using LCOS-based Spatial Light Modulator for Mode Conversion," in *Proc. ECOC 2011, Paper Th.12.B.2*, Geneva, Switzerland, 2011.

[126] C. Koebele, M. Salsi, D. Sperti, P. Tran, P. Brindel, H. Mardoyan, S. Bigo, A. Boutin, P. Sillard, F. Cerou, and G. Charlet, "Two-Mode Transmission with Digital Inter-Modal Cross-Talk Mitigation," in *Proc. ECOC 2011, Paper Tu.5.B.4*, Geneva, Switzerland, 2011.

[127] M. Salsi, C. Koebele, D. Sperti, P. Tran, H. Mardoyan, P. Brindel, S. Bigo, A. Boutin, F. Verluise, P. Sillard, M. Astruc, L. Provost, and G. Charlet, "Mode-Division Multiplexing of 2 x 100 Gb/s Channels Using an LCOS-Based Spatial Modulator," *Journal of Lightwave Technology*, vol. 30, no. 4, pp. 618–623, Feb. 2012.

[128] J.-F. Cardoso and B. H. Laheld, "Equivariant adaptive source separation," *IEEE Transactions on Signal Processing*, vol. 44, no. 12, pp. 3017–3030, Dec. 1996.

[129] S. Randel, A. Sierra, S. Mumtaz, A. Tulino, R. Ryf, P. J. Winzer, C. Schmidt, and R.-J. Essiambre, "Adaptive MIMO Signal Processing for Mode-division Multiplexing," in *Proc. OFC 2012*, Los Angeles, California, 2012.

Bibliography of the Author

Publications as First Author

[I] C. Koebele, M. Salsi, G. Charlet, and S. Bigo, "Nonlinear Effects in Long-Haul Transmission over Bimodal Optical Fibre," *in Proc. ECOC 2010, Paper Mo.2.C.6*, Torino, Italy, 2010.

[II] C. Koebele, M. Salsi, G. Charlet, O. Bertran-Pardo, J. Renaudier, H. Mardoyan, P. Tran, and S. Bigo, "Impact of Transmitter Bandwidth on Transmission Performance of Coherent 112-Gb/s PDM-QPSK Systems," *IEEE Photon. Technol. Lett.*, vol. 22, no. 24, pp. 1859–1861, Oct. 2010.

[III] C. Koebele, M. Salsi, G. Charlet, and S. Bigo, "Nonlinear Effects in Mode Division Multiplexed Transmission over Few-Mode Optical Fiber," *IEEE Photon. Technol. Lett.*, vol. 23, no. 18, pp. 1316–1318, Jun. 2011.

[IV] C. Koebele, M. Salsi, D. Sperti, P. Tran, P. Brindel, H. Mardoyan, S. Bigo, A. Boutin, F. Verluise, P. Sillard, M. Astruc, L. Provost, F. Cerou, and G. Charlet, "Two mode transmission at 2x100Gb/s, over 40km-long prototype few-mode fiber, using LCOS-based programmable mode multiplexer and demultiplexer," *Optics Express*, vol. 19, no. 17, pp. 16593–16600, Aug. 2011.

[V] C. Koebele, M. Salsi, D. Sperti, A. Boutin, P. Sillard, S. Bigo, and G. Charlet, "Transmission Optique Multiplexée en Mode à 2x100Gb/s sur 40km de Fibre Prototype Légèrement Multimodale," *in Proc. JNOG 2011*, Marseille, France, 2011.

[VI] C. Koebele, M. Salsi, D. Sperti, P. Tran, P. Brindel, H. Mardoyan, S. Bigo, A. Boutin, P. Sillard, F. Cerou, and G. Charlet, "Two-Mode Transmission with Digital Inter-Modal Cross-Talk Mitigation," *in Proc. ECOC 2011, Paper Tu.5.B.4*, Geneva, Switzerland, 2011.

[VII] C. Koebele, M. Salsi, L. Milord, R. Ryf, C. A. Bolle, P. Sillard, S. Bigo, and G. Charlet, "40km Transmission of Five Mode Division Multiplexed Data Streams at 100Gb/s with low MIMO-DSP Complexity," *in Proc. ECOC 2011, Postdeadline Papers, Paper Th.13.C.3*, Geneva, Switzerland, 2011.

Publications as Co-Author

[VIII] O. Bertran-Pardo, J. Renaudier, G. Charlet, M. Salsi, M. Bertolini, P. Tran, H. Mardoyan, C. Koebele, and S. Bigo, "System Benefits of Temporal Polarization Interleaving with 100Gb/s Coherent PDM-QPSK," *in Proc. ECOC 2009, Paper 9.4.1*, Vienna, Austria, 2009.

[IX] M. Salsi, H. Mardoyan, P. Tran, C. Koebele, E. Dutisseuil, G. Charlet, and S. Bigo, "155x100Gbit/s coherent PDM-QPSK transmission over 7200km," *in Proc. ECOC 2009, Postdeadline Papers, Paper PD 2.5*, Vienna, Austria, 2009.

[X] O. Bertran-Pardo, J. Renaudier, G. Charlet, M. Salsi, M. Bertolini, H. Mardoyan, P. Tran, C. Koebele, and S. Bigo, "PDM-QPSK: on the system benefits arising from temporally interleaving polarization tributaries at 100Gb/s," *Optics Express*, vol. 17, no. 22, pp. 19902–19907, Oct. 2009.

[XI] M. Salsi, C. Koebele, P. Tran, H. Mardoyan, S. Bigo, and G. Charlet, "80x100-Gbit/s transmission over 9,000km using erbium-doped fibre repeaters only," *in Proc. ECOC 2010, Paper We.7.C.3*, Torino, Italy, 2010.

[XII] M. Salsi, C. Koebele, P. Tran, H. Mardoyan, E. Dutisseuil, J. Renaudier, M. Bigot-Astruc, L. Provost, S. Richard, P. Sillard, S. Bigo, and G. Charlet, "Transmission of 96×100Gb/s with 23% Super-FEC Overhead over 11,680km, using Optical Spectral Engineering," *in Proc. OFC 2011, Paper OMR2*, Los Angeles, California, 2011.

[XIII] M. Salsi, C. Koebele, D. Sperti, P. Tran, P. Brindel, H. Mardoyan, S. Bigo, A. Boutin, F. Verluise, P. Sillard, M. Astruc, L. Provost, F. Cerou, and G. Charlet, "Transmission at 2x100Gb/s, over Two Modes of 40km-long Prototype Few-Mode Fiber, using LCOS-based Mode Multiplexer and Demultiplexer," *in Proc. OFC 2011, Postdeadline Papers, Paper PDPB9*, Los Angeles, California, 2011.

[XIV] D. Sperti, M. Salsi, C. Koebele, P. Tran, H. Mardoyan, S. Bigo, A. Boutin, P. Sillard, and G. Charlet, "Experimental Investigation of Modal Crosstalk using LCOS-based Spatial Light Modulator for Mode Conversion," *in Proc. ECOC 2011, Paper Th.12.B.2*, Geneva, Switzerland, 2011.

[XV] M. Salsi, C. Koebele, D. Sperti, P. Tran, H. Mardoyan, P. Brindel, S. Bigo, A. Boutin, F. Verluise, P. Sillard, M. Astruc, L. Provost, and G. Charlet, "Mode-Division Multiplexing of 2 x 100 Gb/s Channels Using an LCOS-Based Spatial Modulator," *Journal of Lightwave Technology*, vol. 30, no. 4, pp. 618–623, Feb. 2012.

[XVI] M. Salsi, C. Koebele, G. Charlet, and S. Bigo, "Mode Division Multiplexed Transmission with a weakly-coupled Few-Mode Fiber," *in Proc. OFC 2012*, Los Angeles, California, 2012.

[XVII] M. Salsi, J. Vuong, C. Koebele, P. Genevaux, H. Mardoyan, P. Tran, G. Le Cocq, L. Bigot, Y. Quiquempois, A. Le Rouge, P. Sillard, M. Bigot-Astruc, and G. Charlet, "In-Line Few-Mode Optical Amplifier with Erbium Profile Tuned to Support LP01, LP11, and LP21 Mode Groups," *in Proc. ECOC 2012, Paper Tu.3.F.1,* Amsterdam, Netherlands, 2012.